Methanol dehydration using MFI – the role of framework composition and binder

Alexander Leishman Munnoch

Submitted in partial fulfilment of the requirements for the degree of

Doctor of Philosophy

School of Chemistry

College of Science and Engineering

University of Glasgow

Abstract

Methanol dehydration is currently of industrial interest as a means of dimethyl ether production. Pertinently, dimethyl ether may be used as an alternative LPG fuel. This reaction is acid catalysed and in this study a number of microporous catalysts, containing the unique MFI framework structure, have been investigated. Attention has also been directed towards the application of binders and their effects.

Temperature ranges for selective dimethyl ether formation were found to be 150-275 °C over H-ZSM-5, 300-350 °C over Na-ZSM-5 and 150-350 °C over γ-Al_2O_3 catalysts (where ZSM-5 = MFI zeolites). Comparison of commercial ZSM-5 materials with a wide range of SiO_2/Al_2O_3 ratios (23-1500) showed methanol dehydration to increase with increasing framework aluminium content. B-MFI, Fe-MFI and Ga-MFI zeotypes were synthesised for comparison to zeolites. ^{11}B and ^{71}Ga MAS-NMR measurements showed boron and gallium to be tetrahedrally coordinated within their MFI frameworks. The following ranking of methanol dehydration activity: Al > Ga > Fe > B was observed. Large scale zeolite and zeotype applications require the use of binders such as silicas and aluminas to provide desirable physical properties. Despite their necessity in scale-up, zeolite binding and its effects have been largely ignored and there is a general misconception that they are inert components. Silica binders were found to decrease the activity of the catalyst by dilution, alkali metal poisoning and pore filling. Sodium content had a stronger negative effect than binder dilution and pore blockage on the methanol dehydration activity. Furthermore, increasing sodium content resulted in decreasing extra-framework aluminium formation. Arrenhius plots of sodium-exchanged zeolites showed increasing sodium content to decrease the number of zeolite active sites. The methanol dehydration activity of H-ZSM-5 (1500) was increased in the presence of an alumina binder and the method of binding had little effect on the catalytic activity. A small degree of aluminium insertion into the zeolite framework was indicated by ^{27}Al and ^{29}Si MAS-NMR in bound and aluminium impregnated systems. ^{27}Al and ^{29}Si MAS-NMR also showed the change of the nature of active sites in Arrenhius plots of extremely calcined and extremely steamed aluminium-impregnated ZSM-5 (1500) catalysts to be the result of zeolite dealumination.

Contents

List of figures

List of tables

Acknowledgements

I would like to express my gratitude to the following for enabling and contributing to the completion of this body of work. The University of Glasgow; BP Chemicals Ltd. and the EPSRC for funding my CASE award Ph.D. studentship; Dr. D. J. Price (University of Glasgow) for the kind use of his hydrothermal synthesis equipment, Mrs. K. Wilson (University of Glasgow) for CHN elemental analysis, Mr. J. Gallagher for his assistance with the SEM-EDX imaging; Mr. M. Beglan (University of Glasgow) for assistance with flame photometry; Dr. D. C. Apperley and Mr. A. F. Markwell (University of Durham – EPSRC solid state NMR service) for solid state MAS-NMR measurements and Mr. A. Monaghan (University of Glasgow) for instrument training.

A special thank you must go to my Ph. D. supervisor Dr. J. S. J. Hargreaves for his unwavering encouragement, guidance and patience throughout my time at the University of Glasgow.

A sincere thank you must be extended to my industrial supervisor Dr. G. Armitage (BP Chemicals Ltd.) for his constructive discussions and providing zeolite elemental analyses.

I would also like to thank all of the members of the catalysis group at Glasgow, past and present, for making my time there a memorable one.

Lastly, I would like to express a heartfelt thank you to my family and friends for all of their encouragement and support

Author’s declaration

The work contained within this thesis, submitted for the degree of Doctor of Philosophy, is my own original work, except where due reference is made to others. No material within has been previously submitted for a degree at this or any other university.

List of accompanying material

CD-R containing isothermal catalytic testing results used in the production of Arrenhius plots.

1 Introduction

1.1 Introduction to inorganic molecular sieves

Molecular sieve is a general term, most synonymous with zeolites, used to describe any material with properties sufficient to selectively filter chemicals on the molecular scale. More specifically, the property required is well defined microporosity (pores ≤ 20 Å in diameter) which can be inherent to materials such as zeolites, charcoals, silicas and MOFs (Metal-Organic Frameworks). Of these materials, zeolites and isostructural zeotypes will be the focus of this body of work.

1.1.1 Zeolites and MFI

An account of the history of zeolites is given by Masters and Maschmeyer [1]. Zeolites were first reported in *ca*. 1756 by A. F. Cronsted but it was not until 1948 and the development of the hydrothermal zeolite synthesis method by Barrer that zeolites found wider application. A wide variety of unique framework structures have been recognised and new framework types continue to be discovered (Fig. 1.1) with a steady increase being observed since 1998.

Zeolites are microporous crystalline aluminosilicate materials whose framework comprises extended networks of corner sharing TO_4 tetrahedral units where T = silicon or aluminium. As a general rule, aluminium tetrahedra cannot corner share with other aluminium tetrahedra because of bond strain and will not generally be found neighbouring one another [2]. Corner-sharing silicon tetrahedra are electrically neutral but aluminium tetrahedra are negatively charged and must be compensated with a cationic species, typically alkali metal cations or protons. It is this required charge compensation that provides zeolites with cation-exchange properties. Zeolite cation-exchange is the most utilised property of zeolites worldwide where zeolites are used as water softeners, where harder polyvalent cations preferentially exchange with the softer sodium cations of the zeolite. On the other hand, protonic zeolites may be used as solid acid catalysts for a wide variety of chemical reactions *vide infra*. In use as acid catalysts, the extent of hydration determines the proportions of Brőnsted or Lewis acidity (Fig 1.2).

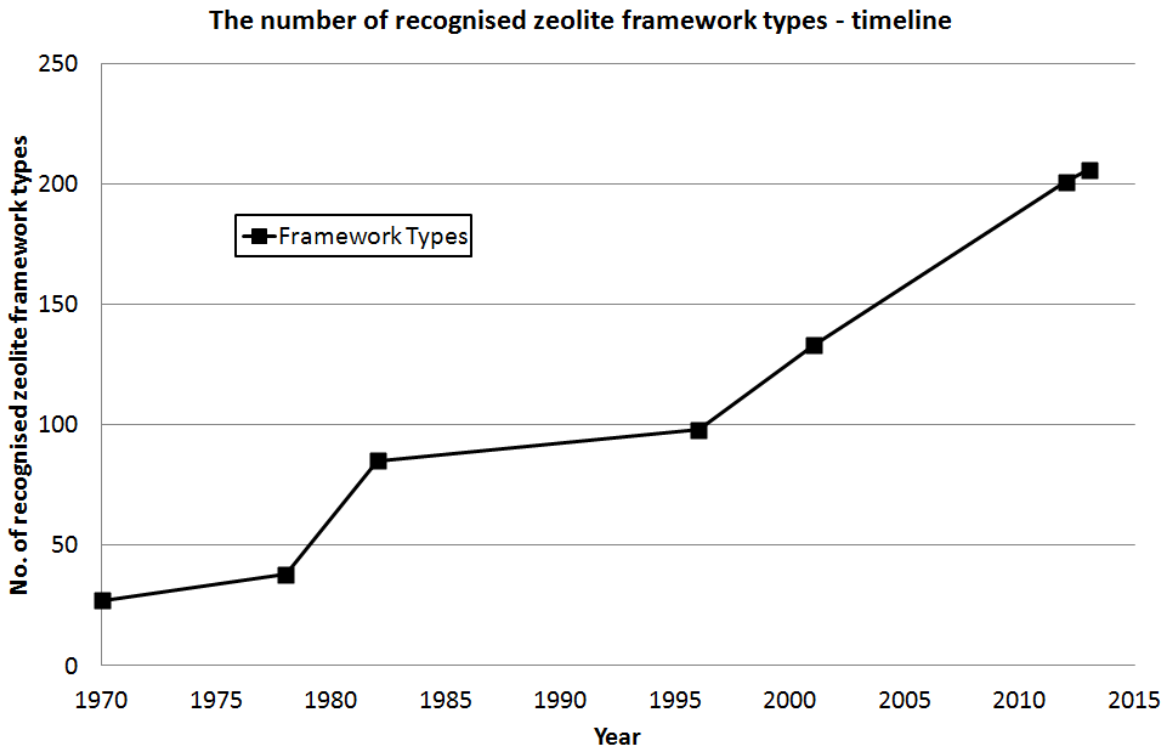

Figure 1.1: Zeolite framework recognition timeline. Data up to 2001 were obtained from ref. [3]. The two most recent data points were obtained from ref. [4] on the 5th of June 2012 and the 12th of September 2013.

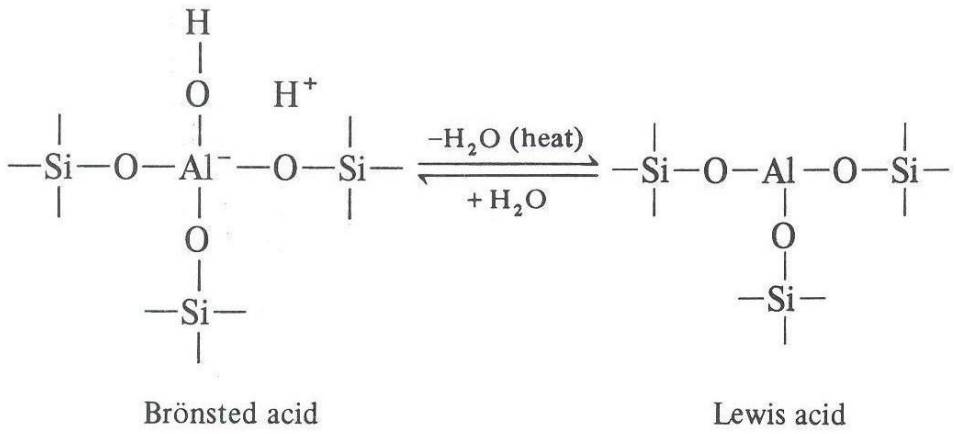

Figure 1.2: Postulated framework silica-alumina acid sites. This figure was obtained from ref. [5].

Of particular interest in this study are zeolites and zeotypes of the MFI (Mobil Five) unit cell structure.

The synthesis of ZSM-5 (Zeolite Socony Mobil Five) which possesses the MFI structure, was patented in 1969 [6] and was originally thought to be a purely synthetic zeolite. Subsequently, a natural analogue has been found at Mt. Adamson in Antarctica and was named Mutinaite [7,8].

ZSM-5 is of key importance to the petrochemical industry because of its unique pore structure (Fig. 1.3). The 3D porous network is constructed of straight vertical channels of diameter *ca*. {5.3 Å – 5.6 Å} and horizontal/sinusoidal channels *ca*. {5.1 Å – 5.5 Å} in diameter. Shape selective catalytic properties of ZSM-5 catalysts arise from these structural features [9,10] whereby the narrow channel dimensions can: exclude large molecules from even entering the pore network; restrict the diffusion of molecules through the network to varying extents; sterically hinder transition states and consequently change the catalyst activity and product distribution. Notably, ZSM-5 is believed to be relatively coke resistant due to the steric constraints imposed by the channel structure [11].

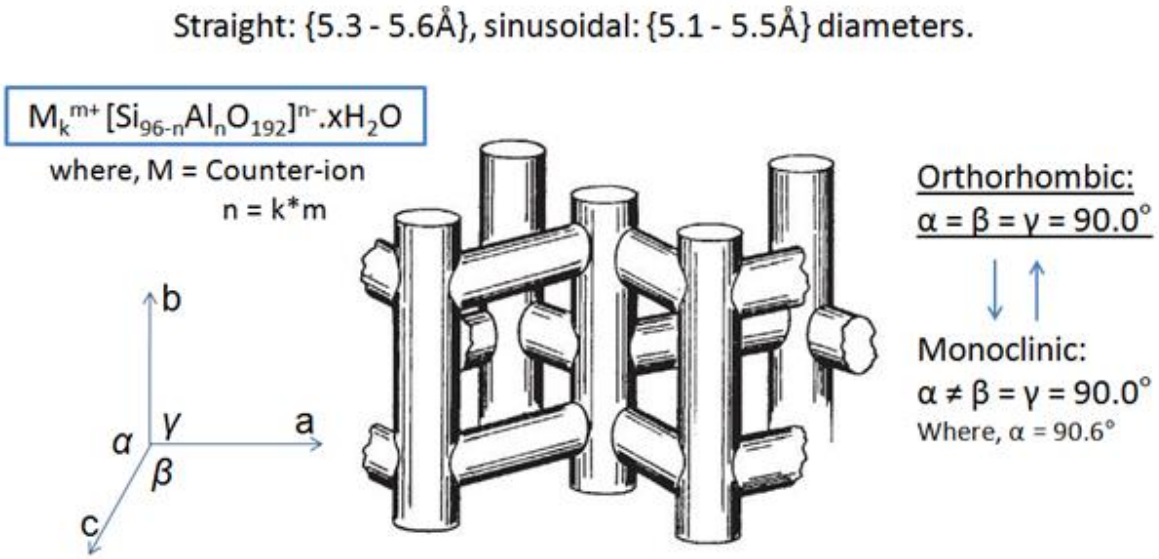

Figure 1.3: An orthorhombic MFI channel structure schematic. This figure was adapted from ref. [12].

1.1.2 **Zeotypes and MFI**

Zeotypes are isostructural with zeolites but contain framework elements other than (or in addition to) silicon, aluminium and oxygen. Examples of zeotypes include

AlPO-34 - an aluminium phosphate with the structure of chabazite [13] and **[**Ga-Al-Si-O**]**-**FAU -** a galloaluminosilicate with the faujasite structure [14].

A wide variety of MFI materials may be synthesised where the inclusion of non-aluminosilicate framework components can allow for an increase in the breadth of chemistry beyond ion-exchange, molecular sieving and acid/base catalysis. In particular, this can include redox chemistry. TS-1 (titanosilicalite-1) is a Ti-MFI zeotype [15] which can be applied to a wide variety of industrially relevant selective oxidation reactions including phenol hydroxylation, propylene epoxidation and cyclohexanone ammoximation when used with hydrogen peroxide [16,17]. The use of TS-1 could be greatly beneficial in the aqueous cyclohexanone ammoximation process particularly as TS-1/H_2O_2 can provide high selectivities and the reactant, H_2O_2, decomposes to water reducing the requirement of waste treatment [18]. The active species is believed to be framework titanium species [19] where extra-framework titanium is believed to activate the H_2O_2 selectively rather than undertake selective oxidation reactions [20]. However, the role of extra-framework titanium species has been recently complicated [21] with results indicating a synergetic effect between framework titanium and low levels of extra-framework anatase-like titanium species.

Although synthesised as zeotype materials, the redox active species of Fe-MFI and Ga-MFI zeotypes are believed to be extra-framework [22-24].

1.2 Introduction to binders

Binders are required as an adhesive to aggregate materials allowing them to be formed into bodies of desirable shape and size (Fig. 1.4).

Figure 1.4: Shaped catalysts. This figure was kindly provided by BP Chemicals Ltd.

Commonly both organic (e.g. polymerised alcohols, cellulose ethers, glycols etc.) and inorganic (silicas, aluminas and clays etc.) binders are suitable for this task [25]. However, only common inorganic binders are sufficiently abundant, cheap and physically robust (following thermal treatment) for large scale petrochemical processing. The physical durability of thermally processed inorganic binders is imparted by inter-particle cross-linking *via* dehydration of terminal hydroxyl groups [26]. This cross-linking may not be exclusive to the binder phase and may also include zeolite or zeotype components.

The primary functions of a binder are to: increase control over catalyst body shape and size; increase mechanical strength and increase attrition resistance where necessary. Despite their perceived chemically inert properties, a number of effects of binders upon catalytic performance have been recently reviewed [27] and sub-divided into the following categories:

(i) modification of the catalyst coking characteristics,

(ii) entrapment of poisons,

(iii) transfer of chemical species to or from the active phase,

(iv) modification of heat transfer/thermal characteristics

(v) modification of porosity characteristics,

(vi) improvement of physical durability.

It may be overly simplistic to make these sub-divisions because of the possibility of inter-relationship between them. For example, the transfer of chemical species to or from the active phase may impact upon the coking characteristics.

Of the typical inorganic binders previously mentioned, silicas and aluminas are of particular interest in this study.

1.2.1 **Silica**

Silicas are one of the most abundant minerals in the Earth's crust and exhibit a rich diversity of structures (Fig. 1.5).

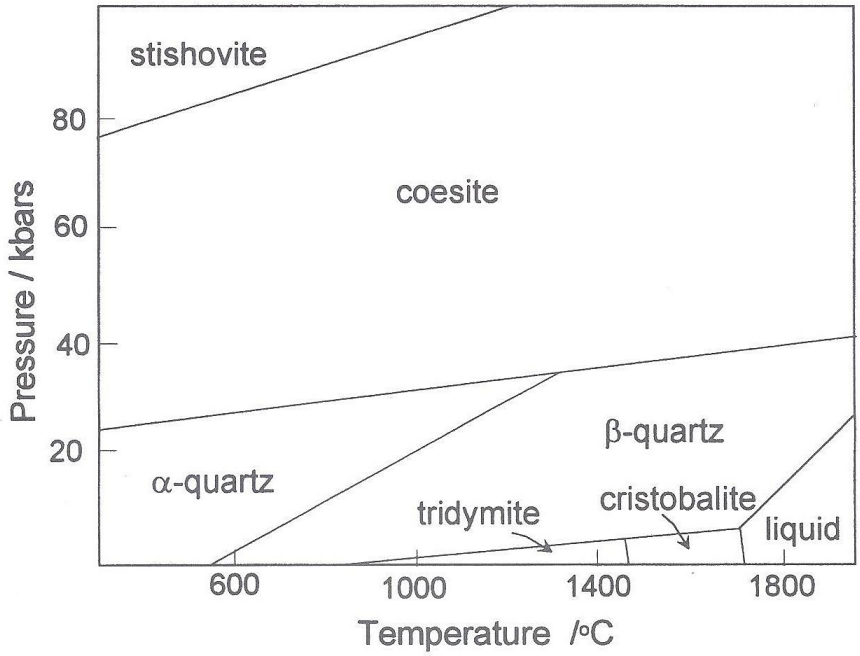

Figure 1.5: The pressure and temperature dependent phase diagram of SiO_2**.** This figure was taken from ref. [28]

Silica may form several polymorphs (Fig. 1.5) but are commonly found as glasses better described as continuous random networks (Fig. 1.6). These networks, although not displaying long-range order, may exhibit short-range order where 4-7

member ring structures are preferentially formed. The short range order may even be close to that of the crystalline forms [30]. However, long-range order is not generally observed because of the freedom of rotation around the bridging oxygen atoms during the crystallisation process.

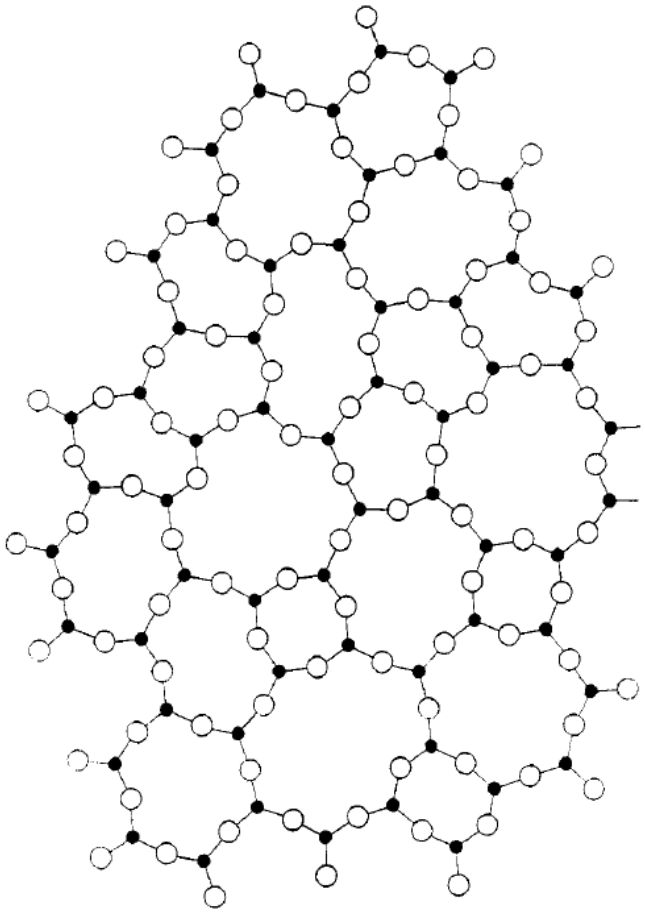

Figure 1.6: A typical random network from the Zachariasen model for a 2D A_2O_3 glass (where A = Trivalent cation). This figure was obtained from ref. [29].

Silicas applied to catalysis are typically prepared by dissolving alkali metal silicates (e.g. ortho-, meta- and phyllosilicates). Acid dissolution forms silicic acid which may undergo self-condensation to form silica hydrogel. Basic dissolution, with appropriate pH control, may form sols or (with drying) hydrogels. Both hydrogels and sols are common catalyst binders. Calcination of the hydrogel or sol results in a porous silica xerogel. This xerogel is the porous silica matrix of a silica-bound catalyst [31]. Further structural, textural and catalytic properties will be described in

chapter 5 but it is widely considered that silica matrices are inactive in most petrochemical processes.

1.2.2 **Alumina**

Aluminium oxides are also abundant minerals with a rich diversity of structures (Fig.1.7). Corundum, or α-Al_2O_3, is commonly employed as an abrasive because of its high mechanical strength and is a common constituent of ceramics. Gibbsite, boehmite and bayerite may be used as zeolite binding materials, which following partial dehydration may form transitional aluminas (chi, eta, gamma, kappa or theta depending on the source) which have desirable chemical and physical properties for use in petrochemical catalysts.

Conditions favoring transformations

Conditions	Path *a*	Path *b*
Pressure, atm	> 1	1
Atmosphere	Moist air	Dry air
Heating rate, °C/min	> 1	< 1
Particle size, μm	> 100	< 10

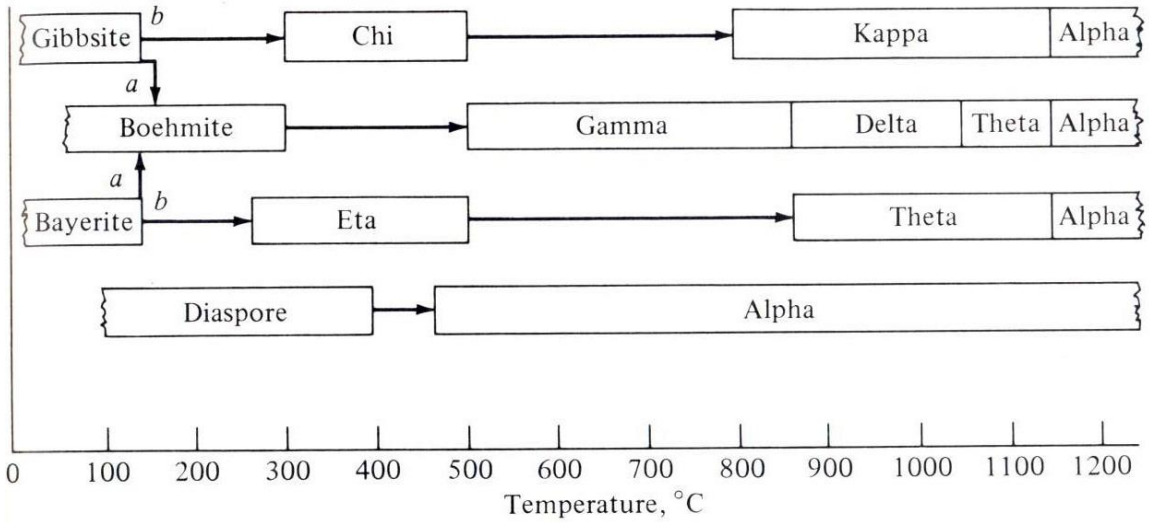

Figure 1.7: The temperature dependent phase diagram of alumina**.** This figure was obtained from ref. [31].

Of specific interest in this study are boehmite and γ-Al_2O_3. Boehmite, a commonly employed binder and alumina precursor, may be produced from gibbsite which is produced by the Bayer Process. This involves dissolution of bauxite (aluminium ore) in sodium hydroxide at *ca*. 175 °C to produce a mixture of $Al(OH)_{3(aq)}$ and 'red mud'. 'Red mud', so named because of its high iron oxide content, is removed by filtration and disposed of whilst the $Al(OH)_{3(aq)}$ precipitates upon cooling to form gibbsite. The layered structure of boehmite is built from distorted edge-sharing [AlO_6] octahedra [32] (Fig. 1.8).

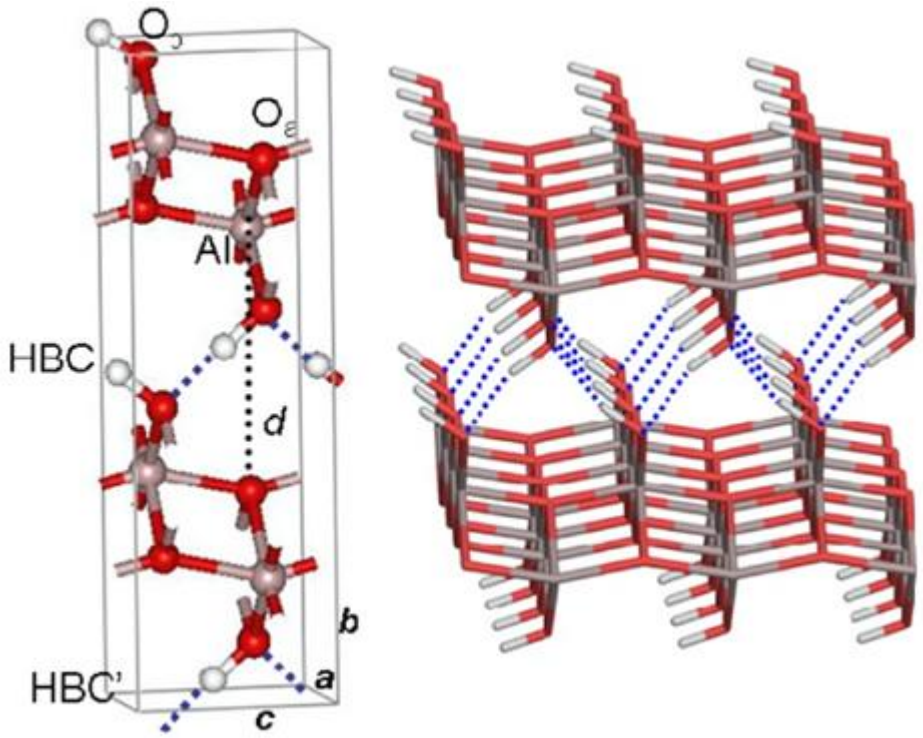

Figure 1.8: Boehmite crystal structure**.** Grey = Aluminium, Red = Oxygen and White = Hydrogen. This figure was obtained from ref. [33].

Boehmite may be transformed into mesoporous γ-Al_2O_3 by calcination. Further structural, textural and catalytic properties will be described in chapter 6 but it is generally accepted that alumina matrices are catalytically active particularly where Lewis acidity can impact upon a reaction.

1.2.3 **Binder-free zeolites**

Although binders are generally required for the production of technical catalysts, macrosized binder-free zeolite catalysts may be produced with sufficient durability for use in some reactor systems. This has been achieved by grafting the zeolite to a support using partial dissolution [34] and the hydrothermal crystallisation of pre-formed zeolite precursor extrudates [35]. Ozcan and Kalipclar prepared a non-zeolitic extrudate consisting of HEC (Hemi-Ethyl Cellulose) solution and amorphous aluminosilicate powder. Following drying at room temperature and calcination to remove the HEC organic binder the extrudates were subjected to hydrothermal crystallisation, converting the amorphous aluminosilicate into zeolite A. It was proposed that the zeolite A extrudates retained their shape and moderate mechanical strength because of the rapid growth and intergrowth of zeolite A crystals and the slow dissolution of the amorphous precursor. The crush strength of the extrudates following zeolitisation may be as high as 0.4 MPa for samples calcined at 600 °C. It should also be noted that zeolite crystals formed on the external surfaces of the extrudate have undergone more extensive crystallisation than those of the internal surfaces presumably because of diffusion limitations during the crystallisation treatment.

1.2.4 **Bound zeolite catalysis**

Despite the existence of binder-free zeolite catalysts, technical catalysts are required to be much more physically robust with a prime example being FCC (Fluidised Catalytic Cracking) catalysts. In catalysis, the largest use of zeolites is the use of highly tailored zeolite Y (faujasite) containing catalysts for FCC of crude oil fractions [36]. Heavier fractions are cracked to more valuable lighter fractions and this process is currently undertaken in riser reactors (Fig. 1.9) with fluidised catalyst beds.

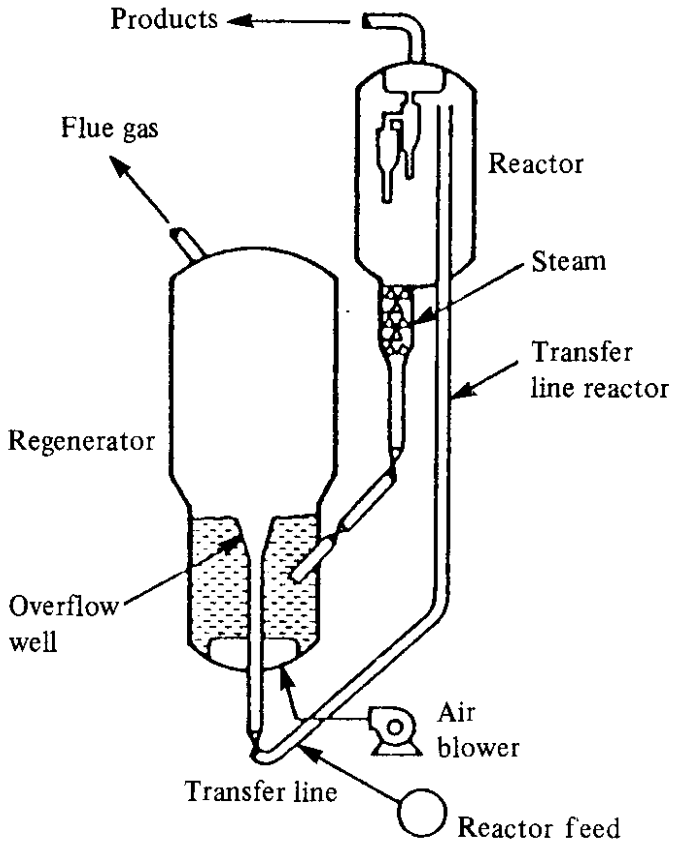

Figure 1.9: A typical FCC riser-regenerator reactor**.** This figure was obtained from ref. [31].

In a riser reactor, the feed is vaporised and contacted with the fluidised catalyst bed. The catalyst cracks the fraction and the new lighter products are collected at the top of the reactor. Cracking rapidly cokes the FCC catalyst, resulting in deactivation after which the bed is then cycled through a steam regenerator and back to the riser. In order to fluidise the bed, catalyst particles must be small and consistently sized to be circulated through the reactor. To achieve this, the catalysts are prepared by spray-drying. Furthermore, the extreme conditions, coupled with the high velocity circulation of the catalyst bed in FCC processing, requires the catalysts to be very robust. Both the mechanical strength towards impact and attrition resistance towards grinding have a major impact on the lifetime of the FCC catalyst [37]. These catalysts typically contain 10 - 50 wt. % zeolite, 50 - 90 wt. % matrix and 0 - 10 wt. % additives [38]. The relatively high matrix to zeolite content may be surprising given that the matrix is relatively chemically

inactive but it is essential for shaping/sizing, physical durability, heat and mass transfer and ultimately optimisation of catalyst performance [27].

The literature documenting binder effects is sparse for methanol dehydration. The work of Vishwanathan *et al*. [39] investigated the use of partially sodium-exchanged H-ZSM-5 catalysts for methanol dehydration of crude (20 - 30 % water containing) methanol. They observed that high-silica zeolites such as ZSM-5 are both more active and hydrophobic than typical γ-Al_2O_3 dehydration catalysts. Sodium-modified zeolites were completely selective to DME between 230-340 °C. The lack of coke and hydrocarbon formation at higher temperatures was attributed to the neutralisation of strong acid sites following partial sodium-exchange. Competitive adsorption of water to dehydration catalysts is a major issue and water content in the feed is minimised because of this, by expensive distillation. Furthermore, if high-silica zeolites are more tolerant to the effects of competitive methanol and water adsorption than aluminas, the use of zeolites may ultimately lead to decreased running costs Continuation of this research extended into the inclusion of an alumina binder [40]. In addition to the partial sodium-exchange, dispersion of the zeolite component through the alumina matrix allows the alumina to act as a heat sink. This prevents the formation of localised hotspots and therefore more extensive reaction leading to hydrocarbon formation even at temperatures as high as 380 °C.

1.3 Dimethyl ether production

1.3.1 Methanol dehydration

Methanol dehydration is currently the most common method of dimethyl ether production. Its production is currently of widespread interest because of its potential use as an alternative (clean burning) fuel, aerosol propellant and refrigerant [41,42].

Methanol dehydration is an exothermic process and two regimes may be envisaged (Fig 1.10):

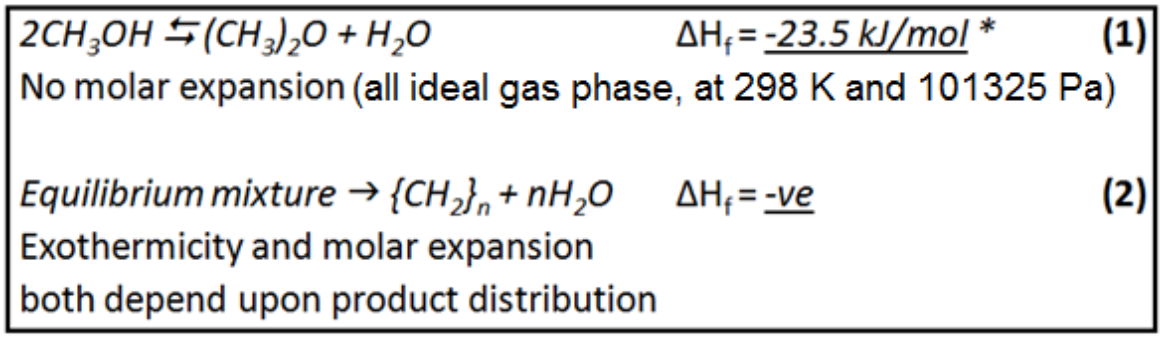

Figure 1.10: Methanol dehydration reaction scheme. * the ΔH_f values were determined from ref. [43].

Regime (1) is the lower temperature methanol dehydration to dimethyl ether reaction and regime (2) is the higher temperature hydrocarbon formation reaction. Both methanol and dimethyl ether may be converted to hydrocarbons with increasing temperature [44].

The methanol dehydration to dimethyl ether reaction mechanism is believed to proceed *via* the bi-molecular interaction of adsorbed species. Knőzinger *et al*. believed the mechanism to proceed sequentially *via* the interaction of aluminium alkoxide species with neighbouring molecularly adsorbed methanol over alumina [45]. Recently, computational studies by Carr and co-workers suggested a route from neighbouring adsorbed methanol molecules to occur over Keggin polyoxometallate clusters and H-BEA zeolite [46]. The work of Ha *et al*. refers to the range of proposed reaction pathways for methanol dehydration to dimethyl ether [47]. Their own findings, over Brőnsted acid sites, were consistent with a proposed sequential pathway with dimethyl ether formation occurring *via* the condensation of adsorbed methyl carboxonium cations (Zeo^- - $CH_3OH_2^+$) with adsorbed carbenium ions (Zeo^- - CH_3^+).

1.3.2 Syngas to dimethyl ether

An alternative to methanol dehydration as a means of dimethyl ether production is the direct syn-gas to dimethyl ether process which may employ a composite of modified H-ZSM-5 and methanol synthesis catalyst ($Cu/ZnO/Al_2O_3$) [48,49]. DME production from syngas may become more cost effective than methanol

dehydration as the technology matures [50]. However, optimisation of the process and the bifunctionality of the hybrid catalyst would not be trivial [51].

1.4 Scope of thesis

This thesis aims to establish: reaction conditions for methanol conversion to dimethyl ether; which of B-MFI, Al-MFI, Fe-MFI and Ga-MFI solid acid catalysts provides the greatest selective methanol conversion rate and the effects of silica-sol and boehmite binding. In addition to the binding studies, partially sodium-exchanged and aluminium-impregnated zeolites were studied to differentiate the effects of sodium content and extra-framework aluminium species from those of the binder materials. As noted in a recent review, the effects of binders on zeolite catalysis are generally underappreciated by the academic community and further elucidation of their behaviour is of interest [27].

1.5 References

[1] A. F. Masters and T. Maschmeyer, Microp. Mesop. Mater., 142 (2011) 423-438.

[2] W. Lőwenstein, Am. Miner., 39 (1954) 92.

[3] Atlas of zeolite framework types, 5th rev. Ed., (2001), Ch. Baerlocher, W. M. Meier and D. H. Olson, ISBN: 0444507019.

[4] www.iza-structure.org/databases/ (accessed on the 5th of June 2012 and the 12th of September 2013).

[5] C. N. Satterfield, Heterogeneous Catalysis in Practice, 2nd Ed., (1991) p210, ISBN: 0070548862.

[6] R. J. Argauer, D. H. Olson and G. R. Landolt, G.B. Patent 1161974 (1969).

[7] E. Galli, G. Vezzalini, S. Quartieri, A. Alberti and M. Franzini, Zeolites, 19 (1997) 318-322.

[8] G. Vezzalini, S. Quartieri, E. Galli, A. Alberti, G. Cruciani and A. Kvick, Zeolites, 19 (1997) 323-325.

[9] M. Stőcker, Microp. Mesop. Mater., 82 (2005) 257-292.

[10] M. Richter, W. Fiebig, H. G. Jerschkewitz, G. Lischke and G. Ohlmann, Zeolites, 9 (1989) 238-245.

[11] S. M. Csicsery, Zeolites, 4 (1984) 202-213.

[12] E. L. Wu, S. L. Lawton, D. H. Olson, A. C. Rohrman Jr. and G. T. Kokotailo, J. Phys. Chem., 83, 27 (1979) 2777-2781.

[13] M. M. Harding, and B. M. Kariuki, Acta Crystallogr., C50 (1994) 852-854.

[14] M. L. Occelli, A. E. Schweizer, C. Fild, G. Schwering, H. Eckert and A. Auroux, J. Catal., 192 (2000) 119-127

[15] M. Taramasso, G. Perego and B. Notari, U. S. Patent: 4410501 (1983).

[16] C. Perego, A. Carati, P. Ingallina, M. Angela Mantegazza and G. Bellussi, Appl. Catal. A: Gen., 221 (2001) 63-72.

[17] H. Ichihashi and H. Sato, Appl. Catal. A: Gen., 221 (2001) 359-366.

[18] M. A. Mantegazza, G. Petrini, G. Spano, R. Bagatin and F. Rivetti, J. Mol. Catal. A: Chem., 146 (1999) 223-228.

[19] N. Wilde, C. Worch, W. Suprun and R. Gläser, Microp. Mesop. Mater., 164 (2012) 182-189.

[20] D. R. C. Huybrechts, P. L. Buskens and P. A. Jacobs, Stud. Surf. Sci. Catal., 72 (1992) 21-31.

[21] C. Liu, J. Huang, D. Sun, Y. Zhou, X. Jing, M. Du H. Wang and Q. Li, Appl. Catal. A: Gen., 459 (2013) 1-7.

[22] J. B. Taboada, A. R. Overweg, P. J. Kooyman, I. W. C. E. Arends and G. Mul, J. Catal., 231 (2005) 56-66.

[23] G. Giannetto, R. Monque and R. Galiasso, Catal. Rev. –Sci. Eng., 36(2) (1994) 271-304.

[24] R. Fricke, H. Kosslick, G. Lischke and M. Richter, Chem. Rev., 100 (2000) 2303-2405.

[25] R. Moreno, J. Am. Ceram. Soc. Bull., 71 (1992) 1647-1657.

[26] J. Freiding, F.-C. Patcas and B. Kraushaar-Czarnetzki, Appl. Catal. A: Gen., 328 (2007) 210–218

[27] J. S. J. Hargreaves and A. L. Munnoch, Catal. Sci. Technol., 3 (2013) 1165-1171.

[28] A. R. West, Basic Solid State Chemistry, 2nd Ed. (1999) p267, ISBN: 9780471987567.

[29] W. H. Zachariasen, J. Am. Chem. Soc., 54 (1932) 3841-3851.

[30] D. E. Polk, J. Non-Cryst. Solids, 5 (1971) 365.

[31] C. N. Satterfield, Heterogeneous Catalysis in Practice, 2nd Ed., (1991), ISBN: 0070548862.

[32] B.C. Lippens, Ph.D. Thesis, Delft University (1961).

[33] D. Tunega, H. Pasalic, M. H. Gerzabek and H. Lischka, J. Phys.: Condens. Matter, 23 (2011) 404201.

[34] J. E. Antia and R. Govind, Appl. Catal. A: Gen., 131 (1995) 107.

[35] A. Ozcan and H. Kalipclar, Ind. Eng. Chem. Res., 45 (2006) 4977-4984.

[36] J. Scherzer, Stud. Surf. Sci. Catal., 76 (1993) 145-183.

[37] R. Boerefijn, N. J. Gudde and M. Ghadiri, Adv. Powder Technol., 11 (2000) 145-174.

[38] J. Scherzer, Appl. Catal., 75 (1991) 1-32.

[39] V. Vishwanathan, K.-W. Jun, J.-W. Kim and H.-S. Roh, Appl. Catal. A: Gen., 276 (2004) 251-255.

[40] S. D. Kim, S. C. Baek, Y.-J. Lee, K.-W. Jun, M. J. Kim and I. S. Yoo, Appl. Catal. A: Gen., 309 (2006) 139–143.

[41] G. R. Moradi, J. Ahmadpour and F. Yaripour, Chem. Eng. J., 144 (2008) 88-95.

[42] T. A. Semelsberger, R. L. Borup and H. L. Greene, J. Power Sources, 156 (2006) 497-511.

[43] D. R. Stull, E. F. Westrum and G. C. Sinke, The Chemical Thermodynamics of Organic Compounds, Robert E. Krieger Publishing Company (1987) Malabar Florida, ISBN: 0898747066.

[44] C. D. Chang and A. J. Silvestri, J. Catal., 47 (1977) 249-259.

[45] H. Knőzinger, A. Scheglila and A. M. Watson, J. Phys. Chem., 78, 8 (1968) 2770-2774.

[46] R. T. Carr, M. Neurock and E. Iglesia, J. Catal., 278 (2011) 78-93

[47] K.-S. Ha, Y.-J. Lee, J. W. Bae, Y. W. Kim, M. H. Woo, H.-S. Kim, M.-J. Park and K.-W. Jun, Appl. Catal. A: Gen., 395 (2011) 95-106

[48] Haldor Topsøe, U. S. Patent: 4536485 (1993).

[49] Haldor Topsøe, U. S. Patent: 5189203 (1993).

[50] M. Xu, J. H. Lunsford, D. W. Goodman and A. Bhattacharyya, Appl. Catal. A: Gen., 149 (1997) 289-301.

[51] Y. Fu, T. Hong, J. Chen, A. Auroux and J. Shen, Thermochimica Acta, 434 (2005) 22-26.

2 Experimental

This chapter covers all of the work undertaken in addition to specific experimental details which will accompany results where necessary. All zeolites and zeotypes studied were of MFI framework type and as such the ZSM-5 or MFI descriptors are generally omitted.

The following tables collate all of the zeolite materials studied (Table 2.1), binder materials employed (Table 2.2) and all the gases and solutions used for catalytic testing and material analyses and syntheses (Table 2.3). All zeolites and binders were obtained from commercial suppliers. Some zeolites were procured directly from the manufacturers whereas others were supplied by BP Chemicals. Ltd. Zeotypes were hydrothermally synthesised in-house as will be described in section 2.3.

Zeolite ZSM-5 Material	Description	Manufacturer/Supplier	Alkali metal content (wt. %)
CBV 2314	NH_4(23)	BP Chemicals Ltd.	≤ 0.05
CBV 5524G	NH_4(50)	Zeolyst International	≤ 0.05
CBV 8014	NH_4(80)	BP Chemicals Ltd.	≤ 0.05
CBV 28014	NH_4(280)	BP Chemicals Ltd.	≤ 0.05
HSZ-890HOA	Na(1500)	Tosoh International	≤ 0.07

Table 2.1: Zeolite materials. NH_4 and Na denote the zeolite charge balancing counter ions (NH_4^+ or Na^+), the values in brackets correspond to the SiO_2/Al_2O_3 ratio provided by the manufacturer or supplier and the alkali metal contents correspond to those provided by the supplier.

Binder Material	Manufacturer/Supplier	Alkali metal content (wt. %)
Ludox AS-40 colloidal silica	Sigma-Aldrich	0.05*
Ludox HS-40 colloidal silica	Sigma-Aldrich	0.24*
Pural SCF 55 (boehmite)	Sasol / BP Chemicals Ltd.	≤ 0.01

Table 2.2: Binder materials. * = sodium content as determined by flame photometry of the dried gel.

The binder materials include two colloidal silica (in water) sols; Ludox AS-40 (NH_4^+ counter ion) and Ludox HS-40 (Na^+ counter ion) which are common precursors to silica matrices and Pural SCF 55 (a common boehmite precursor to transitional alumina catalysts). Both Ludox colloidal suspensions contained 40 wt. % silica in H_2O. The alkali metal contents correspond to those provided by the supplier except where stated.

Gases, liquids and solution	Content	Manufacturer/ Supplier	Usage
Pureshield Argon	Ar, ≥ 99.998 % pure	BOC	Carrier gas, *in situ* PXRD
OFN (Oxygen Free Nitrogen)	N_2, ≥ 99.998 % pure	BOC	Surface area and thermal analyses
He	He, ≥ 99.998 % pure	BOC	Surface area analysis
Air	21 ± 0.5 % O_2, N_2 balance	BOC	Thermal analysis
H_2/N_2	5 % H_2, N_2 balance	BOC	Thermal analysis
O_2/Ar	2 % O_2, Ar balance	BOC	Thermal analysis
MeOH	Methanol ≥ 99.8 %	Sigma-Aldrich	Catalytic test reactant
DME	DME, ≥ 99.8 % pure	BOC	Reaction product calibration
$CDCl_3$	$CDCl_3$, ≥ 99.8 % pure	Oxford Isotope Laboratories	^1H- liquid-NMR standard/solvent
$Al(NO_3)_3 .9H_2O$	≥ 98 % pure	Sigma-Aldrich	Aluminium impregnation
Standard sodium solution	1000 ppm $NaNO_3$ in 1M $HNO_{3(aq)}$	Fisher Scientific	Flame photometry calibration

Table 2.3: Gases, liquids and solutions.

2.1 Catalyst preparation

Catalyst preparation is summarised in the following sections as well as briefly in experimental captions which will accompany relevant results and discussion chapters.

2.1.1 Ion-exchange

All ion-exchange treatments were carried out using $NH_4NO_{3(s)}$ (BDH 99.5 %) or $NaNO_{3(s)}$ (Hopkin and Williams 99.5 %) dissolved in appropriate quantities of deionised H_2O. Na^+-forms were produced *via* a treble exchange with 1M (pH 7) $NaNO_{3(aq)}$ at room temperature for 1 h; NH_4^+-forms were produced *via* a treble exchange with 1M (pH 5) $NH_4NO_{3(aq)}$ at room temperature for 1 h for each exchange. Partial Na^+-exchange was achieved using 0.05M or 1M (pH 7) $NaNO_{3(aq)}$ and a single exchange procedure at room temperature for 1 h. Solutions were vacuum filtered through ashless Whatman No. 542 filter paper and the residue was washed repeatedly with deionised H_2O and oven dried at 110 °C overnight. The supplied zeolites of NH_4^+-form underwent no ion-exchange prior to the production of the H^+-form.

2.1.2 Impregnation

Aluminium impregnated NH_4^+-form silicalite, $NH_4Al(1500)$, was prepared *via* incipient wetness impregnation of 1M $Al(NO_3)_{3(aq)}$, pH ≈ 2.5. The inclusion of 'Al' denotes impregnated samples. A nominal loading of 4 wt. % aluminium was applied. The material was then oven dried overnight at 110 °C. CHN elemental analyses provided an aluminium loading of 4.59 ± 0.07 wt. % on $NH_4(1500)$ – as determined by CHN elemental analyses *via* nitrate content (see section 6.3.1).

2.1.3 Pelleting and sieving

All samples were pelleted under 2.25 tonnes/cm^2 pressure using a 13 mm i.d. Specac stainless steel die prior to sieving to between 250-425 μm and then calcination. Material not within the 250-425 μm sieving fraction was recycled into additional pellets. Tests undertaken demonstrated that inclusion of the pelleting

step had no observable effect on the catalytic activity or crystallinity of the pressed materials although a decrease in mesoporosity of the silica materials was observed (see section. 5.1.2).

2.1.4 Calcination and steaming

Following pelleting and sieving, materials were calcined in a horizontal Carbolite MTF 12/38/400 furnace with quartz furnace tube and quartz calcination boat. All calcinations were carried out under an air flow of 10 mL/min. Calcination employed a temperature programme of room temperature to 550 °C at 10 °C/min and followed by holding at 550 °C for 4 h. Extreme calcination required a temperature programme of room temperature to 750 °C at 10 °C/min followed by holding at 750 °C for 72 h. Samples were allowed to cool in the furnace under an air flow. Calcination boat packing, as observed in Fig. 2.1 was undertaken to minimise the effects of deep-bed steaming (a source of calcined sample inhomogeniety). Steam is evolved from samples during calcination; steam evolved from the bottom of the bed must pass through the material above it. As will be shown in chapters 5 and 6, steam can cause significant changes in the materials included in this study. As such, a shallow bed serves to minimise the differing extents of steaming throughout the material during calcination.

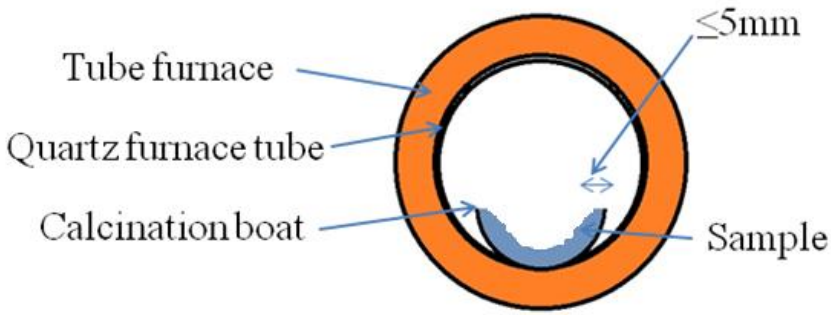

Figure 2.1: Calcination boat. (Schematic not to scale). By minimising calcination bed depth; deep-bed steaming (a source of calcined sample inhomogeniety) is also minimised.

A horizontal fixed-bed plug-flow reactor was employed to undertake all steaming preparations (Fig. 2.2). The catalyst materials, prior to steaming, were sieved to a

particle size of 250-425 μm and calcined at 550 °C for 4 h. Ar carrier gas (20 mL/min) was bubbled through deionised H_2O at 85 °C to produce an approximately 1/2 H_2O in Ar gas mixture (Fig. 2.3).

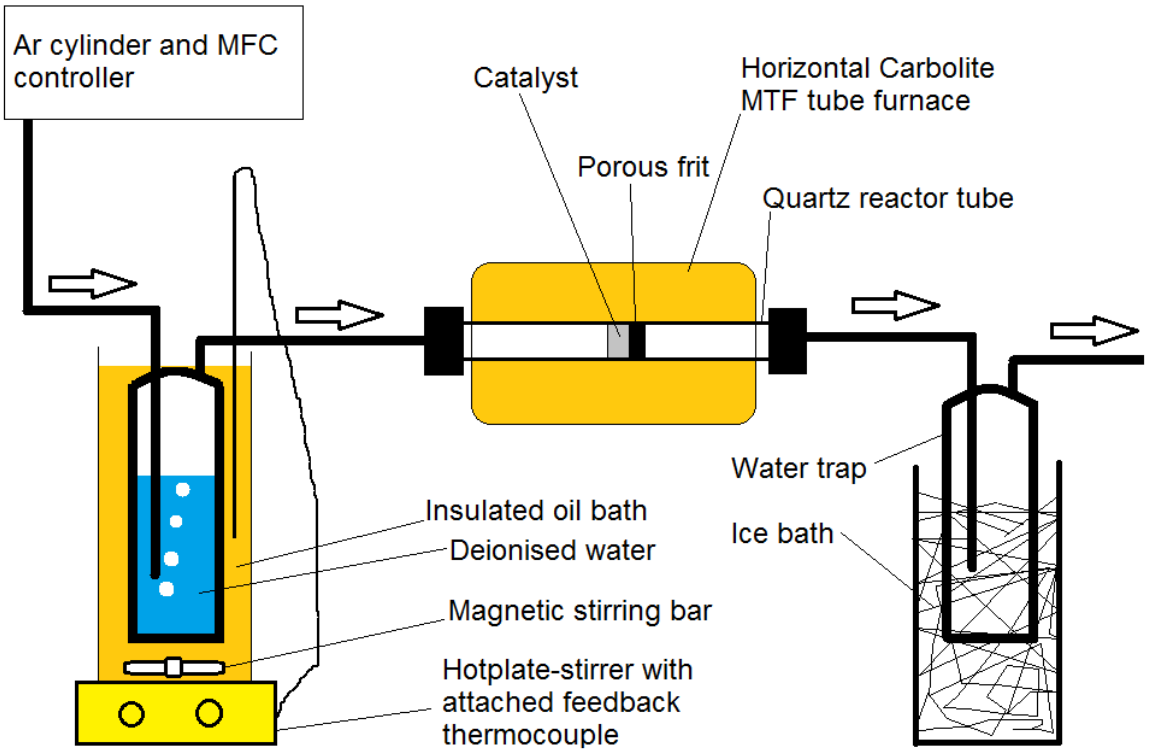

Figure 2.2: Steaming reactor. (Schematic not to scale).

The mass of H_2O in the bubbler prior to commencement of the steaming treatments was *ca*. 40 g. Steaming required a temperature programme of room temperature to 550 °C at 10 °C/min followed by holding at 550 °C for 4 h. Extreme steaming required a temperature programme of room temperature to 750 °C at 10 °C/min followed by holding at 750 °C for 72 h. Once either temperature programme was completed, the sample was allowed to cool under continued Ar flow and the bubbler was cooled with an ice bath.

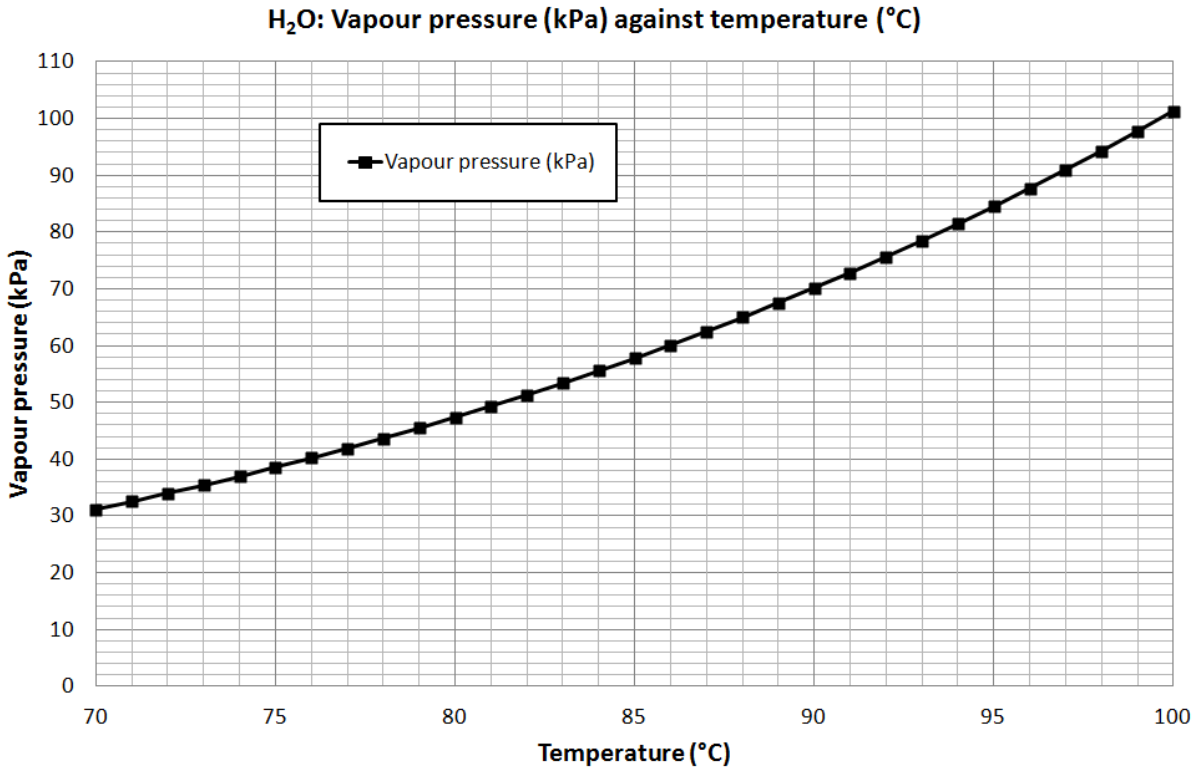

Figure 2.3: Water vapour pressure graph. This information was taken from ref [1]. H_2O vapour pressure increases with increasing temperature towards its boiling point.

Thermally or hydrothermally treated samples are named such that their treatment is stated at the end of their name, for example – H(23) 550 4 h. The treatments are summarised in Table 2.4.

Material	Description
550 4 h	Calcined at 550 °C for 4 h
Steamed	Steamed at 550 °C for 4 h
750 72 h	Calcined at 750 °C for 72 h
Extremely steamed	Steamed at 750°C for 72 h*

Table 2.4: Sample treatment nomenclature. * = It should be noted that during the extreme steaming, all of the H_2O within the bubbler was evaporated after *ca*. 6 h.

2.2 Bound zeolite preparation

Silica-bound and alumina-bound zeolites were prepared by different routes. For silica-bound catalysts, a series of binder-zeolite mixtures were prepared to examine the effects of the binder dilution on the resultant catalyst. For the alumina-bound catalysts, three different binder-zeolite mixing methods were employed to examine the effects of the mixing method on the properties of the resultant catalyst. These were dry-mull mixing, wet-mull mixing and peptisation. Once pelleted and sieved, the bound materials were calcined. An additional steaming treatment was also applied to samples where stated.

2.2.1 Silica binding

Binding with silica sol was achieved by gradual addition of appropriate quantities of uncalcined and unpelleted zeolite into a hand-stirred beaker of silica/water sol of which mixing continued for approx. 5 mins until visibly homogeneous. Manual mixing was employed because of the differing viscosities of the mixtures. Samples were dried overnight at 110 °C, pelleted and sieved. The resultant silica-bound catalysts possessed activated zeolite contents of 75 wt. %, 50 wt. %, 25 wt. % and 12.5 wt. %.

2.2.2 Dry-mull mixing

Dry-mull mixing required the physical mixing of appropriate dry mass percentages of uncalcined binder and zeolite. This was done initially in a sealed Pyrex® beaker in which the mixture was shaken by hand for approx. 5 mins until visably homogeneous prior to dry-mulling using a mortar and pestle, pelleting and sieving.

2.2.3 Wet-mull mixing

Wet-mull mixing required the physical mixing of appropriate dry mass percentages of uncalcined binder and zeolite. This was done initially in a sealed Pyrex® beaker in which the mixture was shaken by hand for approx. 5 mins until visably homogeneous prior to incipient wetness mulling with deionised H_2O using a mortar

and pestle. This was followed by oven drying overnight at 110 °C, pelleting and sieving.

2.2.4 **Peptisation**

Peptisation of a silicalite/boehmite mixture was carried out following a procedure adapted from ref. [2]. A dry mass mixture of 15.00 g of NH_4(1500) and 15.00 g of boehmite was shaken in a sealed Pyrex® beaker for approx. 5 mins until visibly homogeneous, slurried using 30.0 mL of deionised H_2O then peptised by dropwise addition of 5.25 mL of 7 wt. % $HNO_{3(aq)}$ to produce a thick paste. This was followed by drying overnight at 110 °C, pelleting and sieving.

2.3 Zeotype syntheses

All MFI framework zeotypes, B-, Ga- and Fe-, were hydrothermally synthesised in PTFE-lined autoclaves. Template removal was *via* calcination of the washed and dried as-synthesised materials. Ion-exchange to the NH_4^+-form, pelleting and sieving, then an additional calcination produced the H^+-form prior to catalytic testing. All zeotype synthesis reagents are included in Table 2.5.

Precursor Material	Description	Manufacturer/Supplier
1. Sodium metasilicate	$Na_2SiO_3 . 9H_2O$ ≥ 98 %	Sigma-Aldrich
2. Fumed silica	SiO_2 ≥ 99.80 %	Sigma-Aldrich
3. Boric acid	$B(OH)_3$ > 99 %	Sigma-Aldrich
4. Gallium nitrate nonahydrate	$Ga(NO_3)_3 .9H_2O$ ≥ 99.9 %	Sigma-Aldrich
5. Iron(III) sulfate hydrate	$Fe_2(SO_4)_3 .xH_2O$ ≥ 97 %	Sigma-Aldrich
6. Sulfuric acid	$H_2SO_{4(aq)}$ > 95 %	Fisher Scientific
7. Sodium hydroxide	NaOH ≥ 98 %	Sigma-Aldrich
8. Tetrapropylammonium bromide	TPABr ≥ 98 %	Sigma-Aldrich

Table 2.5: Zeotype synthesis materials**.**

The nomenclature of MX-MFI is used to denote zeolites and zeotypes where M is the framework counter-cation and the X is assumed to be the incorporated framework heteroatom.

2.3.1 B-MFI hydrothermal synthesis

B-MFI, nominally SiO_2/B_2O_3 = 8, was synthesised using an adapted verified synthesis method [3]. Solution 1 (0.775 g NaOH + 6.65 g fumed silica + 70 g H_2O) was gradually added to 10.161 g TPABr to give mixture 2. Mixture 3 (56.25 g H_2O + 1.825 g boric acid) was then gradually added to mixture 2. Initial mixture was pH 9 and this was raised to pH 11 using $NaOH_{(aq)}$.The resulting mixture (non-clear) was then divided evenly between 6 PTFE lined autoclaves and oven-heated at 10 °C/min from room temperature to 180 °C and held for 120 h then allowed to cool.

2.3.2 Fe-MFI hydrothermal synthesis

Fe-MFI, nominally SiO_2/Fe_2O_3 = 60, was synthesised using an adapted verified synthesis method [4]. Solution 1 (100 mL deionised H_2O + 22 g H_2SO_4 + 5.62 g $Fe_2(SO_4)_3$.$9H_2O$) was gradually added to solution 2 (163.4 g deionised H_2O + 85.26 g Na_2SiO_3 .$9H_2O$) to produce a thick gel mixture 3. It should be noted that solution 2 required mixing and heating at ≈ 50 °C to achieve sufficient dissolution. Mixture 3 was then added to 13.31 g TPABr. The resulting (non-clear) gel was then evenly divided between 6 PTFE lined autoclaves and oven-heated at 10 °C/min from room temperature to 170 °C and held for 72 h then allowed to cool.

2.3.3 Ga-MFI hydrothermal synthesis

Ga-MFI, nominally SiO_2/Ga_2O_3 = 114, was synthesised using an adapted method from Leth and co-workers [5]. Initially, 7.5 g of fumed silica was incipiently wetted with deionised H_2O. 0.45 g NaOH(s) was dissolved in 22.5 g of deionised water then added to the wet silica to produce Mixture 1. Solution 2 (0.35 g $NaOH_{(s)}$ + 22.5 g H_2O) was added to solution 3 (0.914 g $Ga(NO_3)_3$.$9H_2O$ + 17.3 mL H_2O) then slowly added to 10.16 g TPABr to give mixture 4. Mixtures 1 and 4 were slowly added to one another and mixed for 3 h. The resulting mixture (non-clear) was then

divided evenly between 6 PTFE lined autoclaves and oven-heated at 10 °C/min from room temperature to 180 °C and held for 36 h then allowed to cool.

2.4 Catalytic testing

2.4.1 Methanol dehydration reactor

A vertical, atmospheric pressure, stainless steel, fixed-bed plug-flow reactor with quartz reactor tube was employed to undertake all catalytic testing (Fig. 2.4). Gas cylinder and HPLC pump feeds were fed through heat insulated lines at 150 °C to give a 46.5 / 53.5 v/v MeOH/Ar reaction mixture, where the feeds were BOC Ar Pureshield, 99.998 % pure and Sigma-Aldrich methanol ACS reagent (≥ 99.8 % pure). The Ar feed and HPLC pump feeds were varied where necessary using attached rotameters and pump setting respectively to maintain a 46.5 / 53.5 vol. % mixture at different flow rates. As a safety measure against pressure build-up within the system, check valves were incorporated. An online gas chromatograph with a manual injector and TCD detector was used for product separation and identification. Molecular Sieve 13X, 80-100 mesh (6 feet) and Porapak Q, 80-100 mesh (12 feet) columns were employed for the separation of components in the product stream. The liquid MeOH feed was dried using dried zeolite A beads placed within the feed flask. Additionally, the cylindrical furnace operated in ± 5 °C temperature cycles.

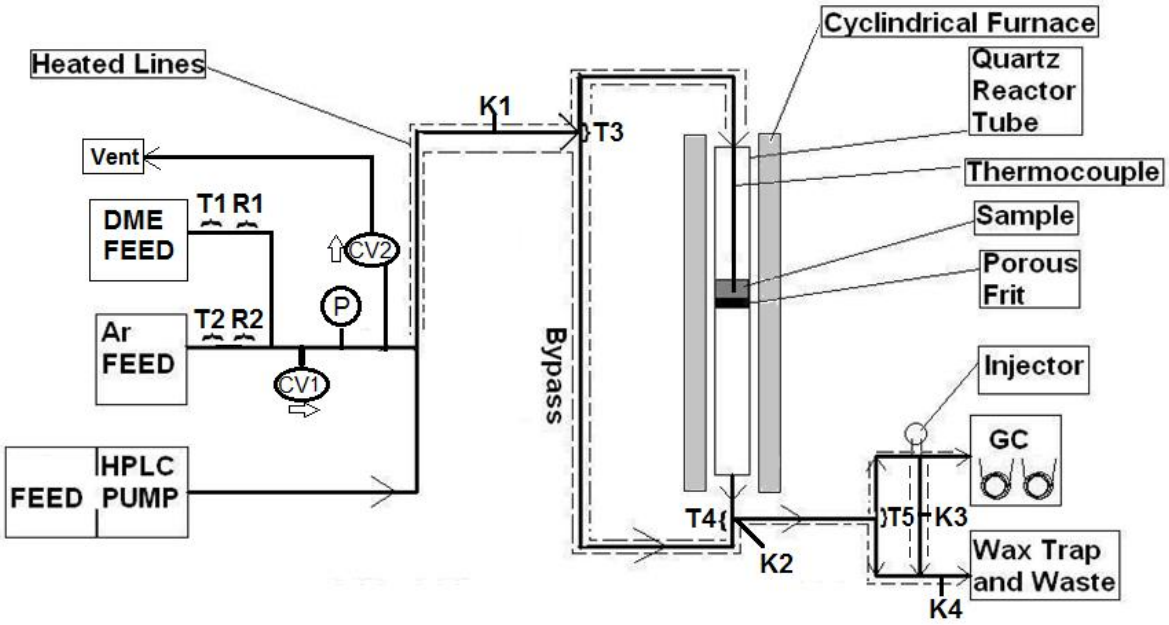

Figure 2.4: Methanol dehydration reactor. (Schematic not to scale). T = Tap, R = Rotameter, CV1 = Check valve (1 psi), CV2 = Check valve (50 psi), P = Pressure gauge and K = K-type thermocouples in feedback with heating tape temperature controllers.

Only for the purposes of calibration, a DME gas cylinder and MeOH/H_2O HPLC pump feeds were used.

2.4.2 **Methanol dehydration reactor calibrations**

Calibrations of HPLC pump rates (Fig. 2.5), Ar flow rate (Fig. 2.6), DME flow rate (Fig. 2.7) and GC detector response (Fig. 2.8) were undertaken and all displayed linearity over the ranges investigated. DME flow rate calibrations were required to determine GC detector response to this component as a function of vol. % accurately. For all calibrations, vertical error bars correspond to the ± 1^{st} standard deviation in data and the horizontal error bars correspond to reading errors except where stated.

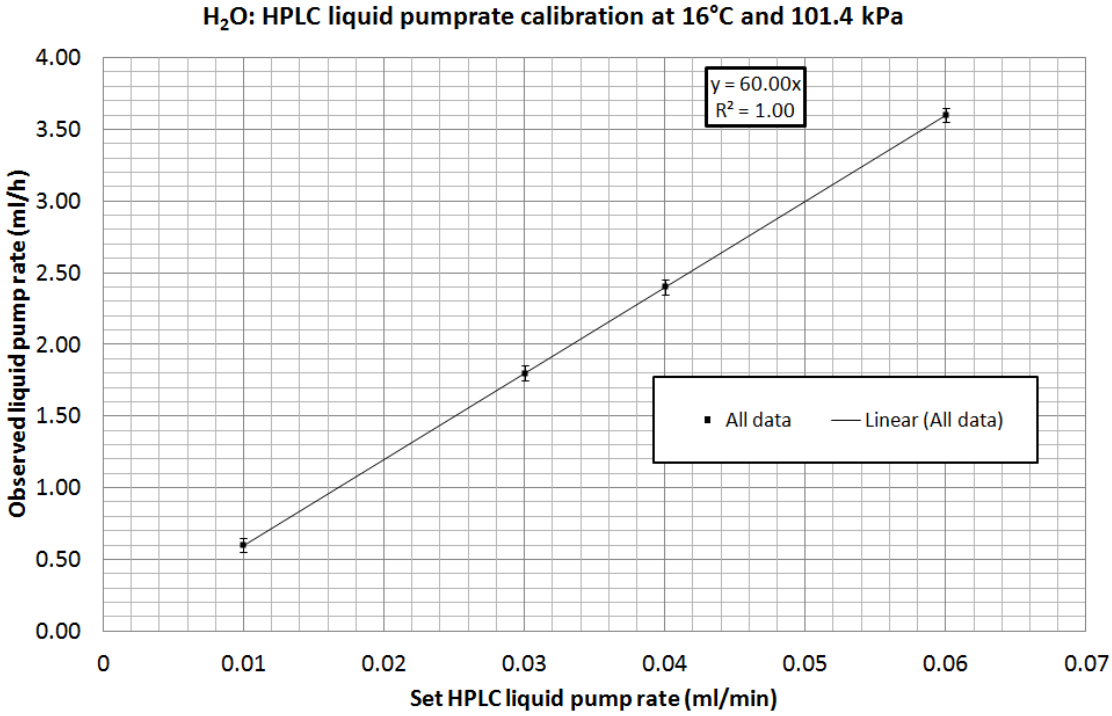

Figure 2.5: HPLC pump rate calibration graph. HPLC pump rate varies linearly with changes in set pump rate. Only one 1 h-long measurement was taken for each of these points and the vertical error bars correspond to reading errors.

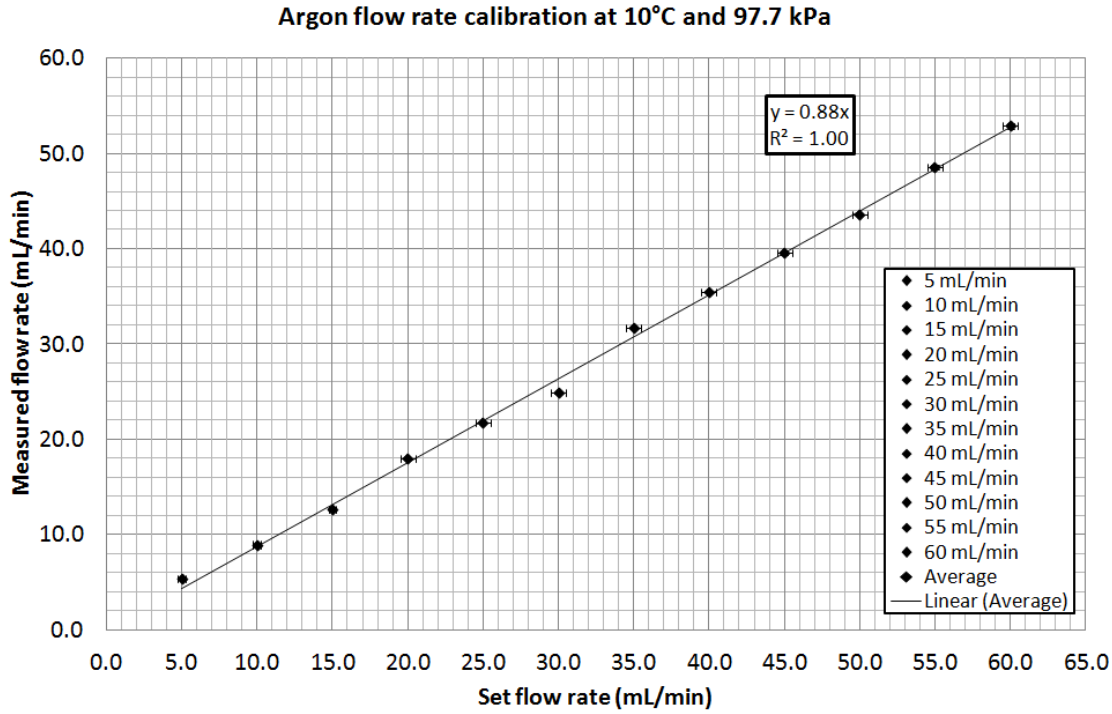

Figure 2.6: Argon flow rate calibration. Argon flow rate varies linearly with changes in set flow rate. A minimum of ten readings were taken for each point.

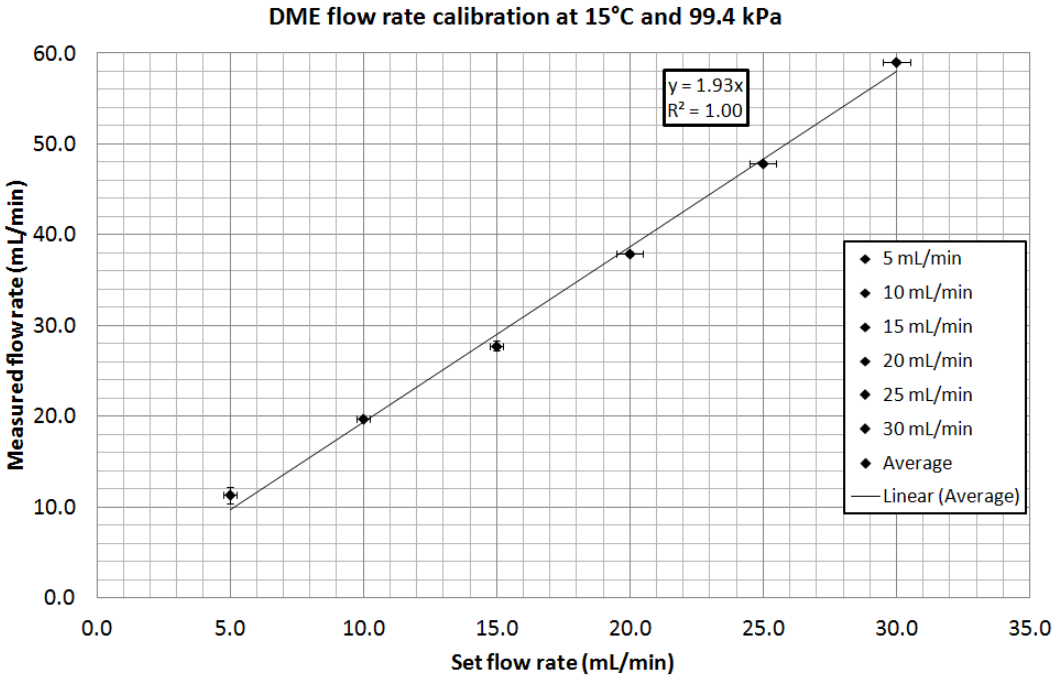

Figure 2.7: Dimethyl ether flow rate calibration. Measured DME flow rate varies linearly with changes in set flow rate. A minimum of six readings were taken for each point.

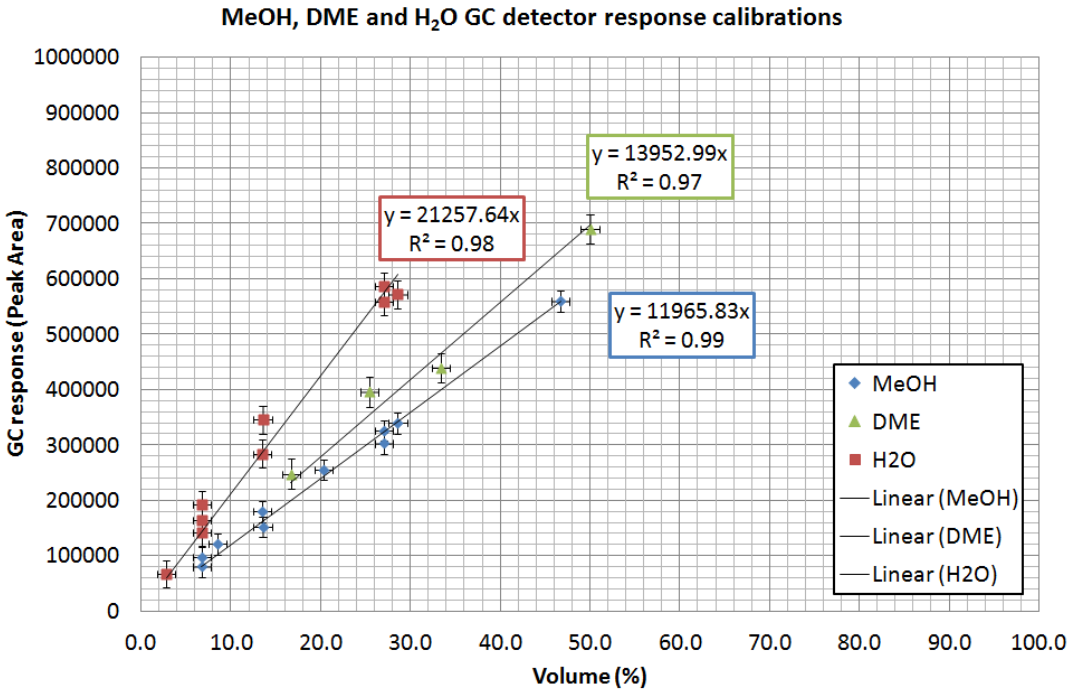

Figure 2.8: GC detector response calibrations. GC detector response varies linearly with changes in partial pressure. A minimum of six readings were taken for each point

2.5 Catalytic testing procedures

All catalytic testing was carried out on pelleted, sieved and calcined samples. A wide range of GHSVs (740-34000 h^{-1}) were examined. These were obtained using different flow rates and/or catalyst volumes.

2.5.1 *In situ* catalyst activation

Prior to reaction with MeOH, the catalysts were activated *in situ* under 30 mL/min of Ar. A temperature programme of room temperature to 550 °C at 10 °C/min and holding at 550 °C for 1 h was employed. Samples were then allowed to cool to the desired reaction temperature.

2.5.2 TGA - Activation mimic

TGA of pre-reaction samples was used to determine the *in situ* mass of catalyst following activation at 550 °C for 1 h and prior to reaction with MeOH. Each run used 10.5 mg ± 1.0 mg, 250-425 µm sample material. All activation mimics were carried out on a TA Q500 under 60 mL/min N_2 with a 10 °C/min temperature ramp from room temperature to 550 °C and held for 1 h in accordance with the *in situ* activation. See Fig. 2.9 for an example.

The TGA activation mimic profile below was from a peptised boehmite/silicalite 1:1 dry mass, wet mixture that has been calcined and then steamed. Close inspection of this sample revealed a final wt. % of 94.52 %. The wt. % at the end of TGA activation mimic runs were used to determine the *in situ* mass of the tested catalysts.

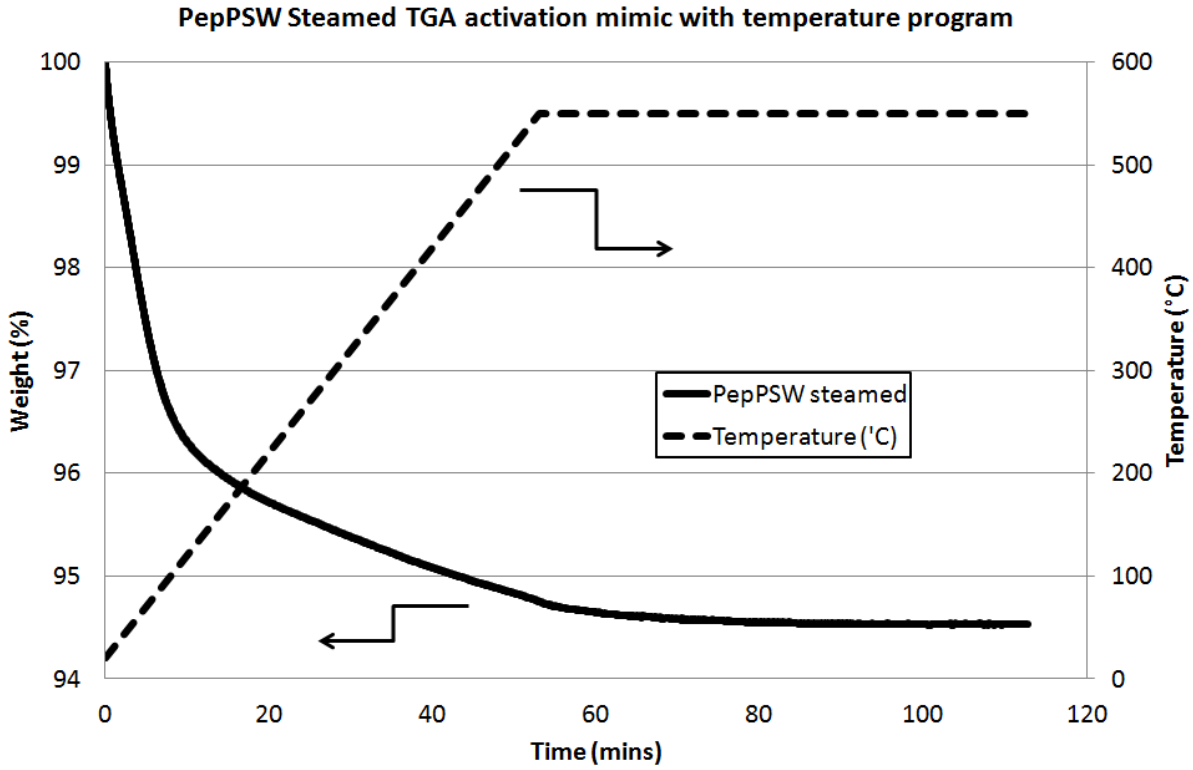

Figure 2.9: TGA activation mimic example.

2.5.3 Running procedures

2.5.3.1 Temperature programmed experiments

TP (Temperature Programmed) experiments were operated for 5h as shown in Fig. 2.10. The reactor temperature was increased in steps of 50 °C every hour at 10 °C/min with GC samples taken at the indicated points on the profile.

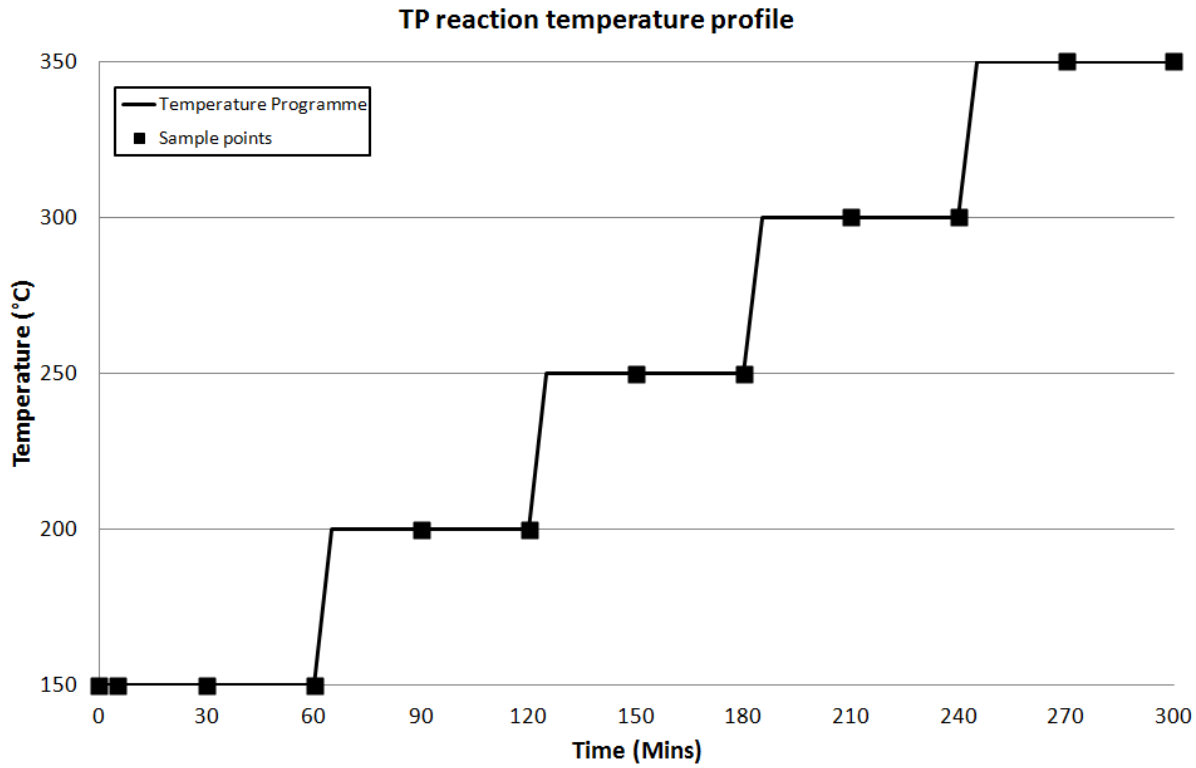

Figure 2.10: TP reaction temperature profile.

2.5.3.2 **Isothermal experiments**

Series of isothermal experiments were undertaken in order to collect sufficient data for analyses as discussed in the results chapter. GC sampling was generally taken prior to reaction (plotted as 0 min) then at 5 min, 30 min and continuing 30 min intervals thereafter until sufficient data was collected.

2.5.4 **Shutdown**

Reactions were halted by stopping the HPLC pump and switching-off the reactor furnace while maintaining trace heating at 150 °C and continued Ar flow. Samples were removed once both reactor and catalyst had returned to room temperature.

2.6 Analytical equipment specifications

For all *ex situ* analytical techniques, samples were physically mixed until visibly homogeneous prior to any analyses.

2.6.1 ICP elemental analysis

ICP (Inductively Coupled Plasma) emission spectrometry was used for elemental analyses of zeolite materials. Samples were dissolved in two stages, HF/HNO_3 at 200 °C for 20 mins then in boric acid at 170 °C for 10 mins followed by appropriate H_2O dilution for accurate elemental quantification. These results were kindly provided by BP Chemicals Ltd.

2.6.2 Flame photometry

Atomic emission spectrometry, through employment of a Sherwood M410 Flame Photometer, was used for Na^+ quantification in ion-exchanged ZSM-5 (23) samples and the sodium content in dried Ludox SiO_2 gels. Standards were produced using a 1000 ppm sodium in 1M $HNO_{3(aq)}$ standard solution from Fisher Scientific which was diluted to appropriate degrees with deionised H_2O (Fig. 2.11).

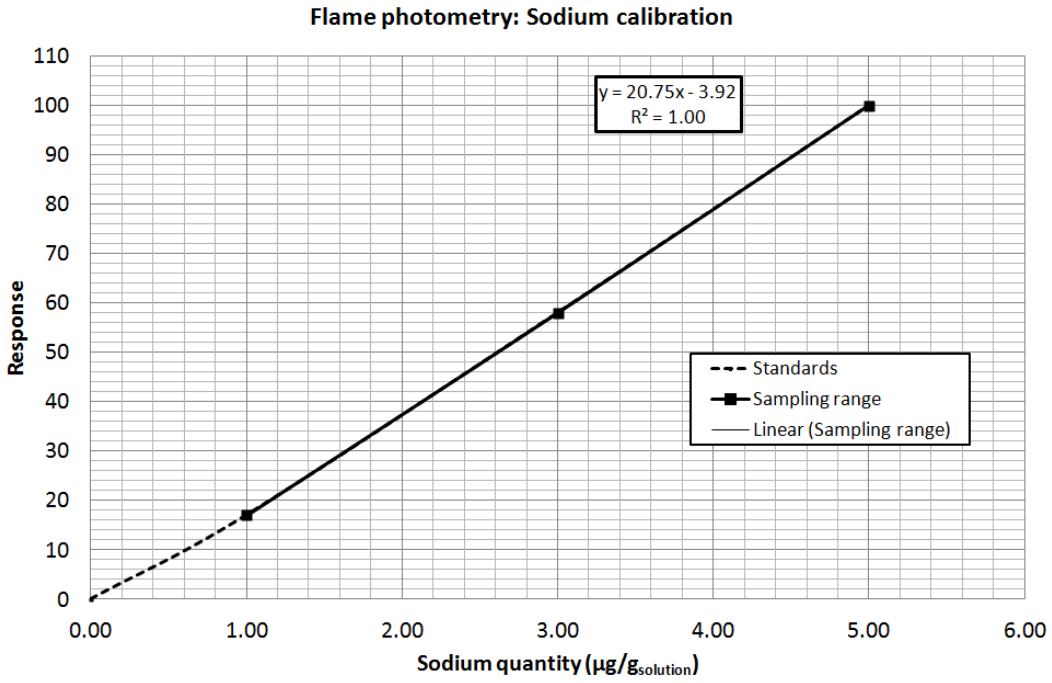

Figure 2.11: Flame photometry calibrations.

Samples were refluxed in aqua regia at 120 °C for 1 h, allowed to cool and then diluted with appropriate quantities of deionised H_2O. The mixture was filtered using Whatman No. 542 filter paper to remove residue.

2.6.3 **CHN elemental analysis**

Carbon, hydrogen and nitrogen analysis was carried out using an Exeter Analytical CE-44 Elemental Analyser, by combustion in a pure oxygen atmosphere and quantified using GC analysis. This work was kindly provided by Mrs. Kim Wilson and all measurements were duplicated and the average was used for all subsequent calculations. An error bar of ± 0.3 wt. % should be applied to all measurements.

2.6.4 **SEM-EDX analyses**

SEM (Scanning Electron Microscope) images were obtained on a Philips XL30 ESEM tungsten filament electron microscope with a secondary electron detector. EDX (Energy Dispersive X-ray) analyses were obtained on an attached Oxford Instruments Inca Energy 250 system with X-Act 10mm^2 $N_{2(l)}$-free detector for spectrometric elemental identification purposes. Typical running pressures were between 10^{-5} - 10^{-6} bar pressure with an acceleration voltage of 25 kV. All samples were coated with Au using a Polaron SC7640 sputter coater to decrease sample charging.

2.6.5 **Nitrogen physisorption measurements**

All nitrogen physisorption isotherms were obtained using a Micromeritics Gemini III 2375 Surface Area Analyzer and Stardriver analysis software. Samples were purged at 110 °C under N_2 flow overnight and reweighed prior to measurements. Helium was used for free-space calibration. Through application of the BET equation [6], t-plot method [7] and BJH method [8] both microporous and external specific surface areas (determined from multi-point analyses), were determined. BJH pore size distributions were obtained from adsorption branches which are believed to be more accurate than desorption branches in materials possessing porous networks [9,10]. Single-point total pore volumes were determined from the highest pressure point of the adsorption branch.

2.6.6 **Powder X-ray diffraction measurements**

For both instruments, a CuK_{α} (1.5418 Å) source was employed and samples were compacted into the sample holders to give a flat surface for measurement.

2.6.6.1 ***Ex situ* measurements**

Measurements were undertaken under ambient conditions on a Siemens D5000 X-ray diffractometer in a Bragg-Brentano arrangement over a 2θ range of 5 °- 85 ° with a step size of 0.020 °2θ, acquisition time of 1 second per step. The sample holder was a silicon single crystal probe (Einkristal Probent, m.V Bruker AXS).

2.6.6.2 ***In situ* measurements**

Measurements were carried out under 100 mL/min Ar on a PANalytical X'Pert Pro HTK flat-plate hotstage in a Bragg-Brentano arrangement following the temperature and measurement profile in Fig. 2.12.

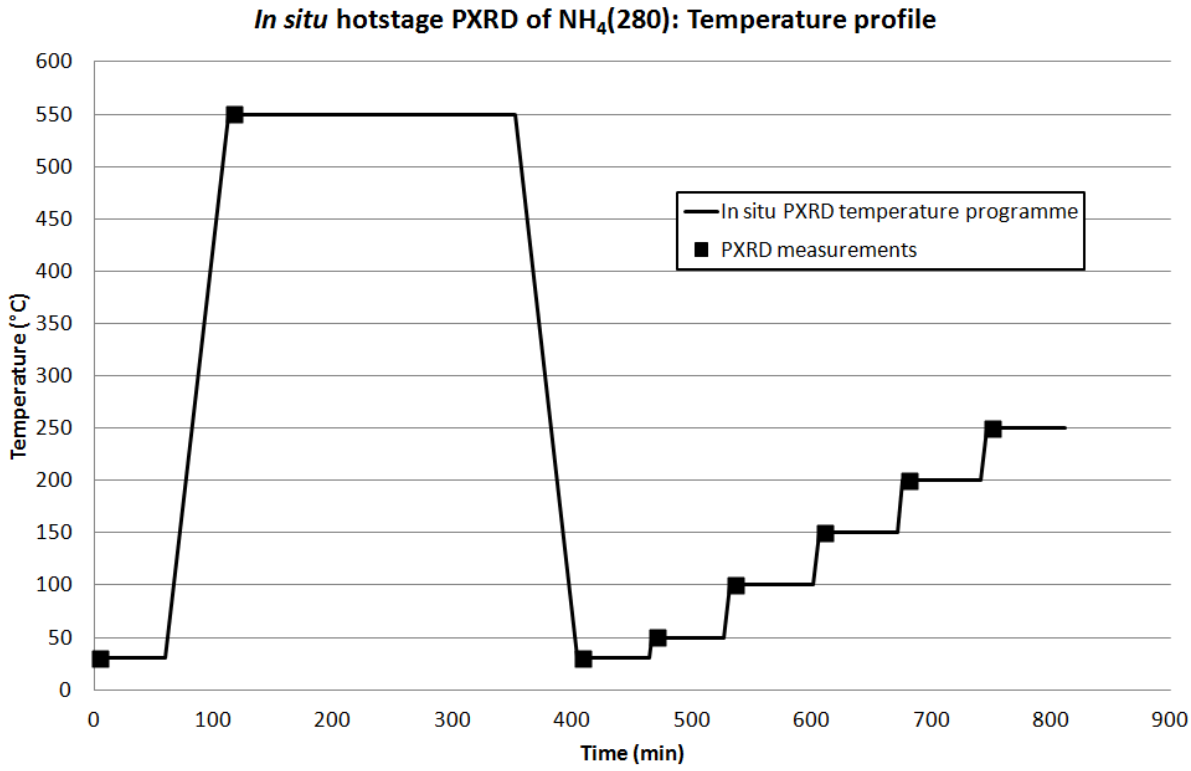

Figure 2.12: *In situ* hotstage PXRD temperature profile.

Measurement parameters were acquisition range = 5 °-55 °2θ, step size = 0.01671 °2θ per s and acquisition time = 1 s per step.

2.6.7 NMR (Nuclear Magnetic Resonance) measurements

2.6.7.1 ^{1}H-NMR of liquid samples

^{1}H-NMR was employed to confirm the identity and purity of the MeOH feed. ^{1}H-NMR spectra were obtained using a Bruker AV400 and $CDCl_3$ as solvent and internal standard (Fig. 2.13). The presence of H_2O can be attributed to the hygroscopic properties of MeOH. Zeolite A drying beads were added to the reactor source of methanol to dry it.

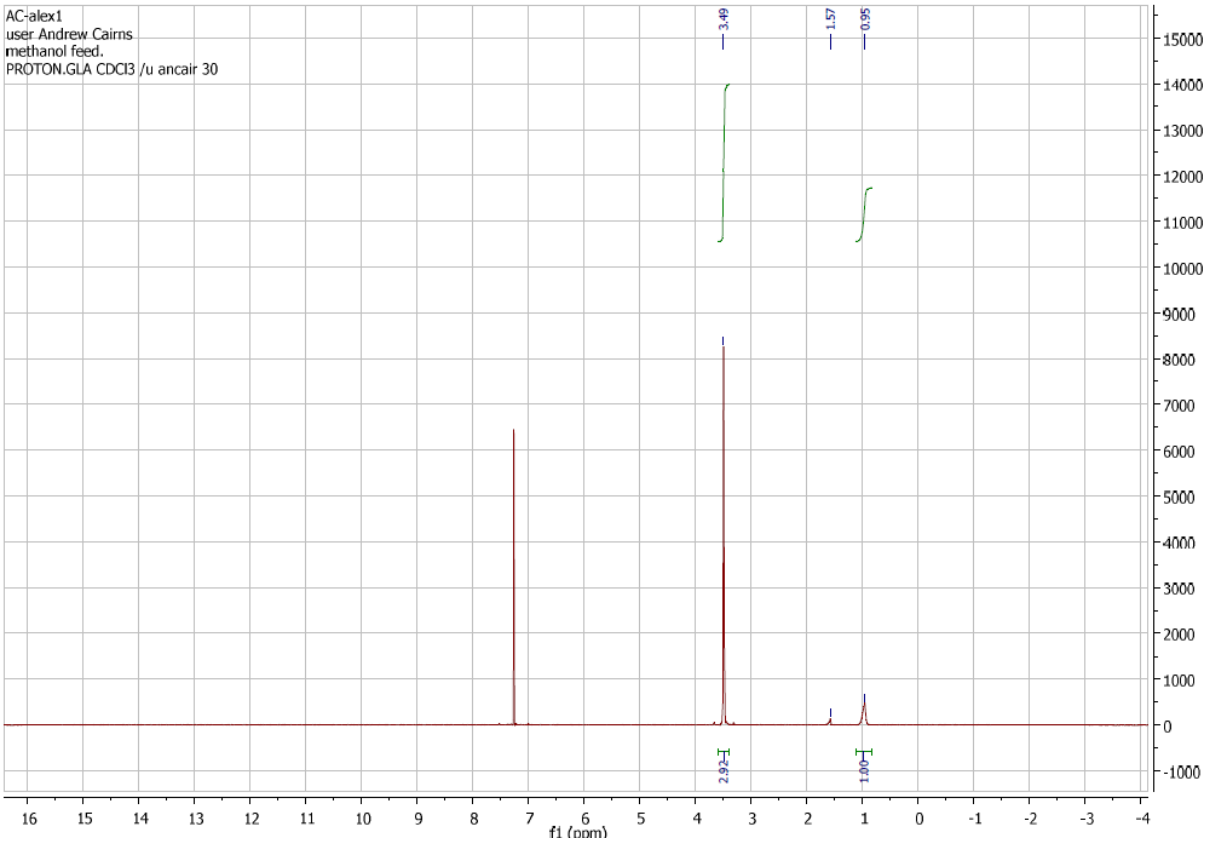

Figure 2.13: ^{1}H-NMR spectra of the methanol feed. Peaks may be assigned as follows 0.95 ppm (CH_3-OH), 1.57 ppm (H_2O) 3.49 ppm (CH_3-O<u>H</u>) and 7.26 ppm ($CHCl_3$). The measurement was kindly performed by Andrew Cairns (Ph.D. student) at the University of Glasgow.

2.6.7.2 **MAS-NMR**

Two instruments were employed to collect the MAS-NMR (Magic Angle Spinning-Nuclear Magnetic Resonance) data presented in this thesis: (i) A Varian VNMRS 400 and (ii) a Varian Unity Inova 300 both using only PTFE rotors. The nuclei examined were ^{1}H, ^{11}B, ^{27}Al, ^{29}Si and ^{71}Ga *via* DE (Direct Excitation). ^{1}H-^{29}Si CP (Cross Polarisation) measurements were also taken. All samples were fully hydrated prior to sample loading and the measurement temperature was 40-60 °C because of the air friction associated with spinning rotor. These measurements were kindly carried out by Dr. D. C. Apperley and Mr. A. F. Markwell at the University of Durham EPSRC solid state NMR service.

2.6.7.2.1 Varian VNMRS 400

Using a 6.0 mm rotor, ^{29}Si DE spectra were typically obtained at a frequency = 79.435 MHz, spectral width = 40322.6 Hz, acquisition time = 30.0 ms, recycle time = 10.0 s, number of repetitions > 100, pulse duration = 4.7 μs, TPPM decoupling = 43.1 kHz, rotor spin rate = 6800 Hz, Gaussian broadening = 0.005 s and an FT size = 8192. ^{1}H-^{29}Si CP spectra were typically obtained under the above conditions with a contact time = 3.00 ms.

Using a 4.0 mm rotor, ^{27}Al spectra were typically obtained at a frequency of 104.198 MHz, spectral width = 416.7 kHz, acquisition time = 10.0 ms, recycle time = 0.2 s, number of repetitions > 2000, pulse duration = 1.0 μs, no proton decoupling, rotor spin rate = 14000 Hz, Gaussian broadening = 0.005 s and FT size = 16384. All peaks in all ^{27}Al spectra observed at < -25 ppm and > 100 ppm are assigned to spinning side-bands.

2.6.7.2.2 Varian Unity Inova 300

Using a 7.5 mm rotor, ^{29}Si DE spectra were typically obtained at a frequency = 59.557 MHz, spectral width = 29996.3 Hz, acquisition time = 30.0 ms, recycle time = 30.0 s, number of repetitions ≥ 20, Cw decoupling, rotor spin rate = 5090 Hz, Gaussian broadening = 0.015 s and an FT size = 8192. ^{1}H-^{29}Si CP spectra were typically obtained under the above conditions with a recycle time = 1 s, number of repetitions ≥ 450 and a contact time = 1.00 ms.

2.6.8 Thermogravimetric analyses

For thermogravimetric analyses a TA instruments Ltd. Q500 with platinum pans as well as a SDT Q600 with ceramic pans were employed. Results were obtained on the TA Q500 with the exception of the zeotype reduction studies. TPO (Temperature Programmed Oxidation) measurements were carried out under air flow at 60 mL/min under a temperature programme of room temperature to 800 °C at 10 °C/min. Each run used 10.5 mg ± 1.0 mg, 250-425 µm sample material.

2.7 Reaction calculations

In all conversion and production calculations: molar flow rates (moles/g_{cat}.s), percentage values are employed as fractions e.g. 94.56 % = 0.9456 for ease of calculation and catalyst masses (g_{cat}) were employed.

2.7.1 Methanol conversion

The rate of MeOH conversion, $MeOH_{CONV}$, (moles/g_{cat}.s) was calculated *via*:

$$MeOH_{CONV}\left(\frac{moles}{g_{cat}.s}\right) = \frac{\left(Molar\ flowrate(\frac{moles}{s})\right) * \left(MeOH_{CONV}(\%)\right)}{Mass\ of\ catalyst\ (g_{cat})}$$

2.7.2 Dimethyl ether production

The rate of DME production, DME_{PROD}, (moles/g_{cat}.s) was calculated *via*:

$$DME_{PROD}\left(\frac{moles}{g_{cat}.s}\right) = \frac{\left(Molar\ flowrate(\frac{moles}{s})\right) * \left(DME_{PROD}(\%)\right)}{Mass\ of\ catalyst\ (g_{cat})}$$

2.7.3 Water production

The rate of H_2O production, H_2O_{PROD}, (moles/g_{cat}.s) was calculated *via*:

$$H_2O_{PROD}\left(\frac{moles}{g_{cat}.s}\right) = \frac{\left(Molar\ flowrate(\frac{moles}{s})\right) * \left(H_2O_{PROD}(\%)\right)}{Mass\ of\ catalyst\ (g_{cat})}$$

2.7.4 **Carbon balance (%)**

The carbon (C) balance, expressed as a percentage of the moles of carbon introduced to the system for each reaction was calculated as follows:

$$Carbon\ balance\ (\%) = \left(\frac{\Sigma C_{OUT}}{\Sigma C_{IN}}\right) * 100$$

Where: ΣC_{OUT} = $\Sigma MeOH_{OUT}$ + 2*ΣDME_{OUT} + (Carbon deposited on the catalyst) and ΣC_{IN} = $\Sigma MeOH_{IN}$

2.7.5 **Determination of thermodynamic limit**

The thermodynamic limit expressed as a percentage of $MeOH_{CONV}$ and a function of temperature was determined as follows:

$$\Delta G_r^{\circ} = -RTlnK_p$$

Where: ΔG_r° = Standard free energy of reaction; R = Ideal gas constant; T = Absolute reaction temperature and K_p = Equilibrium constant

By employing the values for ΔG_r obtained from ref. [11] and taking account of the free energy of vaporisation of both MeOH and H_2O in the reaction and where conditions are 298 K and 101325 Pa produces:

$$2CH_3OH_{(g)} \leftrightarrows (CH_3)_2O_{(g)} + H_2O_{(g)} \qquad \Delta G_{r(298K)} = -16.5\ kJ/mol$$

ΔG_r values were determined over a wide range of temperatures from the data from ref. [11]. From these values and curve fitting, the K_p values in Fig. 2.14 were obtained. The equilibrium constant (K_p) of MeOH dehydration to DME and H_2O may be expressed as:

$$K_p = \frac{P_{DME}P_{H2O}}{(P_{MeOH})^2}$$

Where: P_x = The partial pressure of compound x.

This may be re-expressed in terms of the molar fraction of $MeOH_{CONV}$ ($0 \leq \alpha \leq 1$).

$$K_p = \frac{\alpha^2}{(1-\alpha)^2}$$

α-values were then determined iteratively for the determined values of K_p over the temperature range of data available and scaled to percentages (Fig. 2.14). In chapter 3 and the reaction data in the accompanying material, catalytic testing results will be illustrated in conjunction with rates calculated assuming the attainment of thermodynamic equilibrium. These values were determined from the rate of MeOH ($MeOH_{IN}/g_{cat}$ s) * percentage from Fig. 2.14 corresponding to the reaction temperature.

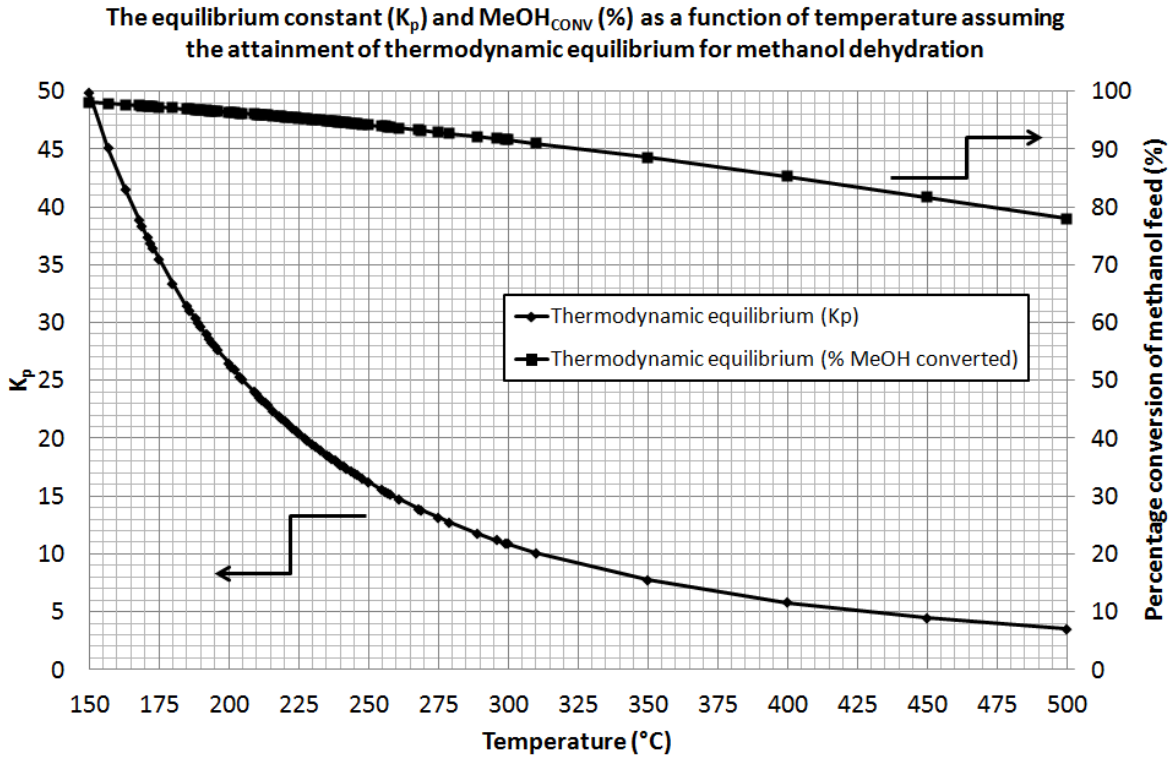

Figure 2.14: Equilibrium constant and $MeOH_{CONV}$ (%) graph.

2.7.6 **Arrenhius analysis**

Arrenhius (ln(rate)) plots were produced *via* plots of the following equation:

$$ln(Rate) = \left(\frac{-E_a}{R}\right) * \left(\frac{1000}{T}\right) + ln(A * P_{MeOH}^{n})$$

Where: *Rate = The rate of $MeOH_{CONV}$; P_{MeOH} = Pressure of MeOH; n = Order of reaction; E_a = The apparent activation energy of reaction; R = Ideal gas constant and T = Absolute temperature*

Only reactions displaying no evidence of side-reactions and operating under kinetic control were interpreted by Arrenhius analysis. By this approach, changes in the number of active sites of the catalysts will manifest themselves as shifts in the y-intercept and changes in the nature of the acid sites will manifest themselves as changes in the gradient.

2.8 References

[1] CRC Handbook of Chemistry and Physics, 90th Ed. (2009) Section 6-5. ISBN: 9781420090840.

[2] S. D. Kim, Seung C. Baek, Y.-J. Lee, K.-W. Jun, M. J. Kim and I. S. Yoo; Appl. Catal. A: Gen., 309, (2006), 139-143.

[3] R. De Ruiter, J. C. Jansen, H. van Bekkum, Synthesis of Microporous Materials, Vol. 1, van Nostrand Reinhold, New York, (1992) p167, ISBN: 0442006616.

[4] A. Brückner, R Lück, W. Wieker and B. Fahlke, Zeolites, 12 (1992), 380.

[5] K. T. Leth, A. K. Rovik, M. S. Holm, M. Brorson, H. J. Jakobson, J. Skibsted and C. H. Christensen, Appl. Catal. A: Gen., 348 (2008) 257-265.

[6] S. Brunauer, P. H. Emmett and E. J. Teller, J. Am. Chem. Soc., 60 (1938) 309-319.

[7] W. D. Harkins and G. J. Jura, J. Chem. Phys., 11 (1943) 431.

[8] E. P. Barrett, L. S. Joyner and P. P. Halenda, J. Am. Chem. Soc., 73 (1951) 373-380.

[9] K. S. W. Sing, D. H. Everett, R. A. W. Haul, L. Moscou, R. A. Pieotti, J. Rouquerol and T. Siemieniewska, Pure & Appl. Chem., 57 (1985) 603-619.

[10] J. C. Groen, L. A. A. Peffer and J. Perez-Ramirez, Microp. Mesop. Mater., 60 (2003) 1-17.

[11] D. R. Stull, E. F. Westrum and G. C. Sinke, The Chemical Thermodynamics of Organic Compounds, Robert E. Krieger Publishing Company Malabar Florida (1987), ISBN 0898747066.

3 Determination of dimethyl ether production conditions

In order to use MeOH dehydration as a probe reaction, it was of importance that the correct reaction takes place and was operated under an appropriate regime. Initial studies into the conditions required for DME production were undertaken to ensure only valid results were included in the Arrenhius plots of the following chapters.

The target conditions aimed for were:

1) The MeOH conversion rate was within the upper limit calculated assuming attainment of the thermodynamic equilibrium for DME production. As such, the limiting values shown were dependent upon the rate of $MeOH_{IN}$, the mass of catalyst employed and reaction temperature (see section 2.7.5).

2) Selective MeOH conversion to DME and H_2O. Gas phase products were quantified by online GC analyses (where DME and H_2O are produced in ≈ 1:1 molar ratios) and adsorbates by post-reaction CHN and TGA analyses of the catalysts – thus indicating no competing reactions occurred (see section 2.7.4).

Following the outlined criteria, this chapter establishes the reaction temperatures over which MeOH was selectively dehydrated to DME at atmospheric pressure over a range of materials.

3.1 The dependence of reaction on both catalyst and temperature

Initial TP (Temperature Programmed) experiments were undertaken to observe MeOH conversion in both DME and hydrocarbon production reactions. Isothermal reactions were then used to determine the reaction switchover temperature more accurately. Finally, TP experiments over both sodium-exchanged zeolite and alumina catalysts were undertaken to show whether the reaction switchover temperature is dependent upon the catalyst employed.

3.1.1 TP reactions over H(50) 550 4 h and H(280) 550 4 h

As described in section 2.7.5, theoretical limiting rate values corresponding to the rates which would be attained were thermodynamic equilibrium for methanol dehydration to produce DME achieved have been calculated. These limits are shown by dashed lines in Figs. 3.1a-b. For the selective MeOH conversion to DME and H_2O, the MeOH conversion rate cannot of course exceed these values. However, these values correspond only to selective MeOH dehydration to DME and H_2O and do not correspond to non-selective methanol conversion, for example, if MeOH was converted to hydrocarbons. The equilibrium MeOH conversion values as a function of temperature are presented in Table 3.1.

Temperature (°C)	$MeOH_{CONV}$ (% of $MeOH_{IN}$)
150	98.0
200	96.4
250	94.2
300	91.6
350	88.5

Table 3.1: Equilibrium MeOH conversion values for selective DME production as a function of reaction temperature.

Therefore, the apparent difference in the equilibrium methanol conversion rates (dashed lines) in Figs. 3.1a-b simply reflects the different catalyst masses used in each experiment.

Figs. 3.1a-b, show a stepwise increase in MeOH conversion with stepwise temperature increases over H(50) 550 4 h and H(280) 550 4 h catalysts. At ≤ 250 °C, DME and H_2O were produced in an ≈ 1:1 ratio. Upon increasing the temperature to ≥ 300 °C, MeOH was converted at a rate in excess of the rate corresponding to the thermodynamic limit for MeOH dehydration to DME in each experiment. MeOH conversion was ≈ 100 %, DME was no longer produced and the C-balance for each experiment was well below 100 % (H(50) 550 4 h TP = 80 %

and H(280) 550 4 h TP = 87 %). An interesting observation was an increase by approx. +15 °C within the first 5 mins of reaction of the catalyst bed, which was attributed to the adsorption of the methanol reactant onto the pre-treated material.

Post-reaction TGA (Fig. 3.2), CHN analyses and N_2-physisorption results (Table 3.2) indicate both the retention of unsaturated hydrocarbons and decreased surface area which resulted from operation of the hydrocarbon production reaction.

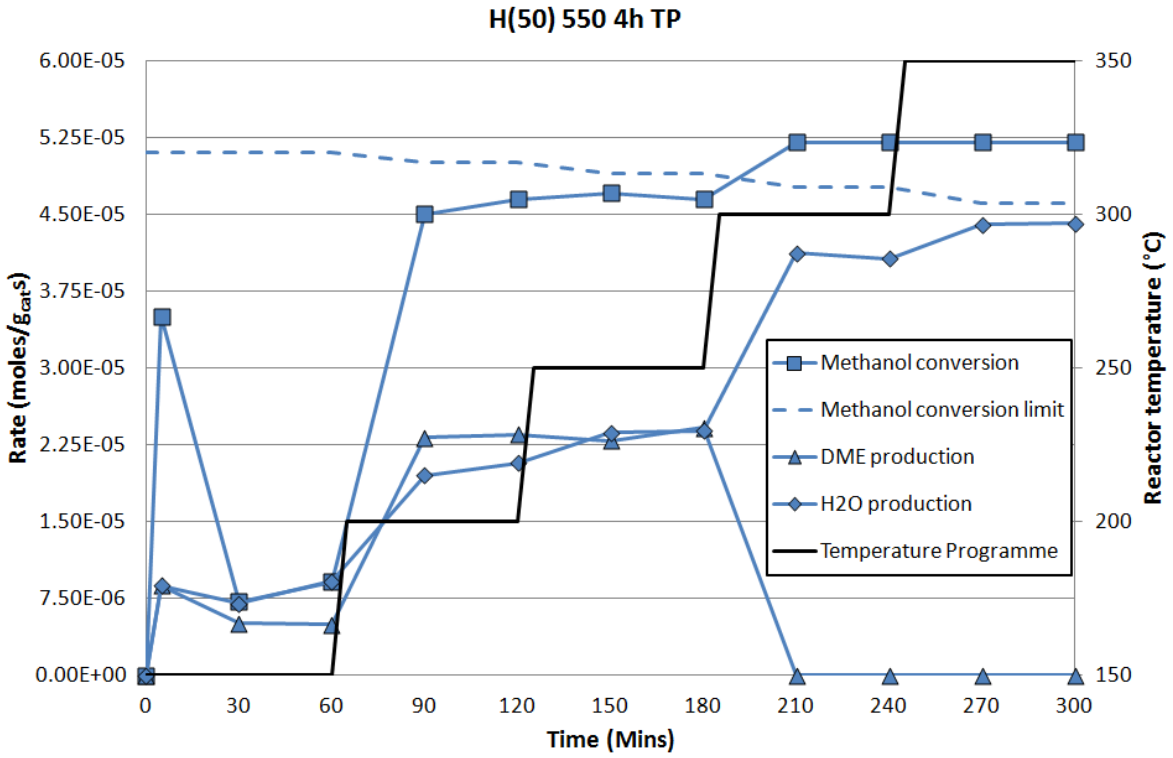

Figure 3.1a: H(50) TP catalytic testing.

Figs 3.1a-b: For H(50) 550 4 h and H(280) 550 4 h: GHSVs = 4400 h^{-1} and 2900 h^{-1} respectively and dry catalyst masses = 0.2294 g and 0.4084 g respectively.

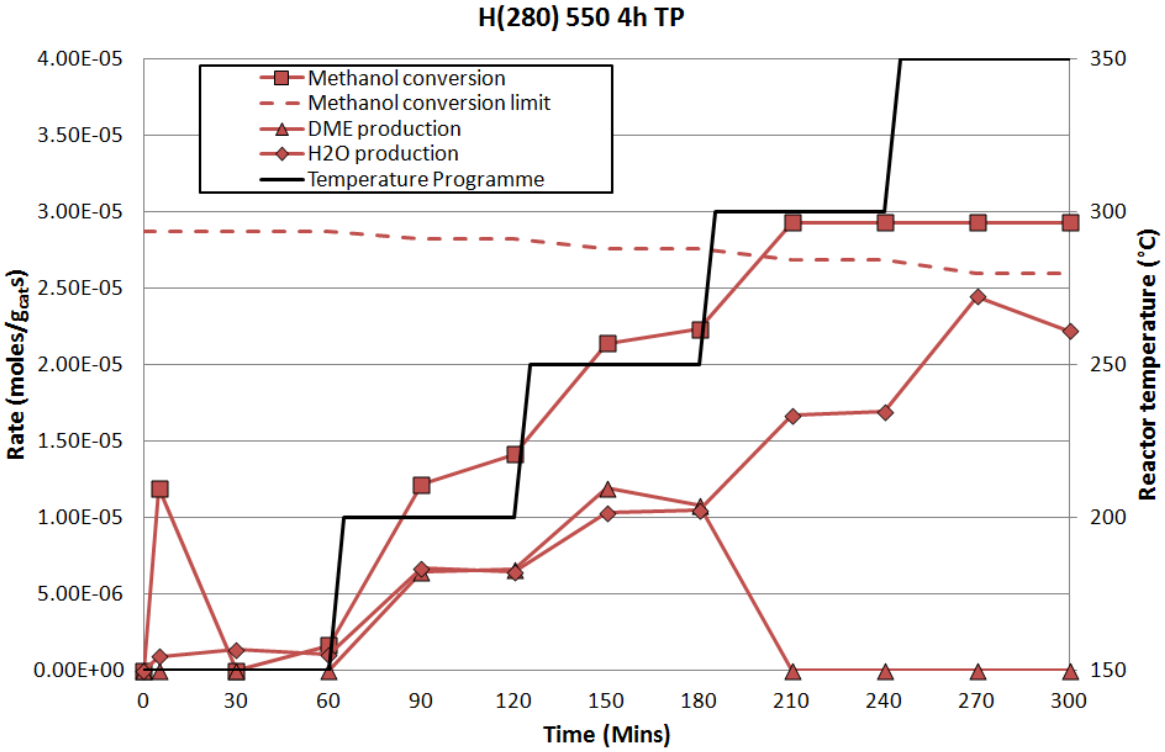

Figure 3.1b: H(280) TP catalytic testing.

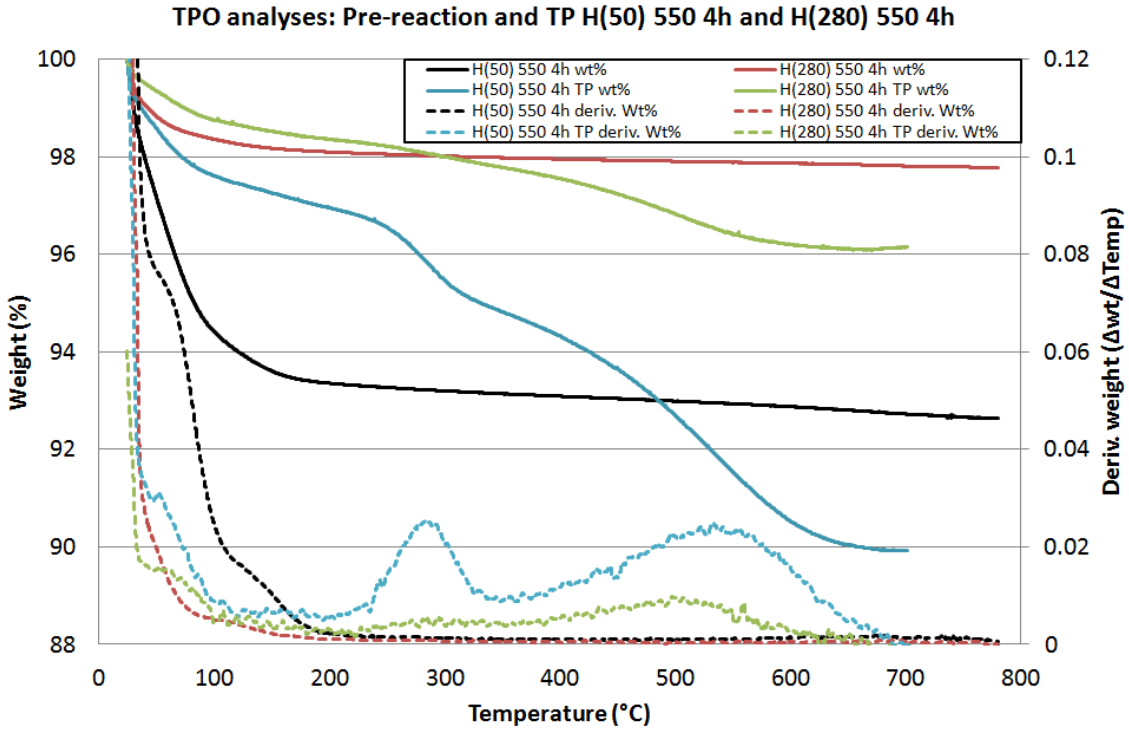

Figure 3.2: H(50) vs. H(280) TP TPO profiles. Experiments were operated as described in the experimental chapter except both TP samples whose final TGA temperatures were ≈ 700 °C.

In the TGA results above (Fig 3.2), for both H(50) 550 4 h and H(280) 550 4 h TP samples, weight loss below 200 °C may be attributed to desorption of MeOH, DME, H_2O and oxidation products of adsorbed species. Additionally, the weight loss from 225 - 700 °C may be attributed to oxidation and desorption of unsaturated hydrocarbon species [1] as well as minor silanol dehydration at ≈ 650 °C. (see section 6.3.2.1)

Catalyst	BET SA (m^2/g)	Total pore vol. (cm^3/g)	Ads. Iso. type	C (wt. %)	H (wt. %)
H(50) 550 4 h	313 ± 8	0.24 ± 0.02	I	0.00	0.48 ± 0.04
H(50) 550 4 h TP	104	0.11	I	5.59 ± 0.05	0.73 ± 0.02
H(280) 550 4 h	358 ± 5	0.21 ± 0.00	I	0.00	0.00
H(280) 550 4 h TP	243	0.16	I	1.78 ± 0.16	0.00

Table 3.2: H(50)-H(280) TP BET and CHN analyses results. Measurements were obtained as described in the experimental chapter. Errors correspond ± the furthest outlier of repeated measurements. BET (1-2 runs) and CHN (duplicated). Ads, Iso. = Adsorption Isotherm. Adsorption isotherms can be found in the appendix.

For both H(50) 550 4 h and H(280) 550 4 h TP experiments, the switchover from DME to hydrocarbon production was observed at *ca*. 300 °C.

3.1.2 **Isothermal methanol conversion over H(50) 550 4 h**

To determine the temperature for reaction switchover from DME to hydrocarbon products with greater accuracy, H(50) 550 4 h was investigated in isothermal experiments at 225 °C, 250 °C, 275 °C and 300 °C. The catalytic results are shown in Figs. 3.3, 3.4 and summarised in Fig. 3.5 with post-reaction analyses in Figs. 3.6 and 3.7. The switchover temperature was found to be *ca*. 275 °C.

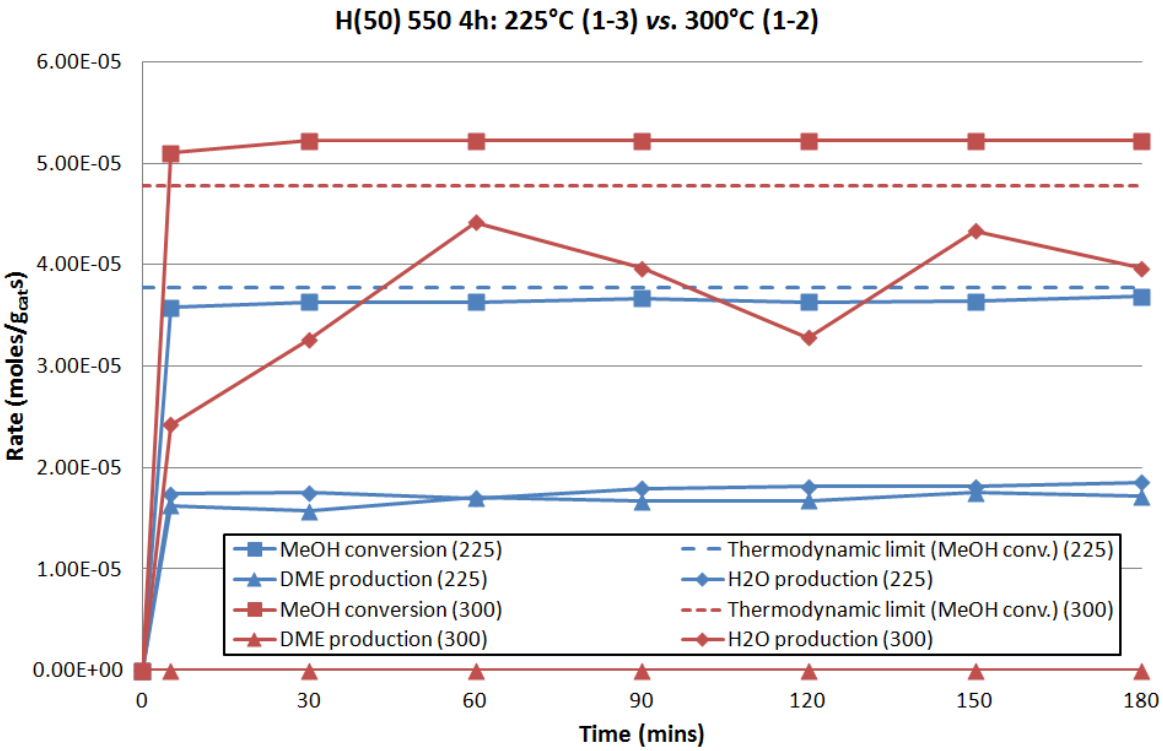

Figure 3.3: H(50) 550 4 h 225 °C and 300 °C catalytic testing. GHSVs = 4500 - 4600 h^{-1}. In the 225 °C (repeated 3x) and 300 °C (duplicated) experiments catalyst masses were = 0.3000 g ± 0.0007 g and 0.2294 ± 0.0000 g, respectively. The data presented are averages of the repeated measurements. The rate refers to the data labels in the figure legend.

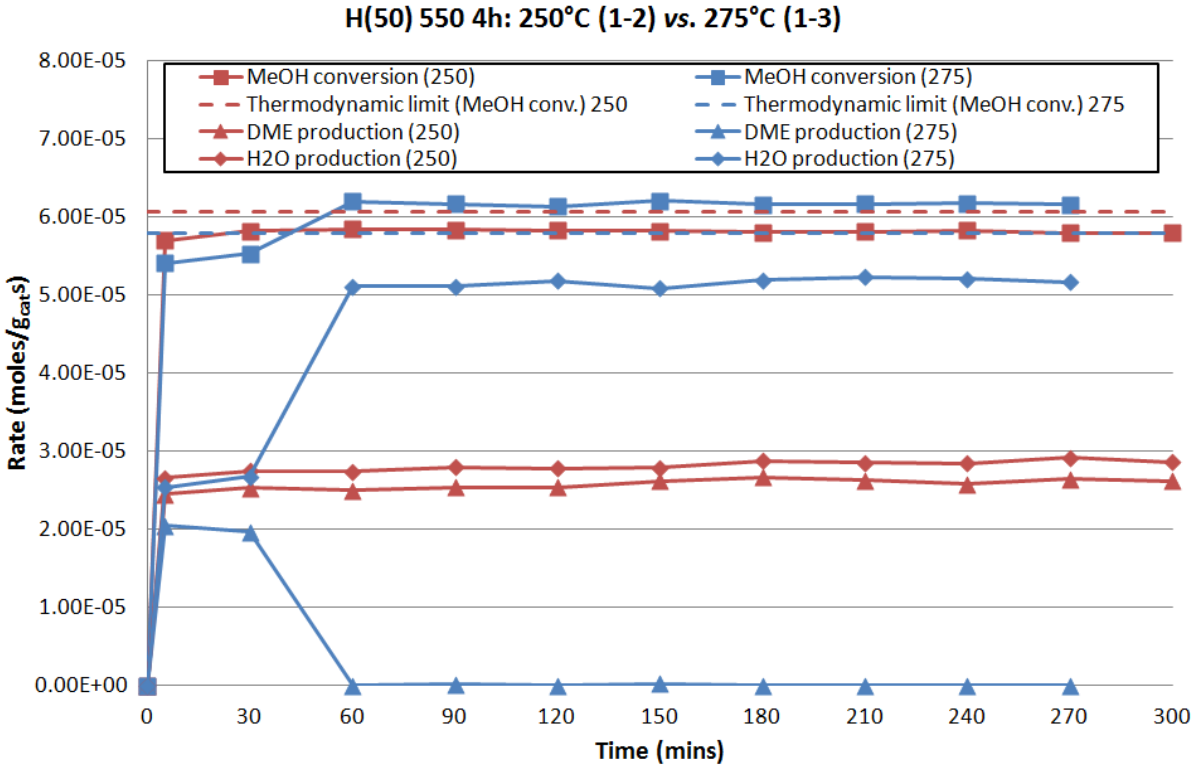

Figure 3.4: H(50) 550 4 h 250-275 °C catalytic testing. For H(50) 550 4 h 250 °C (duplicated) and 275 °C (repeated 3x): GHSVs = 4500 h^{-1} for each experiment and catalyst masses = 0.1859 ± 0.0000 g and 0.1849 g ± 0.0005 g respectively. The rate refers to the data labels in the figure legend.

Fig. 3.5 provides a condensed representation of the data contained within figures 3.3 and 3.4. The reaction switchover temperature at constant GHSV over H(50) 550 4h was shown to be approx. 275 °C. This is in agreement with the results presented in Fig. 3.7.

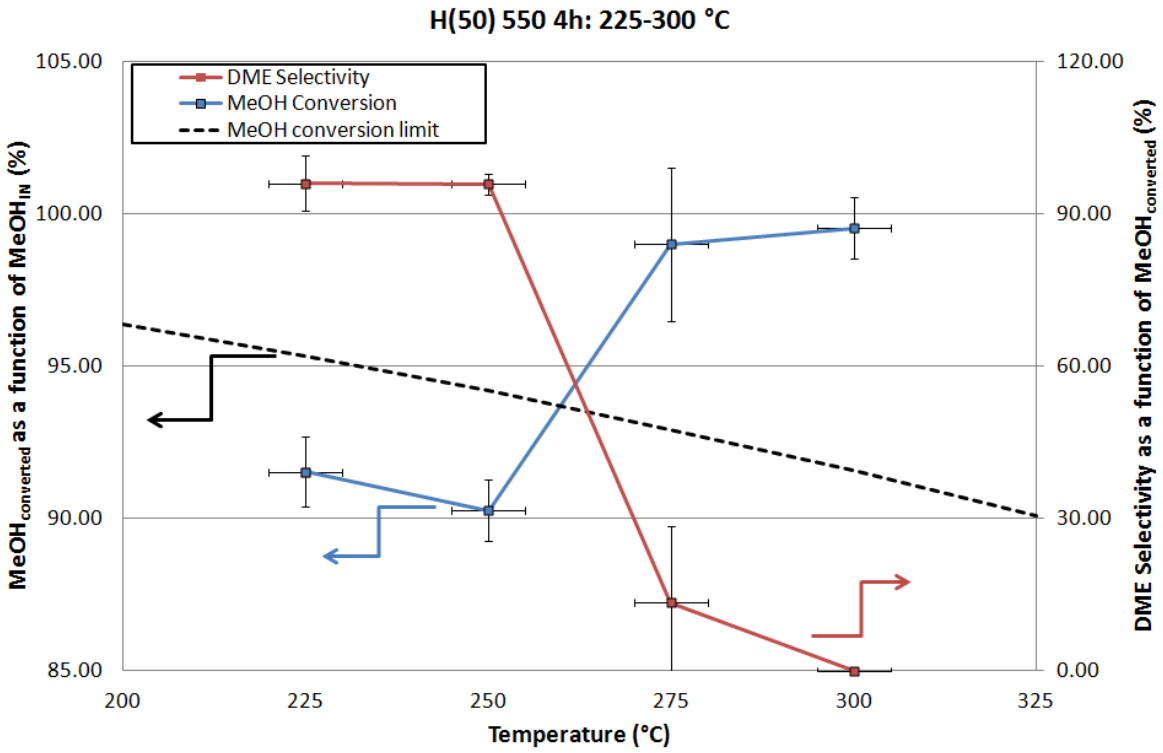

Figure 3.5: Reaction switchover - catalytic testing. MeOH conversion and DME selectivity values are the averages determined from figures 3.3 and 3.4. Vertical error bars represent the spread of data and horizontal error bars represent correspond to reactor temperature cycle. Further experimental details are provided in the captions of figures 3.3 and 3.4.

In Fig. 3.6, all weight loss in the 'Pre' unreacted H(50) 550 4 h material was assigned to H_2O desorption. For both H(50) 550 4 h 225 °C and 250 °C samples, weight loss below 300 °C may be attributed to desorption of MeOH, DME, H_2O and oxidation products of adsorbed species. For H(50) 550 4 h 275 °C and 300 °C samples, the same weight losses occur to a lesser extent, up to approximately 300 °C, in addition to the weight loss from 350 - 725 °C, which may be attributed to oxidation and desorption of unsaturated hydrocarbon species originating from MTH chemistry and minor silanol dehydration at ≈ 650 °C (see section 6.3.2.1).

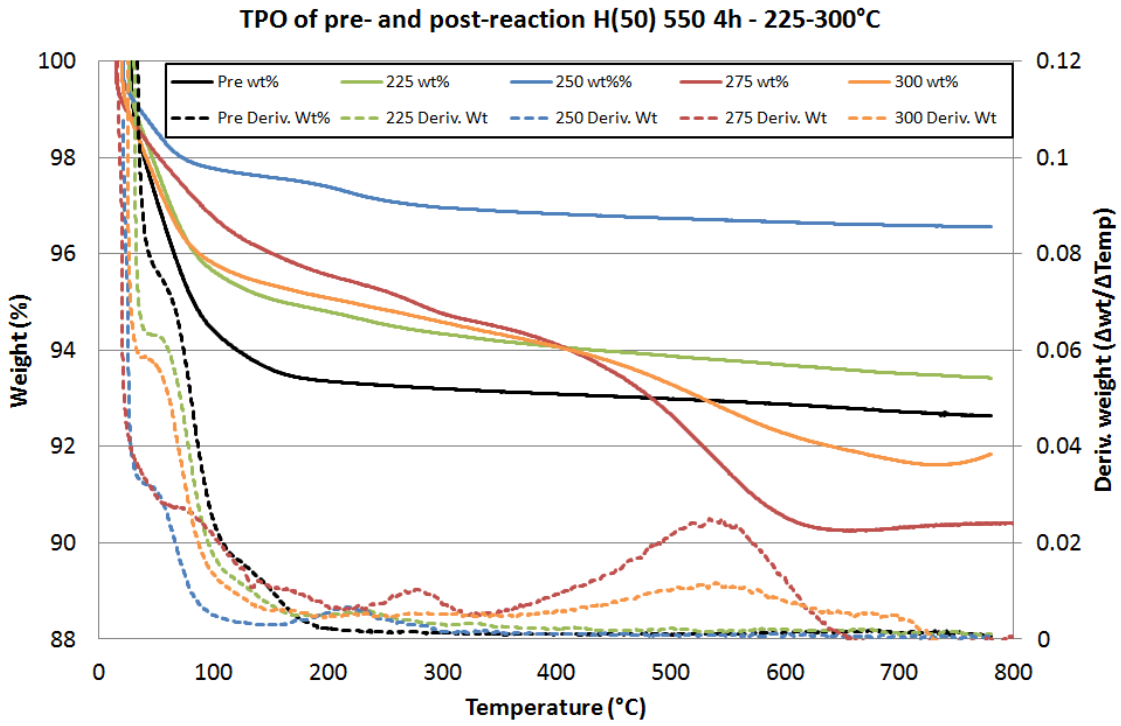

Figure 3.6: H(50) 550 4 h 225-300 °C TPO profiles. Experiments were operated as described in experimental section 2.6.8. In this figure 'Pre' is H(50) 550 4 h.

Fig. 3.7 shows the general loss in BET specific surface area, an increase in C wt. % and the decrease in the H:C ratio of adsorbates with increasing reaction temperature. Adsorbed H_2O contributes to the H:C ratio but this had a lessening effect with increased C wt. % and the H:C ratios at 275 °C and 300 °C indicate the presence of unsaturated hydrocarbon. The sharp change in BET specific surface area, C wt. % and H:C ratio upon increasing the temperature to 275 °C corresponds to the reaction switchover indicated in the catalytic testing.

Considering the TP and isothermal reaction data and post-reaction analyses, the DME production reaction operated at temperatures 150 - 250 °C with a switchover to hydrocarbon production at 275 °C under a narrow range of GHSVs (2900 - 4600 h^{-1}). This was consistent with the results of Chang *et al*. [2] where MeOH conversion over acidic zeolites displayed gasoline formation at ≥ 260 °C at 0.6 - 0.7 LHSV. This approximate reaction switchover temperature has been observed over H^+-form zeolites and as will be shown below, the temperature range over which DME production occurs is dependent upon the catalyst employed.

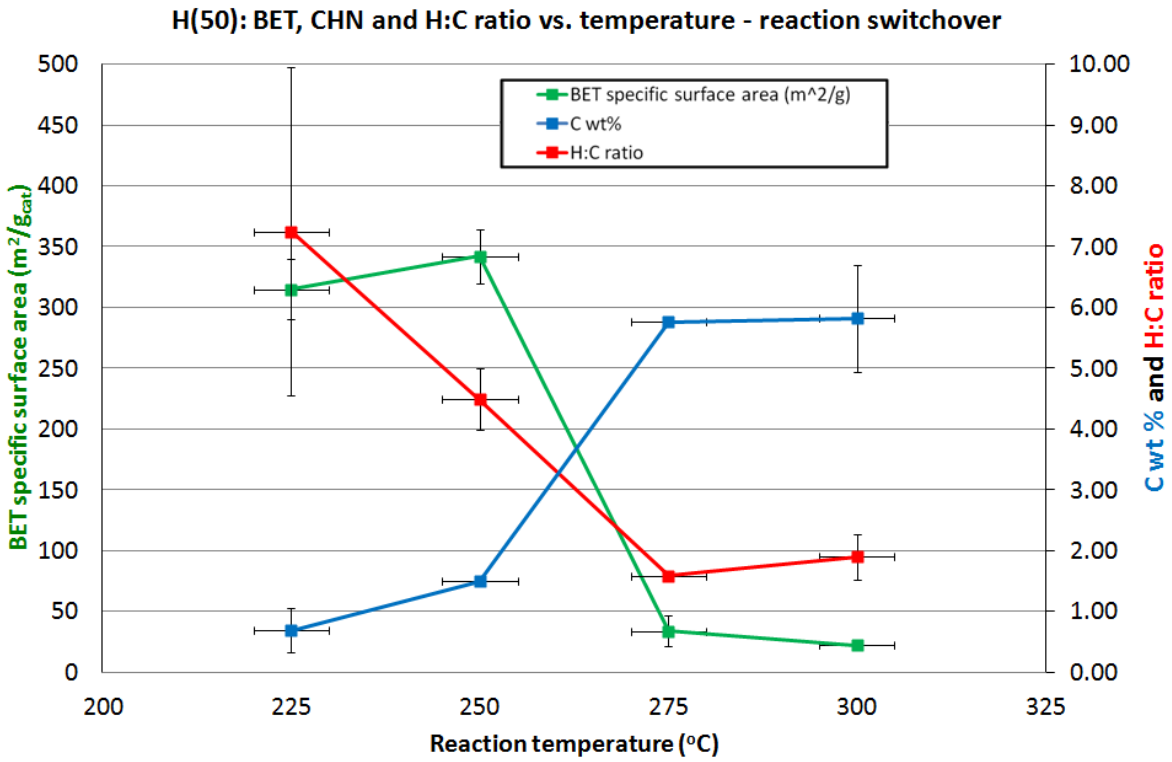

Figure 3.7: H(50) 550 4 h BET,CHN and H:C ratio graph. Results were obtained from post-reaction analyses of H(50) 550 4 h 225-300 °C experiments. BET (repeated 2x) and CHN analyses (repeated 2-16x).Vertical error bars represent the spread of data and horizontal error bars represent correspond to reactor temperature cycle.

3.1.3 TP reactions over Na(23) 550 4 h and Pural 550 4 h

Na(23) 550 4 h catalysts were prepared by treble ion-exchange (at room temperature) of NH_4(23) with 1M $NaNO_{3(aq)}$. Flame photometry has shown Na(23) 550 4 h to contain 0.65 wt. % sodium. Pural 550 4 h is γ-Al_2O_3 obtained by calcination of Pural SCF 55 (boehmite) (see section 6.1.1 for structural analyses).

Despite the observation that the switchover from DME to hydrocarbon production at 275 °C for H(50) 550 4 h, the switchover temperature is dependent on the catalyst employed as has been previously observed [3]. The results in Fig. 3.8 show stepwise increases in MeOH conversion with temperature. Both Na(23) 550 4 h TP and Pural 550 4 h TP meet the targets for DME production.

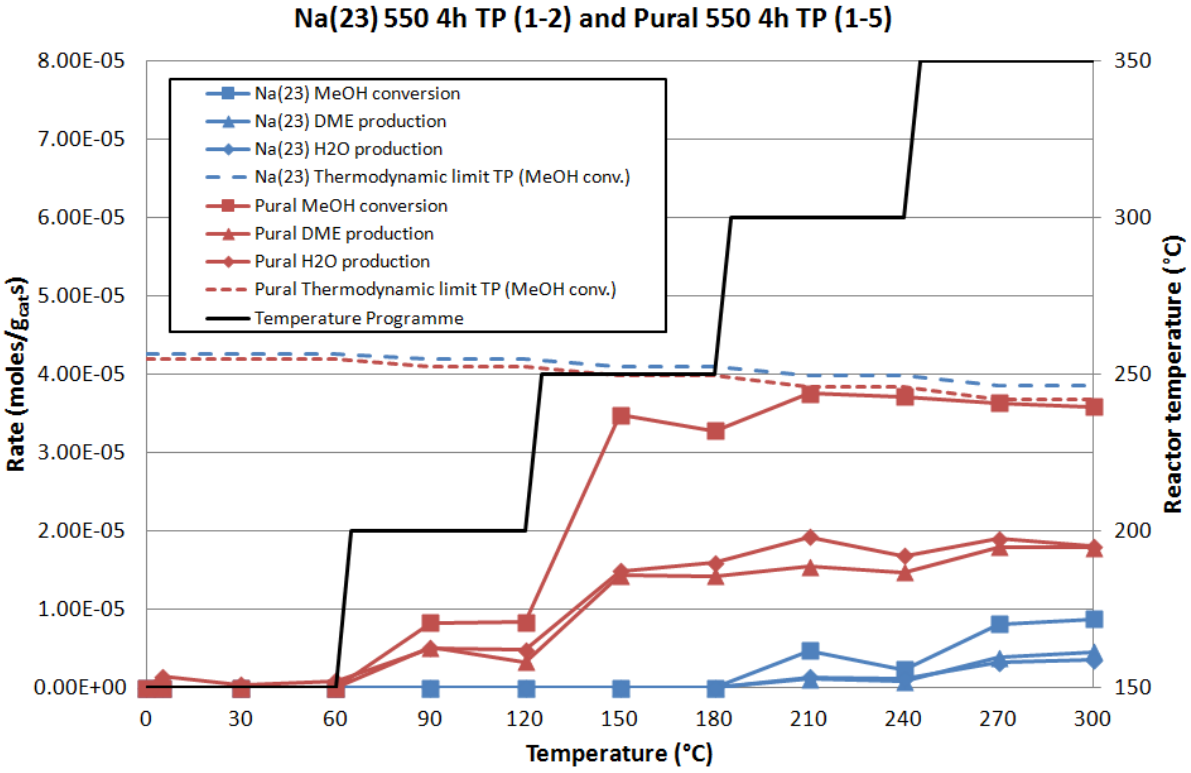

Figure 3.8: Na(23) Pural TP catalytic testing**.** Na(23) 550 4 h TP (duplicated) and GHSVs = 5000 h^{-1} and catalyst mass = 0.2740 ± 0.0000 g. Pural 550 4 h TP (repeated 5x): GHSVs = 7900 h^{-1} and dry catalyst masses = 0.2747 g ± 0.0007 g. The rate refers to the data labels in the figure legend.

Expectedly, the exchanged sodium acts as a poison. Despite Na(23) 550 4 h possessing greater aluminium content than H(50) 550 4 h, the methanol conversion rates are lower in the presence of increased sodium. The effects of sodium content on MeOH conversion, structural and textural properties will be further discussed in section 5.4.

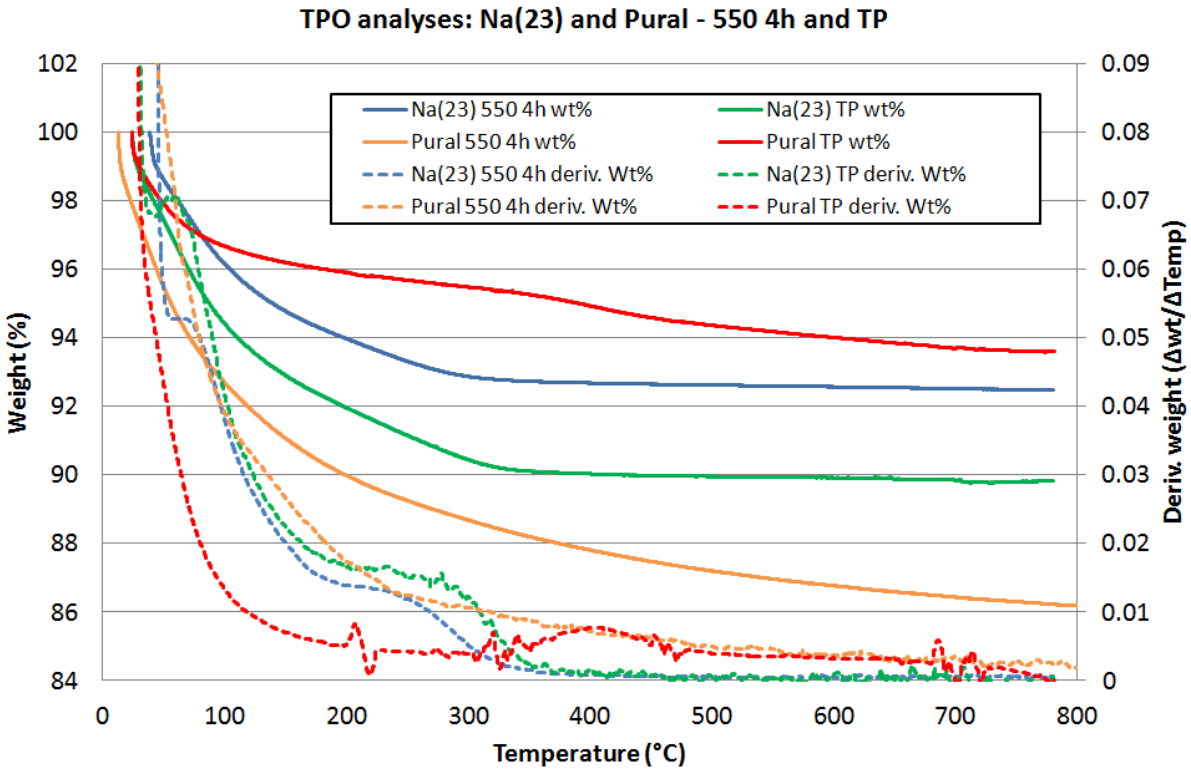

Figure 3.9: Na(23) Pural TPO profiles. These measurements were obtained as described in experimental section 2.6.8. The spiking observed in Pural TP derivative weight were artefacts.

Material	BET SA (m^2/g)	Total pore vol. (cm^3/g)	Ads. Iso. type	C (wt. %)	H (wt. %)
Na(23) 550 4 h	253	0.16	I	0.00	0.00
Na(23) 550 4 h TP	246	0.15	I	1.45 ± 0.03	0.81± 0.01
Pural 550 4 h	241 ± 2	0.39 ± 0.02	IV	0.00	0.00
Pural 550 4 h TP	205 ± 8	0.40 ± 0.01	IV	0.31 ± 0.31	0.60 ± 0.15

Table 3.3: Na(23) and Pural TP N_2-physisorption and CHN analyses. Results were obtained as described in the experimental section 2.6.5. The errors correspond to ± the furthest outlier of repeat measurements. CHN (repeated 2-10x). Ads. Iso. = Adsorption Isotherm. N_2-physisorption isotherms may be found in the appendix.

TPO analyses of Na(23) and Pural 550 4 h and TP catalysts are shown in Fig. 3.9. All weight loss in Na(23) 550 4 h and Pural 550 4 h were assigned to H_2O desorption. Na(23) TP weight loss ≤ 350 °C and Pural TP weight loss ≤ 475 °C was assigned to desorption of MeOH, DME and H_2O. This loss may also include MeOH and DME oxidation products.

N_2-physisorption and CHN elemental analysis results in Table 3.3, show that following TP reactions high BET specific surface areas are retained and relatively low C wt. % adsorbed. As such, analytical results indicate higher hydrocarbon formation did not occur over Na(23) 550 4 h or Pural 550 4 h over the temperature ranges examined.

3.2 Conclusions

According to the targets outlined at the start of the chapter: a reaction switchover from DME production to hydrocarbon production occurred at 275 °C over H(50) 550 4 h; whereas both Na(23) 550 4 h and Pural 550 4 h TP results show DME production up to 350 °C. As would be expected, the conditions under which the DME production reaction operates are dependent upon the reaction temperature and the catalyst employed.

Furthermore, the criteria for determining whether DME production was in operation was fit for the purpose of ensuring further experiments did indeed operate as desired. For this reason, all results included in the Arrenhius plots of the following chapters have met these targets.

3.3 References

[1] D. Däumer, K. Räuchle and W. Reschetilowski, Chem. Cat. Chem., 4 (2012) 802-814 and H. Schulz, Catal. Today, 154 (2010) 183-194.

[2] C. D. Chang and A. J. Silvestri, J. Catal., 47 (1977) 249-259.

[3] S. D. Kim, S. C. Baek, Y.-J. Lee, K.-W. Jun, M. J. Kim and I. S. Yoo, Appl. Catal. A: Gen., 309 (2006) 139–143.

4 Comparison of zeolites and zeotypes

4.1 General introduction

Zeotypes are non-aluminosilicate isomorphs of zeolites. Examples of zeotypes include SAPO-34 a silicoaluminophosphate with the structure of chabazite [1] and aluminogermanates with the sodalite structure [2]. Zeotype materials have been the subject of much academic research, particularly in the field of catalysis where additional and/or altered functionality may be introduced through variation of framework and extra-framework species. Substitution of framework aluminium, for example, has been reported to alter acidity and stability [3]. Through NH_3-TPD, FTIR and combined pyridine adsorption FTIR analyses the acid site strength was shown to generally follow the series Al-MFI > Ga-MFI > In-MFI > B-MFI for the group 3 elements. Fe-MFI possessed similar acid site strengths to Ga-MFI. It was also noted that extra-framework material was present in all of these materials, with contents increasing in the order of Al < Ga, Fe < In < B. The thermal [4] and hydrothermal stability [5] of B-MFI zeotypes have been reported as relatively low compared to Al-MFI zeolites. The lower catalytic activity of boron zeotypes has been previously reported [6] where methanol conversion, under similar conditions, to C_{2+} hydrocarbons was 98-99 % for H-(Al)-ZSM-5 and < 0.2 % for H-(B)-ZSM-5. Brőnsted acid site strength was also observed to follow the series Al-MFI > Fe-MFI > In-MFI by Cejka *et al*. [7]. The authors noted that In-MFI and Fe-MFI zeotypes contain greater quantities of extra-framework material than the Al-MFI zeolite. An explanation for the decreasing Brőnsted acid site strength between Si-OH-Al > Si-OH-B > Si-OH-Si was suggested by Scholle *et al*. [8]. By employment of the electrostatic valence model of Pauling to proposed Brőnsted acid sites, it was shown that the (O-H) bonding in 4-coordinate B^{3+}/Al^{3+} cations is weaker than that of 4-coordinate Si^{4+} cations. The relatively higher strength of the aluminium acid site is then indicated to be a consequence of the greater bond strength of the Al-O-H bond over the B-O-H bond. A ranking of Brőnsted acidity: Al(OH)Si > Ga(OH)Si > Fe(OH)Si >> B(OH)Si > Si(OH) was also observed by Chu and Chang [9] who employed NH_3-TPD and FTIR spectroscopy. In a combined catalytic, computational and NH_3-TPD study the ordering of Al > Ga > Fe > In > B was reported for Brőnsted acid site strength [10]. Notably, the authors commented that

the ranking of acid site strength was not simply a function of the electronegativity of the incorporated heteroatoms and was possibly affected by short-range localised effects.

The MFI framework, as explained in the introduction chapter, is currently of great importance in an industrial context. As such, it was appropriate to establish the DME production activity of isomorphous zeotypes with respect to the industrially significant zeolites. This will be illustrated in Arrenhius plots with accompanying catalyst characterisation.

4.2 Zeolite and zeotype structural analyses

4.2.1 Zeolite and zeotype PXRD analyses

All zeolites and zeotypes were of MFI crystal structure according to PXRD analyses. The approximately equally intense doublet at about 45 °2θ is indicative of MFI rather than the MEL framework type which is a common intergrowth [11].

The MFI structure has been reported to exist in two phases [12]; monoclinic and orthorhombic. The transition between each has been reported as a reversible, low energy displacive [13,14] phase transformation and was believed to occur *via* displacement of the (010) plane along the *c*-direction with the orthorhombic phase appearing to be the higher temperature phase. Furthermore, the transition temperature has been reported as being a function of the SiO_2/Al_2O_3 ratio – increasing with decreasing aluminium content [12]. Additionally, adsorption on the zeolite materials can induce transitions at lower temperatures [15]. Therefore the orthorhombic form would be expected to be present under probe reaction conditions.

To observe this reported reversible phase change, *in situ* PXRD measurements were undertaken on monoclinic ZSM-5 (280), see Fig. 4.1.

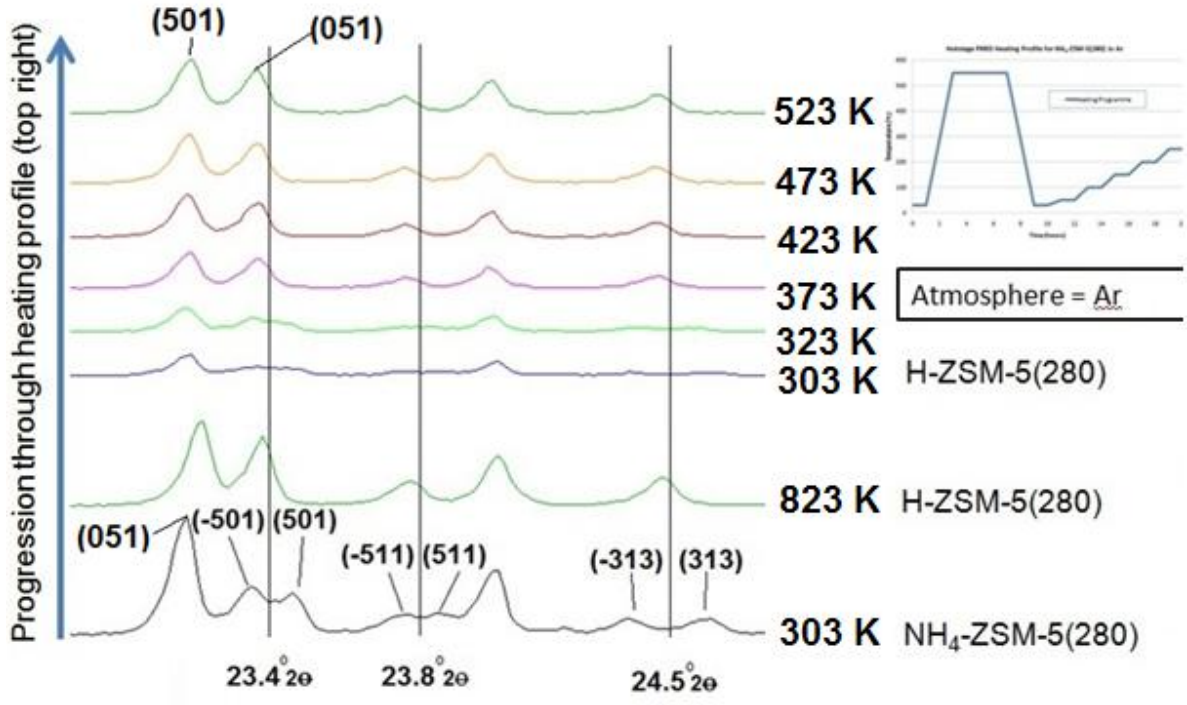

Figure 4.1: *In situ* hotstage PXRD of NH_4-ZSM-5 (280)**.** Measurements were obtained as described in section 2.6.6.2. A 2θ range of approx. 22.8 °- 24.8 ° was examined.

The reflections in Fig. 4.1 were assigned by the indexing of van Koningsveld *et al*. for the monoclinic phase [16] and the orthorhombic phase [15].

For NH_4(280), heating at 550 °C for 4 h under Ar was sufficient to convert the material into the H^+-form, 550 °C was also a sufficient temperature to convert the initially monoclinic sample to the orthorhombic phase. Monoclinic MFI possesses doublet reflections at approximately 23.4 °2θ, 23.8 °2θ and 24.5 °2θ whereas orthorhombic MFI possesses singlet reflections at these angles. Upon cooling to 30 °C, the sample reverted back to the monoclinic phase. Then with stepwise increases in temperature, orthorhombic MFI was once again formed between 50-100 °C as reported by van Koningsveld and co-workers [15].

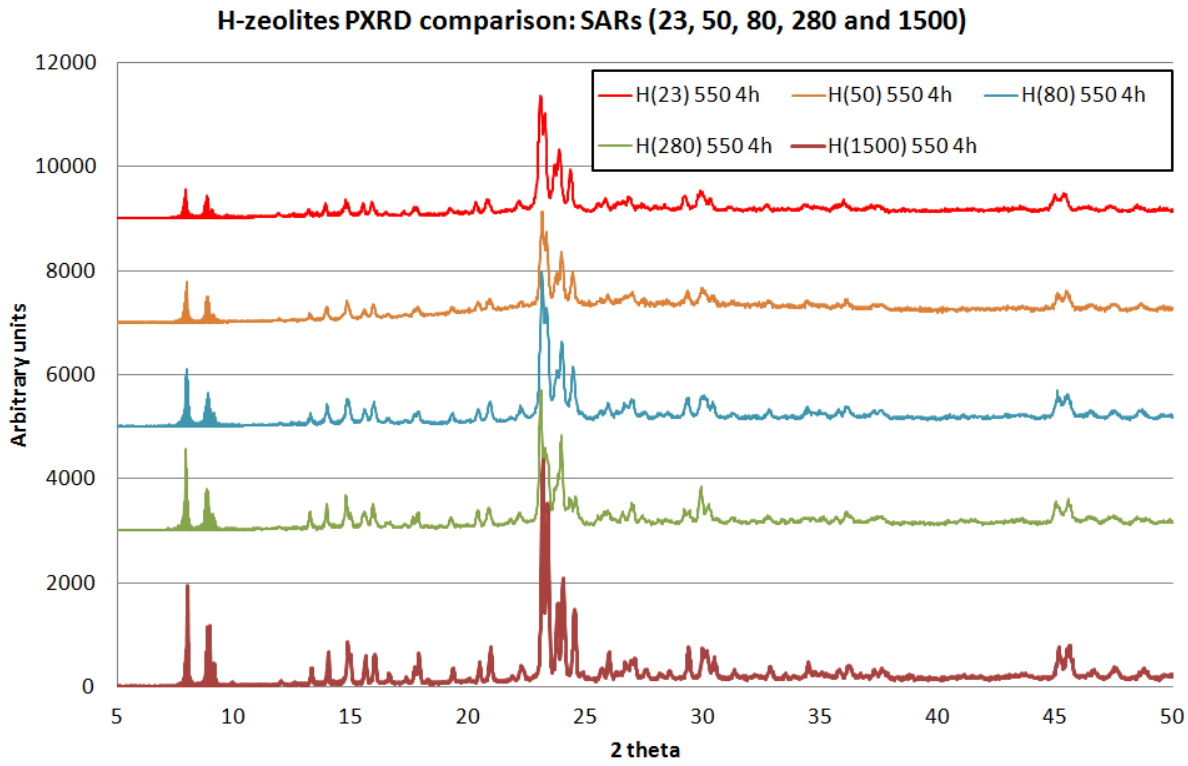

Figure 4.2: PXRD comparison of zeolite with different SiO_2/Al_2O_3 ratios**.** All experiments were undertaken as described in section 2.6.6.1

Fig. 4.2 shows H(23) 550 4 h, H(50) 550 4 h and H(80) 550 4 h were orthorhombic, H(280) 550 4 h was monoclinic but surprisingly H(1500) 550 4 h was orthorhombic. This may be explained by H(1500) 550 4 h possessing a high silanol group content (Figs. 4.5 and 4.6).

All templated zeotypes were of the orthorhombic MFI unit cell structure. This symmetry was retained following template removal, ion-exchange, calcination and catalytic testing as shown in Figs. 4.3a-c.

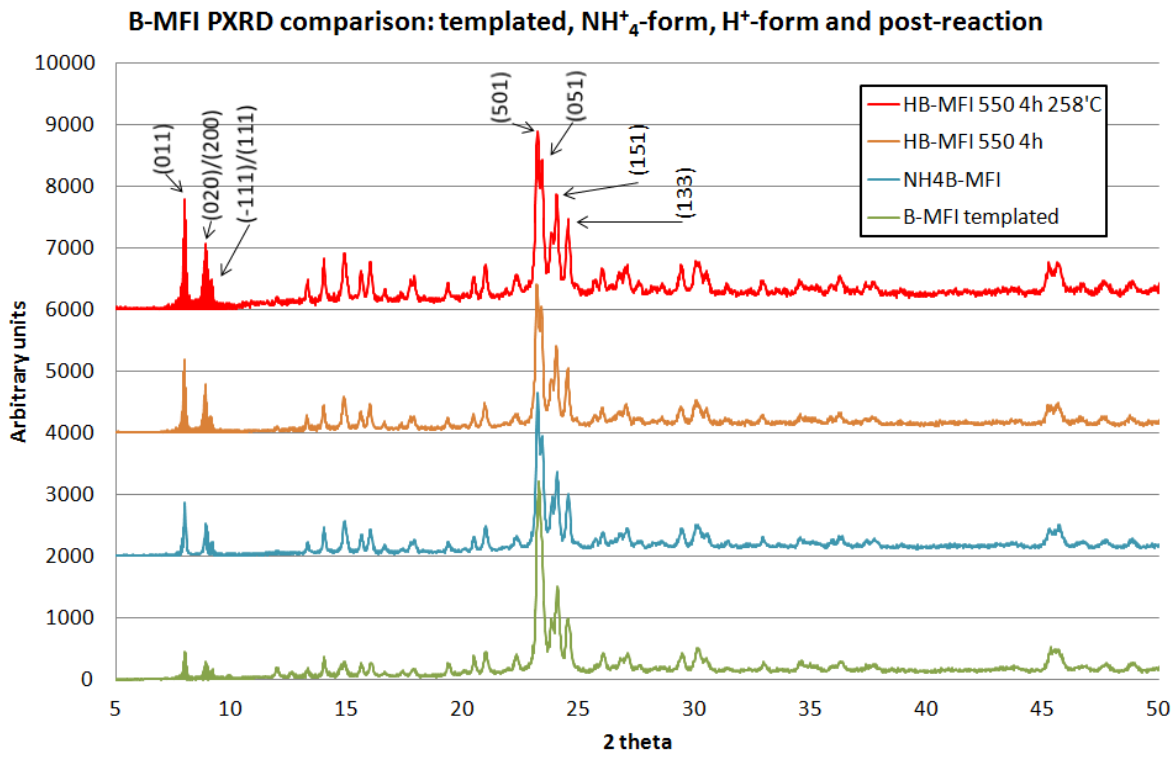

Figure 4.3a: PXRD of B-MFI materials.

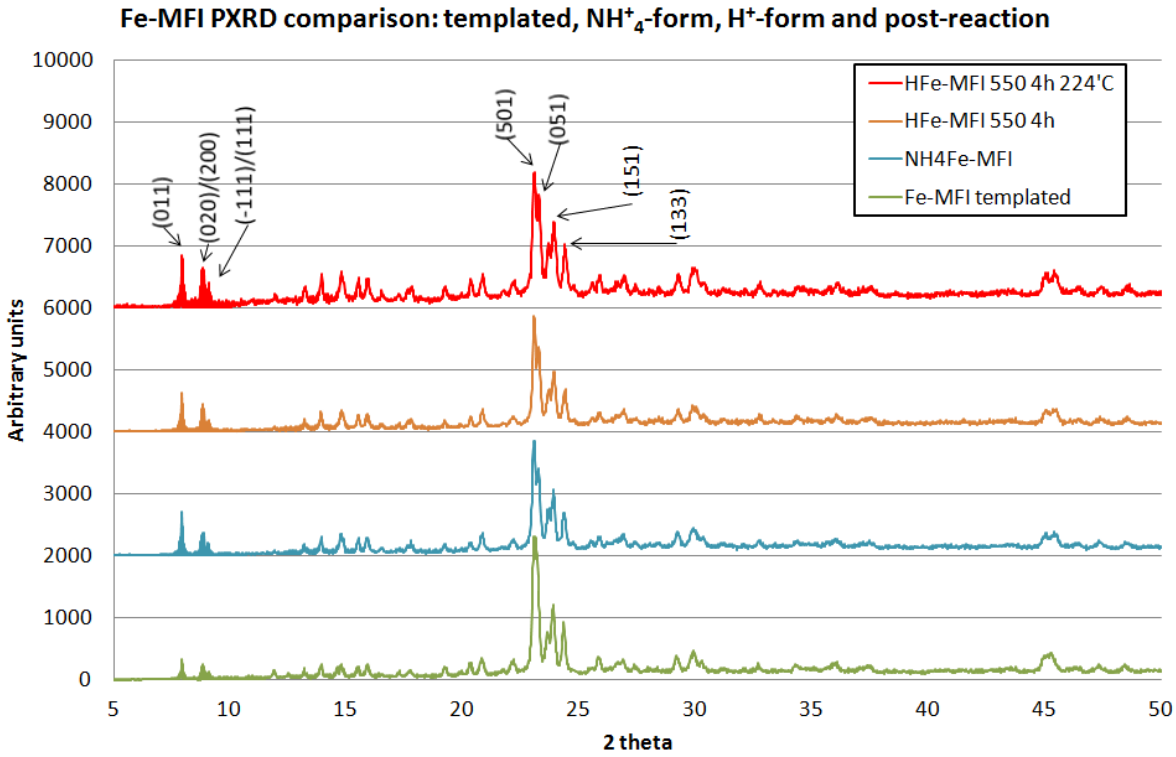

Figure 4.3b: PXRD of Fe-MFI materials.

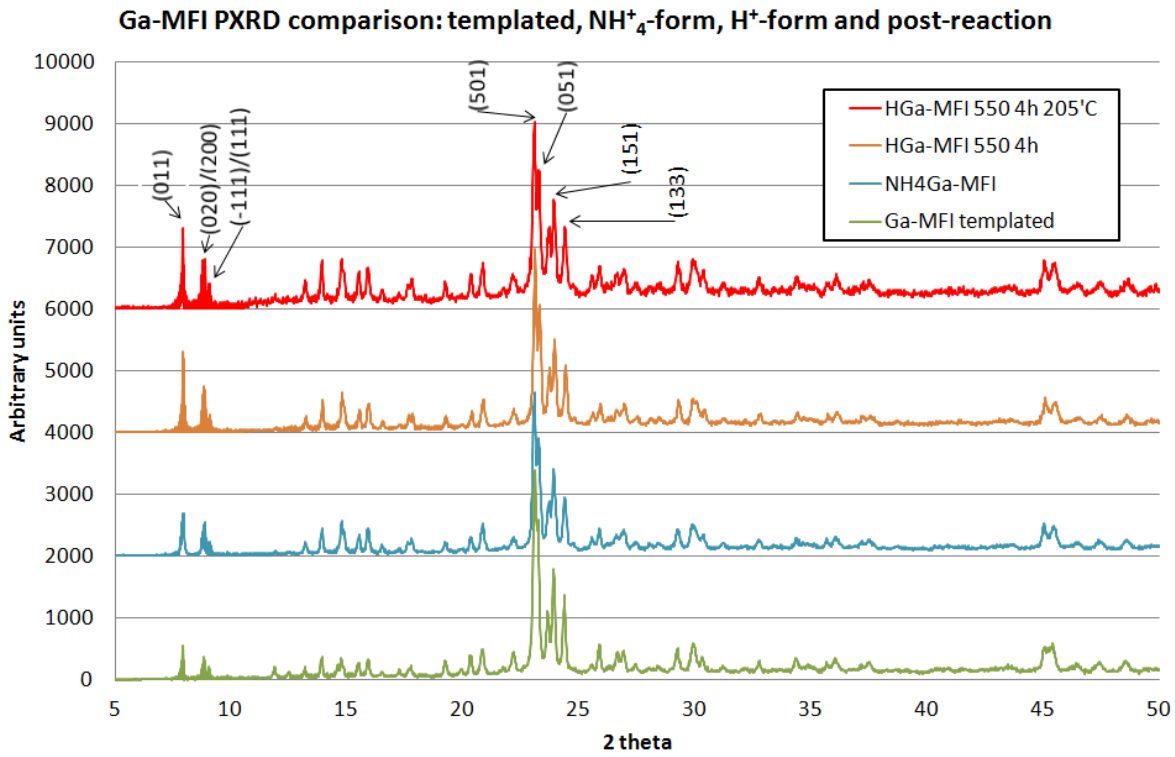

Figure 4.3c: PXRD of Ga-MFI materials**.**

Figures 4.3a-c: All patterns were obtained following the method described in section 2.6.6. The assignment of the reflections was adapted from the study of van Koningsveld *et al*. [15].

Following template removal in air there was a decrease in the sum of (501), (151) and (133) reflection intensity relative to the templated material, indicative of a decrease in material crystallinity [17]. This may be a result of the damage to the framework caused by high exotherms [18] associated with template oxidation. Additionally, the (011), (020)/(200) and (-111)/(111) reflection intensities of the templated zeotypes were relatively low when compared to the (501) reflection and this was indicative of pore filling [19]. These planes all intersect with both sinusoidal and straight pore channels because of the 3-D connectivity associated with the MFI framework type. In this instance, pore-filling causing a decrease in constructively scattered X-ray intensity can be rationalised by considering the templating species as an X-ray scatter and that their locations within the zeotype micropore channels result in destructive scattering from the aforementioned planes. This is possibly also observed in the reflections between 12-18 °2θ and a change in reflection intensity would be expected for all crystal planes associated

with the internal pore structure. Furthermore, changes in the crystallographic structure of the pores with adsorption may also contribute to destructive X-ray scattering.

Despite the crystal structure of each of the synthesised zeotypes being MFI, the PXRD analyses do not show whether the heteroatoms were indeed incorporated into the tetrahedral framework. It is possible that the heteroatoms may exist as extra-framework species which may have adopted a variety of geometries for example: trigonal, tetrahedral and octahedral. As such, MAS-NMR and TPR were employed to determine the extent of heteroatom incorporation.

To test for aluminium, boron and gallium framework incorporation, ^{27}Al, ^{11}B and ^{71}Ga MAS-NMR were employed respectively in conjunction with ^{29}Si and ^{1}H-^{29}Si CP (Cross Polarisation) measurements. ^{57}Fe spectra of Fe-MFI were not obtained because of the isotope's low abundance, low iron content within the material, low sensitivity and the paramagnetism of the Fe^{3+} (the assumed oxidation state of framework iron). The existence of redox active (extra-framework) species in the zeotype materials was also probed using TPR.

4.2.2 Zeolite MAS-NMR and TGA analyses

In Fig. 4.4, the peaks at ≈ 55 ppm may be assigned to tetrahedral aluminium and those at ≈ 0 ppm assigned to octahedral aluminium species. Typically in zeolitic systems tetrahedral aluminium is associated with framework incorporation whereas octahedral aluminium is associated with the presence of extra-framework species [20]. The decreased signal to noise ratio observed for both H(280) and H(1500) samples was consistent with their lower aluminium content. ICP data were obtained for H(50) and H(280) with values of SiO_2/Al_2O_3 = 53 and 265 respectively. As such, the aluminium contents followed the order H(23) > H(50) > H(280) > H(1500). The method of Klinowski [21] whereby Si/Al values may be determined from ^{29}Si peak intensities, could not be employed on H(1500) because it was difficult to separate the contributions from each environment reliably and also due to the low aluminium content of the silicalite material. Using the method of Klinowski on deconvoluted ^{29}Si DE spectra (see Appendix), SiO_2:Al_2O_3 values for

H(23) 550 4 h, H(50) 550 4 h and H(280) 550 4 h were determined to be 23, 88 and 235, respectively.

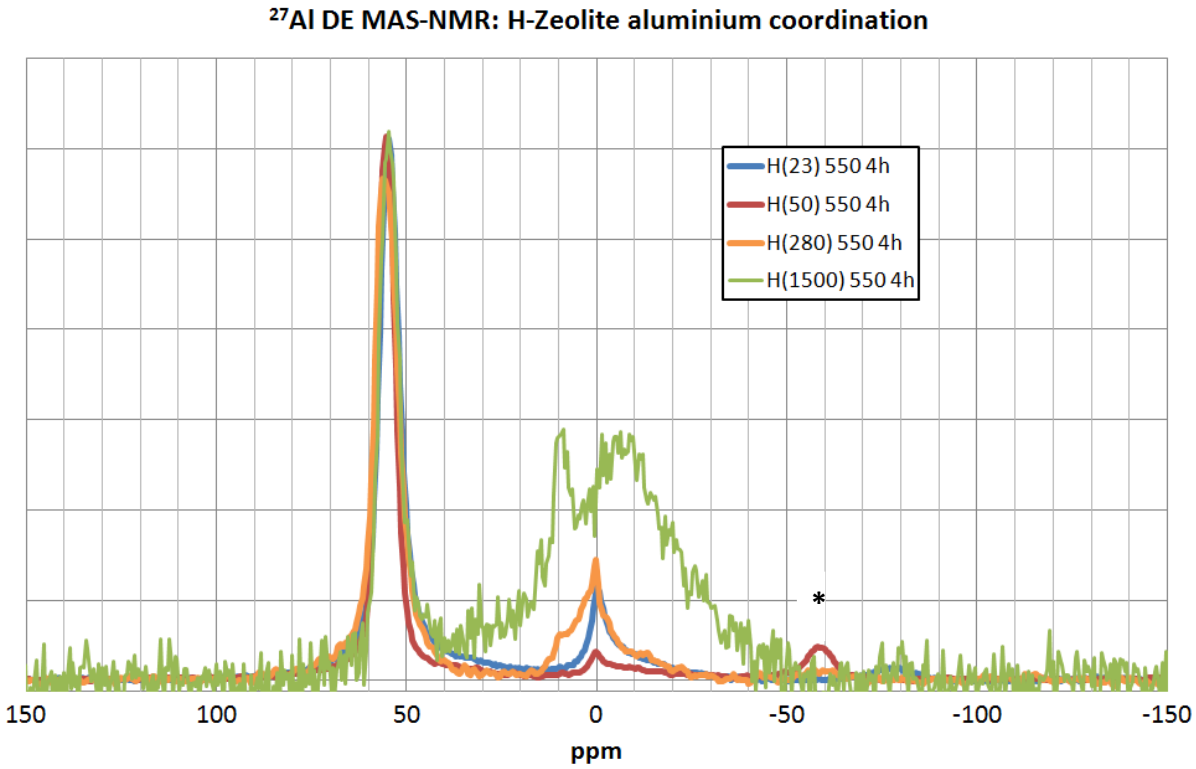

Figure 4.4: ^{27}Al MAS-NMR of zeolites with different SiO_2/Al_2O_3 ratios. All spectra were obtained on a Varian VNMRS 400. Asterisks (*) = Spinning side bands.

It was also possible to gain information regarding the short-range aluminium distribution by considering the ^{29}Si DE spectra. The -103 ppm, -106 ppm and all other peaks in Fig. 4.5 may be assigned to ^{29}Si in silanol, Si(1Al) and Si(0Al) environments respectively [20]. To clarify, Si(nAl) corresponds to [SiO_4] tetrahedra corner-sharing with n = 0-4 aluminium atoms. CP results are not included here for clarity but a peak at ≈ - 103 ppm is present in H(50) 550 4 h and H(1500) 550 4 h samples. It is apparent that H(280) 550 4 h possesses greater homogeneity within the Si(0Al) environments than all other zeolites in this figure and may be related to the low silanol content (see Fig. 4.5 and Fig. 4.6).

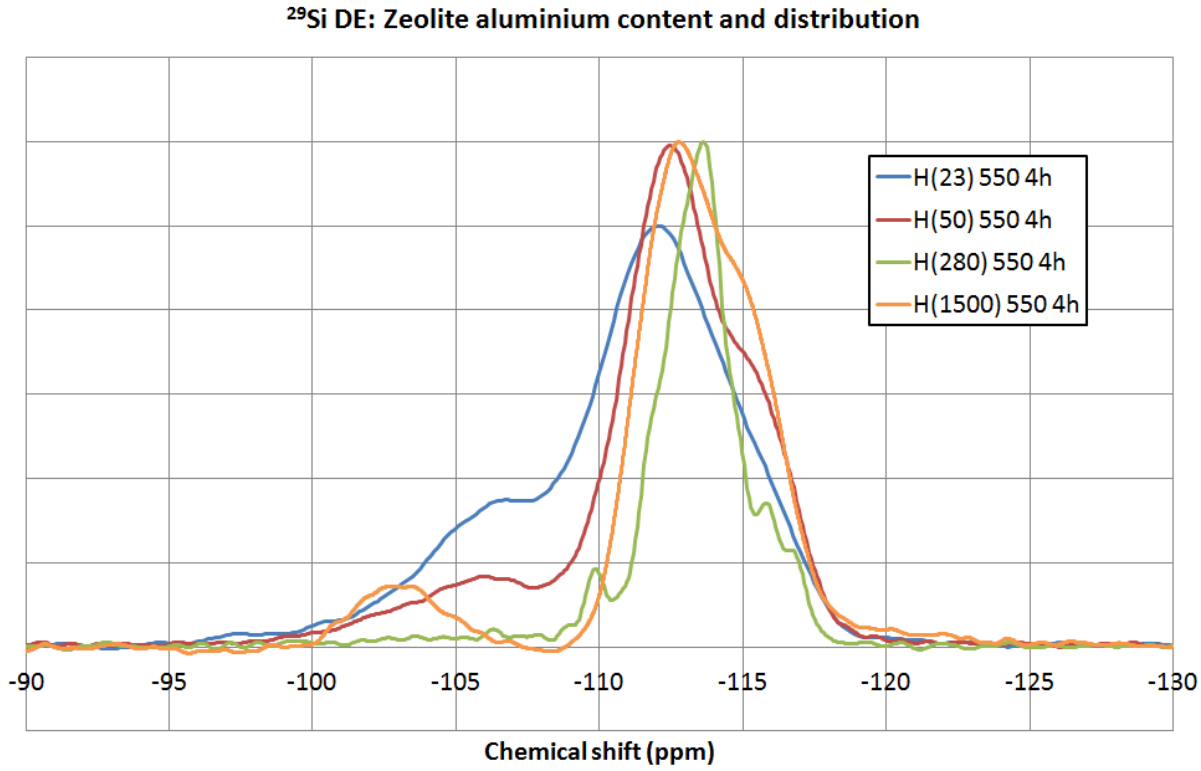

Figure 4.5: ^{29}Si MAS-NMR of zeolites with different SiO_2/Al_2O_3 ratios. H(23) 550 4 h spectra were obtained on a Varian Inova Unity 300 and all others were obtained using a Varian VNMRS 400.

TGA of the zeolite materials showed H_2O loss at low temperatures (< 250 °C) in all samples. With increasing aluminium content, the zeolites became more hydrophilic as shown in Fig. 4.6. However, H(1500) 550 4 h appears anomalous with greater H_2O content than H(280) 550 4 h and a relatively large mass loss at ≈ 650 °C assigned to silanol dehydration.

The pore volumes presented in Table 4.1 were all approximately equal so it would appear as though the hydrophilicity/phobicity of the materials strongly affected H_2O adsorption.

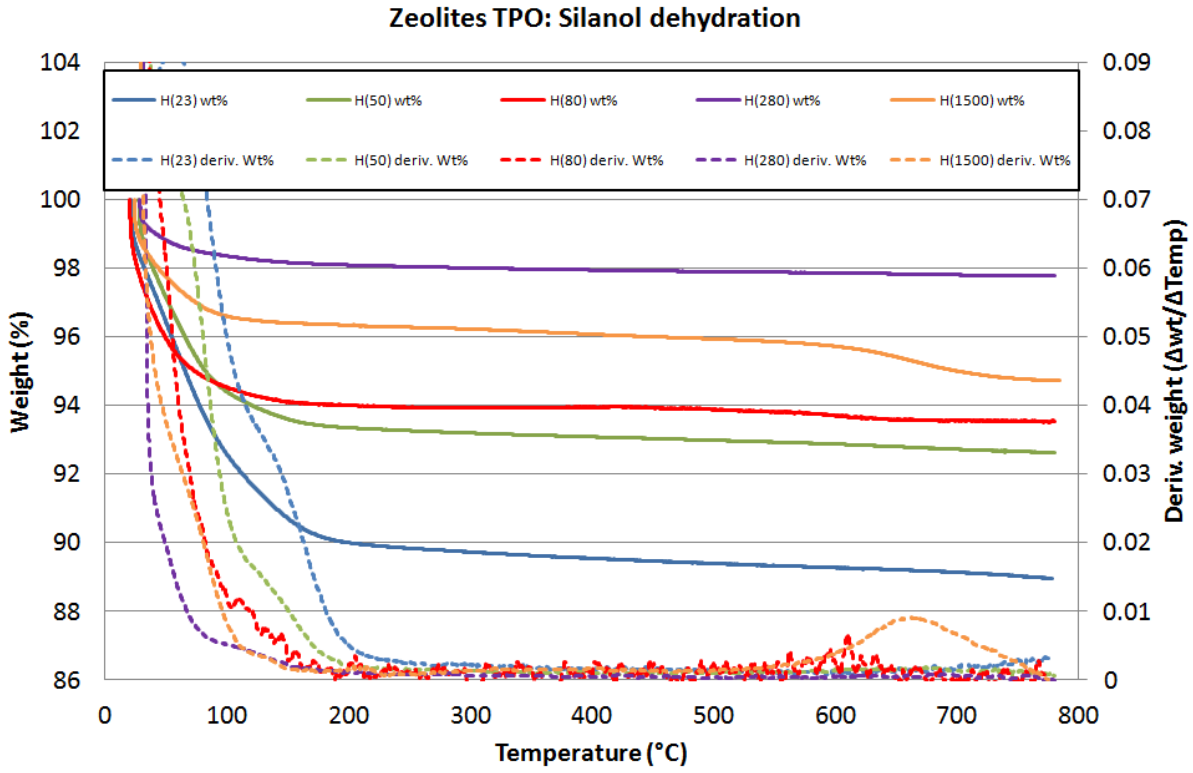

Figure 4.6: TPO measurements of zeolite with different SiO_2/Al_2O_3 ratios. Measurements were carried out as described in section 2.6.8.

The aluminium contents of each zeolite were ranked according to their Si(0-4Al) distribution, the signal-noise ratio in the ^{27}Al spectra and the ICP data. From these considerations it was reasonable to rank the framework aluminium content in order of H(23) > H(50) > H(280) > H(1500). It is also evident that H(1500) 550 4 h contains a relatively greater proportion of silanol species than the other zeolites, this was consistent with the 650 °C weight loss in the H(1500) profile in Fig. 4.6.

4.2.3 **Zeotype MAS-NMR and TGA analyses**

Examination of the ^{11}B NMR spectra in Fig. 4.7 shows boron to be tetrahedrally coordinated [6] despite the material's relative thermal [4] and hydrothermal instability [5]. The peak shift from -4 ppm to -3.6 ppm following template removal may have been a consequence of changing local structure surrounding each boron atom. Following template removal, the boron atoms were hydrated to a greater extent and the smaller downfield shift following protonation was previously observed by Testa *et al*. [22] and appears, in part, affected by the electronegativity of the counter ion. Fig. 4.8 shows gallium was also tetrahedrally coordinated [23,24].

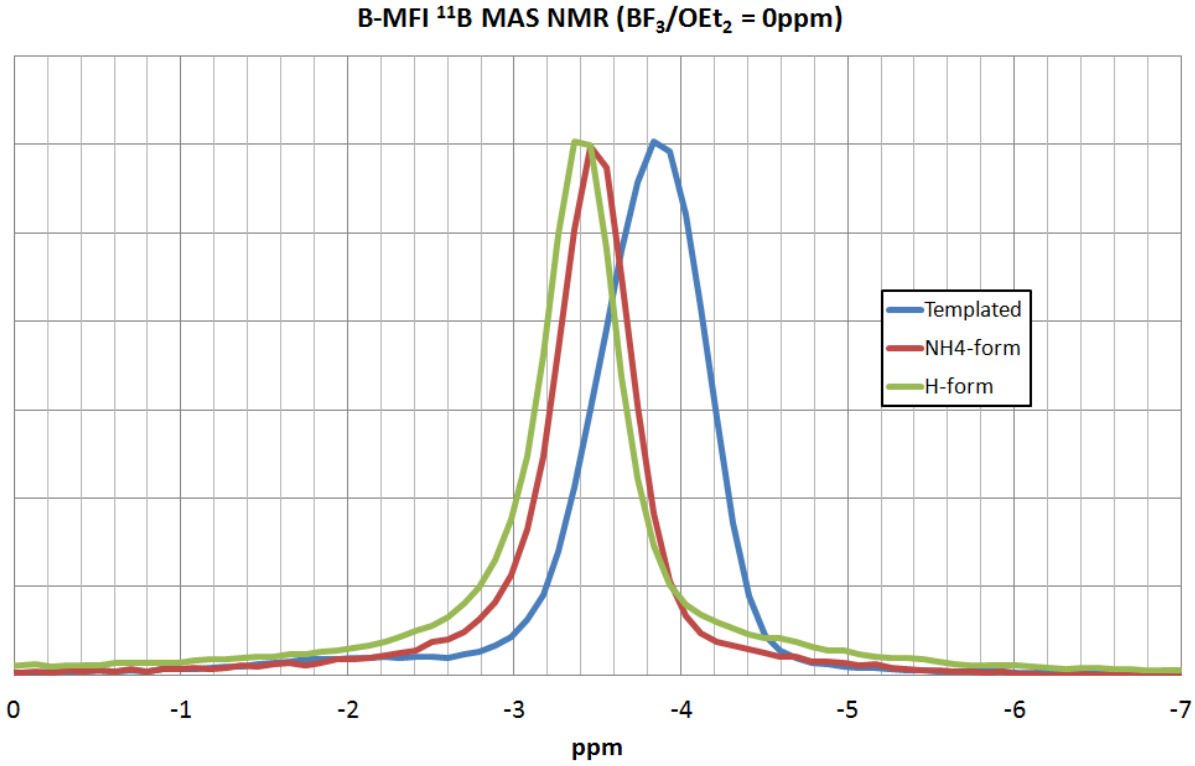

Figure 4.7: ^{11}B MAS-NMR spectra of B-MFI materials. All spectra were obtained using a Varian VNMRS 400.

For the gallium zeotypes, the H^+-form tetrahedral peak was the most downfield shifted of the compared spectra in the ^{71}Ga NMR spectra in Fig. 4.8. This was consistent with the same observation in B-MFI zeotypes.

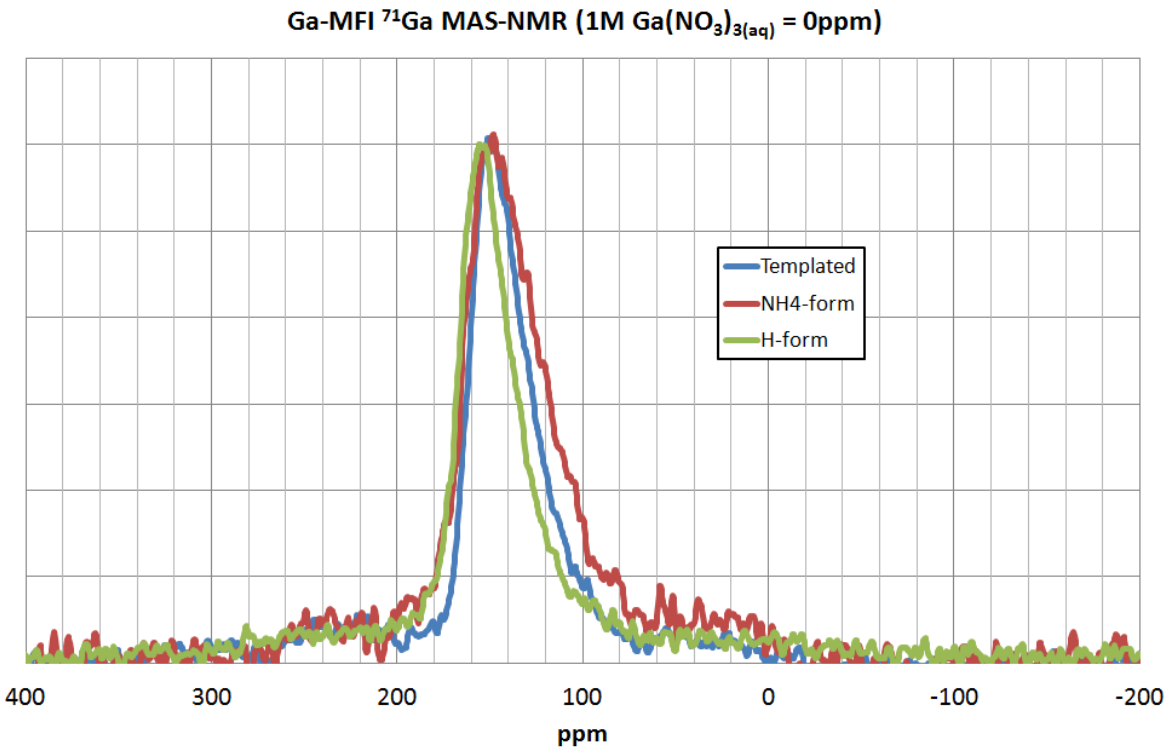

Figure 4.8: ^{71}Ga MAS-NMR spectra of Ga-MFI materials. All spectra were obtained using a Varian VNMRS 400.

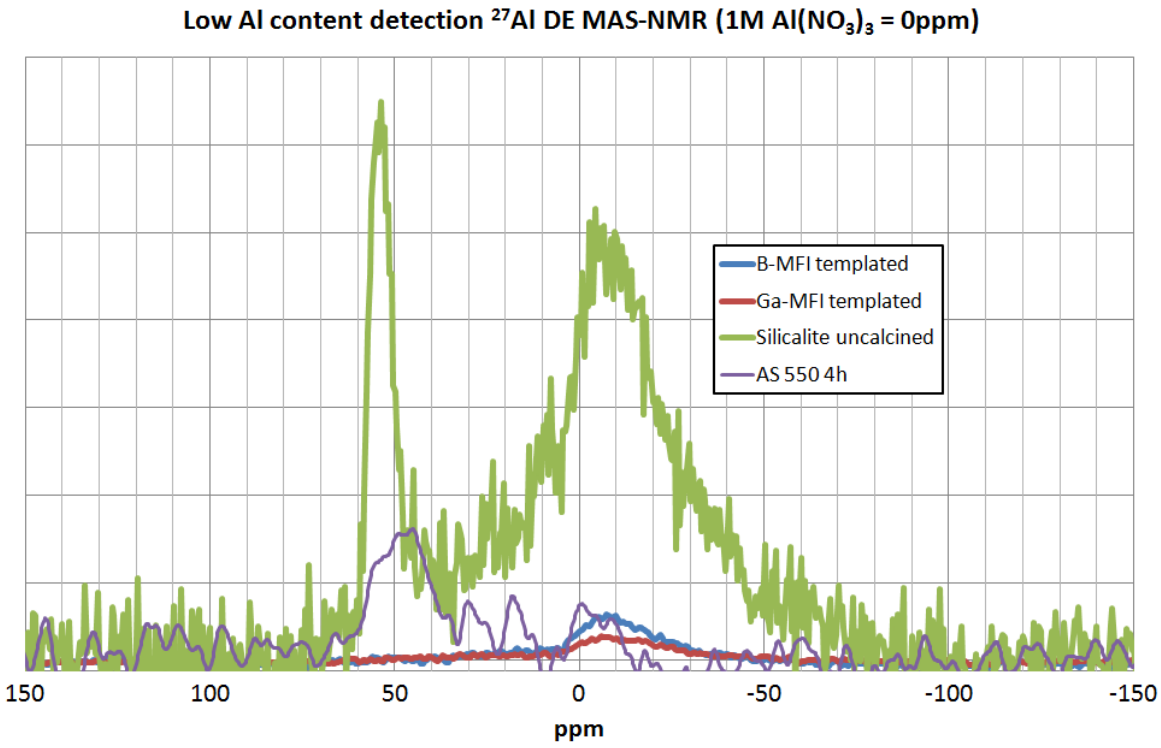

Figure 4.9: ^{27}Al MAS-NMR spectra of low aluminium materials. All spectra were obtained using a Varian VNMRS 400.

The extent of aluminium impurity within the zeotypes was investigated. As shown in Fig. 4.9 the low level of aluminium detected in the zeotypes was approximately equal to background impurity in the PTFE rotors, less than was found in a silica binder (Ludox AS 550 4 h) and much less than that found in silicalite (NH_4(1500)).

The negligible aluminium impurity in boron and gallium zeotypes reflects the 99.80 % pure fumed silica used for their syntheses of B-MFI and Ga-MFI and such low levels may be disregarded as contributing the catalytic activity of both B-MFI and Ga-MFI described later. However, an alternate and lower purity silica source (sodium metasilicate) was used in the Fe-MFI synthesis and the possibility of an aluminium impurity contributing to the observed MeOH dehydration activity of that material cannot be ruled out.

Approximate content and distribution of the boron and gallium heteroatoms through the zeotype MFI frameworks were elucidated by ^{29}Si MAS-NMR spectra (Fig. 4.10).

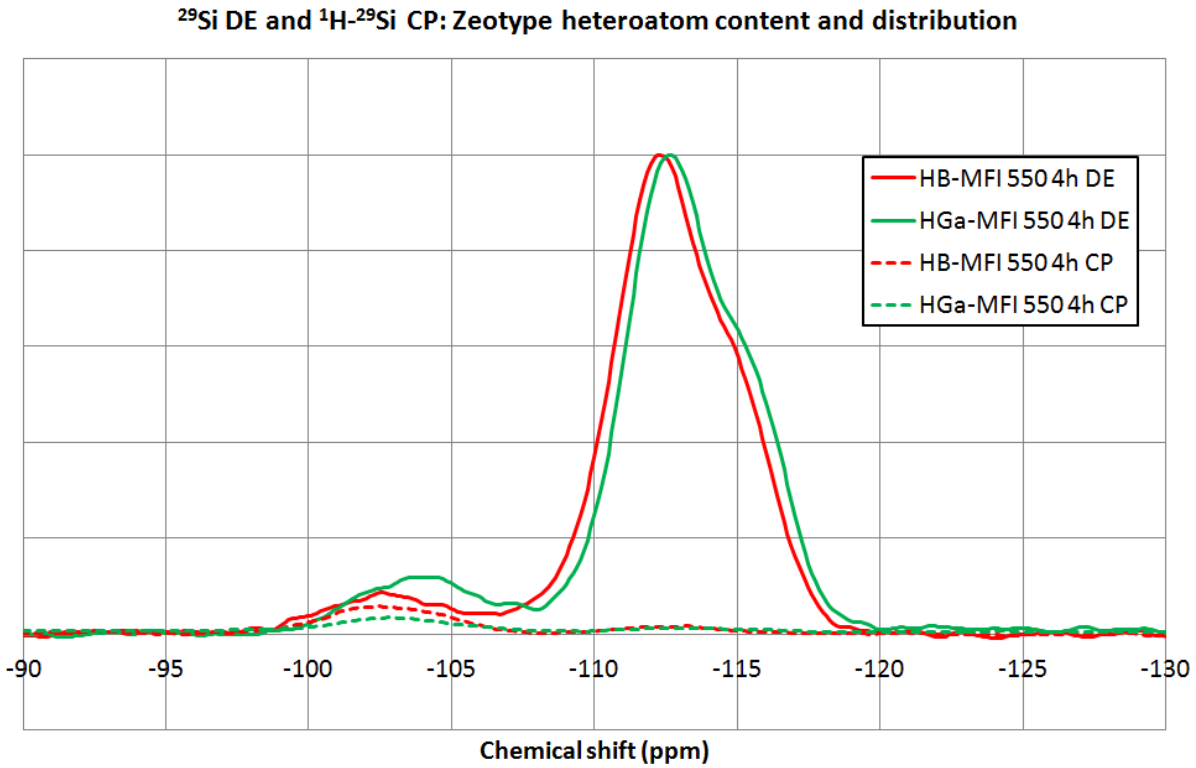

Figure: 4.10: ^{29}Si MAS-NMR spectra of HB-MFI 550 4 h and HGa-MFI 550 4 h. All spectra were obtained using a Varian Inova Unity 300.

DE peaks centred at ≈ -112 ppm and – 116 ppm were assigned to Si(0Al) and those centred ≈ –103 ppm were assigned to silanol groups in accordance with the CP spectra. These spectra indicate heteroatom content for HB-MFI 550 4 h to be significantly lower than the nominal value of SiO_2/B_2O_3 = 8. Incomplete boron framework incorporation was expected from the synthesis method employed (see ref. [3] of the experimental chapter). The authors of the synthesis method used an excess of boric acid and from a nominal SiO_2/B_2O_3 = 2.4 mixture ratio a B-MFI zeotype with a framework ratio of SiO_2/B_2O_3 = 98 was produced. By comparison of Fig. 4.5 and Fig. 4.10, both HB-MFI 550 4 h and HGa-MFI 550 4 h were estimated as $SiO_2/(B \text{ or } Ga)_2O_3$ ≈ 100, where the gallium content in Ga-MFI 550 4h was close to the nominal value of 114. The broadness of the DE spectral peaks, indicative of relatively large heterogeneity within the Si(0 B/Ga) and silanol environments, made quantification difficult.

Brief TPR studies (Fig. 4.11) were undertaken to observe extra-framework redox active heteroatoms. HB-MFI 550 4 h is not expected to be redox active.

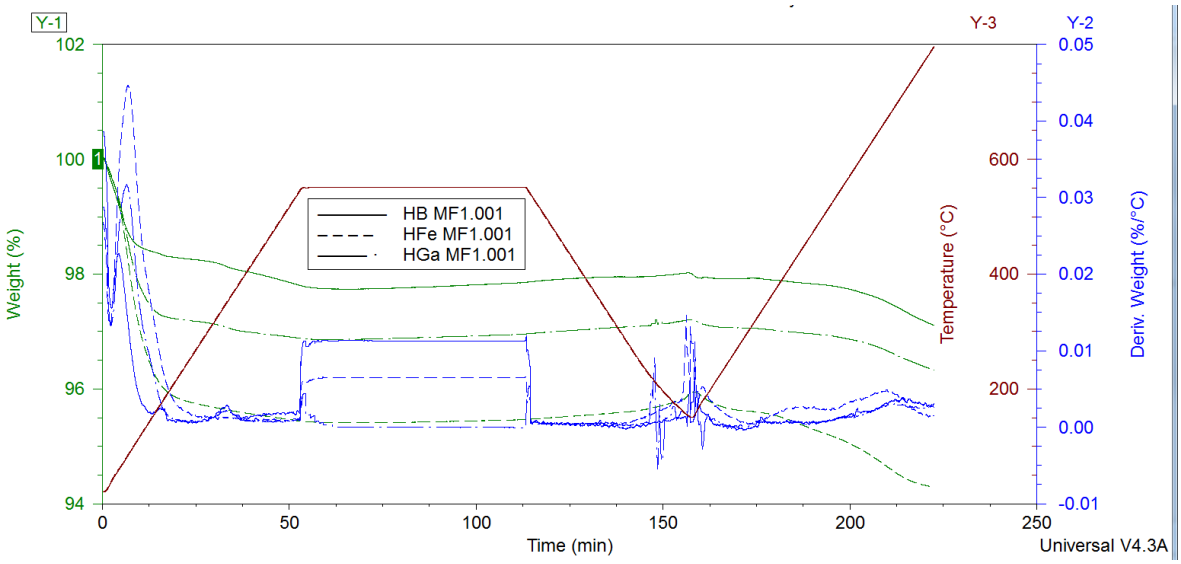

Figure: 4.11: TPR of activated B-MFI, Fe-MFI and Ga-MFI materials**.** These materials were activated *in situ*, cooled to 150 °C, switched to a reducing (5 % H_2/N_2) atmosphere at approx. 160 mins and heated at 10 °C/min.

It was observed that HFe-MFI 550 4 h loses more mass than either HB-MFI 550 4 h or HGa-MFI 550 4 h between 350-600 °C. This may indicate reduction of extra-

framework iron oxide species [25]. It may be expected that extra-framework gallium oxide species would also be reduced within the temperature range of the measurement [26] but these results indicate little/no redox active, extra-framework, gallium species were present in accordance with ^{71}Ga MAS-NMR results. The mass loss at ≈ 650 °C was assigned to silanol dehydration.

4.3 Zeolite and zeotype textural analyses

4.3.1 SEM imaging and EDX analyses of zeolites and zeotypes

All zeolite crystals were too small to determine crystal size or morphology from SEM imaging except for Na(1500) 550 4 h. A representative image is shown in Fig. 4.12. The silicalite crystals were ca. 5 µm in length with a characteristic twinned morphology [27-29].

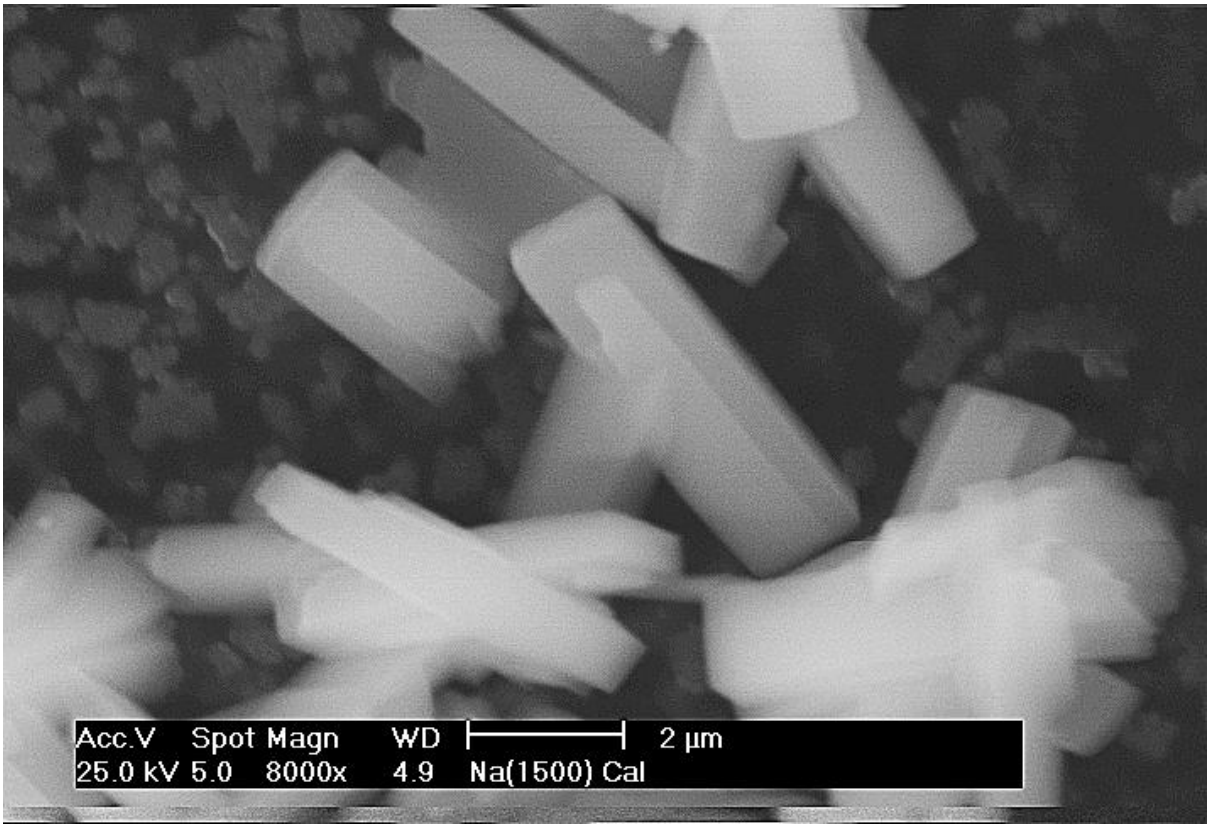

Figure 4.12: SEM image of silicalite. The image was obtained as described in experimental section 2.6.4. The background of the image was an unrepeatable artefact and not evidence of a wide crystal size range.

Representative SEM images of B-MFI and Ga-MFI indicate crystal size to increase in the order of Fe-MFI < B-MFI < Ga-MFI where the Fe-MFI crystal size was too small to determine morphology. However, the morphology of B-MFI and Ga-MFI are noticeably different. The larger, more cuboidal, B-MFI (Fig. 4.13) crystals are approximately 5 μm in length and of a characteristic twinned intergrowth morphology.

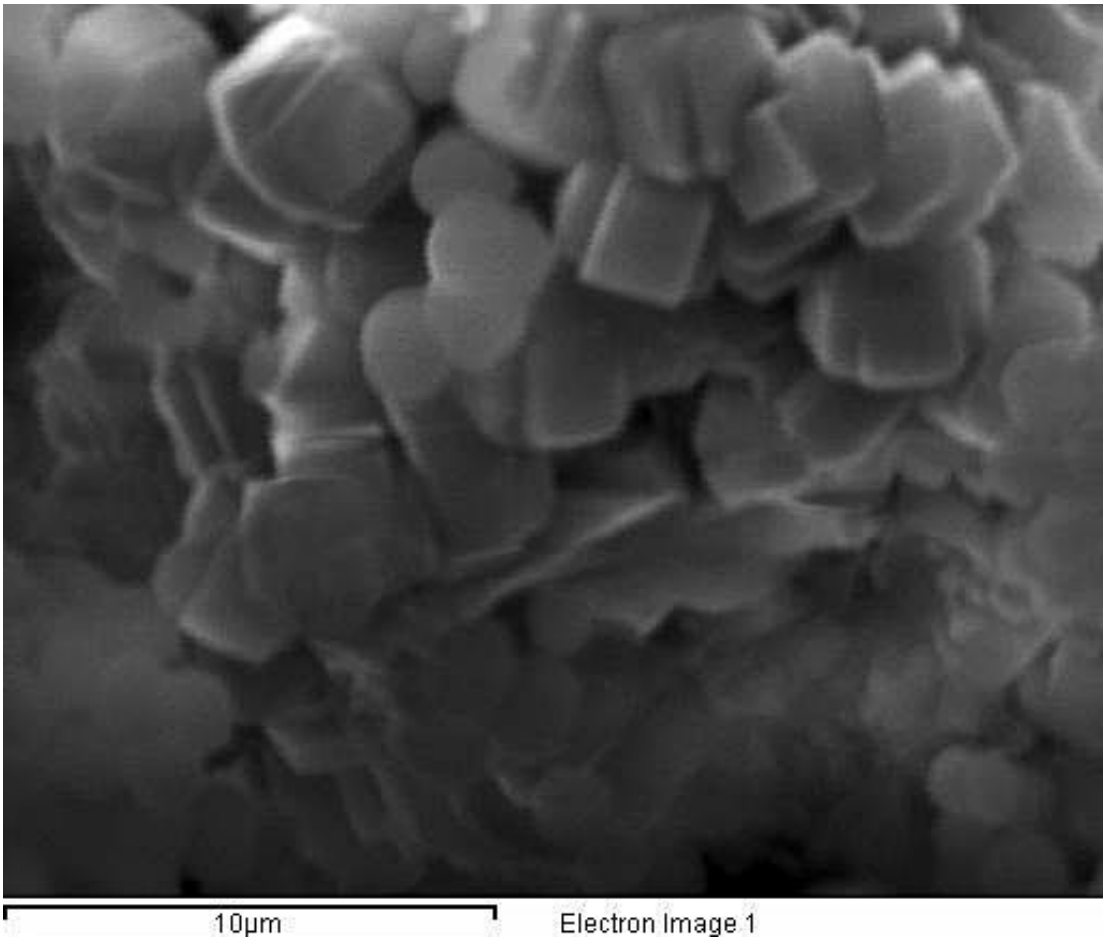

Figure 4.13: SEM image of HB-MFI 550 4 h. The image was obtained as described in experimental section 2.6.4.

The Ga-MFI crystals appeared more intergrown (Fig. 4.14), with larger crystals approximately 13 μm in length.

Accompanying qualitative EDX spectroscopy showed all H^+-form zeolites to contain silicon, aluminium and oxygen (except H(1500) 550 4 h – only silicon and oxygen observed). EDX spectroscopy of the boron zeotype showed only silicon and oxygen to be present (because of the decreased probability of X-ray

interaction with light elements such as boron). Analysis of the iron zeotype showed only silicon, iron and oxygen to be present. Measurements taken for the gallium zeotype showed only silicon, gallium and oxygen to be present. Having already shown negligible aluminium content in the B-MFI and Ga-MFI materials using MAS-NMR, it is possible that an aluminium impurity may yet exist in Fe-MFI as EDX signal intensities are subject to attenuation effects.

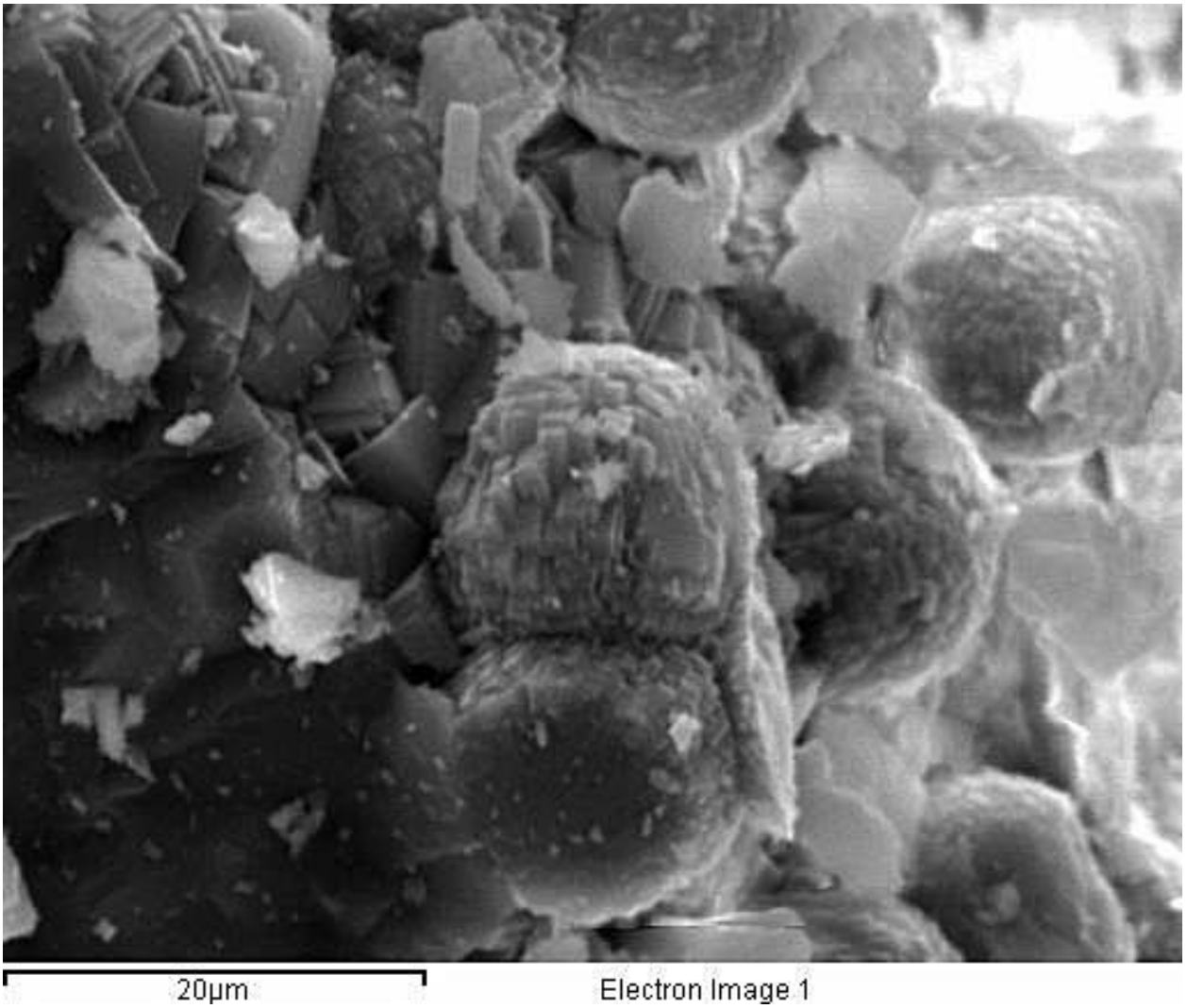

Figure 4.14: SEM image of HGa-MFI 550 4 h. The image was obtained as described in experimental section 2.6.4.

4.3.2 N_2-physisorption measurements of zeolites and zeotypes

N_2-physisorption studies of NH_4^+-form, H^+-form and post-reaction zeolites generally show slightly decreased surface areas in the calcined zeolites (Table 4.1). This is

ascribed to the presence of extra-framework aluminium in all H^+-form zeolites as shown in Fig.4.4. The adsorption isotherms were assigned as type I [30] in all materials [31] (see appendix). ZSM-5 (280) samples possessed a low pressure step at *ca.* 0.2 P/P_o which is explained in section 6.3.2.2.

Material	BET SA (m^2/g)	Total pore vol. (cm^3/g)	Ads. Iso. Type
NH_4(23)	319	0.20	I
H(23) 550 4 h	318 ± 48	0.20 ± 0.01	I
H(23) 550 4 h 200 °C	311	0.24	I
NH_4(80)	404	0.29	I
H(80) 550 4 h	373	0.25	I
H(80) 550 4 h 211 °C	353	0.25	I
NH_4(280)	381	0.22	I
H(280) 550 4 h	358 ± 5	0.21 ± 0.00	I
H(280) 550 4 h 239 °C	353	0.21	I
NH_4(1500)	334	0.20	I
H(1500) 550 4 h	326	0.19	I
H(1500) 550 4 h 236 °C	299	0.17	I

Table 4.1: N_2-physisorption results of zeolites with different SiO_2/Al_2O_3 ratios**.** Where the materials with temperatures 258 °C, 224 °C and 205 °C in their name refer to samples obtained from catalytic testing at those temperatures. Ads. Iso. = Adsorption Isotherms. All measurements were obtained as described in section 2.6.5.

Material	BET SA (m^2/g)	Total pore vol. (cm^3/g)	Ads. Iso. Type
B-MFI temp.	7	0.02	V**
NH_4B-MFI	280	0.16	I
HB-MFI 550 4 h	300	0.17	I
HB-MFI 550 4 h 258 °C	276	0.17	I
Fe-MFI temp.	35	0.05	I
NH_4Fe-MFI	312	0.21	I
HFe-MFI 550 4 h	290	0.19	I
HFe-MFI 550 4 h 224 °C	234	0.18	I
Ga-MFI temp.	2*	0.01	V**
NH_4Ga-MFI	277	0.16	I
HGa-MFI 550 4 h	319	0.18	I
HGa-MFI 550 4 h 205 °C	289	0.19	I

Table 4.2: N_2-physisorption results of zeotype materials. Where the materials with temperatures 258 °C, 224 °C and 205 °C in their name refer to samples obtained from catalytic testing at those temperatures. Ads. Iso. = Adsorption Isotherm. "temp" refers to template containing samples. * indicates a single point BET surface area value. ** low N_2-physisorption levels make assignment difficult. Adsorption isotherms may be observed in the appendix.

N_2-physisorption studies of templated, NH_4^+-form, H^+-form and post-reaction zeotypes are shown in Table 4.2. Following oxidative template removal, a dramatic increase in surface areas and pore volumes were observed and may be attributed to liberation of the MFI microporosity.

In contrast to the calcined zeolites, boron and gallium zeotypes slightly increased in surface area following calcination. No evidence of extra-framework boron and gallium species was found from ^{11}B and ^{71}Ga MAS-NMR spectra (Fig. 4.7 and Fig. 4.8). HFe-MFI 550 4 h has a lower surface area than NH_4Fe-MFI but this may be due to extra-framework species decreasing pore accessibility. A subsequent decrease in surface area was observed with all post-reaction samples and was attributed to adsorbed carbonaceous species (originating from the MeOH dehydration reaction) occupying surface area thus preventing N_2-physisorption.

4.3.3 **TPO studies on zeolites and zeotypes**

With increasing temperature from room temperature to 800 °C at 10 °C/min, all zeolites (Figs. 4.14a-d) lose H_2O < 250 °C and this was then followed by the loss of adsorbed carbonaceous material and/or ammonia (for post-reaction and NH_4^+-form samples respectively) and silanol dehydration ≈ 650 °C.

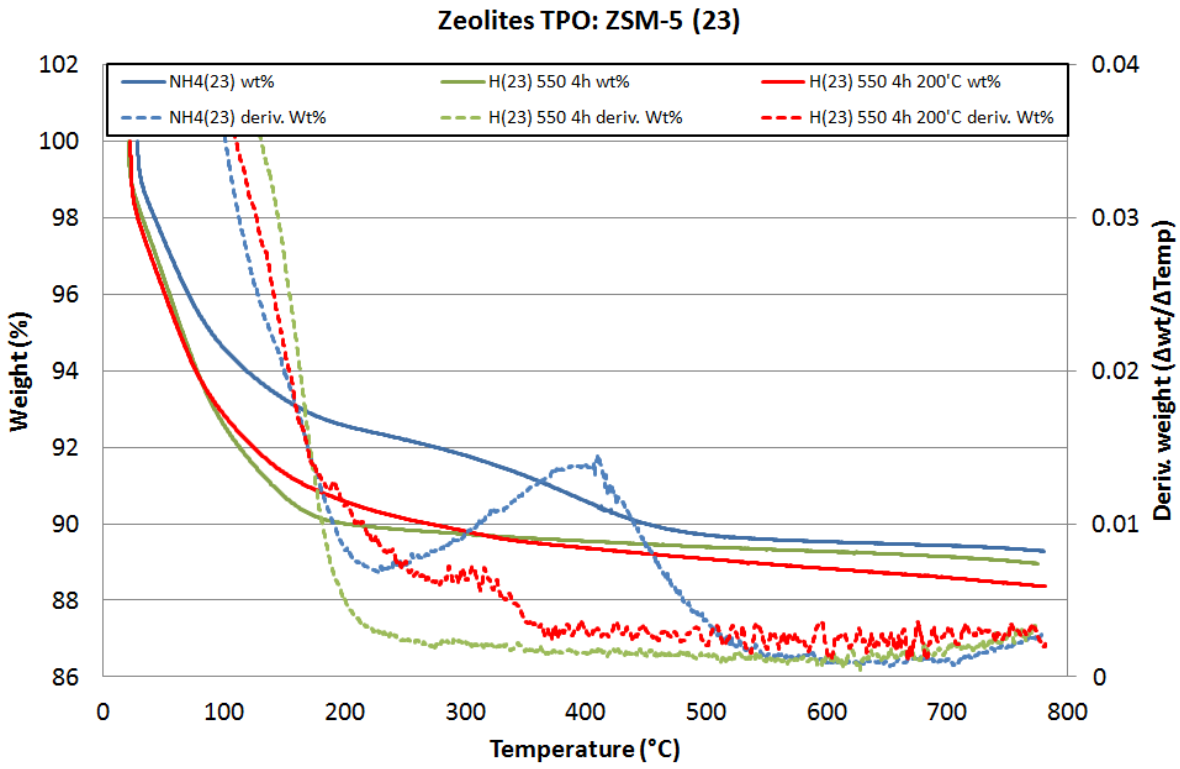

Figure 4.14a: TPO measurements of ZSM-5 (23) materials.

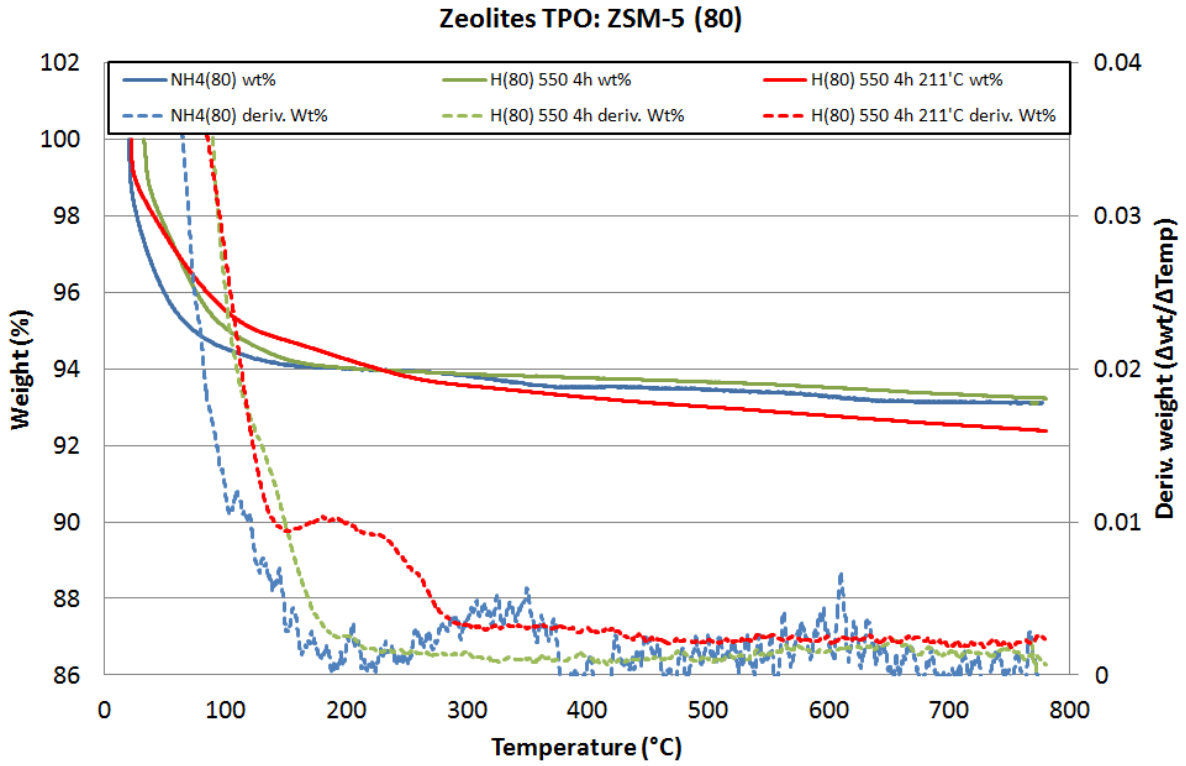

Figure 4.14b: TPO measurements of ZSM-5 (80) materials.

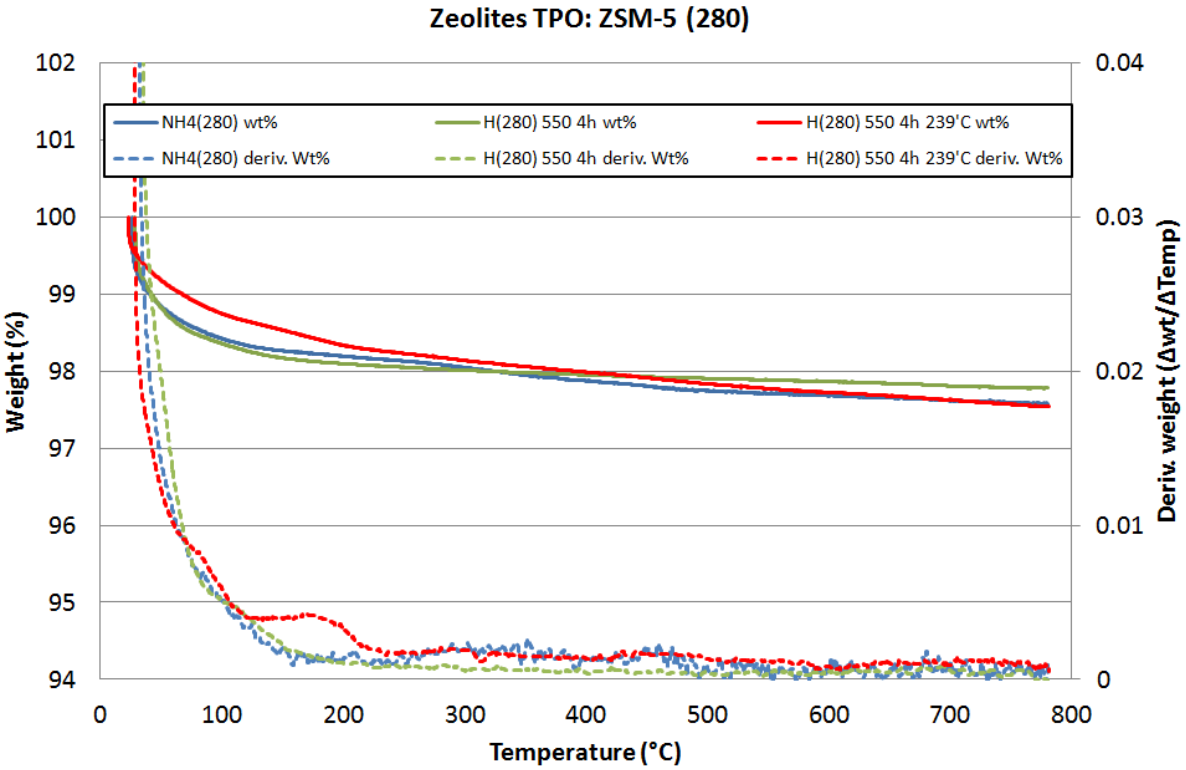

Figure 4.14c: TPO measurements of ZSM-5 (280) materials.

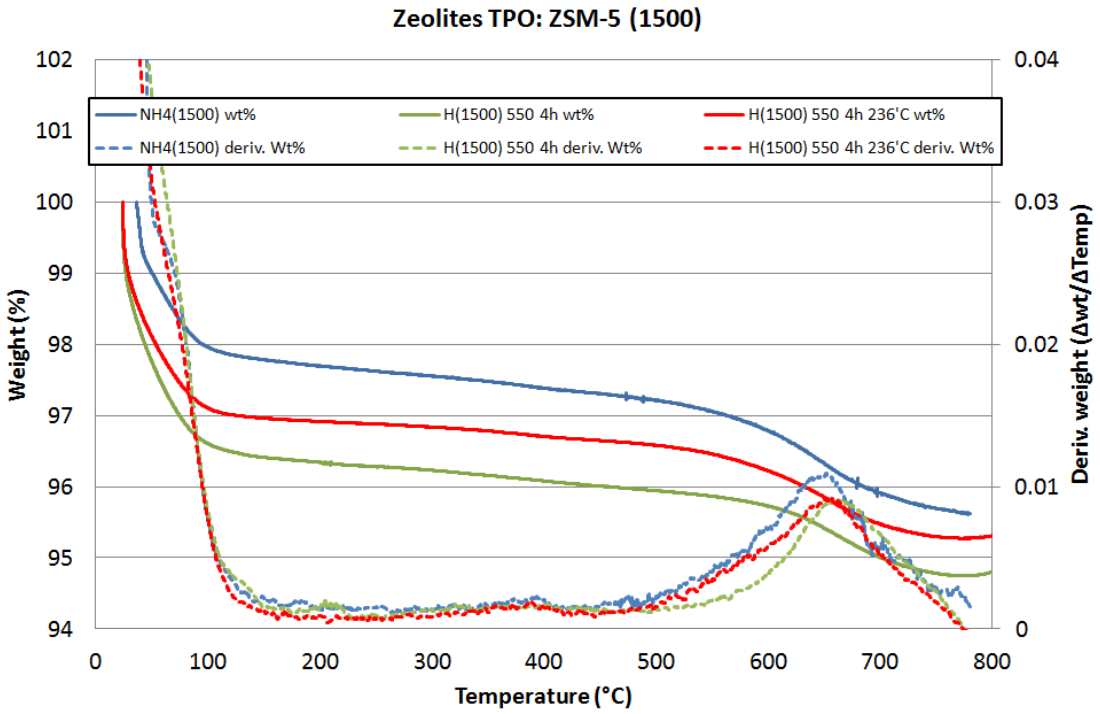

Figure 4.14d: TPO measurements of ZSM-5 (1500) materials.

Figures 4.14a-d: All measurements are described in the experimental chapter.

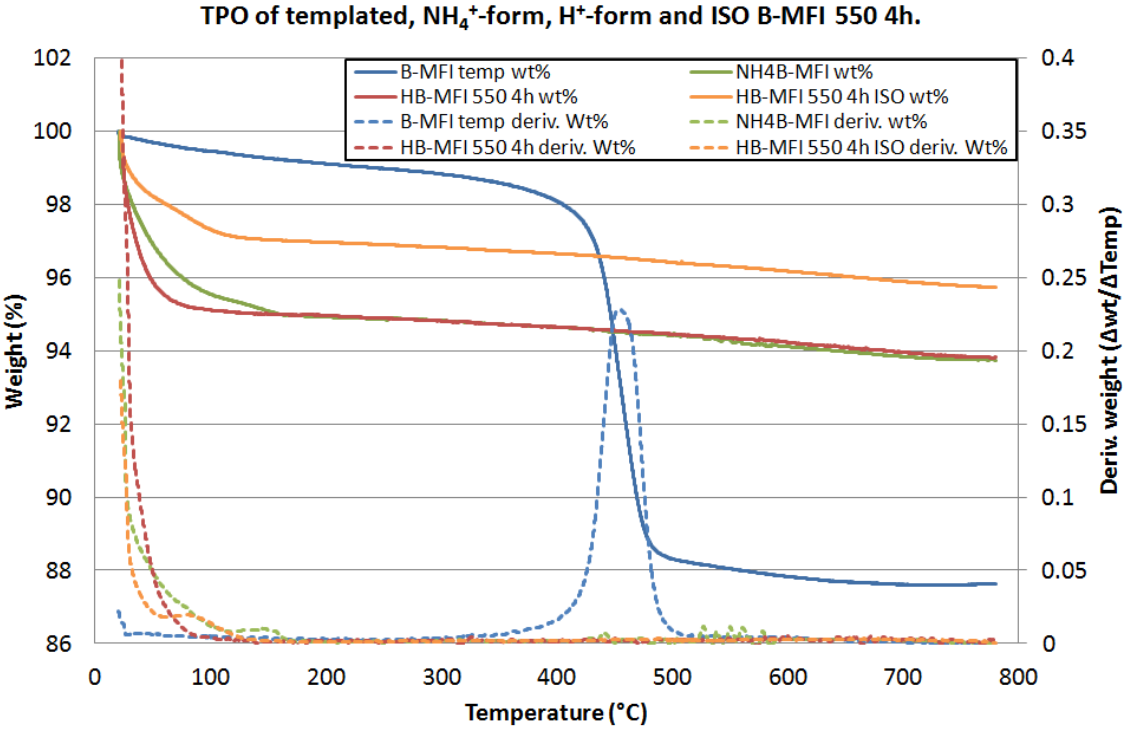

Figure 4.15a: TPO measurements of B-MFI materials**.** The post-reaction sample was obtained from catalytic testing at 258 °C.

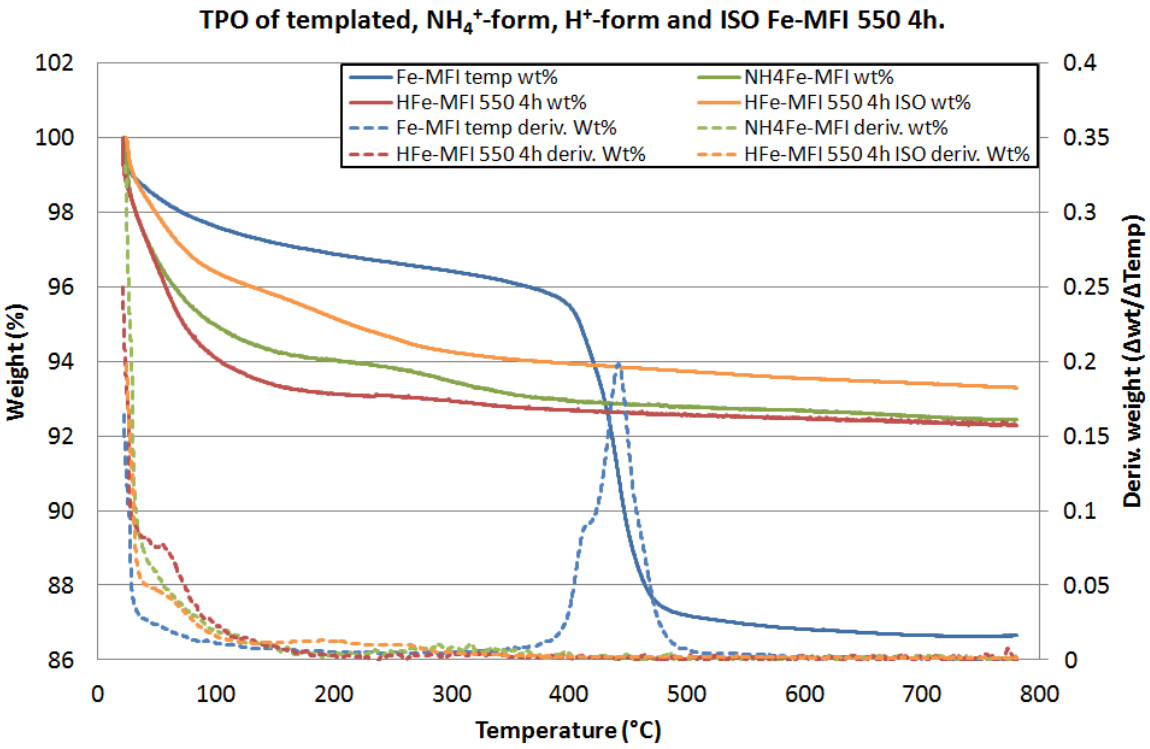

Figure 4.15b: TPO measurements of Fe-MFI materials**.** The post-reaction sample was obtained from catalytic testing at 224 °C.

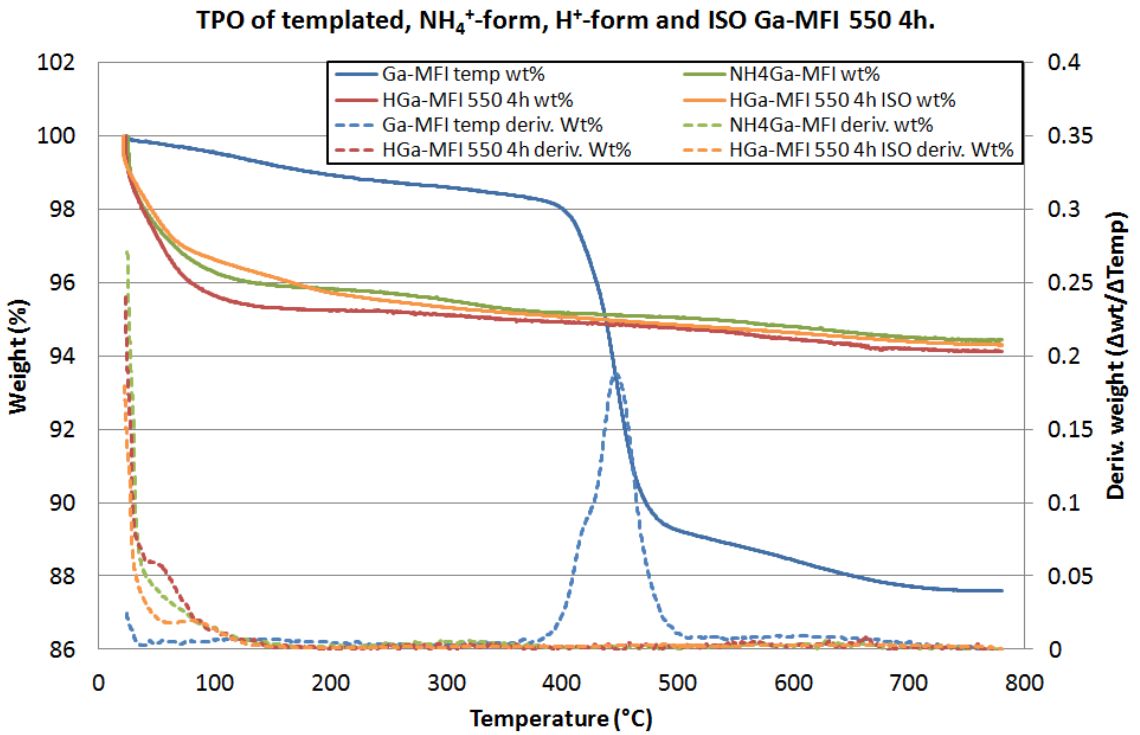

Figure 4.15c: TPO measurements of Ga-MFI materials. The post-reaction sample was obtained from catalytic testing at 205 °C.

Figures 4.15a-c: All measurements are described in the experimental chapter. Similar weight losses were observed in zeotypes with the exception of template removal between 300-600 °C

Two apparent features of the templated zeotype TPOs were the shifts in peak position and the differences in shape of the derivative weight loss peaks. Template was removed in order of increasing temperature from Fe-MFI ≈ Ga-MFI < B-MFI. Both Fe-MFI and Ga-MFI derivative weight peaks showed a shoulder at ≈ 415 °C. These observations do not correlate with zeotype porosity, crystal morphology and/or size which may have affected the mass transfer rates in and out of the internal pore system. Instead it is conceivable that the iron and gallium species of their respective zeotypes may act as oxidation catalysts for the template removal [32]. Boron is not expected to be redox active.

H_2O loss, template removal, ammonium ion decomposition and carbonaceous adsorbate removal in zeolitic and zeotype materials as observed by CHN elemental analyses are discussed overleaf.

4.3.4 **CHN analysis of zeolites and zeotypes**

Material	C (wt. %)	H (wt. %)	N (wt. %)
NH_4(23)	0.00	1.58 ± 0.02	0.79 ± 0.00
H(23) 550 4 h	0.00	0.00	0.00
H(23) 550 4 h 200 °C	1.61 ± 0.01	0.00	0.00
NH_4(80)	0.00	0.75 ± 0.04	0.36 ± 0.01
H(80) 550 4 h	0.00	0.00	0.00
H(80) 550 4 h 211 °C	1.15 ± 0.08	0.00	0.00
NH_4(280)	0.00	0.00	0.00
H(280) 550 4 h	0.00	0.00	0.00
H(280) 550 4 h 239 °C	0.00	0.00	0.00
NH_4(1500)	0.00	0.00	0.00
H(1500) 550 4 h	0.00	0.00	0.00
H(1500) 550 4 h 236 °C	1.44 ± 0.20	0.41 ± 0.04	0.00

Table 4.3: CHN elemental analyses of zeolites with different SiO_2/Al_2O_3 ratios. The materials with temperatures 200 °C, 211 °C, 239 °C and 236 °C in their name refer to samples obtained from catalytic testing at those temperatures. The error presented within the table represents the spread of the 2 data points used to obtain the average wt. % value within the table. All measurements were obtained as described in section 2.6.3.

Following 550 °C 4 h calcination in air, the ammonium counter-ions of NH_4(23) and NH_4(80) were decomposed to produce the H^+-form 550 4 h zeolites (Table 4.3). This is believed to occur in NH_4(280) and NH_4(1500) materials but it cannot be confirmed by CHN due to the low nitrogen content. The hydrogen contents in NH_4^+-form (23) and (80) are attributed to the presence of adsorbed water. Low carbon content is evident following catalytic testing.

Material	C (wt. %)	H (wt. %)	N (wt. %)
B-MFI temp.	7.76 ± 0.06	1.58 ± 0.02	0.79 ± 0.00
NH_4B-MFI	0.00	0.00	0.00
HB-MFI 550 4 h	0.00	0.00	0.00
HB-MFI 550 4 h 258 °C	0.96 ± 0.06	0.00	0.00
Fe-MFI temp.	7.25 ± 0.10	1.53 ± 0.06	0.73 ± 0.01
NH_4Fe-MFI	0.00	0.00	0.65 ± 0.01
HFe-MFI 550 4 h	0.00	0.00	0.00
HFe-MFI 550 4 h 224 °C	1.35 ± 0.02	0.00	0.00
Ga-MFI temp.	7.95 ± 0.27	1.60 ± 0.09	0.77 ± 0.07
NH_4Ga-MFI	0.00	0.00	0.36 ± 0.02
HGa-MFI 550 4 h	0.00	0.00	0.00
HGa-MFI 550 4 h 205 °C	1.15 ± 0.07	0.36 ± 0.01	0.00

Table 4.4: CHN elemental analyses of zeotypes. The materials with temperatures 258 °C, 224 °C and 205 °C in their name refer to samples obtained from catalytic testing at those temperatures. “temp” refers to template containing samples. The error presented within the table represents the spread of the 2 data points used to obtain the average wt. % value within the table. All measurements were obtained as described in section 2.6.3.

Following 550 4 h calcination in air, the TPABr template is removed (Table 4.4). Treble ammonium-exchange results in the removal of residual alkali metals and increased nitrogen content and an additional 550 °C calcination step decomposed the ammonium counter-ion to produce the H^+-form 550 4 h zeotypes. Low carbon content is apparent following catalytic testing.

4.4 Zeolite and zeotype catalytic testing

Arrenhius plots were constructed to compare the methanol dehydration rates of the zeotypes against the zeolites which have both been characterised above.

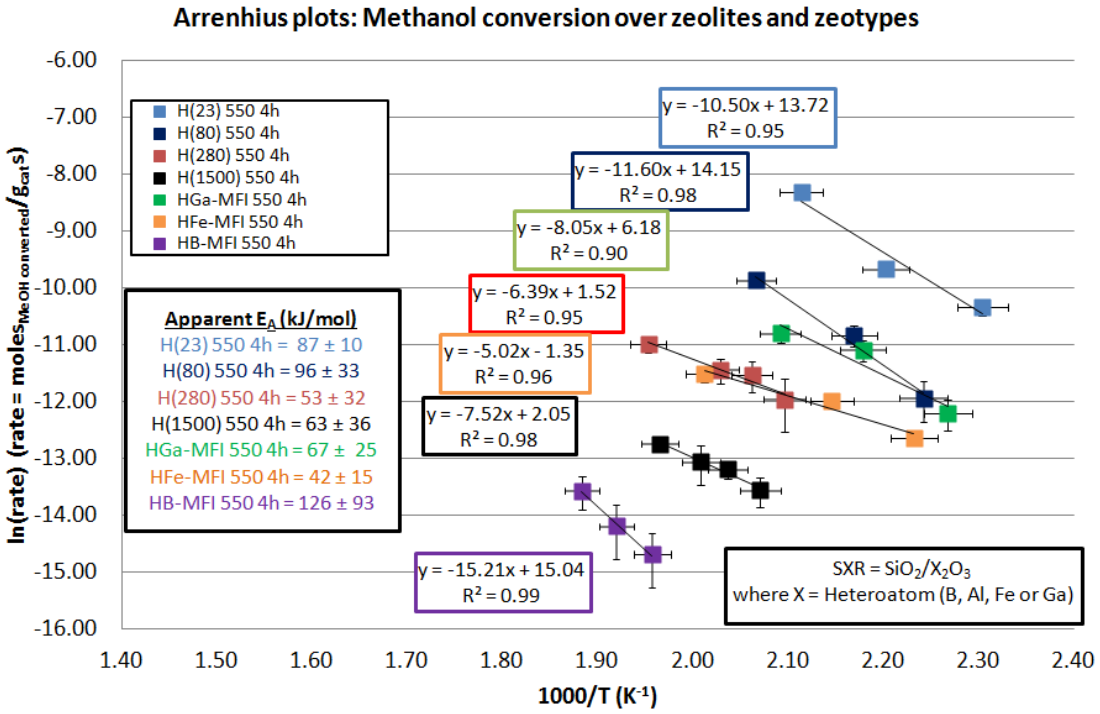

Figure 4.16: Arrenhius plots of a range of zeolites and zeotypes. Vertical error bars represent the 1st standard deviation in the values obtained for each point.

For the zeolite materials in Fig. 4.16 the rate of MeOH conversion, at fixed temperatures between 160 °C and 239 °C, increases with increasing nominal framework aluminium content. This was expected as zeolite acidity is associated with the aluminium component [33] and the reaction is an acid catalysed process. For all zeolite plots, the gradients are rather similar and not outwith the error of one another. The y-intercepts and therefore the number of active sites, generally decrease with decreasing aluminium content. These observations do not appear to be complicated by dealumination (Fig. 4.4) where dealumination may be expected to alter both the apparent activation energy and the number of active sites. However, extra-framework aluminium may also lower the number of accessible active sites through channel plugging. The effects of extra-framework aluminium in the zeolite systems on the methanol dehydration behaviour are not clear.

All zeotype plots in Fig. 4.16 show zeotypes to possess comparable MeOH conversion rates to those obtained over zeolites. As described in the general introduction, Brőnsted acid site strength is expected to follow the trend Al > Ga > Fe > B > Si. Additionally, comparison of the methanol dehydration rates over H(80) 550 4 h and zeotypes at fixed temperatures between 168 °C and 258 °C gives a heteroatom ranking of Al > Ga > Fe >> B for MeOH dehydration to DME in agreement with the literature.

The apparent activation energy values of zeolites and zeotypes are rather similar and generally within error of one another. As such, no definitive conclusion can be drawn from the effect of heteroatom type on the apparent activation energy of the reaction. Additionally, the surprisingly high y-intercept values obtained for H(1500) 550 4 h and HB-MFI 550 4 h may be explained by the contribution of weakly acidic silanol species to methanol conversion.

4.5 Conclusions

Comparison of the structural, textural and catalytic properties of both zeolites and zeotypes furnished some interesting results.

In situ hotstage PXRD studies indicate the orthorhombic MFI phase is the most likely to exist under catalytic testing conditions for all of the MFI materials examined. Using ^{27}Al MAS-NMR it was demonstrated that all H^+-form 550 4 h zeolites possessed varying contents of extra-framework aluminium with no obvious trend in the variation. By both MAS-NMR and ICP studies, zeolites' aluminium contents followed H(23) > H(50) > H(80) > H(280) > H(1500) and their nominal content values were approximately accurate. The hydrophilicity of zeolites appears to be a function of both aluminium and silanol group content. Water content in H^+-form 550 4 h zeolites generally decreased with decreasing aluminium content. However, H(1500) 550 4 h was found to be significantly more hydrophilic than initially expected, adsorbing more water than H(280) 550 4 h and this appeared to be a result of relatively high silanol group content in H(1500) 550 4 h.

B-MFI, Fe-MFI and Ga-MFI were successfully synthesised by hydrothermal methods as shown by PXRD analyses. Using ^{11}B MAS-NMR and ^{71}Ga MAS-NMR,

both boron and gallium were shown to retain tetrahedral coordination following template removal, ammonium-exchange and calcination to yield the H^+-form. The high degree of framework boron retention was unexpected because of its reported relative instability. Furthermore, ^{29}Si MAS-NMR spectra indicated $SiO_2/B_2O_3 \approx 100$, significantly higher than the nominal value of $SiO_2/B_2O_3 = 8$. TPR studies showed the iron zeotype to contain redox active extra-framework species. Zeotype aluminium impurities were determined by EDX and ^{27}Al MAS-NMR and shown to be negligible for B-MFI and Ga-MFI. However, an impurity may yet be present in the iron zeotype material. The TPABr template was retained within the zeotypes following hydrothermal synthesises and successfully removed by calcination in air at 550 °C for 4 h. The oxidative template removal increased the BET specific surface area by liberation of the internal pore channels but also decreased crystallinity. Template removal from Fe-MFI and Ga-MFI materials was also enhanced by the presence of the heteroatom.

SEM imaging showed Na(1500) 550 4 h, B-MFI (temp) and Ga-MFI (temp) to possess characteristically intergrown morphologies. All other materials had crystal sizes to too small to characterise.

Zeolite catalysts all possessed active sites of similar nature but the number of active sites decreased with decreasing aluminium content, as would be expected for an acid catalysed reaction. Comparison of zeolite and zeotype methanol conversion activities at fixed temperatures between 168 °C and 258 °C gave a heteroatom ranking of Al > Ga > Fe >> B for materials of similar heteroatom content.

4.6 References

[1] B. M. Lok, C. A. Messina, R. L. Patton, R. T. Gajek, T. R. Cannan and E. M. Flanigen, J. Am. Chem. Soc., 106 (1984) 6092-6093.

[2] X. Bu, P. Feng, T. E. Gier, D. Zhao and G. D. Stucky, J. Am. Chem. Soc., 120 (1998) 13389-13397.

[3] H. Berndt, A. Martin, H. Kosslck and B. Lucke, Micro. Mater., 2 (1994) 197-204.

[4] M. G. Howden, Zeolites, 5 (1985) 334-338.

[5] C.D. Chang, S. D. Hellring, J. N. Miale, K. D. Schmitt, P.W. Brigandi and E. L. Wu, J. Chem. Soc., Faraday Trans. 1, 81 (1985) 2215-2224.

[6] E. Unneberg and S. Kolboe, Appl. Catal. A:Gen., 124 (1995) 345-354.

[7] J. Cejka, A. Vondrova, B.Wichterlova, G. Vorbeck and R. Fricke, Zeolites, 14 (1994) 147-153.

[8] K. F. M. G. J. Scholle, A. P. M. Kentgens, W. S. Veeman, P. Frenken and G. P.M. van der Velden, J. Phys. Chem., 88 (1984) 5-8.

[9] C. T-W. Chu and C. D. Chang, J. Phys. Chem., 89 (1985) 1569-1571.

[10] R. Zahradnik, P. Hobza, B. Wichterlova and J. Cejka, Collect. Czech. Chem. Commun., 58 (1993) 2474-2488.

[11] S. K. Durrani, S. Amini, A. Dyer and R. Blackburn, Jour. Chem. Soc. Pak., Vol. 16, No. 3 (1994) 174-183.

[12] E. L. Wu, S. L. Lawton, D. H. Olson, A. C. Rohrman Jr. And G. T. Kokotailo, J. Phys. Chem., 83, 21 (1979) 2777-2781.

[13] A. Endoh, Zeolites, 8 (1988) 250-251.

[14] B. F. Mentzen, J.-M. Letoffe and P. Claudy, Thermo. Acta, 288 (1996) 1-7.

[15] H. van Koningsveld, J. C. Jansen and H. van Bekkum, Zeolites, 7 (1987) 564-568.

[16] H. van Koningsveld, J. C. Jansen and H. van Bekkum, Zeolites, 10 (1990) 235-242.

[17] K. S. Triantafyllidis, L. Nalbandian, P. N. Trikalitis, A.K. Ladavos, T. Mavromoustakos and C. P. Nicolaides, Microp. Mesop. Mater., 75 (2004) 89-100.

[18] L. Shirazi, E. Jamshidi and M. R. Ghasemi, Cryst. Res. Technol., 43 (2008) 1300- 1306).

[19] J.S.J. Hargreaves, Cryst. Rev., 11, 1, 2005, 21-34.

[20] J. Klinowski, Progress in NMR spectroscopy, 16 (1984) 237-309.

[21] J. Klinowski, Ramdas, J.M. Thomas, C. A. Fyfe and J. S. Hartman, Chem. Soc. Faraday Trans. II, 78 (1982) 1025.

[22] F. Testa, R. Chiappetta, F. Crea, R. Aiello, A. Fonseca, J.-C. Bertrand, G. Demortier, J.-L. Guth, L. Delmotte and J. B. Nagy, J. Porous Mater., 14, (2007), 191-204.

[23] K. T. Leth, A.K. Rovik, M.S. Holm, M. Brorson, H.J.Jakobsen, J. Skibsted and C. H. Christensen, Appl. Catal. A:Gen., 348 (2008) 257-265.

[24] V.R. Choudhary, P. Devadas, A.K. Kinage and M.Guisnet, Appl.Catal. A:Gen., 162 (1997) 223-233.

[25] W. K. Jozwiak, E. Kaczmarek, T. P. Maniecki, W. Ignaczak and W. Maniukiewicz, Appl. Catal. A:Gen., 326 (2007) 17-27.

[26] R. Carki, C. L. Bianchi, R. Giannantonio and V. Ragaini, J. Mol. Catal., 83 (1993) 379-389.

[27] T. Sano, H. Ikeya, T. Kasuno, Z. B. Wang, Y. Kawakami and K. Soga, Zeolites, 19 (1997) 80-86.

[28] J. C. Groen, T. Bach, U. Ziese, A. M. Paulaime-van Donk, K. P. de Jong, J. A. Moulijn and J. Perez-Ramirez, J. Am. Chem. Soc., 127 (2005) 10792-10793.

[29] M. H. F. Kox, E. Stavitski, J. C. Groen, J. Perez-Ramirez, F. Kapteijn and B. M. Weckhuysen, Chem. Eur. J., 14 (2008) 1718-1725.

[30] S. Brunauer, L. S. Deming, W. S. Deming, E. Teller, J. Amer. Chem. Soc., 62 (1940) 1723.

[31] K. S. W. Sing, D. H. Everett, R. A. W. Haul, L. Moscou, R. A. Pierotti, J. Rouquerol and T. Siemieniewska, Pure & Appl. Chem., 57 (1985) 603-619.

[32] S. H. Taylor, J. S. J. Hargreaves, G. J. Hutchings and R. W. Joyner, Appl. Catal. A: Gen., 126 (1995) 287-296.

[33] J. Weitkamp, Solid State Ionics, 131 (2000) 175-188.

5 Silica-bound ZSM-5

Having established both the temperature range of selective DME production in Chapter 3 and the greater methanol dehydration activity of zeolites than zeotypes in Chapter 4, bound-zeolites are discussed in Chapters 5 and 6 where binders are necessary for scale-up of zeolite catalysts [1,2]. This chapter focuses on the effects of silica binding upon ZSM-5.

Silica binding has been associated with altering porosity and acidity characteristics. In the work of Wu [3], binding with silica reduced the micropore surface area to less than that predicted from the sum of constituent parts. This was attributed to zeolite micropore blockage by the binder. Additionally, the silica sources employed contained alkali metals which were exchangeable with the protons of the Brőnsted acid sites of the zeolite component. The combination of these effects was reported to lower catalytic activity for both butane transformation and ethylene oligomerisation. By comparison of dry-mixed and wet-mixed silica-zeolite catalysts, alkaline metal cations were demonstrated to migrate more readily during wet preparations than during dry preparations as measured by total acid site measurements using NH_3-TPD. Additionally, the effect of solid-state ion-exchange during calcination was minimal compared to the wet-mixing preparations.

In addition to micropore blockage and alkali metal poisoning, silica may also display additional effects. The trapping of extra-framework aluminium by silica has been reported [4,5]. This may result in preservation of the catalyst acidity and can be beneficial or deleterious depending upon the reaction undertaken. Preservation of crystallinity by the insertion of mobile silica species under hydrothermal conditions has been shown for FCC [6,7] and amorphous silica-alumina-bound mordenite catalysts [8]. Retardation of extra-framework aluminium formation by the binder's associated alkali metal contents may also occur [9]. Although alkali metal content may improve the stability of a zeolite catalyst by retarding dealumination; in the presence of steam the alkali metal will degrade the silica framework of the zeolite.

In this chapter on silica-bound ZSM-5, the effects of binder dilution, sodium content and thermal/hydrothermal treatment will be discussed with respect to structural, textural analyses and methanol dehydration catalytic performance.

Two different silica binders were studied – Ludox AS 40 and Ludox HS 40 silica sols. Following binding, the resulting binder materials were named as follows in Table 5.1.

Material	Description
AS(23)	Ludox AS 40-bound H-ZSM-5 (23)
HS(23)	Ludox HS 40-bound H-ZSM-5 (23)

Table 5.1: Silica-bound catalyst nomenclature. All samples were prepared such that 50:50 dry wt. % of zeolite and binder are present in the activated catalysts.

5.1 Silica binder materials

5.1.1 Structural analyses

Both Ludox AS 40 (designated AS) and Ludox HS 40 (designated HS) silica sols were alkaline with pH values of 9 and 10 respectively. Following overnight drying at 110 °C and calcination, both silica binders were found to be X-ray amorphous solids Fig. 5.1.

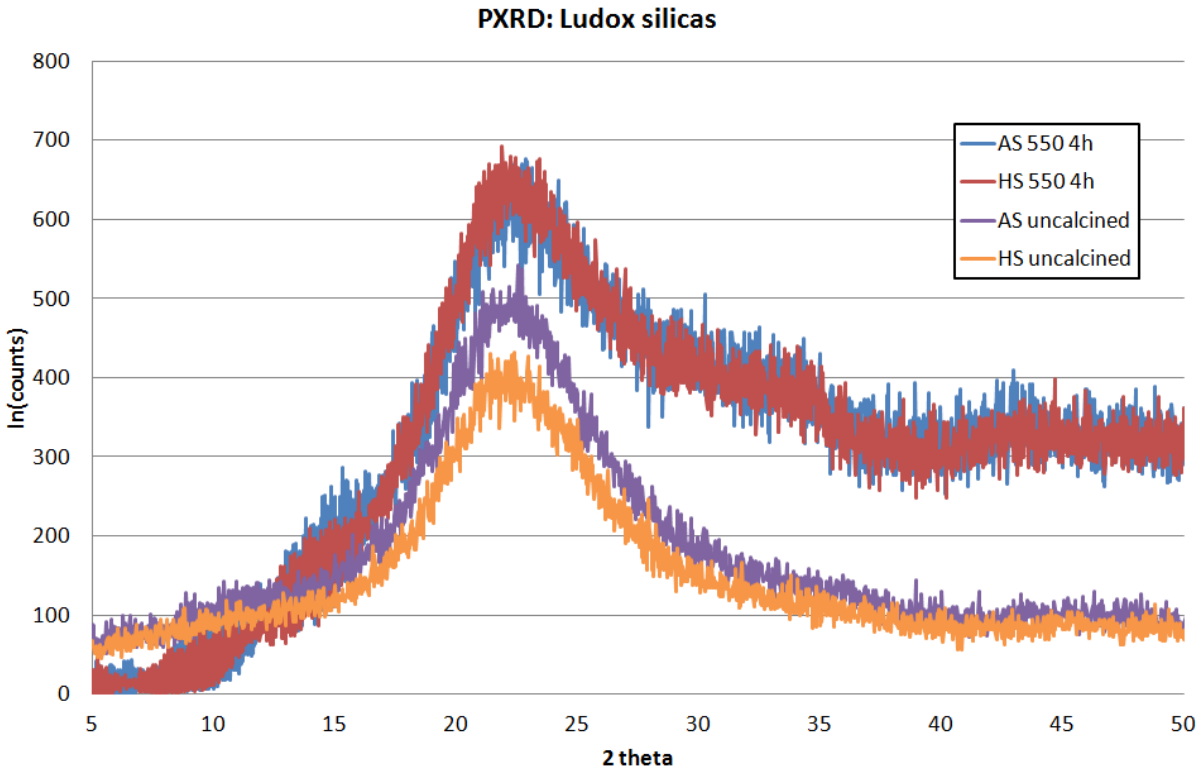

Figure 5.1: PXRD patterns of Ludox silicas**.** Measurements were obtained as described in experimental section 2.6.6.

The short-range order in the structure of the silica materials was determined using ^{29}Si MAS-NMR Fig. 5.2.

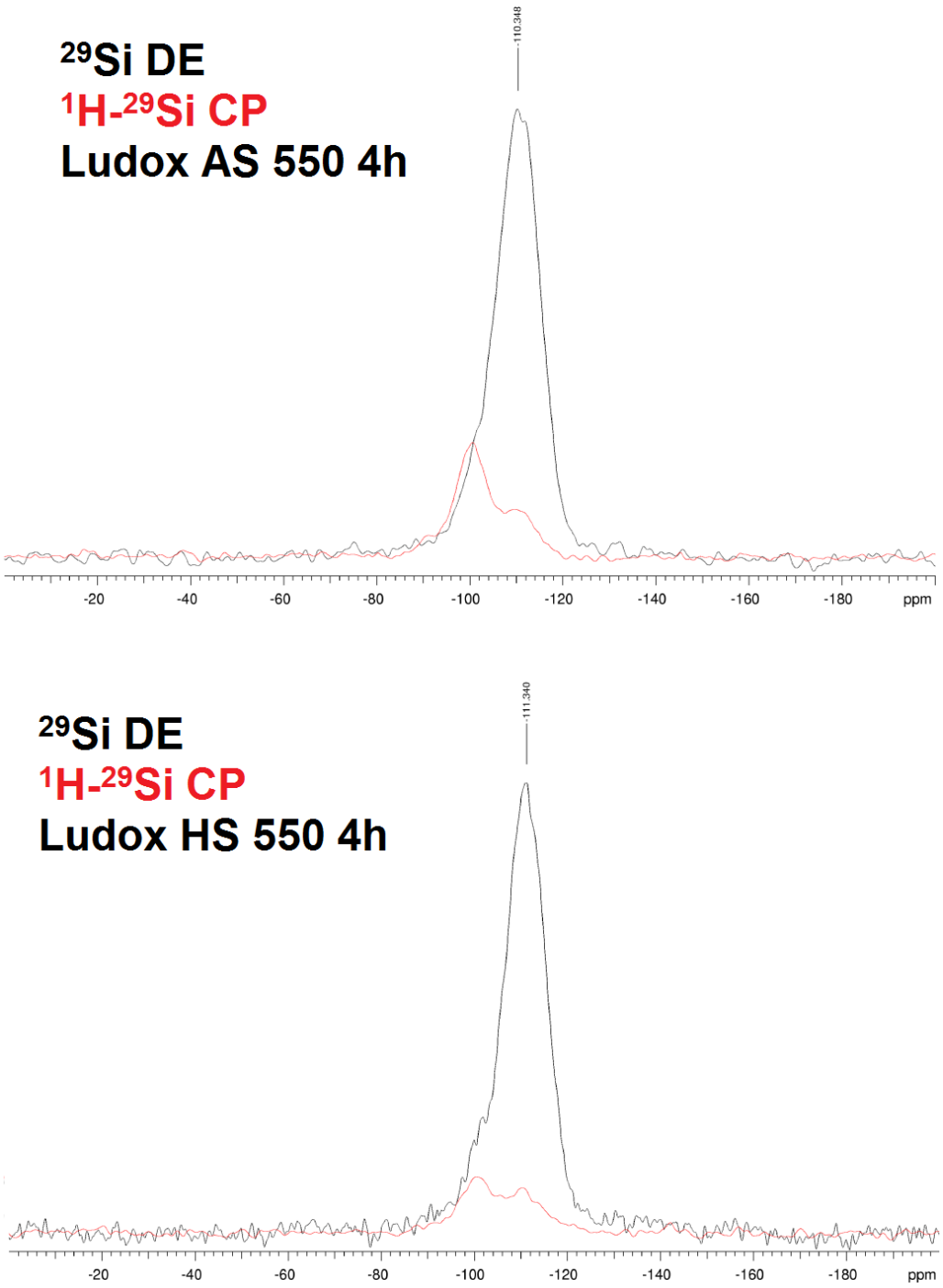

Figure 5.2: ^{29}Si MAS-NMR spectra of Ludox silicas. All spectra were obtained on a Varian VNMRS 400. ^{1}H-^{29}Si CP spectra were overlaid and shown in red.

The broad ^{29}Si DE and ^{1}H-^{29}Si CP spectra show silicon to exist in heterogeneous Si(0Al) (*ca*. – 111 ppm) and silanol environments (*ca*. – 103 ppm).

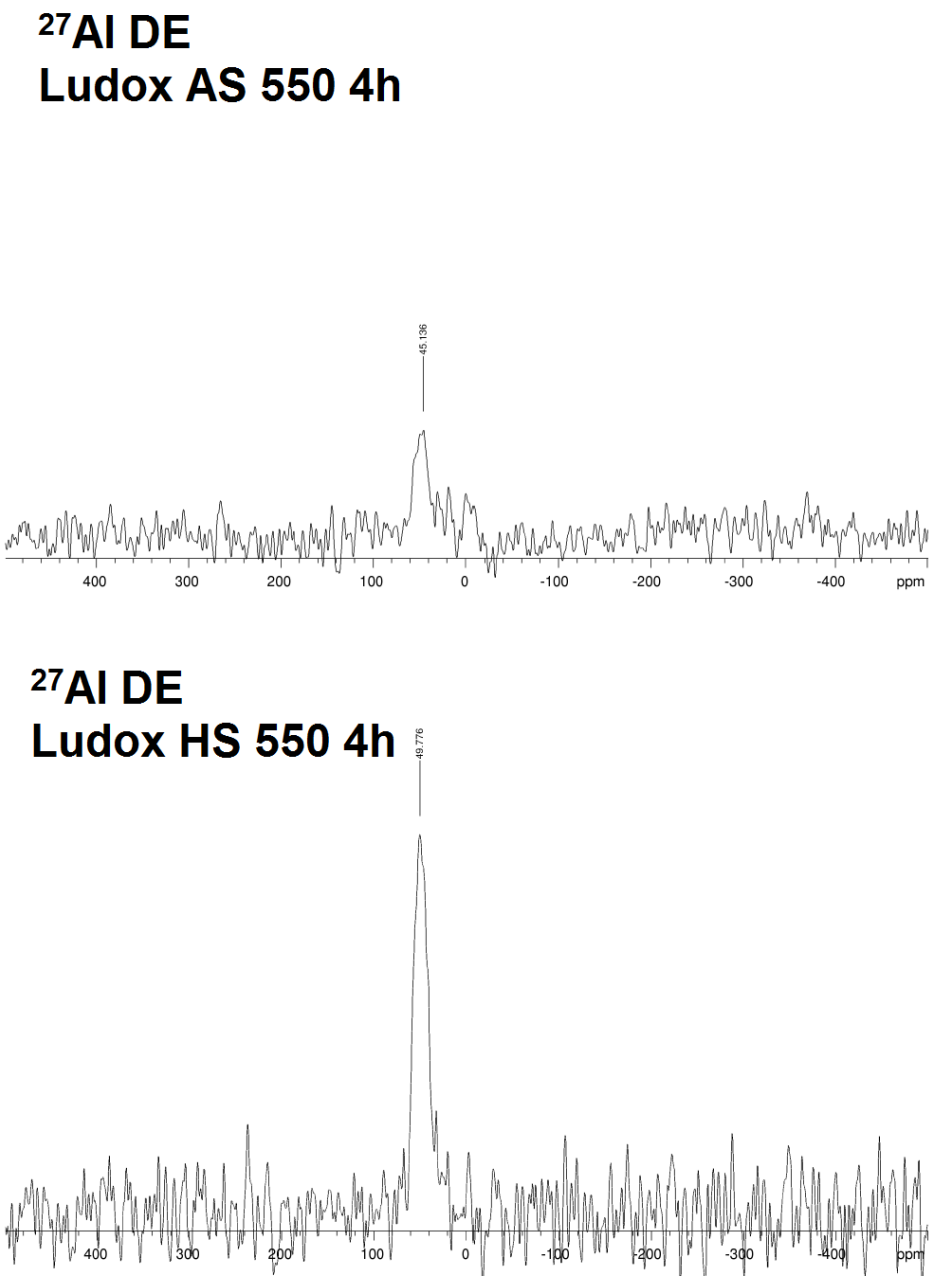

Figure 5.3: ^{27}Al MAS-NMR spectra of Ludox silicas. All spectra were obtained on a Varian VNMRS 400.

The ^{27}Al spectra above indicate the presence of a small, predominantly tetrahedral, aluminium impurity in both silica materials. As indicated in Chapter 4, the level of aluminium impurity was lower than that present in silicalite. Thermal analyses show that the silanol species of the calcined silicas account for < 1 wt. % of the silica samples (Fig. 5.4).

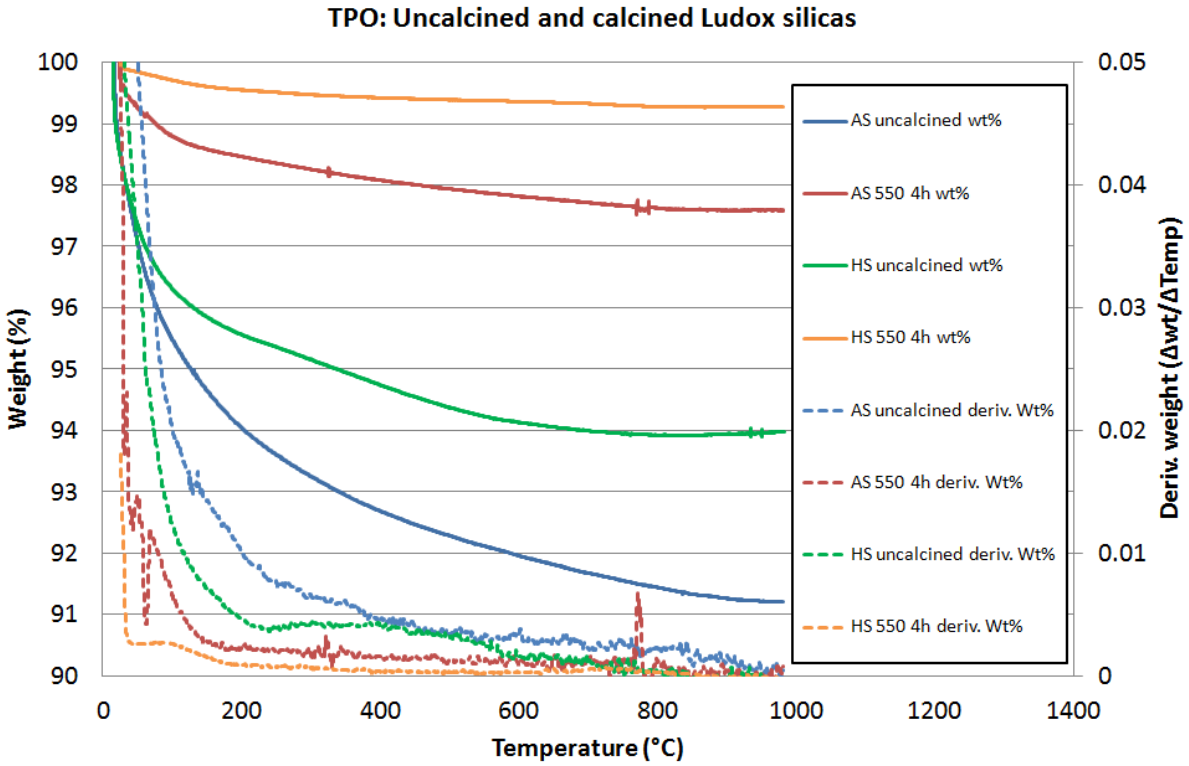

Figure 5.4: TPO measurements of uncalcined and calcined Ludox silicas. Measurements were obtained as described in experimental section 2.6.8.

For all silica materials, all weight loss during the TGA measurement was assigned to water desorption. CHN analyses showed no carbon or nitrogen content.

5.1.2 Textural analyses

Porosity in materials such as bound-zeolites may be divided into intra- or interparticle porosity. Sources of intraparticle porosity include open crystallographic structures such as those commonly found in zeolites and zeotypes as well as defects purposefully introduced through dealumination, desilication and templating processes [10]. The open crystallographic structure of zeolitic and zeotypic materials are not generally affected by mechanical stresses during catalyst preparation e.g. compaction. However, interparticle porosity is dependent upon the packing arrangement of the catalyst components. The packing arrangement is dependent upon factors including particle size and shape but may also be a function of applied mechanical pressure e.g. through pelleting [11].

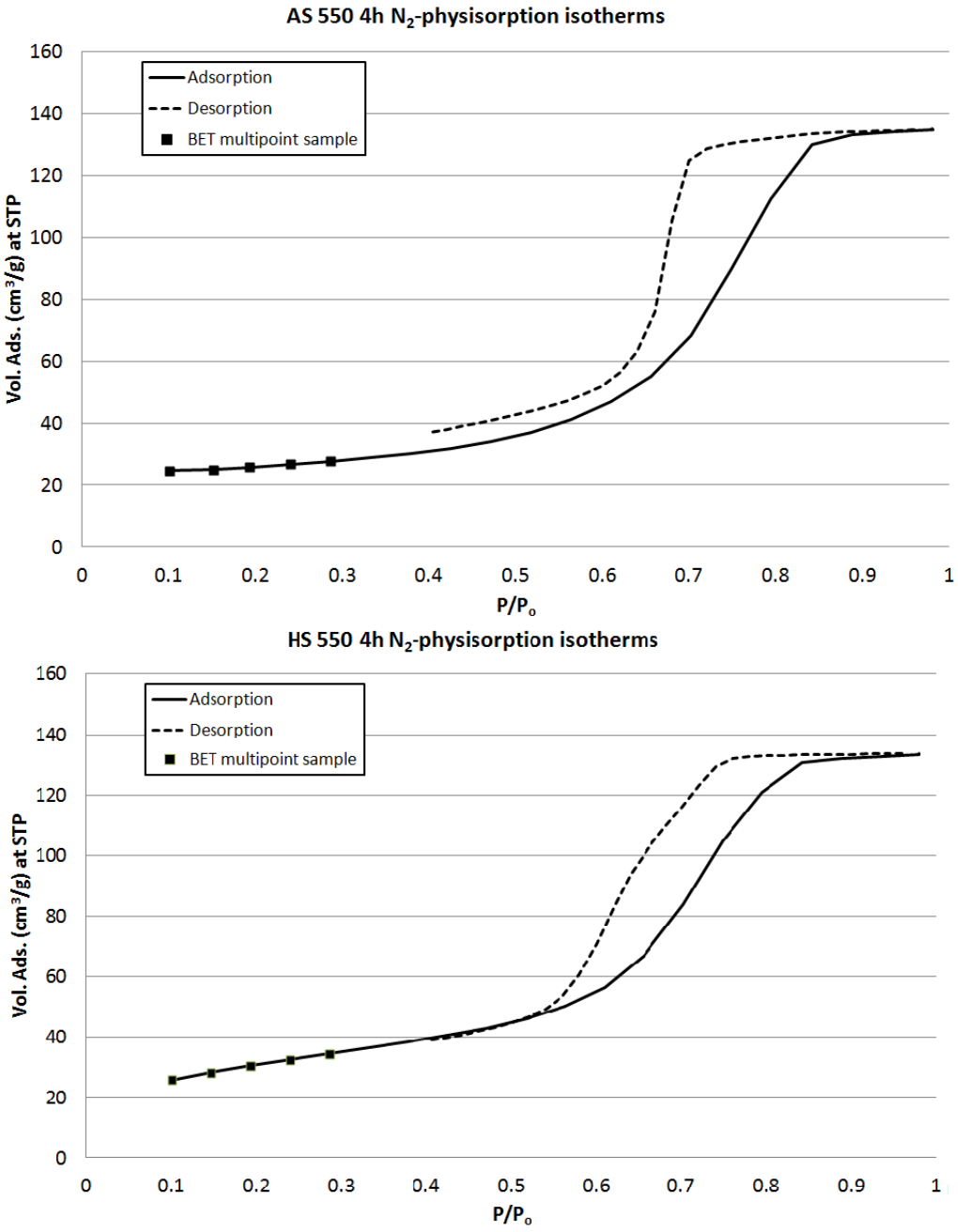

Figure 5.5: N_2-physisorption isotherms of pressed Ludox silicas. All measurements were obtained as described in experimental section 2.6.5.

The N_2-physisorption isotherms of Ludox AS 550 4 h and Ludox HS 550 4 h are shown in Fig. 5.5. Both are type IV adsorption isotherms, indicative of mesoporosity.

Furthermore, hysteresis loops are type H2-like and as such pore size distributions may be subject to network effects [12]. Both silicas possess similar mesopore diameters with Ludox AS 550 4 h possessing a slightly wider distribution (Fig. 5.6).

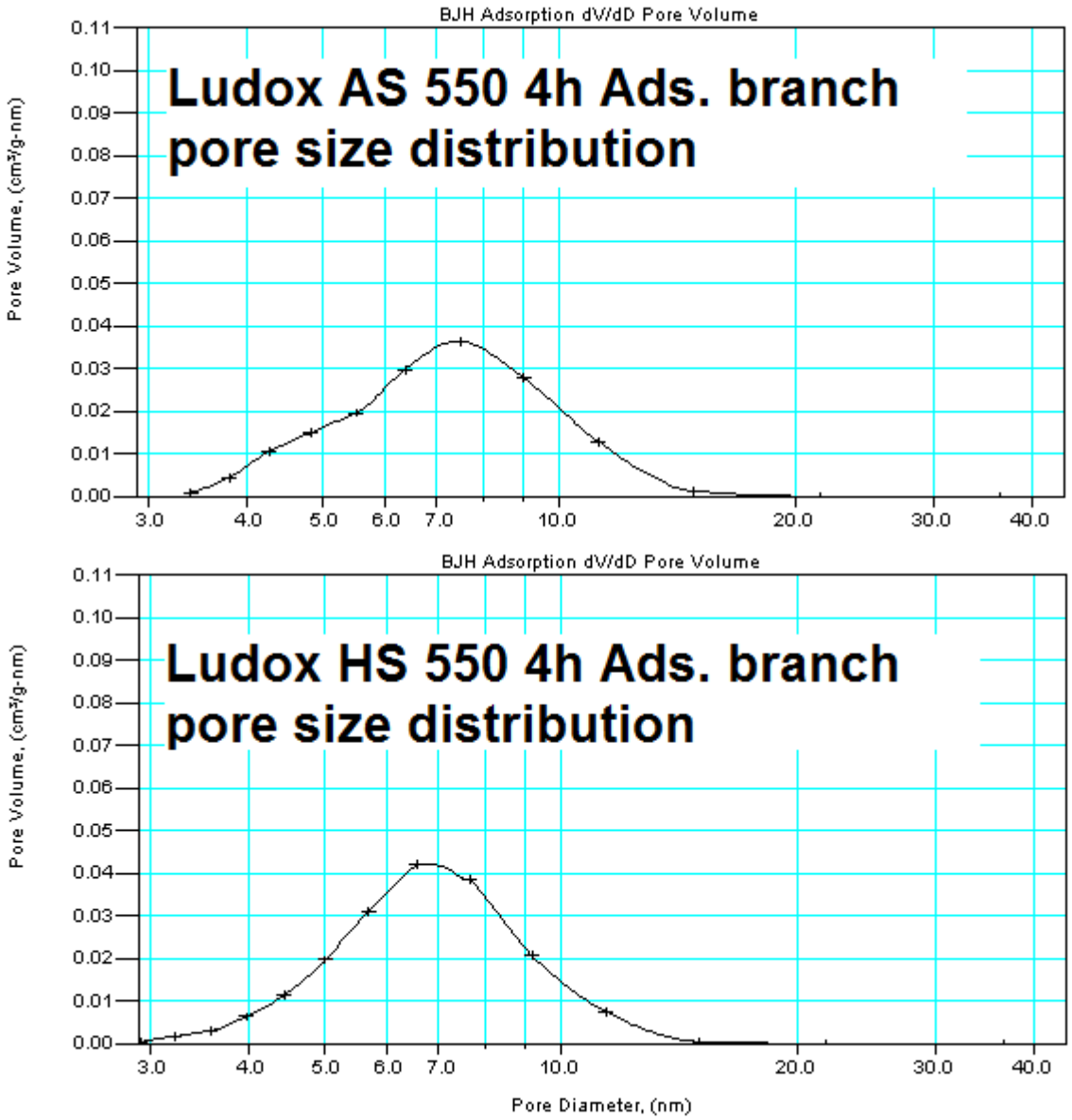

Figure 5.6: BJH pore size distributions of Ludox silicas. Measurements were obtained as described in experimental section 2.6.5.

BET specific surface areas of 83 m^2/g and 110 m^2/g were obtained for Ludox AS 550 4 h and Ludox HS 550 4 h and both had total pore volumes of 0.21 cm^3/g.

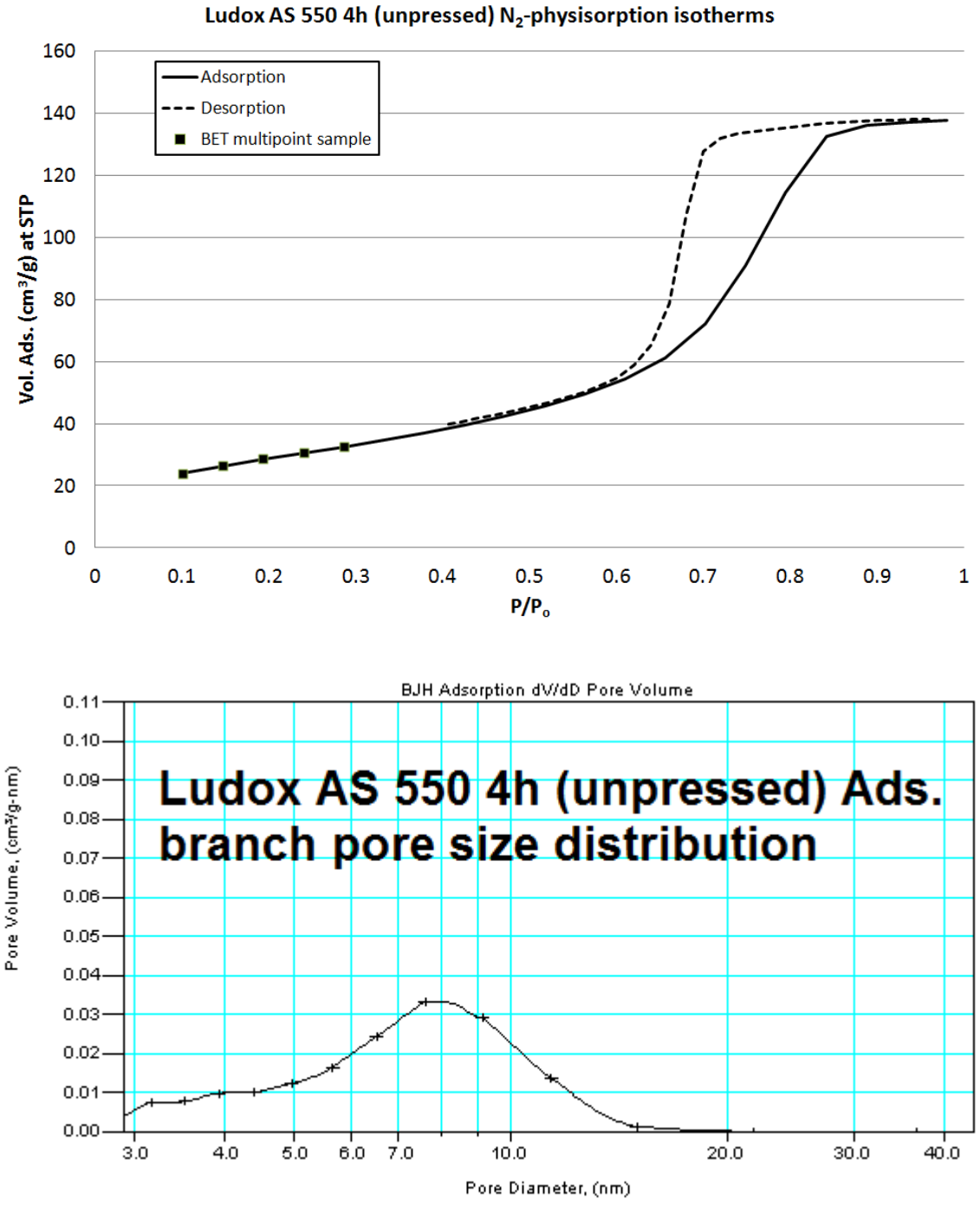

Figure 5.7: N_2-physisorption isotherm and BJH pore size distribution of Ludox AS (unpressed). All measurements were obtained as described in experimental section 2.6.5.

Without the pressing step, the type-IV adsorption isotherm (Fig. 5.7) provided a BET surface area of 105 m^2/g and a total pore volume of 0.21 cm^3/g.

Pressing does affect BET surface area and the pore size distribution of Ludox AS 550 4 h whereby pressing increases the uniformity of the mesopore size distribution. However, the generation of the observed mesoporosity has been mainly attributed to the loss of water during the calcination procedure [13].

5.1.3 Sodium content

Flame photometry showed dried Ludox AS 40 contained 0.05 ± 0.00 wt. % sodium and Ludox HS 40 silicas contained 0.24 ± 0.01 wt. % sodium (see section 2.6.2).

5.1.4 Catalytic analyses

Both Ludox AS 40 550 4 h and Ludox HS 40 550 4 h materials were inactive for methanol dehydration.

5.2 Binder dilution

The simplest effect of zeolite binding is the dilution of the zeolite phase by the binder component. The structural, textural and catalytic effects of Ludox AS 40 binder dilution on NH_4(23) are discussed below.

5.2.1 Sample preparation

NH_4(23) was bound with Ludox AS 40 or Ludox HS 40 in mixing ratios as described in section 2.2.1 H(23) 550 4 h contents of 100 wt. %, 75 wt. %, 50 wt. %, 25 wt. %, 12.5 wt. % and 0 wt. % in silica were prepared as shown below.

5.2.2 Structural analyses

The intensities of the reflections relating to the zeolite component increase with increasing zeolite content together with a corresponding decrease in the amorphous silica pattern, as would be expected.

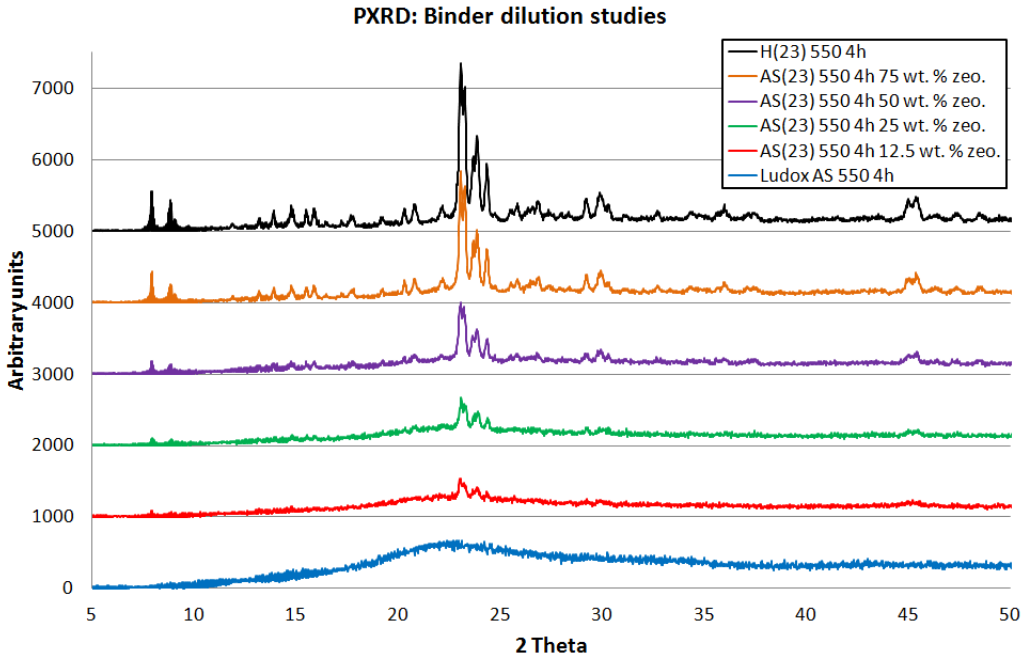

Figure 5.8: PXRD patterns of H(23)/Ludox AS binder dilutions. Patterns were obtained as described in experimental section 2.6.6.

PXRD measurements in Fig. 5.8 do not show the presence of any additional phases and the zeolite component possesses orthorhombic symmetry.

^{27}Al MAS-NMR spectra of the Ludox AS-bound zeolites (Fig. 5.9) show the catalysts to contain greater tetrahedral/octahedral aluminium ratios with increasing binder content. Two explanations from the literature for this observation include: (i) trapping of extra-framework aluminium by the silica binder [4,5] and/or (ii) retardation of extra-framework aluminium formation in the presence of alkali metals [9]. This will be further discussed in section 5.4. If solely dilution occurred, the total aluminium content within a bound zeolite would decrease with increasing silica binder content the ratio of tetrahedral/octahedral aluminium should remain constant. The change in tetrahedral/octahedral ratio with increasing silica is not a consequence of dilution as (a) the silica binder was shown to possess negligible aluminium content and therefore the observed aluminium content would primarily originate from the zeolite component and (b) if the zeolite component is diluted, the same tetrahedral/octahedral signal intensities should persist unless additional binder effects such as extra-framework aluminium trapping or transfer of alkali metal content to the zeolite component occurs.

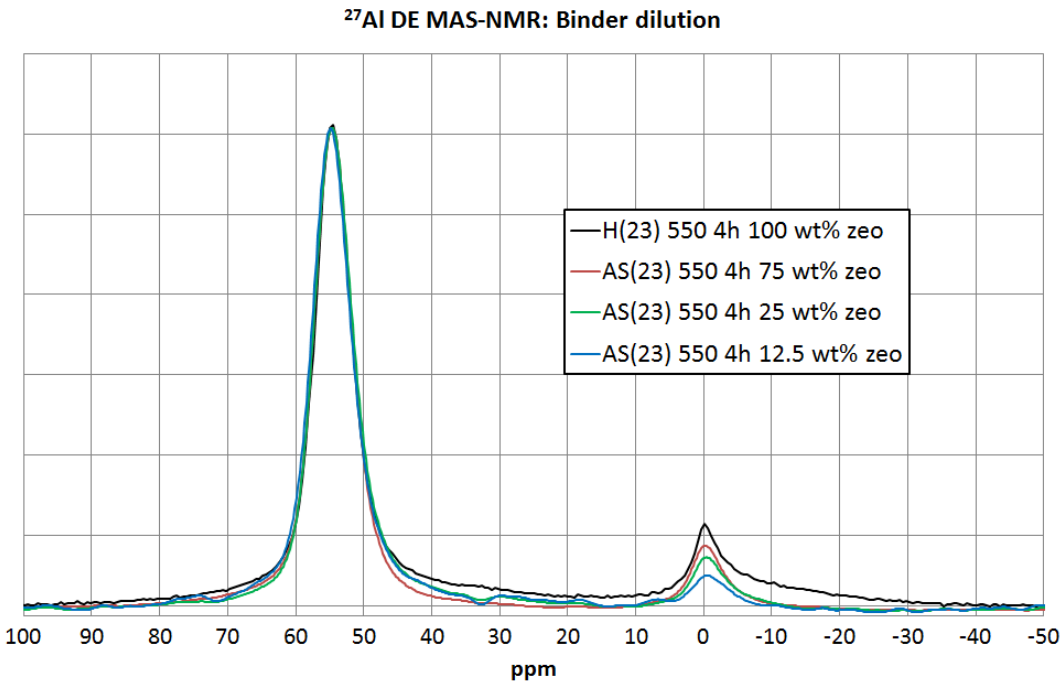

Figure 5.9: ^{27}Al MAS-NMR spectra for binder dilution studies**.** Measurements were obtained on a Varian VNMRS 400. Ludox AS(23) 550 4 h 50 wt. % zeolite has been omitted for clarity.

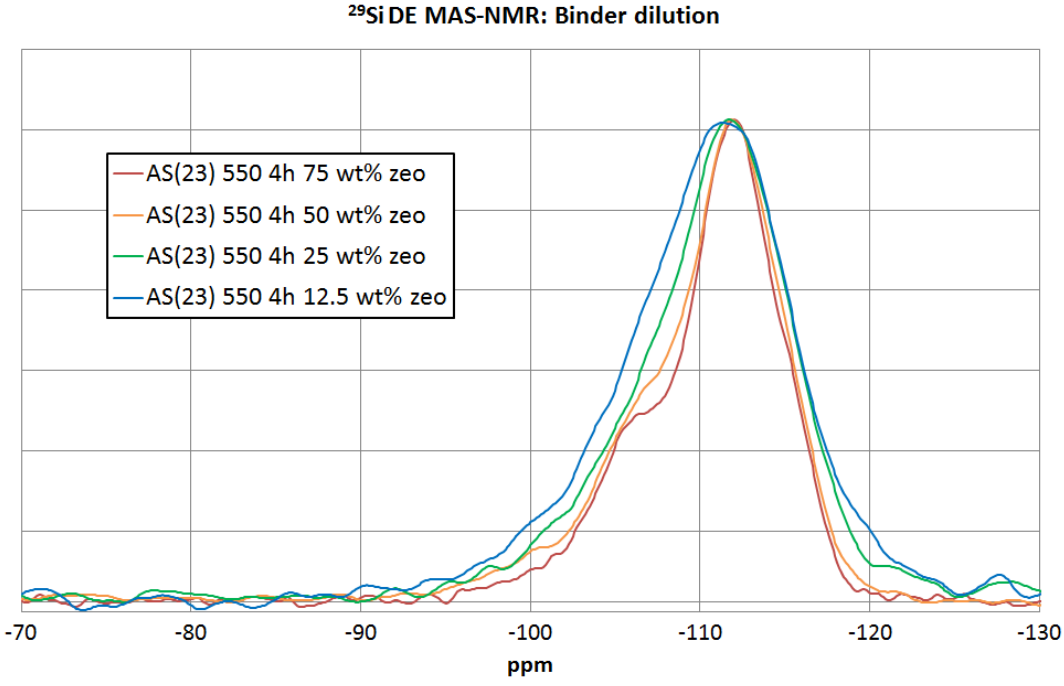

Figure 5.10: ^{29}Si MAS-NMR spectra binder dilution studies. All spectra were obtained on a Varian VNMRS 400. H(23) 550 4 h 100 wt. % zeolite has been omitted for clarity.

With reference to the Ludox AS 550 4 h ^{29}Si spectra in Fig. 5.2, all Ludox AS(23) 550 4 h samples included in Fig. 5.10 appear as composites of their constituent components. No evidence of extra-framework aluminium trapping by the silica matrix was observed. If trapping was to occur, it would be evidenced by increased Si(1Al) peak intensity and/or new peaks corresponding to Si(2-4)Al between – 80 ppm to – 100 ppm.

5.2.3 **Textural analyses**

In addition to providing additional mesoporosity, literature suggests zeolite channel blockage by binder materials may occur [14,15].

Catalyst	Measured BET SA (m^2/g)	Measured t-plot µpore SA (m^2/g)	Total pore vol. (cm^3/g)	Theory BET SA (m^2/g)	Theory t-plot µpore SA (m^2/g)
100 wt. % H(23)	318 ± 48	316 ± 48	0.20 ± 0.01	318 ± 48	316 ± 48
75 wt. % H(23)	267 ± 11	252 ± 19	0.24 ± 0.02	260 ± 41	240 ± 37
50 wt. % H(23)	196 ± 19	166 ± 16	0.23 ± 0.01	201 ± 35	160 ± 26
25 wt. % H(23)	169 + 7	108 ± 7	0.24 ± 0.00	142 ± 28	81 ± 14
12.5 wt. % H(23)	140 ± 1	45 ± 2	0.22 ± 0.00	112 ± 26	42 ± 9
0 wt. % H(23)	83 ± 22	3 ± 3	0.21 ± 0.00	83 ± 22	3 ± 3

Table 5.2: N_2-physisorption results for binder dilution studies. Adsorption isotherms can be found in the appendix. Catalysts contain H(23) 550 4 h in a Ludox AS silica matrix, the wt. % of zeolite in the composite material is shown in the table. Theoretical values were obtained from linear extrapolation between 100 wt. % and 0 wt. % H(23) 550 4 h materials. Errors correspond to the values obtained from ± the furthest outlier of repeated measurements. All measurements were obtained as described in section 2.6.5

Linear extrapolations of BET and micropore surface areas for 100 wt. % zeolite and 0 wt. % zeolite were used to predict the surfaces areas of bound composites. In apparent contradiction to some literature reports [14,15], BET and t-plot results in Table 5.2 show the presence of the Ludox AS 40 550 4 h matrix to increase catalyst total pore volume slightly rather than effect a decrease. Furthermore, the surface areas of 25 wt. % zeolite and 12.5 wt. % zeolite materials area noticeably increased. These increases are not generally outwith the error of the theoretical values. Two possible explanations for this increase may include: lower extra-framework aluminium content, allowing accessibility to previously inaccessible surface area and/or the production of additional microporosity.

Extra-framework aluminium species have been reported as contributing to channel blockage [4,5]. The ^{27}Al MAS-NMR spectra in Fig. 5.9 show the proportion of framework aluminium to extra-framework aluminium content to increase with increasing binder content where AS(23) 550 4 h (12.5 wt % zeolite) possesses the greatest tetrahedral/octahedral ratio. It is therefore believed that the expected lower surface area of the bound materials is obscured by the surface area decrease caused by extra-framework materials in the unbound zeolite component. On the other hand, microporosity itself cannot be solely attributed to the zeolite component as Ludox AS 550 4 h also displayed a degree of microporosity. It was possible that additional microporosity may have been generated by: calcination [13]; the production of additional silicoalumino-phases from mobile zeolite and binder species [16] and/or possibly at interphase boundaries [4,5]. However, no clear structural evidence was found for the production of additional microporosity by PXRD or MAS-NMR. Possibly the formation of additional microporosity is less significant (if it even occurs) than the effects of pore blockage by extra-framework aluminium.

It should be born in mind that the use of N_2-physisorption on materials with 3D pore systems is less sensitive towards partial pore blockage or external surface blockages as channels may be filled with adsorbate through multiple routes [2]. For example, it may be envisaged that if all of the external pores except one were plugged in Fig. 5.12a, the surface area as determined by N_2-physisorption would be largely unaffected. Catalytic activity may be more sensitive to such blockages.

Closer inspection of PXRD results for these materials (Fig. 5.11) shows channel filling to increase with increasing binder content [17]. This would indicate the binder and not extra-framework aluminium to cause zeolite pore filling.

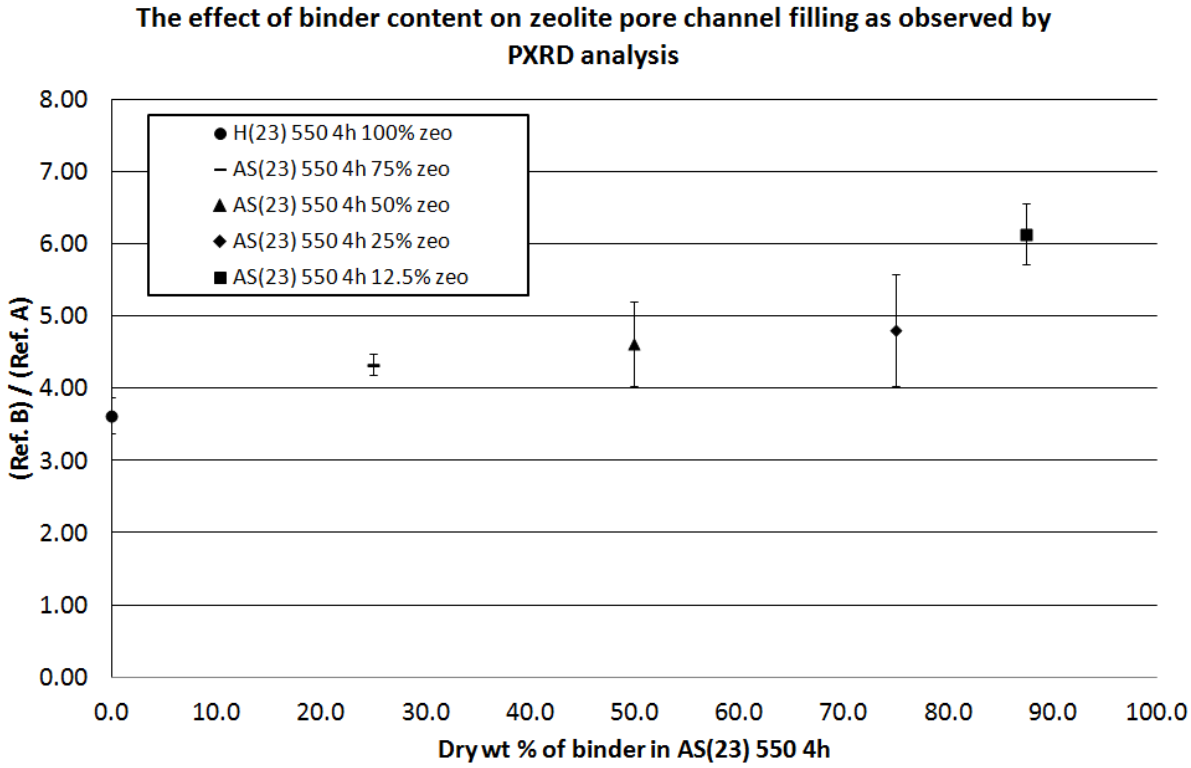

Figure 5.11: PXRD - Zeolite channel filling in binder diluted H-ZSM-5 (23). 'Ref. A' = Σ[(101), (011), (200), (020) and (111) reflection intensities] and 'Ref. B' = Σ[(501), (051), (151), (303) and (133) reflection intensities]. Error bars correspond to ± the furthest outlier of repeat measurements. All measurements were obtained as described in section 2.6.6.

However, the measured BET specific surface areas do not show the expected decrease in BET surface area expected from silica binding [3]. Channel filling may be attributable to both extra-framework and binder species to varied extents and the mode of pore filling may explain the N_2-physisorption and PXRD results. Schematic representations are given as visual aids in this explanation. (Figs. 5.12a-c).

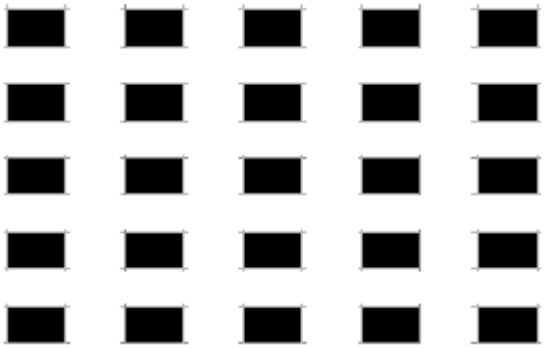

Figure 5.12a: Schematic of ZSM-5 pore channel system with no blockages.

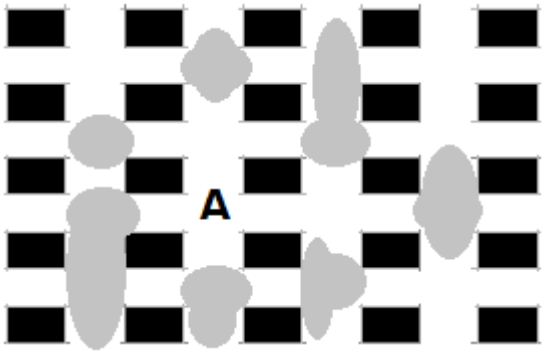

Figure 5.12b: Schematic of ZSM-5 with a ‘plugged’ channel system.

Figure 5.12c: Schematic of ZSM-5 with a ‘filled’ channel system.

Fig. 5.12a is an unblocked pore system with complete surface area accessibility. Assuming the blocking species are immobile, region A of Fig. 5.13b is inaccessible to absorbates and a lower surface area would be measured from physisorption

studies. In addition, Fig. 5.12c would result in the same surface area value. However, the degree of channel filling is different between Fig. 5.12b and Fig. 5.12c. As such, PXRD analyses of MFI systems with 'plugging' blockages would show channel filling to be lower than that of MFI systems with 'filling' blockages. An analogous situation may exist for the binder dilution systems where extra-framework aluminium species result in a greater extent of 'plugging' than 'filling' and *vice versa* for mobile silica species.

It was believed that, from structural and textural characterisation, partial zeolite channel filling had occurred as a result of binding. This was however masked in N_2-physisorption measurements by the pre-existing extra-framework aluminium species generated from the zeolite component during calcination.

5.2.4 **Catalytic testing**

The results in Fig. 5.13 show unbound H(23) 550 4 h to have given the highest methanol conversion rate out of all materials probed. On the other hand, Ludox AS 550 4 h showed no observable methanol dehydration activity although methanol adsorption was observed in the first 5-30mins on stream. It may be expected that the resulting methanol dehydration activity of the Ludox AS-bound H(23) 550 4 h materials to be the sum of the methanol dehydration rates of the constituent components. As shown in the Arrenhius plot below, the methanol dehydration rates were lower than those predicted by the sum of constituent parts and were increasingly lower with increasing binder content as were the apparent activation energies and y-intercepts.

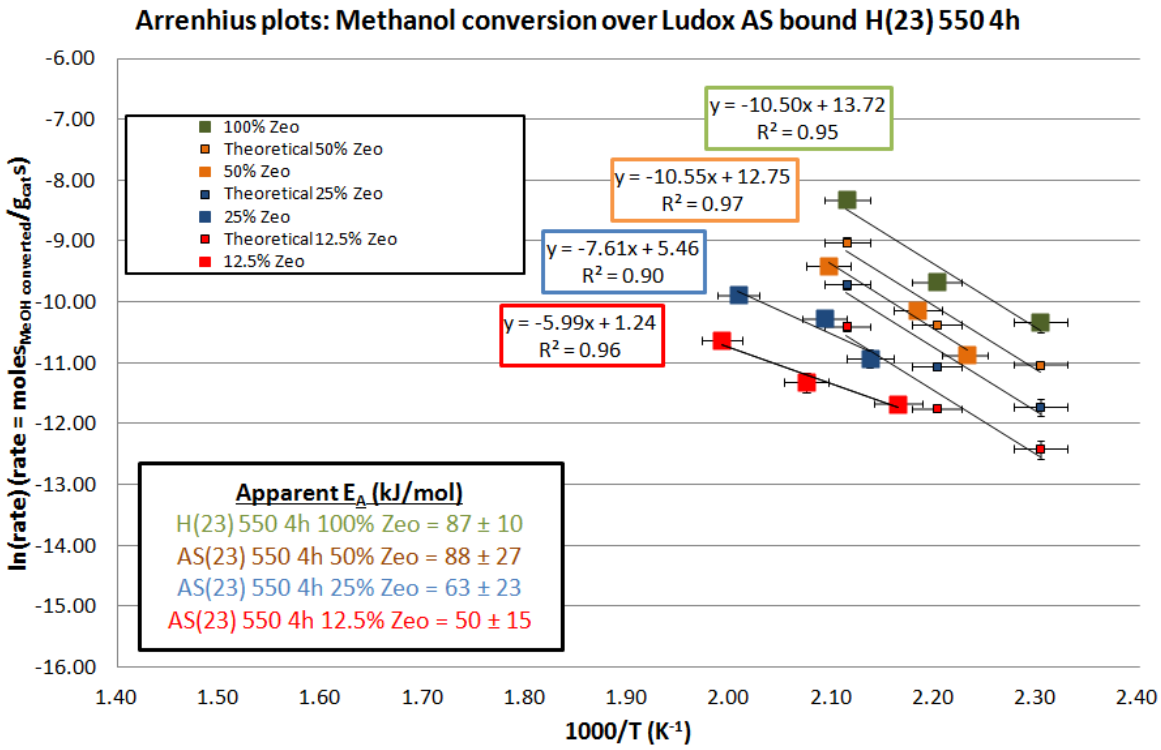

Figure 5.13: Arrenhius plots of a range of zeolites/binder dilutions. Vertical error bars represent the 1st standard deviation in the values obtained for each point. Theoretical values correspond to expected results from the sum of constituent parts.

With increasing binder content the apparent activation energy decreases. This may be attributed to increased tetrahedral aluminium retention and/or pore filling as shown in the ^{27}Al MAS-NMR spectra in Fig. 5.9 and PXRD analyses in Fig. 5.11 respectively. The decreasing methanol conversion rates with increasing binder contents were attributed to a combination of: dilution of the zeolite component; increasing pore filling and increasing sodium content. The effects of sodium content are further discussed in sections 5.3.3 and 5.4.

5.3 Ludox AS 40 and Ludox HS 40 bound ZSM-5 (23)

5.3.1 Structural analyses

PXRD analyses of Ludox AS(23) 550 4 h 50 wt. % zeolite and Ludox HS(23) 550 4 h 50 wt. % zeolite (Fig. 5.14) showed no new crystalline phases to be formed following binding and calcination.

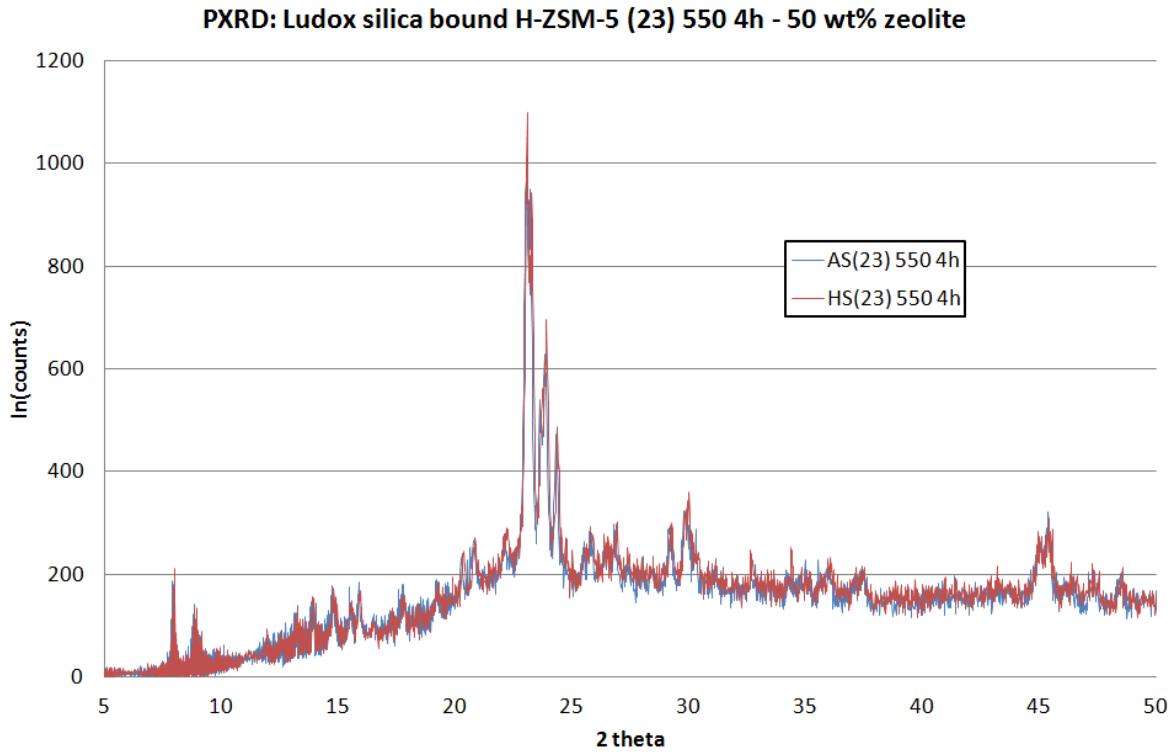

Figure 5.14: PXRD patterns of silica-bound ZSM-5 (23) catalysts. Measurements were obtained as described in experimental section 2.6.6.

The zeolite component of both catalysts was of orthorhombic symmetry, possessed similar crystallinities and extents of channel filling.

^{27}Al MAS-NMR spectra of both bound zeolites (Fig. 5.16) show the materials to contain mostly tetrahedral aluminium with differing octahedral aluminium content.

Flame photometry showed AS(23) 550 4 h to possess 0.05 wt. % sodium and Ludox HS(23) 550 4 h to possess 0.15 wt. % sodium. Both materials contained the same wt. % of silica and were bound by the same method. If extra-framework

aluminium trapping by the silica matrix was the only cause for decreased octahedral aluminium formation then both ^{27}Al spectra should have the same tetrahedral / octahedral ratios, which they do not. Therefore, the differences in extra-framework aluminium contents were attributed to the sodium contents of the bound materials.

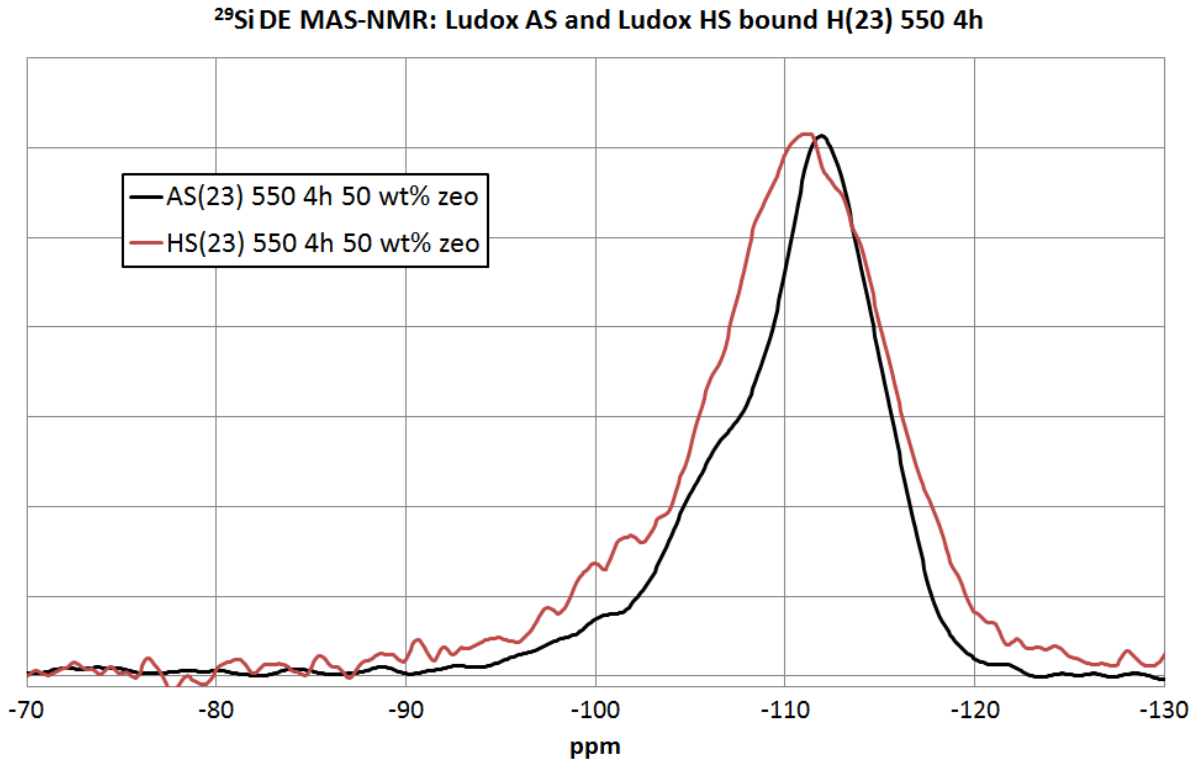

Figure 5.15: ^{29}Si MAS-NMR spectra of silica-bound ZSM-5 (23) catalysts. All spectra were obtained on a Varian VNMRS 400.

Both AS(23) 550 4 h and HS(23) 550 4 h appear as the sum of their constituent parts (Fig. 5.15). A moderately intense shoulder is observable at ≈ -106 ppm for the AS(23) 550 4 h spectra is consistent with the presence of an H(23) 550 4 h component. The Ludox HS(23) 550 4 h spectra are broader than that of Ludox AS(23) 550 4 h, possibly indicating greater disorder. This broadening obscures the Si(1Al) peak of Ludox HS(23) 550 4 h making interpretation of the effect of the binder on the aluminium component difficult.

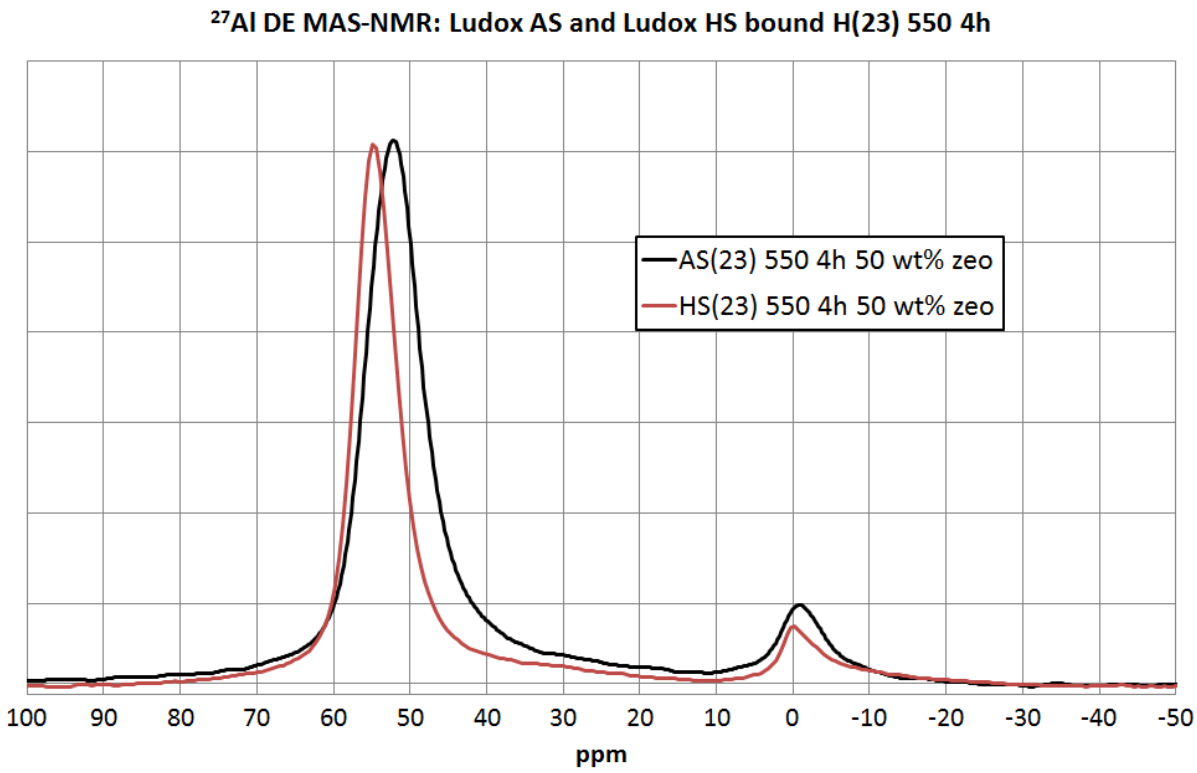

Figure 5.16: ^{27}Al MAS-NMR spectra of silica-bound ZSM-5 (23) catalysts. All spectra were obtained on a Varian VNMRS 400.

The decreased octahedral aluminium content and the downfield shift of the tetrahedral peak in Ludox HS(23) 550 4 h correlates with the increased sodium content. As such, the retardation of extra-framework aluminium formation by sodium was believed to occur. This does not however rule out the possibility of extra-framework aluminium trapping by the silica matrix, as will be further discussed in section 5.4.

5.3.2 **Textural analyses**

N_2-physisorption results in Table 5.3 below show both AS(23) 550 4 h and Ludox HS(23) 550 4 h to possess similar micropore surface areas and pore volumes.

Material	BET SA (m^2/g)	t-plot µpore SA (m^2/g)	Pore vol. (cm^3/g)	Ads. Iso. Type
H(23) 550 4 h	318 ± 48	316 ± 48	0.20 ± 0.01	I
AS(23) 550 4 h	196 ± 9	166 ± 9	0.23 ± 0.01	I/IV
AS 550 4 h	83 ± 22	3 ± 3	0.21 ± 0.00	IV
HS(23) 550 4 h	222	165	0.23	I/IV
HS 550 4 h	110	6	0.21	IV

Table 5.3: N_2-physisorption results for silica-bound ZSM-5 (23) catalysts. Results were obtained as described in the experimental chapter. Errors correspond to the values obtained from duplicate runs. Ads. Iso. = Adsorption Isotherm. Adsorption isotherms can be found in the appendix.

As with Ludox AS 40, binding of ZSM-5 (23) with Ludox HS 40 increases the catalyst porosity beyond the sum of constituent parts. It was believed that, from structural and textural characterisation, partial zeolite channel filling had occurred as a result of binding, in addition to increased silica matrix porosity.

5.3.3 **Catalytic testing**

In Fig. 5.17, the lower methanol conversion rates of HS(23) 550 4 h, over the temperature range tested, were attributed to increased acid site poisoning by the increased sodium content.

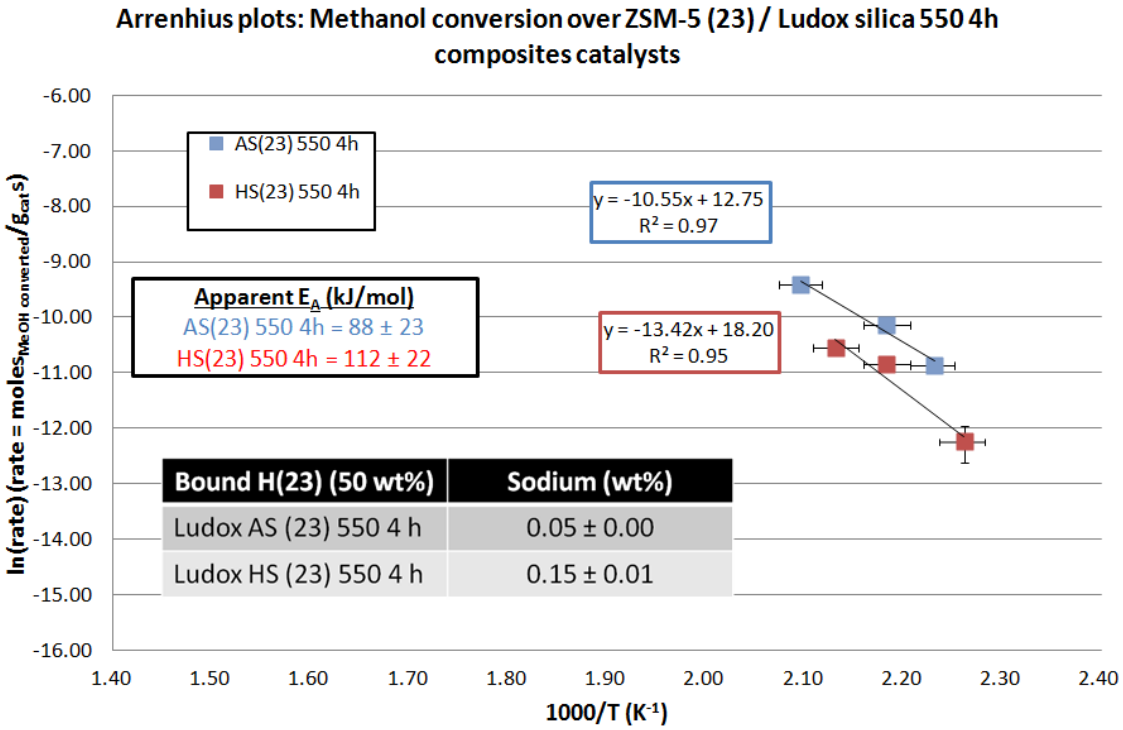

Figure 5.17: Arrenhius plots of silica-bound H(23) 550 4 h catalysts**.** Vertical error bars represent the 1st standard deviation in the values obtained for each point. Sodium contents were determined by flame photometry and the error is the furthest outlier of duplicate measurements.

With similar porosities and binder content, the extent of pore blockage would be expected to be similar for both materials. The lower methanol conversion rates for Ludox HS(23) 550 4 h may be the result of alkali metal poisoning.

5.4 Sodium-exchanged zeolites

5.4.1 Sodium content

To further observe the effect of sodium content on the methanol dehydration rate, a series of partially sodium-exchanged zeolites were prepared as described in the experimental chapter. Their sodium contents were determined by flame photometry and are given below in Table 5.4.

Material	Sodium (wt. %)
H(23) 550 4 h (no exchange)	0.04 ± 0.00
Na/H(23) 0.05M 1Ex 550 4 h	0.24 ± 0.00
Na/H(23) 1M 1Ex 550 4 h	0.55 ± 0.01
Na/H(23) 1M 3Ex 550 4 h	0.65 ± 0.01

Table 5.4: Sodium flame photometry results for ZSM-5 (23) materials. Duplicate measurements were obtained as described in the experimental section 2.6.2.

Flame photometry results in the table above show the sodium contents of the partially exchanged zeolites.

5.4.2 **Structural analyses**

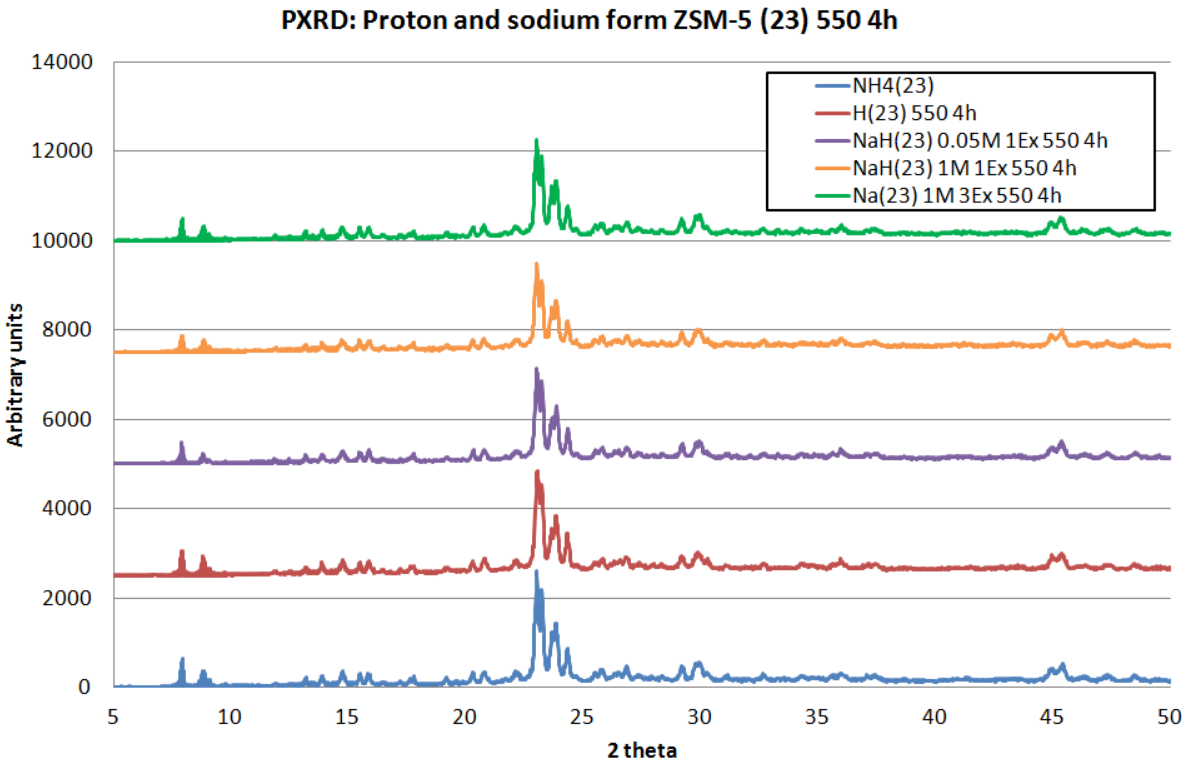

Figure 5.18: PXRD patterns of ion-exchanged ZSM-5 (23) materials. All patterns were obtained as described in section 2.6.6.

PXRD patterns of NH_4^+-, Na^+- and H^+-form 550 4 h ZSM-5 (23) are shown in Fig. 5.18. No significant changes in unit cell structure or symmetry were observed following 550 °C 4 h calcination. Crystallinity decreases slightly following calcination but the sodium content appears to have little effect. No simple correlation between apparent channel filling and sodium content could be determined as presented in Fig. 5.19 overleaf [17].

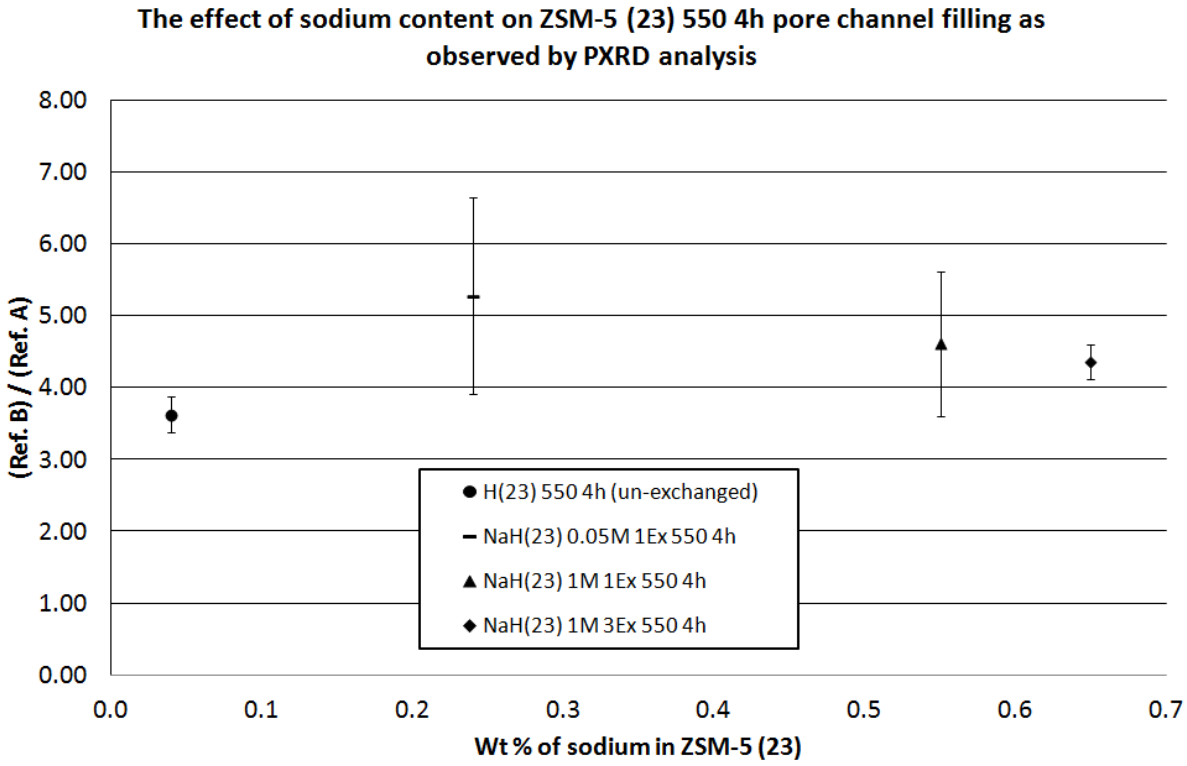

Figure 5.19: PXRD - Zeolite channel filling in sodium-exchanged ZSM-5 (23). 'Ref. A' = Σ[(101), (011), (200), (020) and (111) reflection intensities] and 'Ref. B' = Σ[(501), (051), (151), (303) and (133) reflection intensities]. Error bars correspond to ± the furthest outlier of repeat measurements (repeated ≥ 2x).

MAS-NMR studies of the sodium-exchanged and uncalcined materials show minor differences following sodium-exchange (Figs. 5.20 and 5.21).

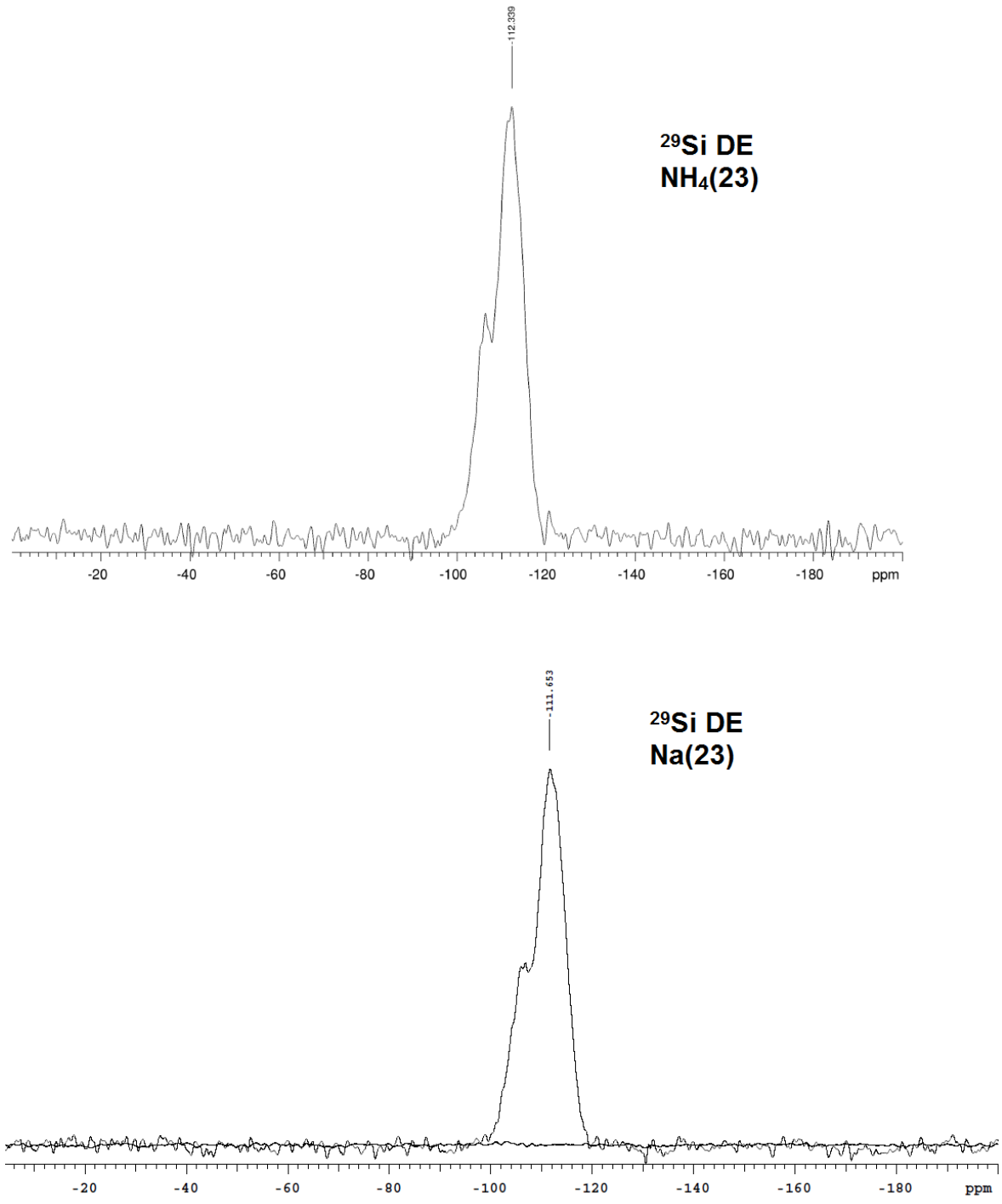

Figure 5.20: ^{29}Si spectra of uncalcined NH_4^+-form and Na^+-form ZSM-5 (23). ^{29}Si spectra for NH_4(23) were obtained on a Varian VNMRS 400 and ^{29}Si spectra of Na(23) were obtained on a Varian Unity Inova 300.

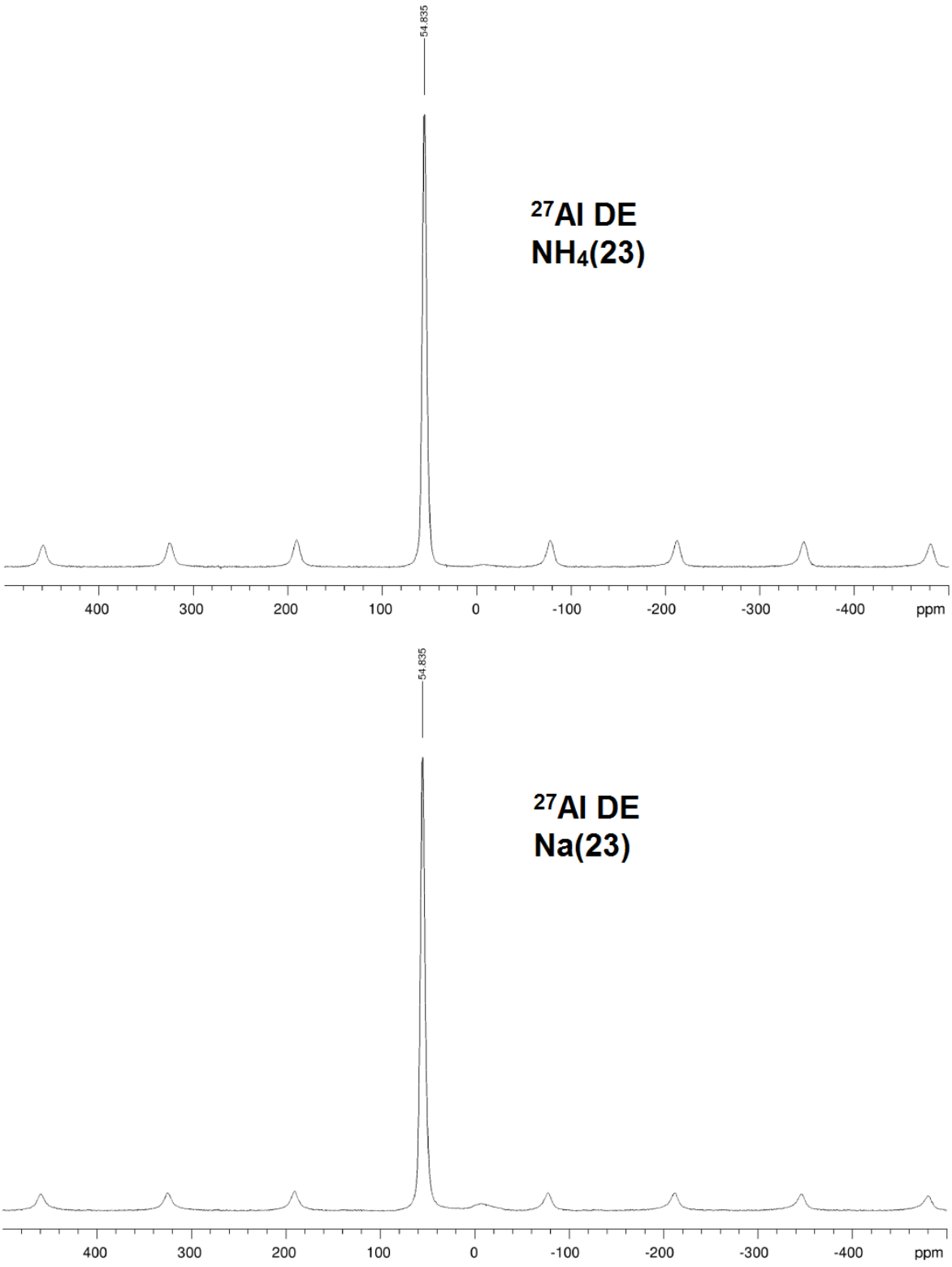

Figure 5.21: ^{27}Al MAS-NMR spectra of NH_4^+-form and Na^+-form ZSM-5 (23). All spectra were obtained on a Varian VNMRS 400.

Both materials retain similar framework aluminium contents and average silicon coordinations of Si(0Al) and Si(1Al). Aluminium is also tetrahedrally coordinated and a very small octahedral content observed in both materials.

Following calcination at 550 °C for 4 h, differences in the materials become more apparent (Figs. 5.22 and Fig. 5.23).

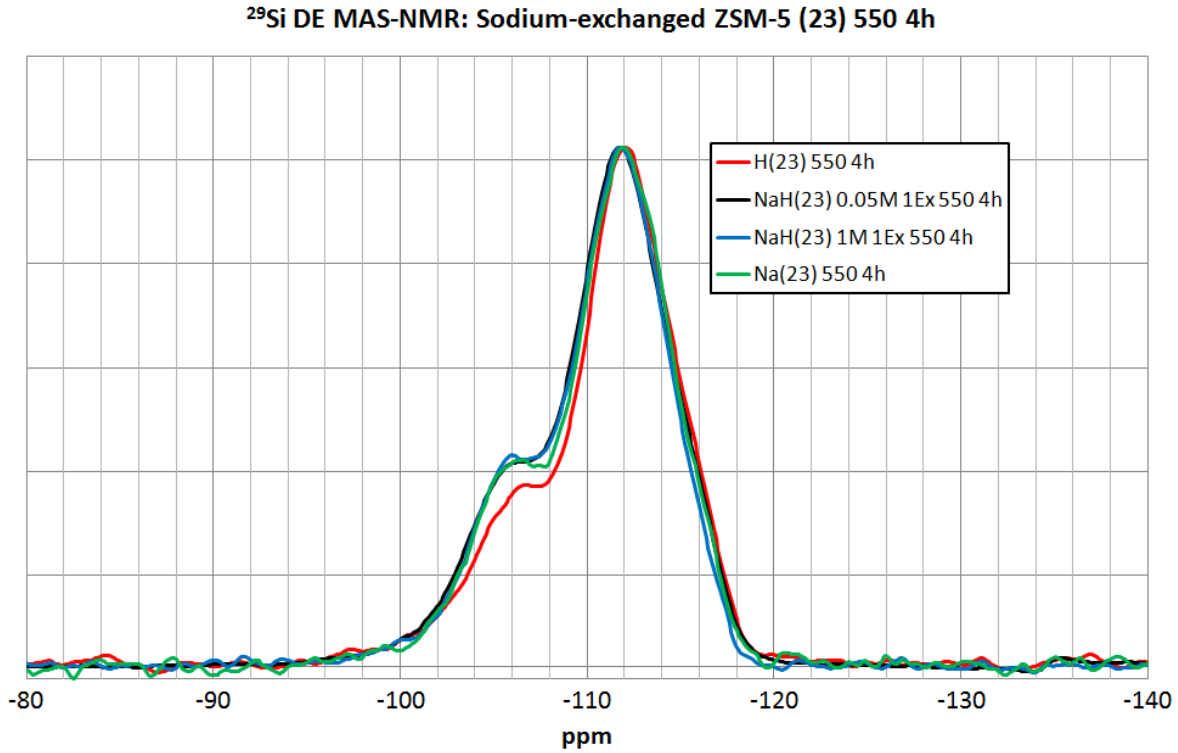

Figure 5.22: ^{29}Si MAS-NMR spectra of partially sodium-exchanged ZSM-5 (23)**.** H(23) 550 4 h ^{29}Si spectra were obtained on a Varian VNMRS 400 and Na(23) 550 4 h ^{29}Si spectra were obtained on a Varian Unity Inova 300.

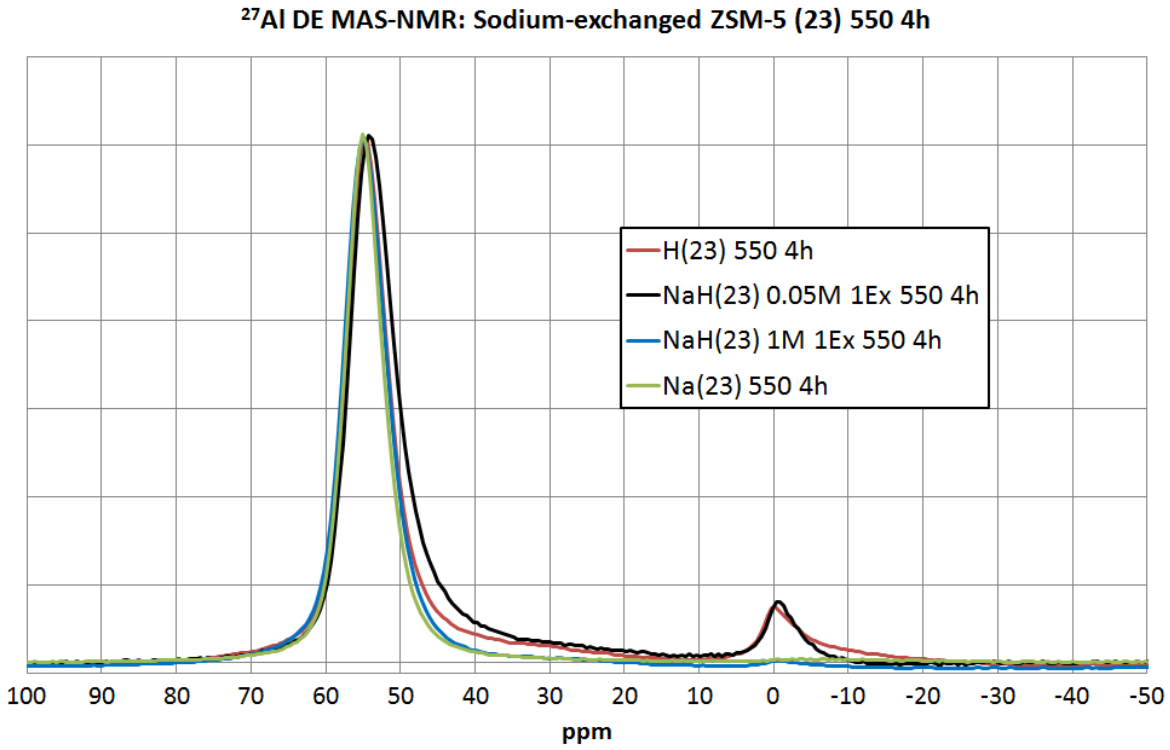

Figure 5.23: ^{27}Al MAS-NMR spectra of partially sodium-exchanged ZSM-5 (23). All spectra were obtained on a Varian VNMRS 400.

Following calcination, the ^{29}Si spectra of all materials broaden, which is indicative of an increase in the heterogeneity of the silicon coordination environments (Fig. 5.22). The Si(1Al) shoulder at *ca*. -107 ppm is lower in the H(23) 550 4 h spectra than the sodium-exchanged ZSM-5 (23) materials, indicating a decrease in framework aluminium content. Additionally, ^{27}Al spectra shows both H(23) 550 4 h and NaH(23) 0.05M 1Ex 550 4 h to possess a lower tetrahedral / octahedral ratio than NaH(23) 1M 1Ex 550 4 h and Na(23) 550 4 h (Fig. 5.23). This is consistent with the observation that the sodium counter ion retards extra-framework aluminium formation.

5.4.3 **Textural analyses**

5.4.3.1 **N_2-physisorption**

Material	BET SA (m^2/g)	Pore vol. (cm^3/g)	Ads. Iso. Type
NH_4(23)	319	0.20	I
Na(23) 1M 3Ex	245 ± 8	0.15 ± 0.01	I
H(23) 550 4 h	318 ± 48	0.20 ± 0.01	I
NaH(23) 0.05M 1Ex 550 4 h	295	0.19	I
NaH(23) 1M 1Ex 550 4 h	271	0.17	I
Na(23) 1M 3Ex 550 4 h	253 ± 7	0.16 ± 0.01	I

Table 5.5: N_2-physisorption results for sodium-exchanged ZSM-5 (23) 550 4 h. All measurements were obtained as described in the experimental chapter. Ads. Iso. = Adsorption Isotherm. Adsorption isotherms may be found in the appendix. Errors represent the further outlier of repeat runs.

The BET specific surface area (Table 5.5) was affected by the presence of the sodium counter ion. Following calcination, surface area decreases with increasing sodium content. This is consistent with the increased channel filling observed by PXRD analyses. Decreased BET specific surface area has been chiefly attributed to strongly adsorbed adsorbate on the sodium-exchanged samples as will be shown by TGA analyses in the following section.

5.4.3.2 **Thermogravimetric analyses**

The observed decrease in N_2-physisorption surface areas with increasing sodium content can be explained by the presence of strongly adsorbed adsorbate on the samples (Fig. 5.24).

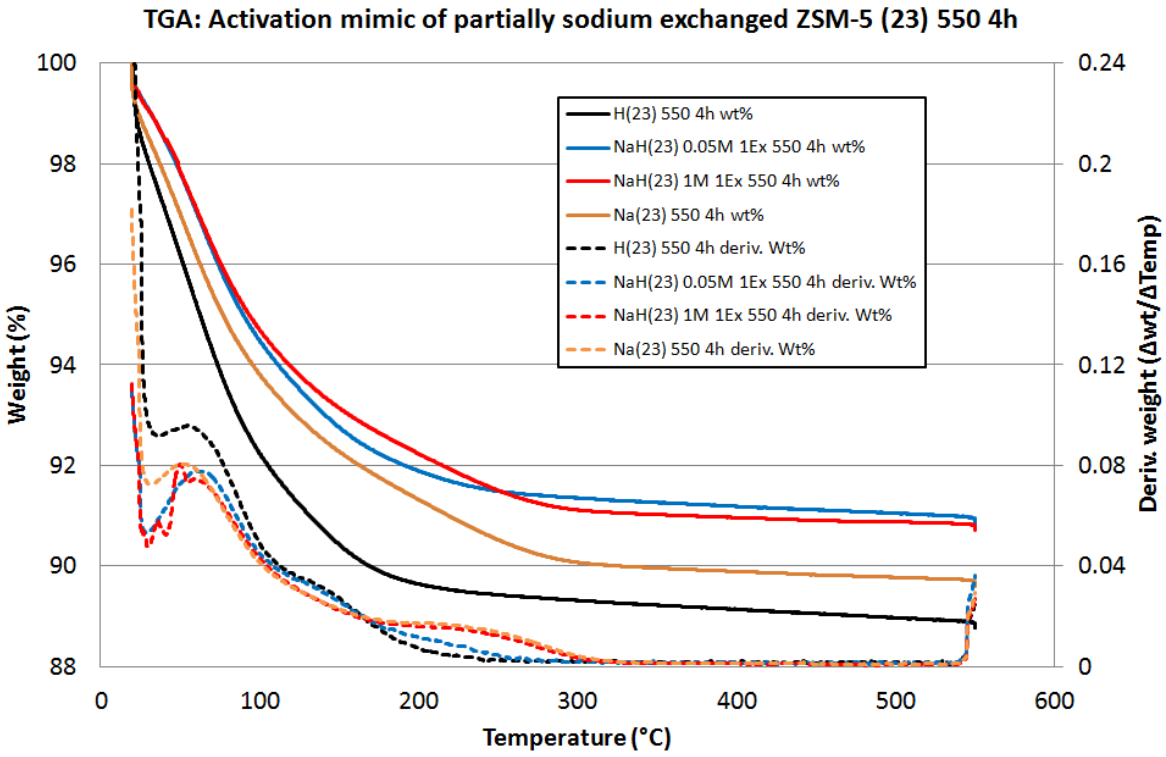

Figure 5.24: TGA measurements of sodium-exchanged ZSM-5 (23) 550 4 h. Measurements were obtained as explained in experimental section 2.6.8.

Overnight degassing at 120 °C, prior to N_2-physisorption measurements, was insufficient to remove all of the adsorbed species observed between *ca*. 180 °C - 300 °C. Weight loss within this temperature range increases with increasing sodium content. Therefore, any changes in the surface area of the zeolites themselves with sodium-exchange are obscured by the decrease associated with incomplete degassing. The evolution temperature of the strong adsorbate is lower than both sodium carbonate [18] and sodium nitrate [19] decomposition temperatures and as such the identity of the strong adsorbate was undetermined.

5.4.4 **Catalytic testing**

The strong effect of sodium content on methanol dehydration rates is clearly observable in Fig. 5.25. The decrease in methanol dehydration rates is much greater than those observed *via* binder dilution.

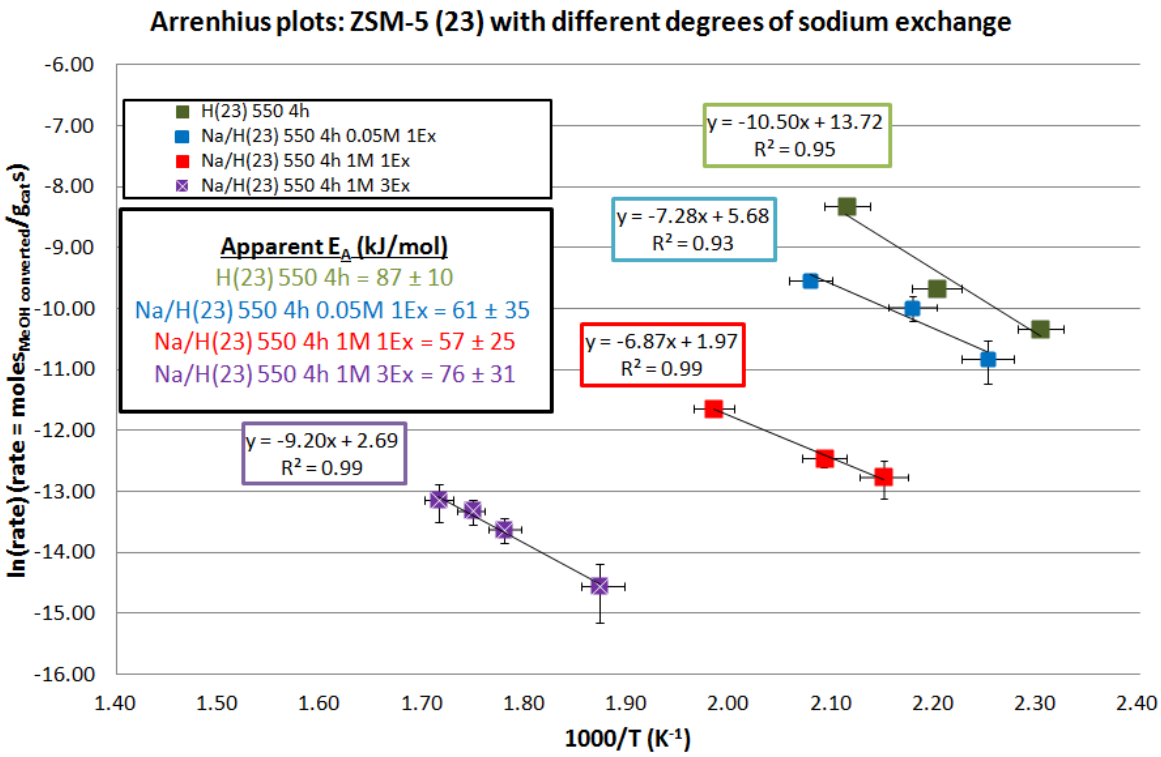

Figure 5.25: Arrenhius plots of sodium-exchanged ZSM-5 (23) catalysts. Vertical error bars represent the 1st standard deviation in the values obtained for each point.

The apparent activation energies of the sodium-exchanged samples are largely similar and within the error of one another. As such, the primary affect of sodium on the catalytic activity of the ZSM-5 catalysts is to reduce the number of active sites as shown by a decrease in the y-intercept. The dramatic decrease in y-intercept and methanol conversion rates between 160-310 °C was attributed to acid site neutralisation by the sodium counter ions.

5.5 Extreme calcination and steaming

Higher calcination temperatures and steaming treatments are common practices in industrial zeolite chemistry. Zeolite catalysts are known to be purposefully steamed to affect catalytic properties such as acid site number, strength, mechanical properties and/or lifetime desirably. Steaming has been reported as increasing acid site strength, e.g. in USY [20]. Relative to low-silicon-containing zeolites such as faujasite, high-silica zeolites such as ZSM-5 have been reported as being more resistant to the effects of steam treatment [21]. Nonetheless, it was of interest to study the effects associated with increased calcination temperature and steaming treatments. The treatments employed are described in Table 5.6.

Material	Description
550 4 h	Calcined at 550 °C for 4 h
Steamed	Steamed at 550 °C for 4 h
750 72 h	Calcined at 750 °C for 72 h
Extremely steamed	Steamed at 750 °C for 72 h*

.

Table 5.6: The nomenclature for calcination and steaming treatments**.** These procedures were undertaken with a 1/2 H_2O in Ar mixture. * = the water source evaporated after *ca*. 6 h.

In this section Ludox AS-bound H-ZSM-5 (23) and Ludox HS-bound ZSM-5 (23) are treated under the different thermal and hydrothermal conditions stated in Table 5.6 and their structural, textural and catalytic properties are compared.

5.5.1 Ludox AS(23) and Ludox HS(23) 50 wt. % zeolite materials

5.5.1.1 Structural analyses

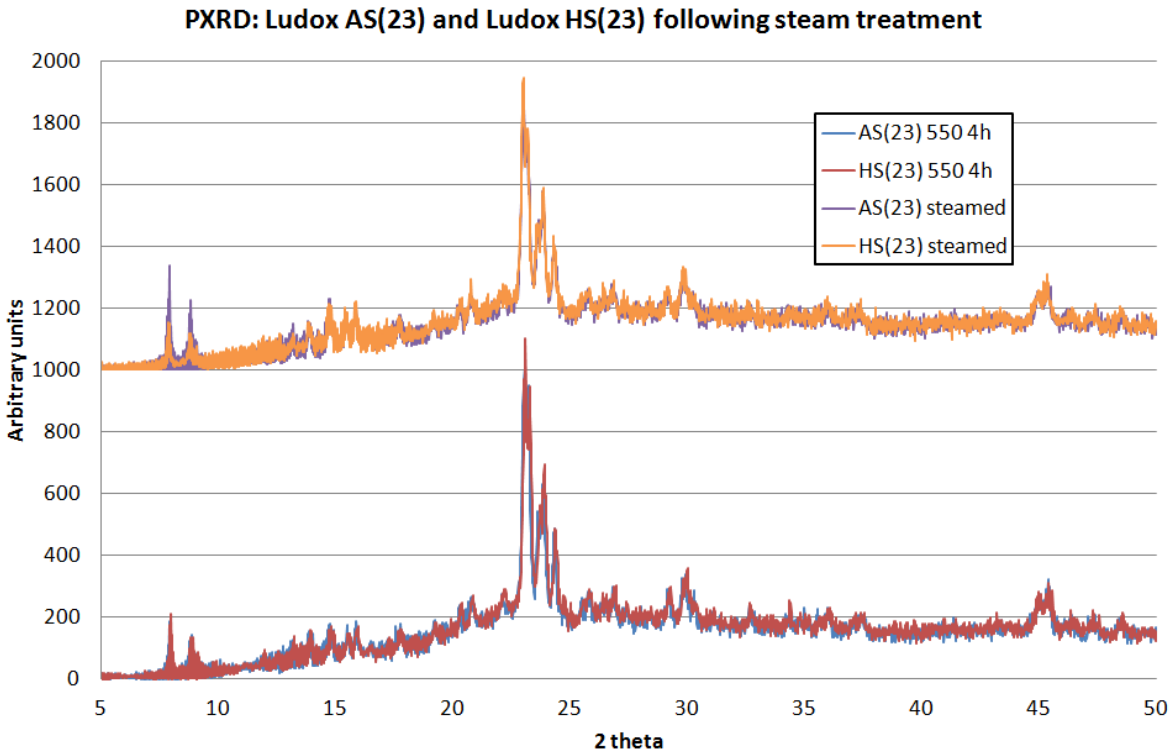

Figure 5.26: PXRD patterns of silica-bound ZSM-5 (23) catalysts following calcination or steaming. Measurements were obtained as described in the experimental chapter.

Following steam treatment, both Ludox AS(23) steamed and Ludox HS(23) steamed possessed similar extents of crystallinity. Both materials retain orthorhombic symmetry and there was no apparent change in unit cell dimensions. However, low-angle peak intensities suggested Ludox HS(23) steamed to possess a greater degree of pore filling than Ludox AS(23) steamed [17].

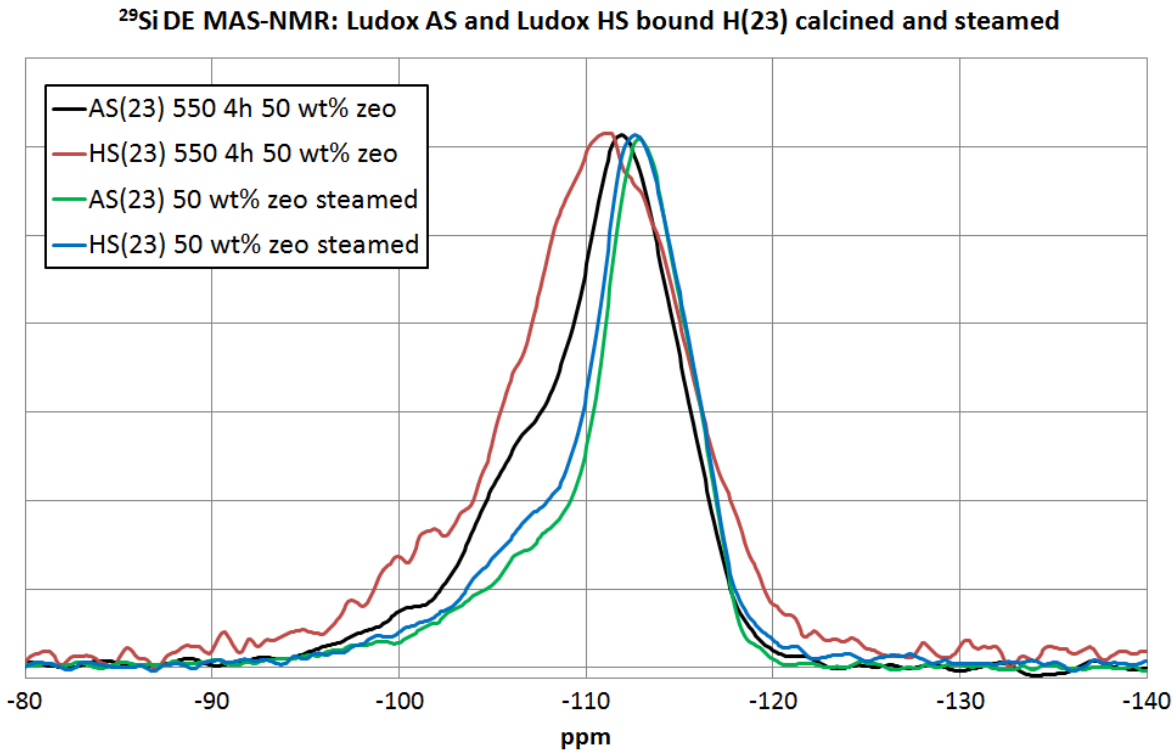

Figure 5.27: ^{29}Si MAS-NMR spectra of silica-bound ZSM-5 (23) catalysts following calcination or steaming**.** All spectra were obtained on a Varian VNMRS 400.

In Fig. 5.27, the shoulder peak at ca. -106 ppm which is assigned to Si(1Al) decreases in both Ludox AS(23) and Ludox HS(23) materials following steaming. This is indicative of dealumination of the zeolite. Closer inspection of the two steamed samples shows Ludox HS(23) steamed to retain slightly more Si(1Al) than Ludox AS(23) steamed – this may be attributed to retardation of extra-framework formation in the presence of increased sodium content. Examination of the ^{27}Al MAS-NMR spectra (Fig. 5.28) shows both Ludox AS(23) 550 4 h and steamed samples to possess a greater proportion of octahedral aluminium than either Ludox HS(23) 550 4 h or HS(23) steamed. This is once again attributed to the increased sodium content of the catalyst and more specifically, the migration of sodium from the binder component to the zeolite component. Whilst predominantly tetrahedral, both materials show non-tetrahedral aluminium geometries, octahedral aluminium is clearly observed *ca*. 0 ppm as well as 5-coordinate aluminium *ca*. 30 ppm. The assignment is based upon ^{27}Al MAS-NMR of Andalusite [22] and the assignment of 5-coordinate aluminium in zeolitic environments is still a subject of debate [23,24].

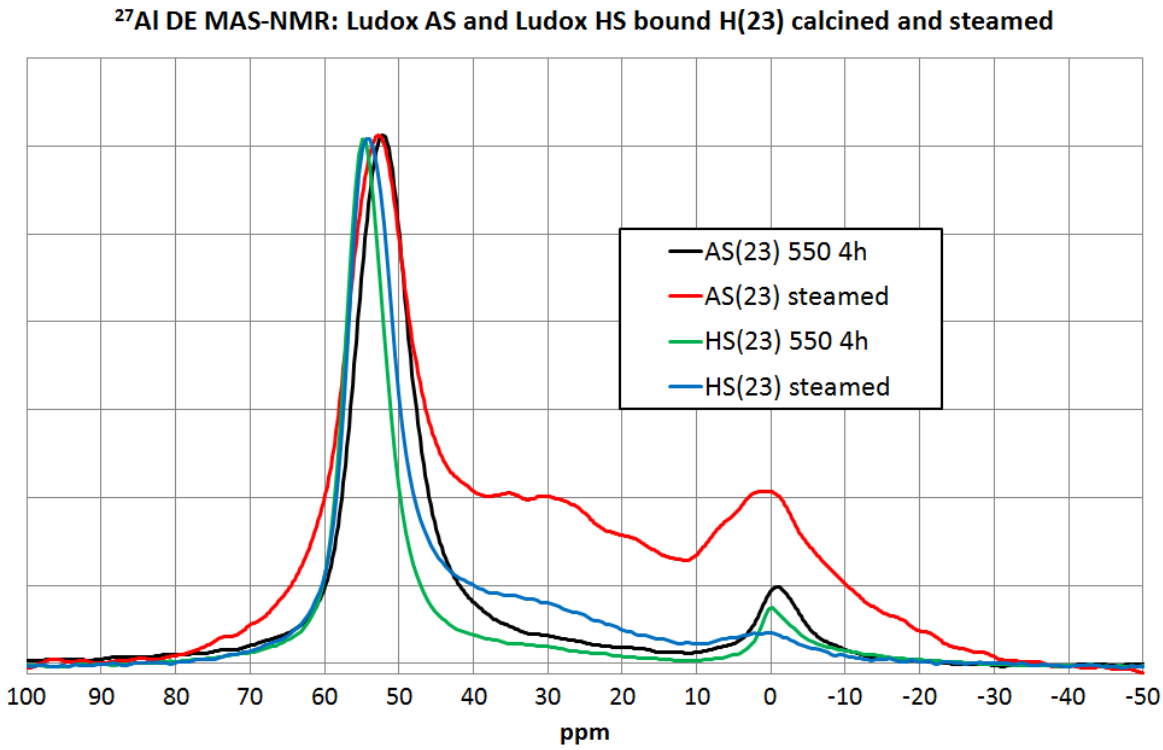

Figure 5.28: ^{27}Al MAS-NMR spectra of silica-bound ZSM-5 (23) following calcination or steaming. All spectra were obtained on a Varian VNMRS 400.

5.5.1.2 **Textural analyses**

Surprisingly, for silica-bound ZSM-5 (23), BET specific surface areas and total pore volumes were not greatly affected by steam treatment Table 5.7.

Material	BET SA (m^2/g)	t-plot µpore SA (m^2/g)	Pore vol. (cm^3/g)	Ads. Iso. Type
Ludox AS (23) 550 4 h	196 ± 19	130 ± 9	0.23 ± 0.01	I/IV
Ludox AS (23) steamed	212 ± 19	101 ± 7	0.23 ± 0.00	I/IV
Ludox HS (23) 550 4 h	222	136	0.23	I/IV
Ludox HS (23) steamed	212 ± 15	136 ± 6	0.22 ± 0.03	I/IV

Table 5.7: N_2-physisorption results for silica-bound ZSM-5 (23) following calcination or steaming**.** Ads. Iso. = Adsorption Isotherm. Measurements were obtained as described in experimental section 2.6.5. Adsorption isotherms may be found in the appendix.

Both silica-bound ZSM-5 (23) materials possessed similar BET specific surface areas before and after steaming. The decreased microporosity of Ludox AS (23) following steaming may be attributable to micropore blockage by newly formed extra-framework aluminium species. The retention of a similar micropore surface area in calcined and steamed Ludox HS (23) materials may be the result of lower extra-framework aluminium content. As with the Ludox AS(23) 550 4 h binder dilution studies, not all microporosity may be associated with the zeolite component.

5.5.1.3 **Catalytic testing**

Following steam treatment, the apparent activation energy and the y-intercept decreased for both materials (Fig. 5.29)

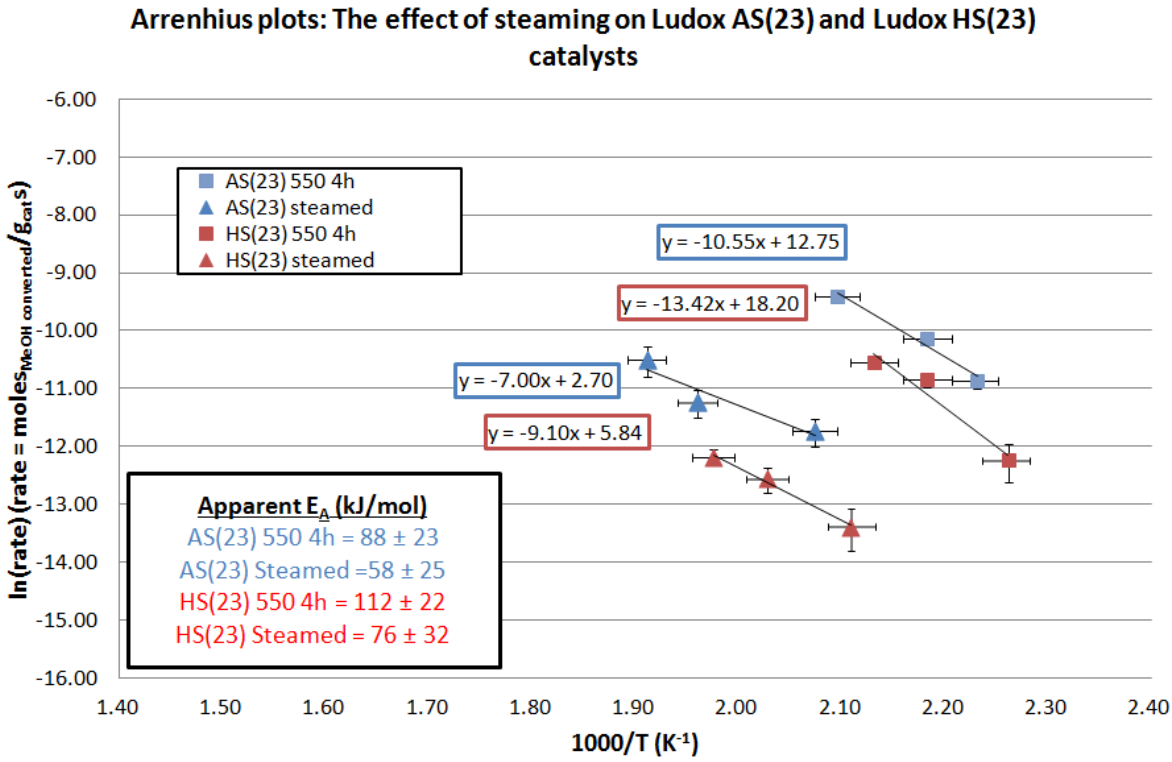

Figure 5.29: Arrenhius plot of silica-bound ZSM-5 (23) following calcination or steaming. Vertical error bars represent the 1st standard deviation in the values obtained for each point.

The apparent activation energies of both calcined and steamed silica-bound catalysts are similar and both decrease following steaming. The decrease in the y-intercept may be associated with the increase in extra-framework aluminium content and partial channel blockage following steaming of both materials.

5.5.2 H-ZSM-5 (23) and Na-ZSM-5 (23) materials

5.5.2.1 Structural analyses

The MFI unit cell structure of H(23) was surprisingly robust to the different calcination and steam treatments applied (Fig. 5.30).

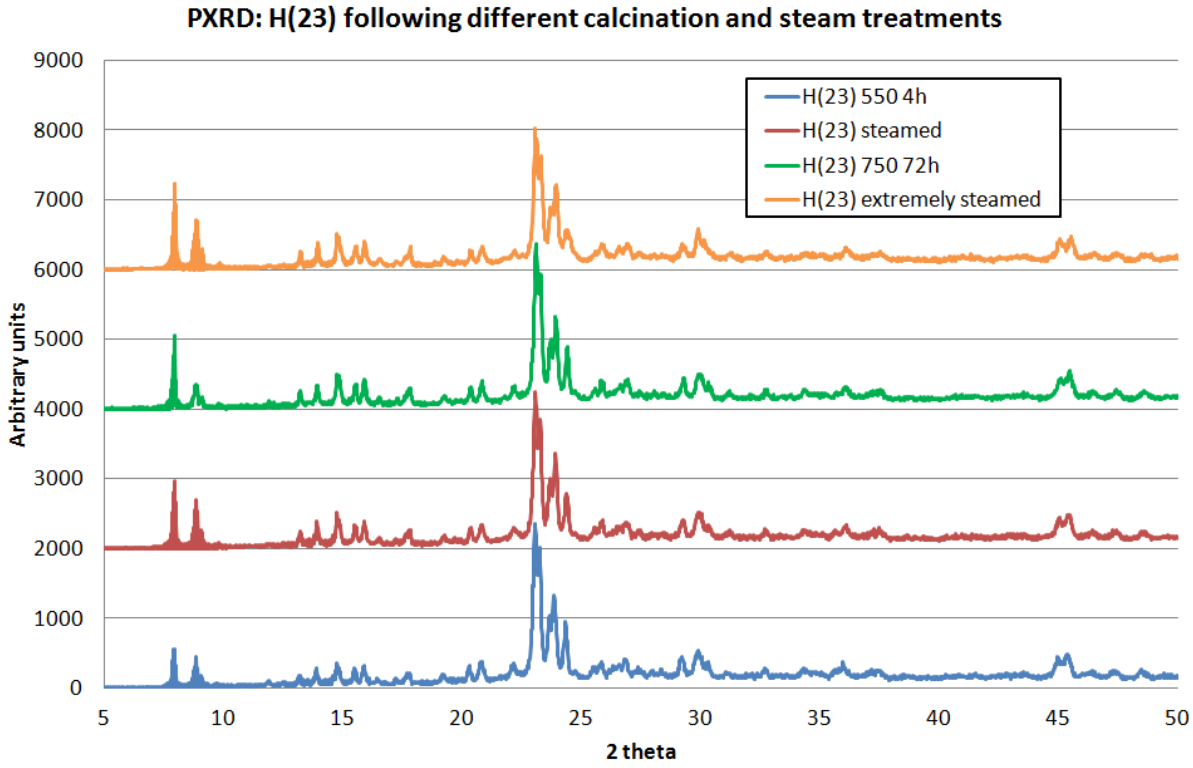

Figure 5.30: PXRD patterns of H(23) following increasing treatment severity**.** Patterns were obtained as described in section 2.6.6.

Relative to H(23) 550 4 h, crystallinity decreases in the order 550 4 h > 750 72 h > steamed > extremely steamed. Also, pore filling decreases in the same order [17]. No clear changes in unit cell dimensions or symmetry were observed.

In Figs. 5.31a-b, the Si(1Al) shoulder peaks at *ca*. -107 ppm decreased with increased treatment severity. The framework aluminium contents of the thermally and hydrothermally treated H-ZSM-5 (23) decreased in the following order H(23) 550 4 h > steamed ≈ 750 72 h > extremely steamed. As aluminium was removed from the frameworks, significant changes in the local environment of the aluminium were observed (Figs. 5.32a-b)

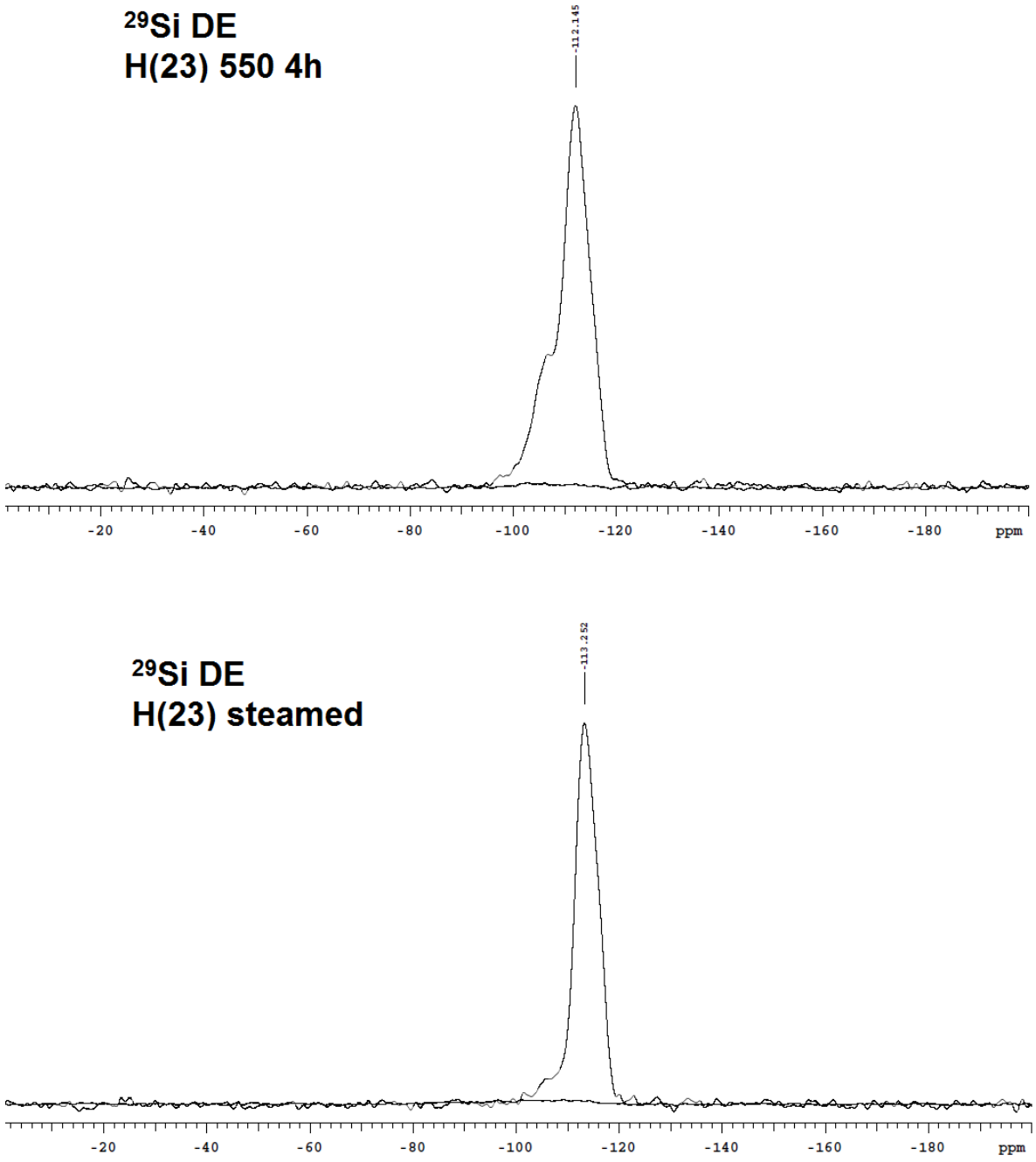

Figure 5.31a: ^{29}Si MAS-NMR spectra of H(23) – calcined and steamed. All spectra were obtained on a Varian Unity Inova 300.

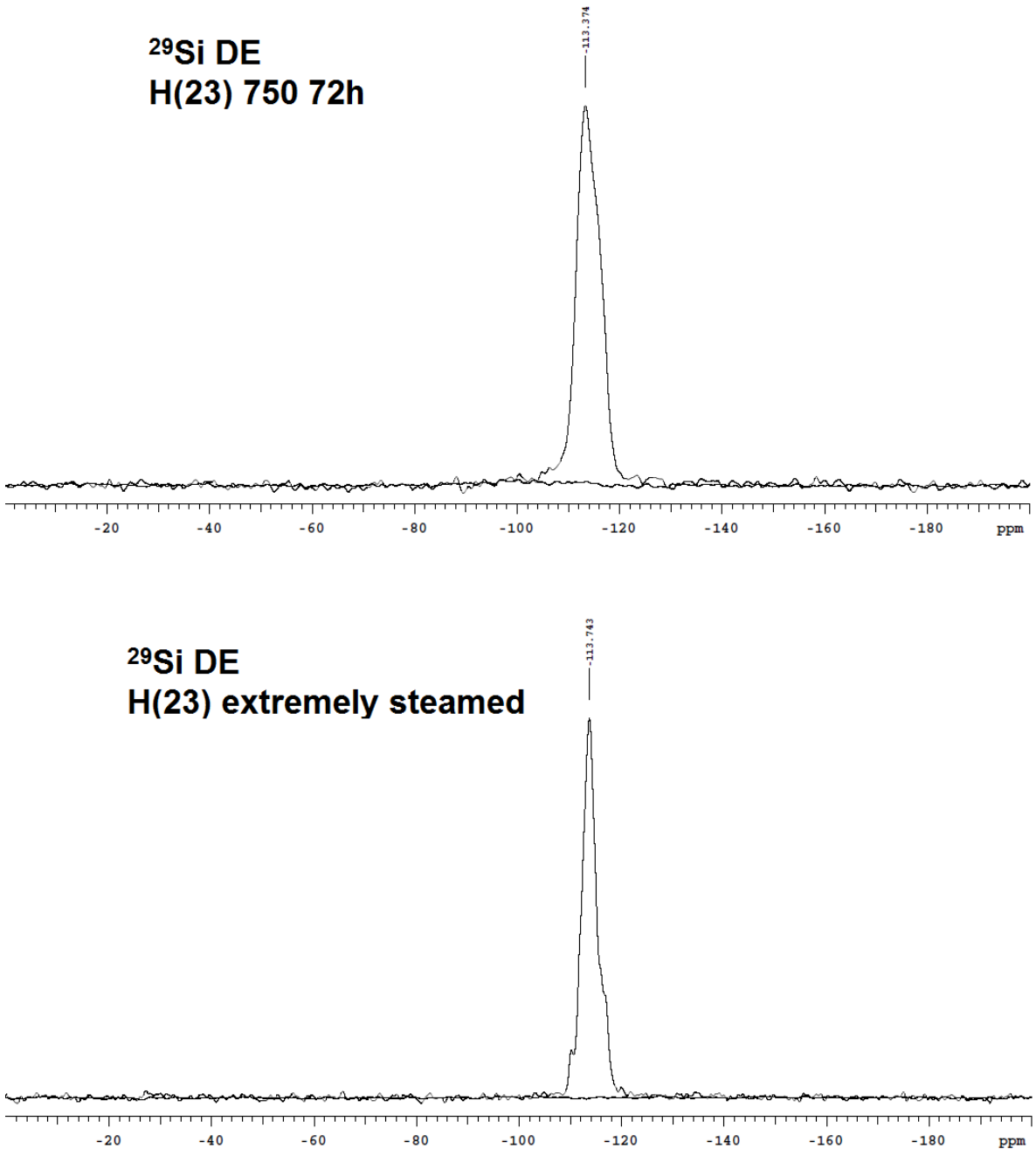

Figure 5.31b: ^{29}Si MAS-NMR spectra of H-ZSM-5 (23) - extremely treated**.**

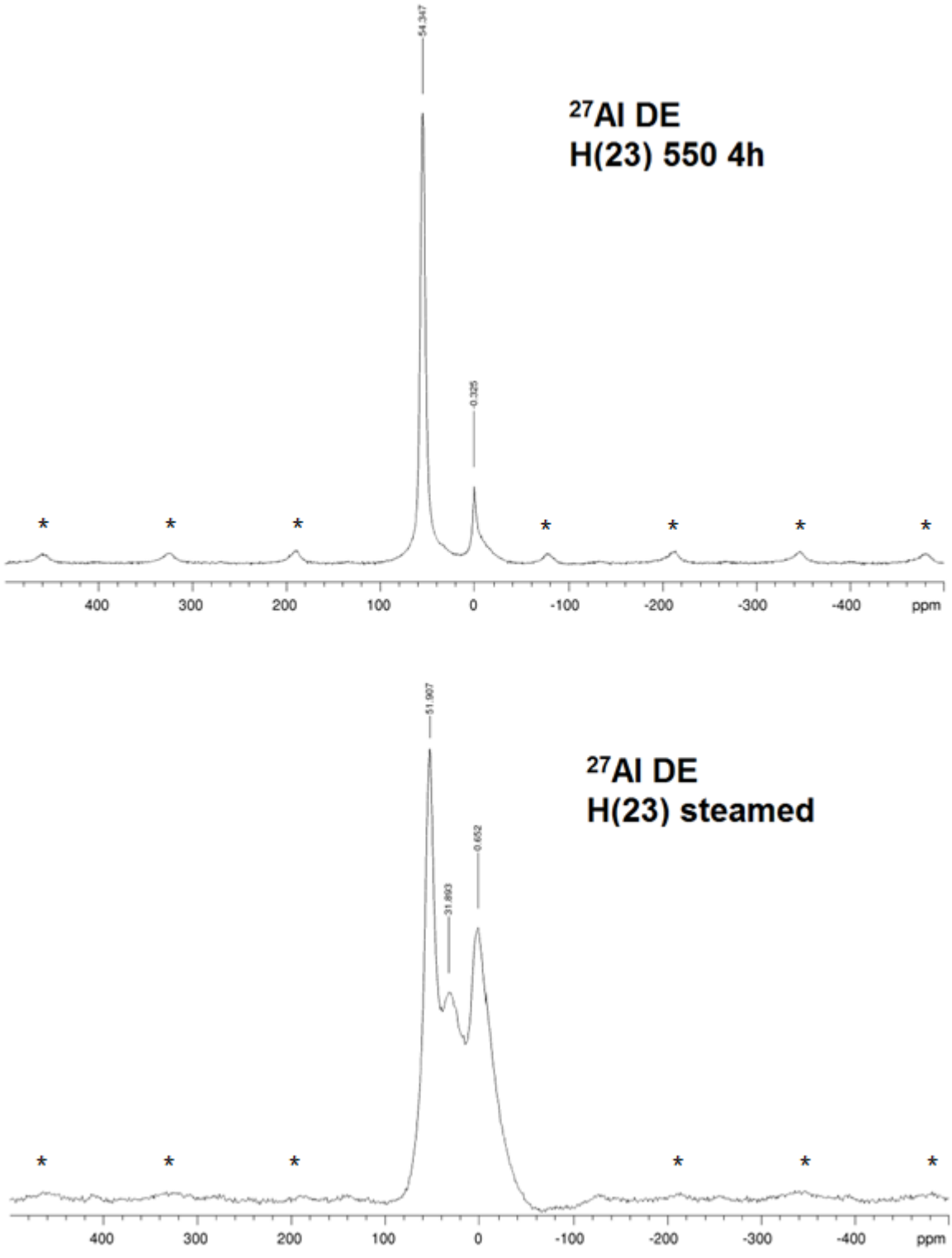

Figure 5.32a: ^{27}Al MAS-NMR spectra of H(23) – calcined and steamed. All spectra were obtained on a Varian VNMRS 400. Asterisks (*) = Spinning side bands

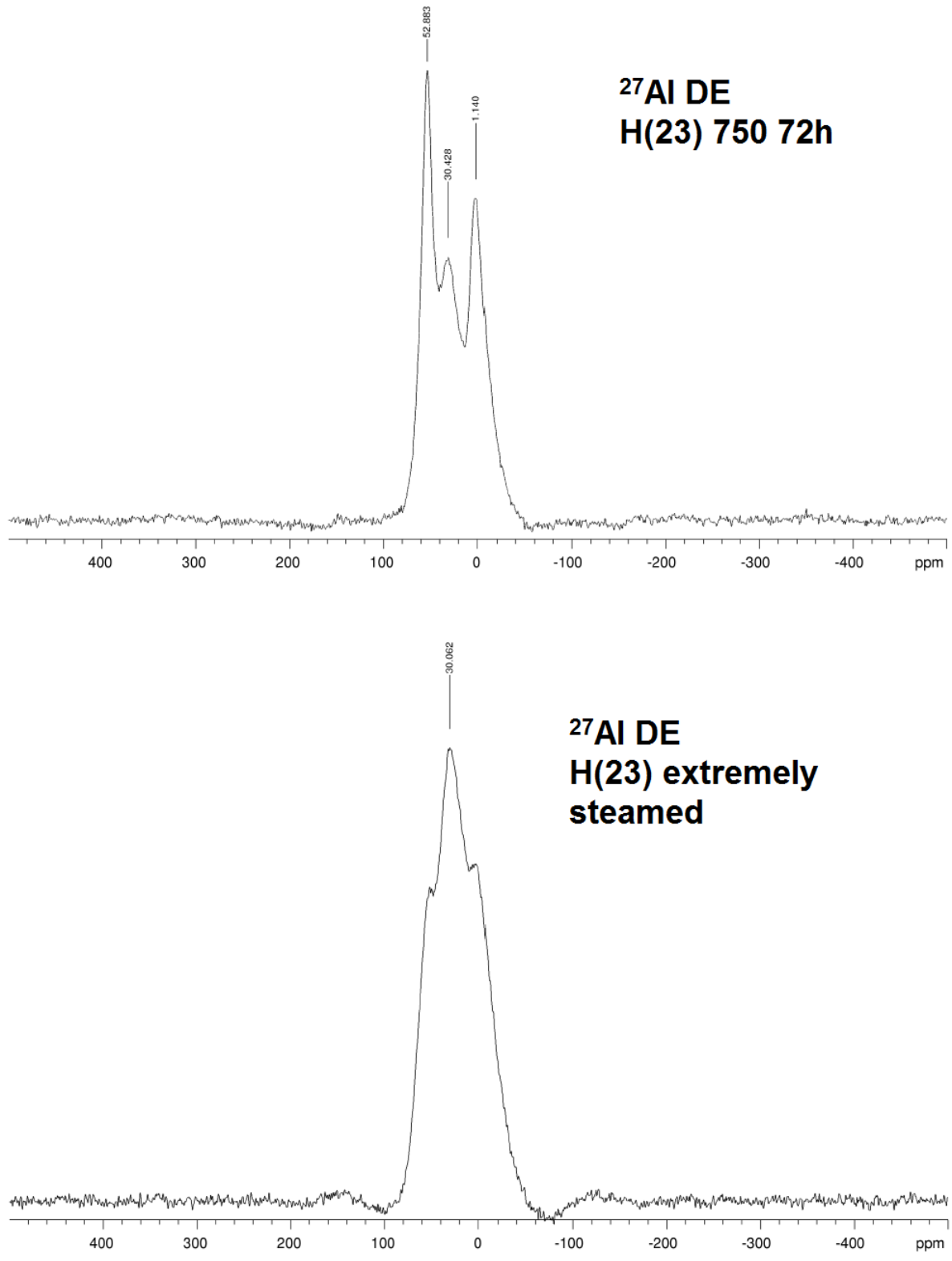

Figure 5.32b: ^{27}Al MAS-NMR spectra of H(23) – extremely treated. All spectra were obtained on a Varian VNMRS 400.

Both H(23) steamed and H(23) 750 72 h samples gave similar spectra clearly displaying tetrahedral (*ca*. 50 ppm), 5-coordinate (*ca*. 30 ppm) and octahedral (*ca*. 0 ppm) aluminium. Unexpectedly, H(23) extremely steamed contained mostly 5-coordinate aluminium.

The MFI unit cell structure of Na(23) was less resistant than H(23) to the different calcination and steaming treatments applied.

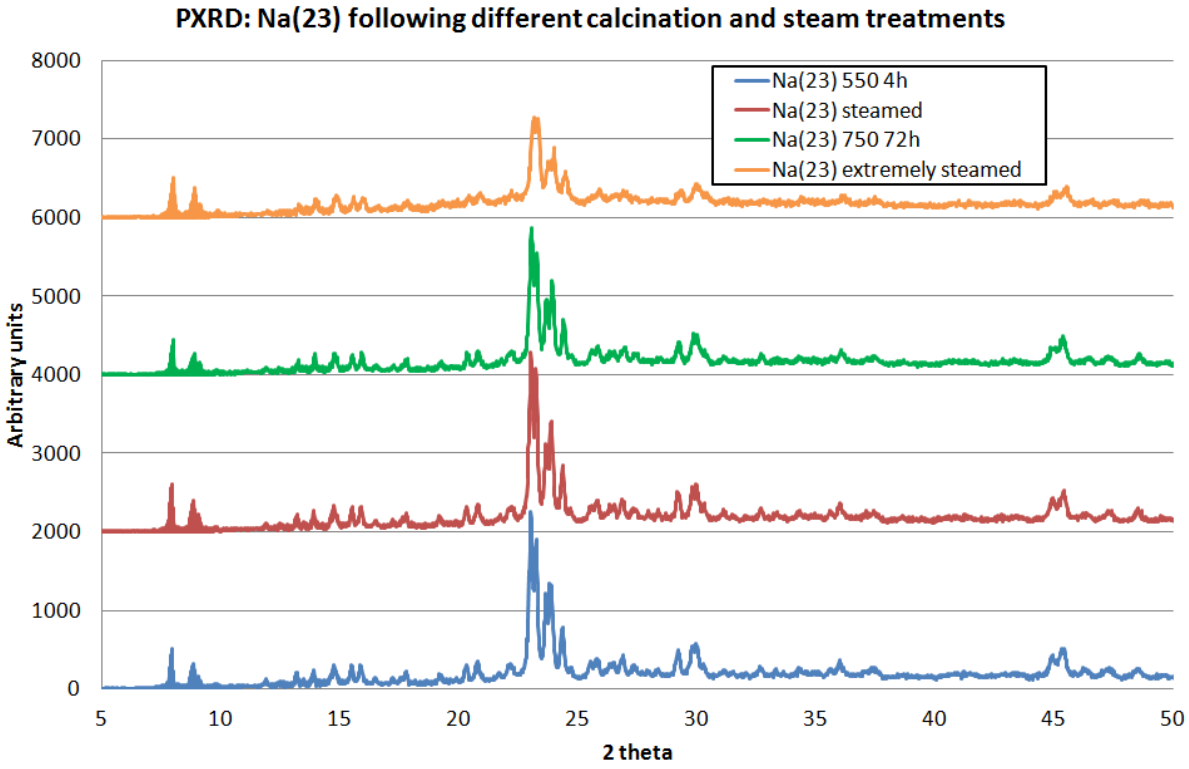

Figure 5.33: PXRD patterns of Na(23) following increasing treatment severity. Patterns were obtained as described in section 2.6.6.

With increased treatment severity, the crystallinity of Na(23) decreases in the order Na(23) 550 4 h > Na(23) steamed > Na(23) 750 72 h > Na(23) extremely steamed. These decreases in crystallinity were because of the presence of both sodium and steam, at calcination temperatures, destroying the MFI framework.

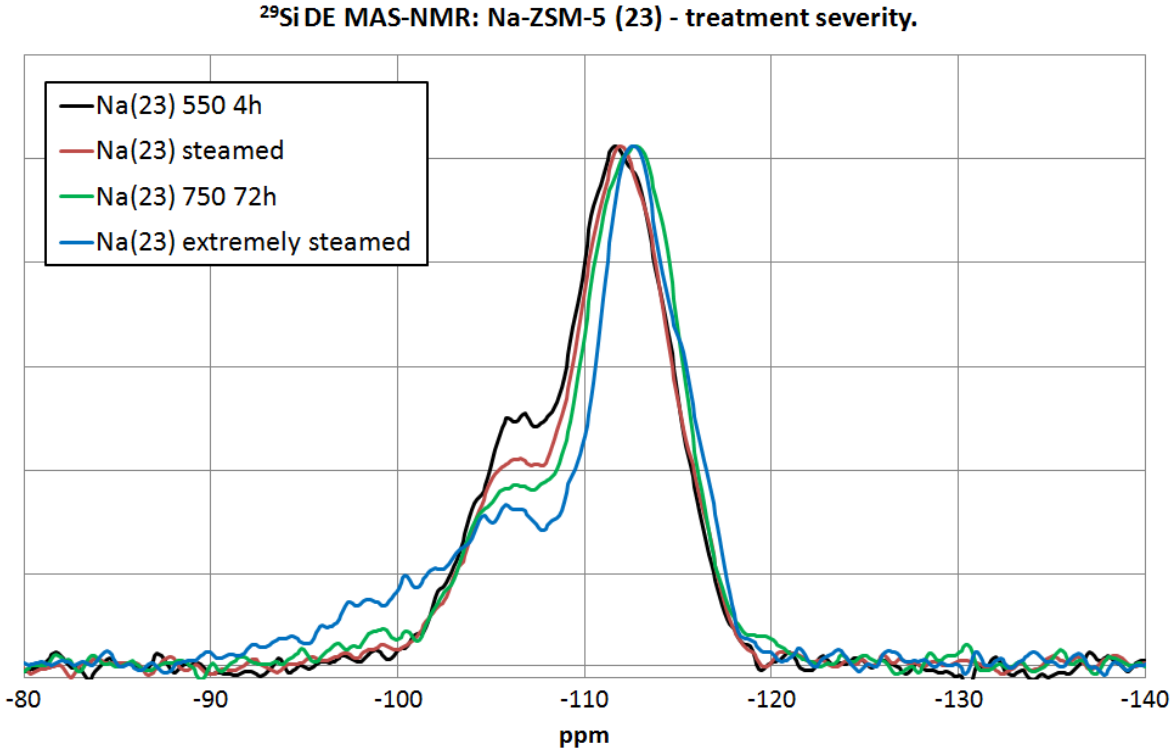

Figure 5.34: ^{29}Si MAS-NMR spectra of Na(23) following increasing treatment severity. Spectra were obtained on a Varian Unity Inova 300.

Despite the decreased crystallinity with increased treatment severity, the framework aluminium content (as indicated by the Si(1Al) peak intensity in the ^{29}Si spectra of Figs. 5.34 only slightly decreases. However, the spectra do broaden significantly indicating an increase in the heterogeneity of the ^{29}Si environments.

Fig. 5.35 shows little effect of treatment on the proportion of octahedral aluminium species. Broadening of the tetrahedral aluminium peak at *ca*. 55 ppm and an increase in 5-coordinate aluminium *ca*. 30 ppm is observed in the extremely steamed sample. This increase in the heterogeneity of aluminium speciation corresponds to the degradation of the MFI framework. Despite the damage to the crystal structure shown by PXRD, the sodium continues to retard extra-framework aluminium formation even through extreme calcination and extreme steaming treatments as shown by the strong tetrahedral aluminium signal at *ca*. 55 ppm,

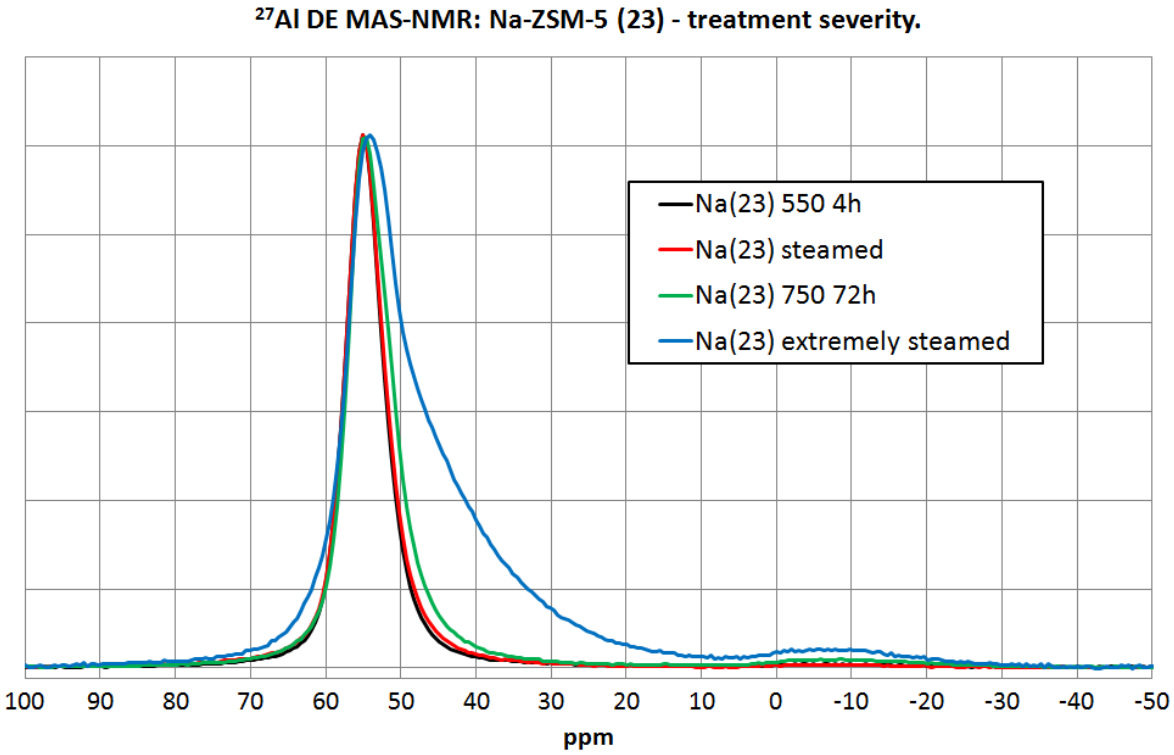

Figure 5.35: ^{27}Al MAS-NMR spectra of Na(23) following increasing treatment severity**.** Spectra were obtained on a Varian VNMRS 400.

5.5.2.2 **Textural analyses**

N_2-physisorption studies provided the following results (Table 5.8).

Material	BET SA (m^2/g)	t-plot µpore SA (m^2/g)	Pore vol. (cm^3/g)	Ads. Iso. Type
H(23) 550 4 h	318 ± 48	316 ± 48	0.20 ± 0.01	I
H(23) S	307	290	0.20	I
H(23) 750 72 h	287	272	0.20	I
H(23) XS	214	184	0.15	I
Na(23) 550 4 h	253 ± 7	246 ± 7	0.16 ± 0.01	I
Na(23) S	254	244	0.17	I
Na(23) 750 72 h	246	244	0.15	I
Na(23) XS	N. Q.	N. Q.	N. Q.	-

Table 5.8: N_2-physisorption results for both H^+-form and Na^+-form ZSM-5 (23). Measurements were obtained as described in section 2.6.5. Adsorption isotherms may be found in the appendix. Ads. Iso. = Adsorption Isotherm. S = Steamed and XS = Extremely steamed materials. N. Q. = Not Quantifiable.

For all materials presented in Table 5.8, little change occurs in the materials until subjected to extreme steaming. Following extreme steaming, H(23) retains more than half its microporosity and possessed an adsorption step at *ca*. 0.2 P/Po which is discussed in greater detail in section 6.3.2.2. Na(23) showed no measurable surface area. PXRD analysis of Na(23) extremely steamed showed a decrease in crystallinity. It is believed that the significant decrease in the extent of N_2-physisorption is due to channel blockage. Blockages arise from the extra-framework species produced by the sodium and steam-mediated zeolite framework degradation. As was shown in the ^{27}Al MAS-NMR spectra, aluminium is mostly of tetrahedral geometry.

5.5.2.3 **Catalytic testing**

Methanol conversion rates decrease, over fixed temperatures between 160-245 °C, with increasing severity of steam treatment (Fig. 5.36). Compared to H(23) 550 4 h, steam treatments decrease both the apparent activation energy and the y-intercept.

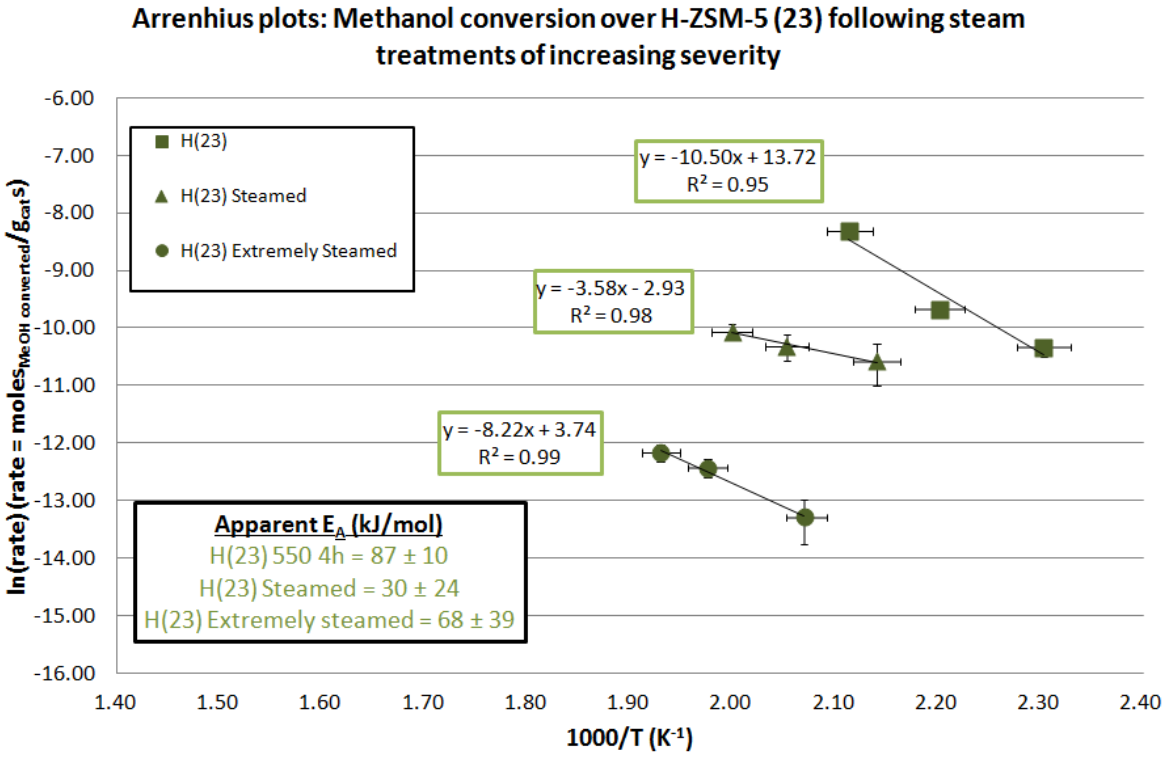

Figure 5.36: Arrenhius plots of steam treated H-ZSM-5 (23) materials. Vertical error bars represent the 1st standard deviation in the values obtained for each point.

Both H(23) 550 4 h and H(23) extremely steamed plots provide similar gradients and therefore catalytic studies indicate no significant change in the nature of the active sites. However, H(23) steamed appears subject to mass transfer limitations as both the apparent activation energy and the y-intercept values are very low. This may be because of partial channel blockage by extra-framework material of which both N_2-physisorption and PXRD analyses provide no indication. Following either steam treatments, the y-intercept decreases – indicating a decrease in the number of active sites.

Furthermore, both Na(23) steamed and Na(23) extremely steamed showed no measurable methanol conversion activity. This was attributed to acid site neutralisation and zeolite degradation as was found by Letzsch and co-worker [25].

5.6 Conclusions

Both Ludox AS and Ludox HS silica binder materials formed amorphous mesoporous matrices following calcination as shown by PXRD patterns and N_2-physisorption studies. Surface area and pore volume were slightly decreased by pre-calcination pelleting and an increase in mesopore size uniformity was observed by BJH pore size distribution analyses.

From the binder dilution studies, modification of porosity characteristics was evidenced. The BET specific surface area and micropore surface areas of the calcined catalysts were generally within the error of those predicted by the sum of constituent parts. ^{27}Al MAS-NMR indicated the proportion of extra-framework aluminium to framework aluminium decreased with increasing binder content with the 100 wt. % H(23) 550 4 h possessing the most extra-framework aluminium of binder dilution study materials. However, this was not an effect of dilution but a consequence of increasing sodium content with increasing binder content, as was shown by ^{27}Al MAS-NMR of sodium-exchanged ZSM-5 (23) possessing much lower octahedral aluminium content than the H^+-form. Furthermore, PXRD analyses showed the 12.5 wt. % zeolite in Ludox AS 550 4 h sample to possess the least extra-framework aluminium content but the highest degree of channel ‘filling’. Therefore, it was concluded that zeolite N_2-physisorption results were artificially low because of pre-existent pore ‘plugging’ extra-framework aluminium species. With increasing binder content the mode of blockage gradually switched from pore ‘plugging’ by extra-framework aluminium species to pore filling by binder species. As such, transfer of chemical species from the binder to the zeolite was believed to be the cause of such surface area observations.

Silica-bound catalysts are less active than the sum of constituent parts. Results are consistent with sodium migrating from the binder to the zeolite, neutralising zeolite acid sites as well as pore blockage by non-framework silica species.

No clear evidence of extra-framework aluminium trapping by the silica matrix was observed by MAS-NMR measurements.

Sodium-exchange studies showed no structural changes were observed following sodium-exchange. However, with increasing thermal and hydrothermal treatment severity the protonated and sodium-form zeolites showed obvious differences. Increased sodium content decreased MFI crystallinity, retarded extra-framework aluminium formation; decreased surface areas and pore volumes *via* textural analyses and decreased methanol conversion rates.

5.7 References

[1] J. S. J. Hargreaves and A. L. Munnoch, Catal. Sci. Technol., 3 (2013) 1165-1171.

[2] S. Mitchell, N-L. Michels and J. Perez-Ramirez, Chem. Soc. Rev., 42 (2013) 6094-6112.

[3] X. Wu, Ph.D. Thesis, Texas A. M. University (2003).

[4] A. Corma, M. Grande, V. Fornes, S. Cartlidge and M. P. Shatlock, Appl. Catal., 66 (1990) 45–57.

[5] A. Corma, M. Grande, V. Fornes and S. Cartlidge, Appl. Catal., 66 (1990) 247–255.

[6] P. Gélin and C. Gueguen, Appl. Catal., 38 (1988) 225-233.

[7] P. Gélin and T. Des Couriéres, Appl. Catal., 72 (1991) 179-192.

[8] Z. M. M. Noronha, J. L. F. Monteiro and P. Gélin, Microp. Mesop. Mater., 23 (1998) 331–344.

[9] M. Xu, X. Liu and R. J. Madon, J. Catal., 207 (2002) 237-246.

[10] J. C. Groen, J. A. Moulijn and J. Perez-Ramirez, J. Mater. Chem., 16 (2006) 2121–2131.

[11] S. J. Gregg and K. S. W. Sing, Adsorption Surface Area and Porosity, 2nd Ed., (1982) p155. ISBN: 0123009561.

[12] K. S. W. Sing, D. H. Everett, R. A. W. Haul, L. Moscou, R. A. Pieotti, J. Rouquerol and T. Siemieniewska, Pure & Appl. Chem., 57 (1985) 603-619.

[13] J. Benbow and J. Bridgwater, Paste Flow and Extrusion, Oxford Series on Advanced Manufacturing, Clarendon Press, Oxford, (1993) ISBN: 9780198563389.

[14] M. A. Uguina, J. L. Sotelo and D. P. Serrano, Appl. Catal., 76 (1991) 183-192.

[15] J. Freiding, F-C. Patcas and B. Kraushaar-Czarnetzki, Appl. Catal A: Gen. 328 (2007) 210-218.

[16] D. S. Shihabi, W. E. Garwood, P. Chu, J. N. Miale, R. M. Lago, C. T.-W. Chu and C. D. Chang, J. Catal., 93 (1985) 471–474.

[17] J.S.J. Hargreaves, Cryst. Rev., 11, 1, 2005, 21-34.

[18] A. E Newkirk and I. Aliferis, Anal. Chem., 30, 5 (1958) 982-984.

[19] K. H. Stern, J. Phys. Chem. Ref. Data., 1, 3 (1972) 747-771.

[20] H. S. Cerqueira, G. Caeiro, L. Costa and F. Ramoa Ribeiro, J. Mol. Catal. A: Chem. 292 (2008) 1-13.

[21] K. Campbell, D. M. Bibby, J. M. Coddington, R. F. Howe and R. H. Meinhold, J. Catal., 161 (1996) 338 -349

[22] L. B. Alemany and G. W. Kirker, J. Am. Chem. Soc., 108 (1986) 6158.

[23] S. E. Ashbrook, K. J. D. MacKenzie and S. Wimperis, Solid State Nuclear Magnetic Resonance, 20 (2001) 87-99.

[24] L. H. Ong, M. Domok, R. Olindo, A. C. van Veen and J. A. Lercher, Microp. Mesop. Mater., 164 (2012) 9-20.

[25] W. S. Letzsch and D. N. Wallace, Oil & Gas Journal, (Nov 29, 1982) 58-68.

6 Alumina-bound ZSM-5

Having addressed the application and effects of silica binders in chapter 5; the application and effects of alumina binders will be considered in this chapter.

Despite the general lack of studies in this area [1], the effect of alumina binding methods have been examined previously by Wu [2] with respect to catalyst texture and catalytic activity. Boehmite-binding of ZSM-5, through dry-powder-mixing and wet-powder-mixing methods, resulted in reduced micropore surface area. This was attributed to pore blockage. Additionally, similar micropore surface area values were obtained for both dry-powder and wet-powder mix samples indicating similar degrees of micropore blockage. FTIR, pyridine-adsorption FTIR and NH_3-TPD measurements indicated boehmite-binding (*via* both dry and wet methods) to lower both total and Brőnsted acidities of H-ZSM-5. This was interpreted as evidence of alkali metal exchange from boehmite to the zeolite component occurring as readily through both solution (wet-mixing then calcination) and solid-state (powder mixing then calcination) exchange mechanisms. Butane transformation (cracking and disproportionation) allowed a comparison of acid site densities between dry- and wet-bound boehmite/ZSM-5 catalysts. The wet-bound material showed a greater molar ratio of cracking/disproportionation products. Butane disproportionation requires two adjacent active sites [3], therefore the wet-bound catalyst possessed a lower acid site density than in the dry-bound equivalent.

Pore blockage and alkali metal poisoning are not the only documented effects of binders on zeolite catalysts. Aluminium insertion into high-silica zeolites was reported by Shihabi and co-workers. [4]. Methanol conversion for hydrocarbon production was shown to increase when ZSM-5 was applied in the form of alumina extrudates. Furthermore, the use of a propylene oligomerisation probe reaction demonstrated the significance of the binding method upon the rate of propylene conversion, with wet extrusion increasing conversion. Steaming treatments of alumina-bound ZSM-5 were also found to increase the rate constant for n-hexane cracking relative to that of a standard amorphous silica-alumina. As well as dry and wet binding mixtures, boehmite may also be dispersed into a sol using appropriate quantities of acid (peptising) [5]. This peptising step (which takes place prior to

calcination and decreases the boehmite particle size) is believed to increase binder-zeolite interaction and improve rheological properties with the aim of ultimately enhancing both the catalytic activity and stability of the bound materials [6,7].

In this chapter on alumina-bound ZSM-5 catalysts, the effects of binding method, aluminium impregnation and thermal/hydrothermal treatment will be described.

6.1 Alumina binder materials

6.1.1 Structural analyses

Pural SCF 55 (boehmite) was used in the following binder studies. As shown in the alumina phase diagram (Fig. 1.7), boehmite was expected to transform into γ-Al_2O_3 following calcination at 550 °C for 4 h [Fig. 6.1].

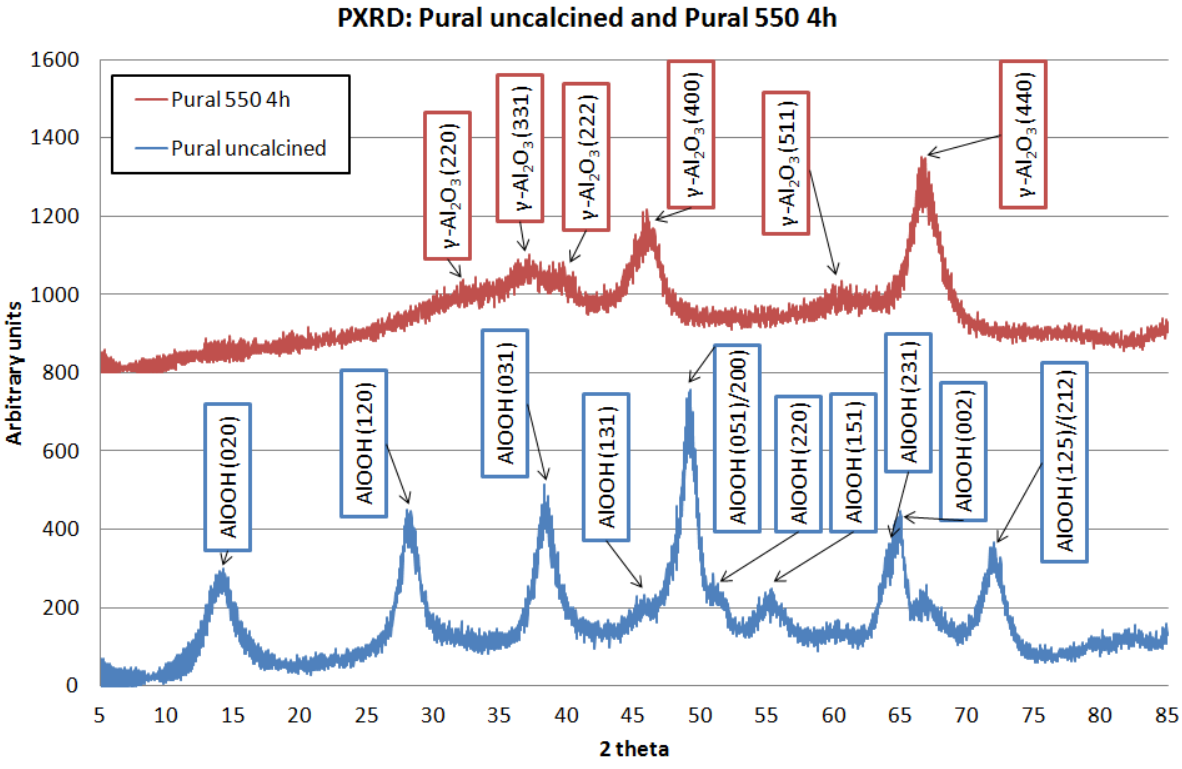

Figure 6.1: PXRD patterns of uncalcined and calcined Pural. Measurements were obtained as described in section 2.6.6.

Boehmite reflection assignments and γ-Al_2O_3 reflection assignments were adapted from refs. [8,9] respectively, consistent with γ-Al_2O_3 formation. ^{27}Al MAS-NMR in Fig. 6.2 shows the change in aluminium environments following calcination.

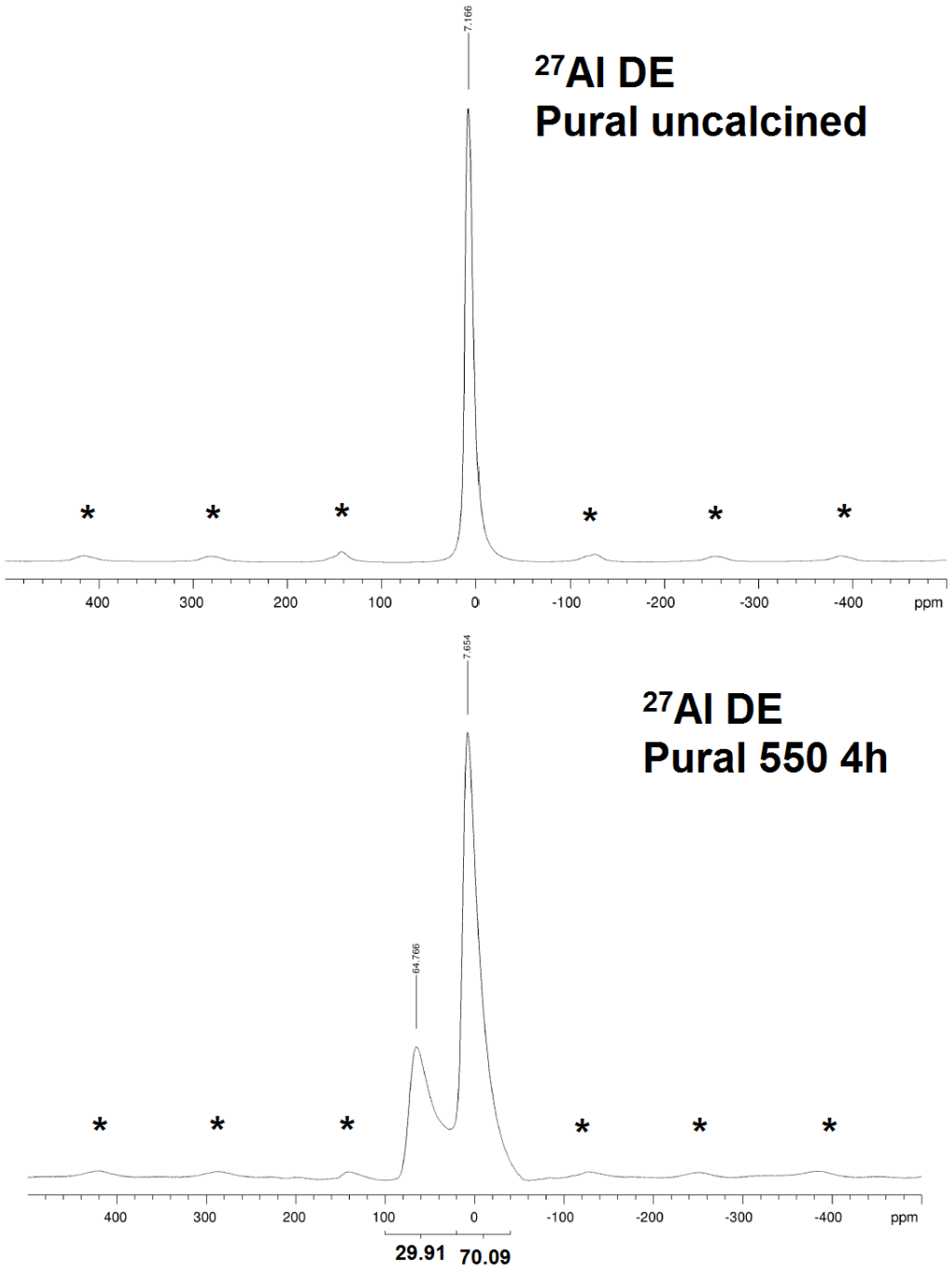

Figure 6.2: ^{27}Al MAS-NMR spectra of uncalcined and calcined Pural. All spectra were obtained on a Varian VNMRS 400. Asterisks (*) = Spinning side bands.

The 100 % octahedral aluminium of boehmite was converted by calcination to γ-Al_2O_3 with an aluminium distribution of *ca*. 30 % tetrahedral (*ca*. 65 ppm) : 70 % octahedral (*ca*. 8 ppm). This ratio has been previously reported for γ-Al_2O_3 under similar conditions [10]. Notably, the observed 30 % : 70 % ratio is consistent with the defective spinel structure [11].

A large weight loss was observed in Fig. 6.3 between approx. 150-500 °C and was consistent with the dehydration of boehmite to yield alumina [12].

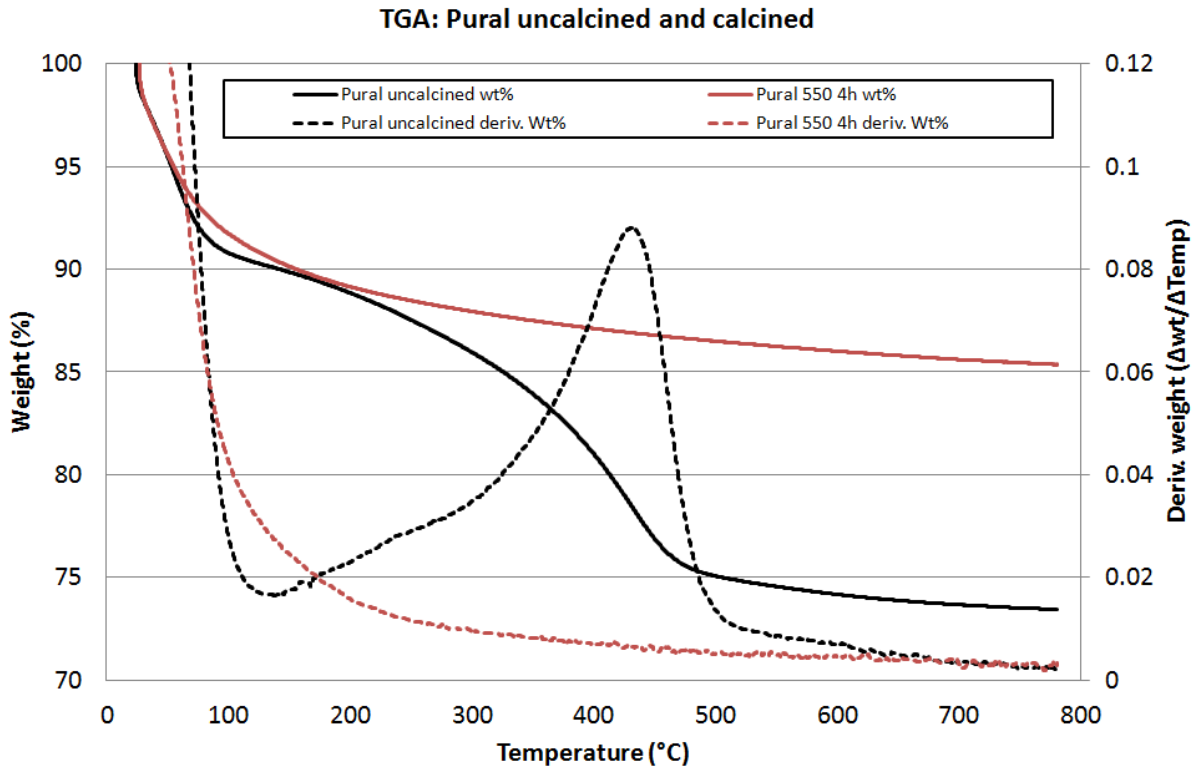

Figure 6.3: TGA measurement of uncalcined Pural. Measurements were obtained as described in experimental section 2.6.8.

6.1.2 **Textural analyses**

As previously noted for silica binders (section 5.2.3), binder materials are commonly associated with providing additional porosity.

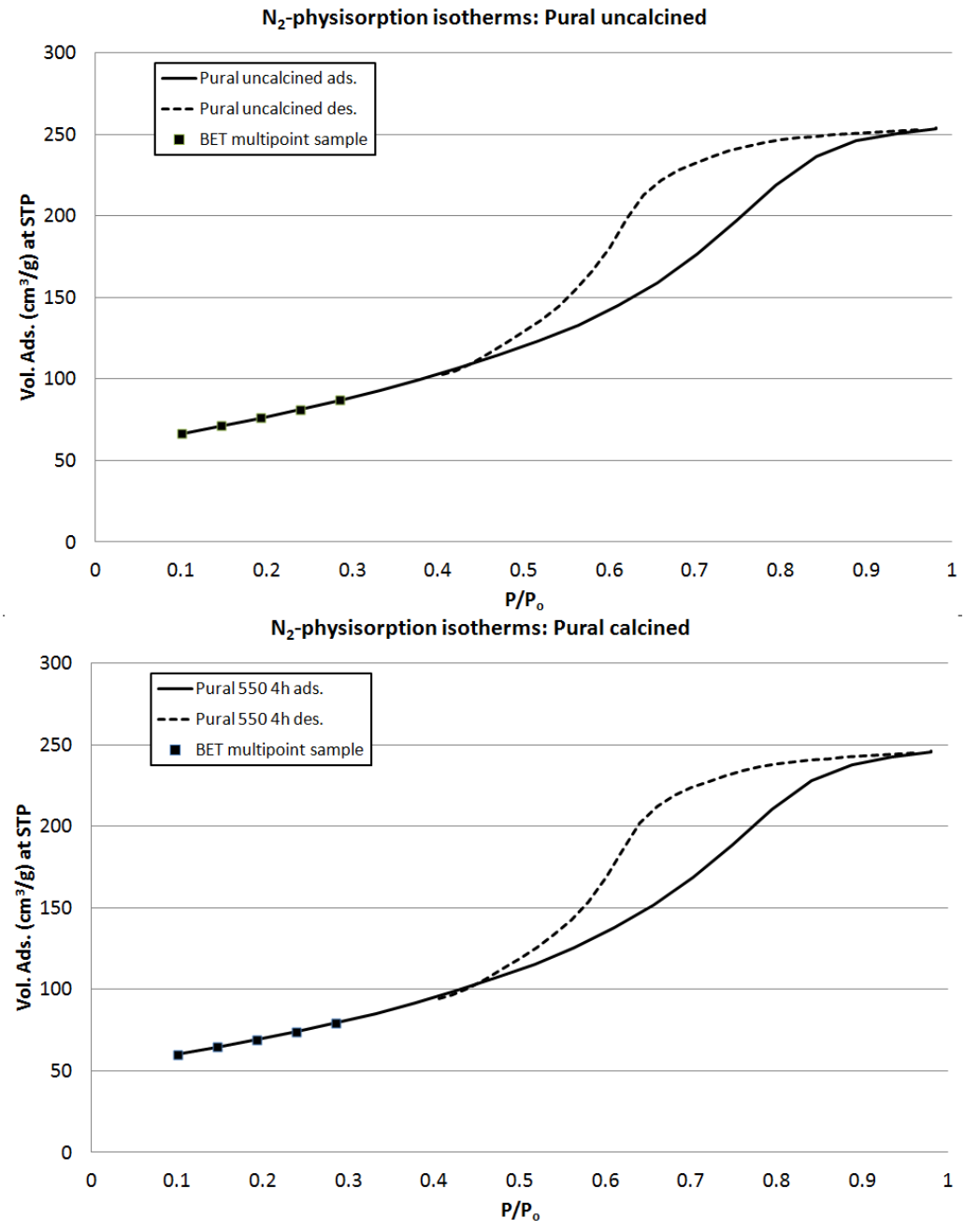

Figure 6.4: N_2-physisorption isotherms of Pural. All measurements were obtained as described in section 2.6.5.

Fig. 6.4 clearly shows type IV adsorption isotherms for both Pural uncalcined and Pural 550 4 h.

BET specific surface areas of 275 m^2/g and 241 m^2/g were obtained for Pural uncalcined and Pural 550 4 h and both had total pore volumes of 0.39 cm^3/g. Micropore surface areas were 19 m^2/g and not quantifiable, respectively.

The porosity and surface area of Pural 550 4 h was mostly unaffected by pressing prior to calcination (Fig. 6.5 and Fig. 6.6).

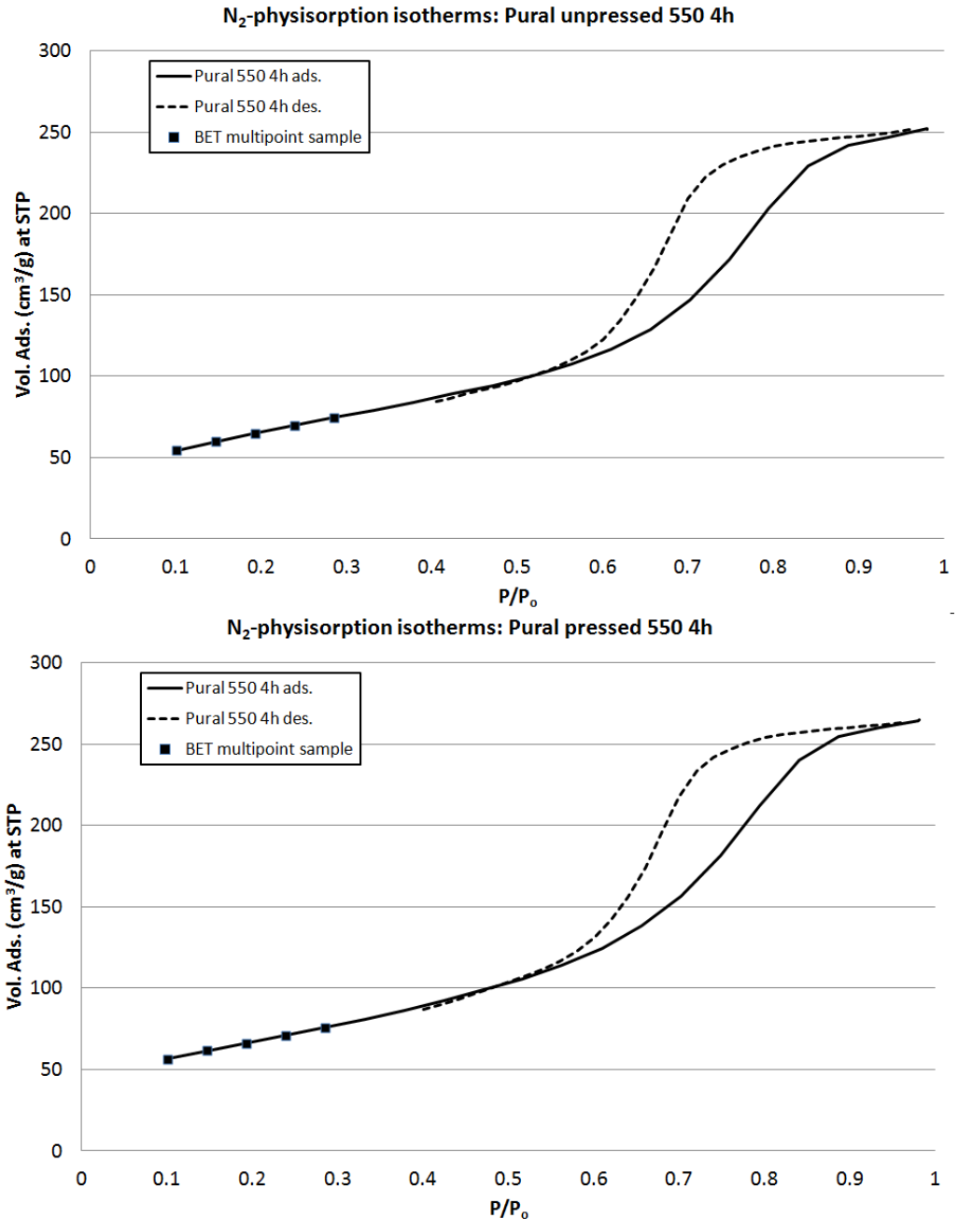

Figure 6.5: N_2-physisorption isotherms of Pural 550 4 h - pressing. Adsorption isotherms were obtained as described in section 2.6.5.

A BET specific surface area of 243 m^2/g was obtained for Pural 550 4 h (pressed) and a total pore volume of 0.41 cm^3/g. The micropore surface area was not quantifiable.

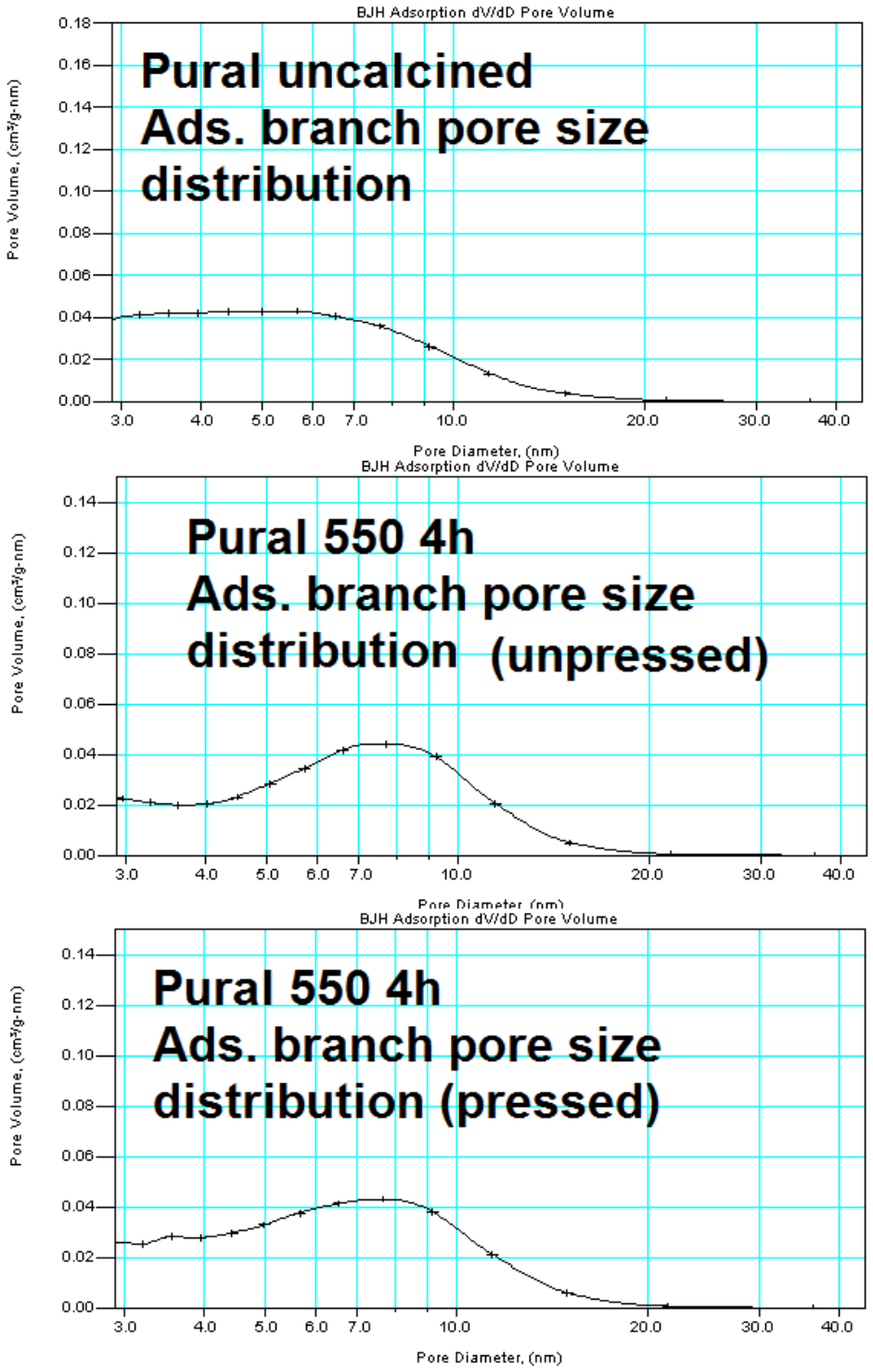

Figure 6.6: BJH pore size distributions of Pural samples. Measurements were of obtained as described in section 2.6.5.

Comparing unpressed and pressed Pural 550 4 h materials, a small increase in pore volume was observed following pressing. This may be attributed to an increase in adsorption in the 3-6 nm pore diameter range (Fig. 6.6).

6.1.3 Catalytic testing

Pural 550 4 h was shown to be catalytically active for methanol dehydration in Chapter 3 and Pural 550 4 h Arrenhius plots will be shown below.

6.2 Binding methods

A brief examination into the effects of binding method on calcined Pural-bound NH_4(1500) were undertaken. Three different binding methods were examined; dry-mull mixing, wet-mull mixing and peptised mixing and the structural, textural and catalytic results of which will be discussed below.

6.2.1 Sample preparation

Dry-mull, wet-mull and peptised mixing methods were described in section 2.2. As shown in Table 6.1 alumina-bound materials are denoted as PSD = Pural/Silicalite Dry-mulled; PSW = Pural/Silicalite Wet-mulled and PepPSW = Peptised Pural/Silicalite Wet-mulled.

Material	Description
PSD	Pural-bound Silicalite – Dry-mull mixed.
PSW	Pural-bound Silicalite – Wet-mull mixed
PepPSW	Pural-bound silicalite – Peptised mixture

Table 6.1: Alumina-bound zeolite nomenclature. Where silicalite refers to H(1500) 550 4 h. All samples were prepared such that 56:44 dry wt. % of zeolite and binder are present in the activated catalysts.

6.2.2 **Structural analyses**

All alumina-bound silicalite catalysts in Fig. 6.7 contain γ-Al_2O_3 and MFI phases in *ca*. 56:44 wt. % mixtures.

PXRD measurements did not show the presence of any additional phases (Fig. 6.7) and the zeolite was of orthorhombic symmetry. Additionally, the binding method did not appear to seriously affect channel filling according to the PXRD patterns [13] (Fig. 6.8).

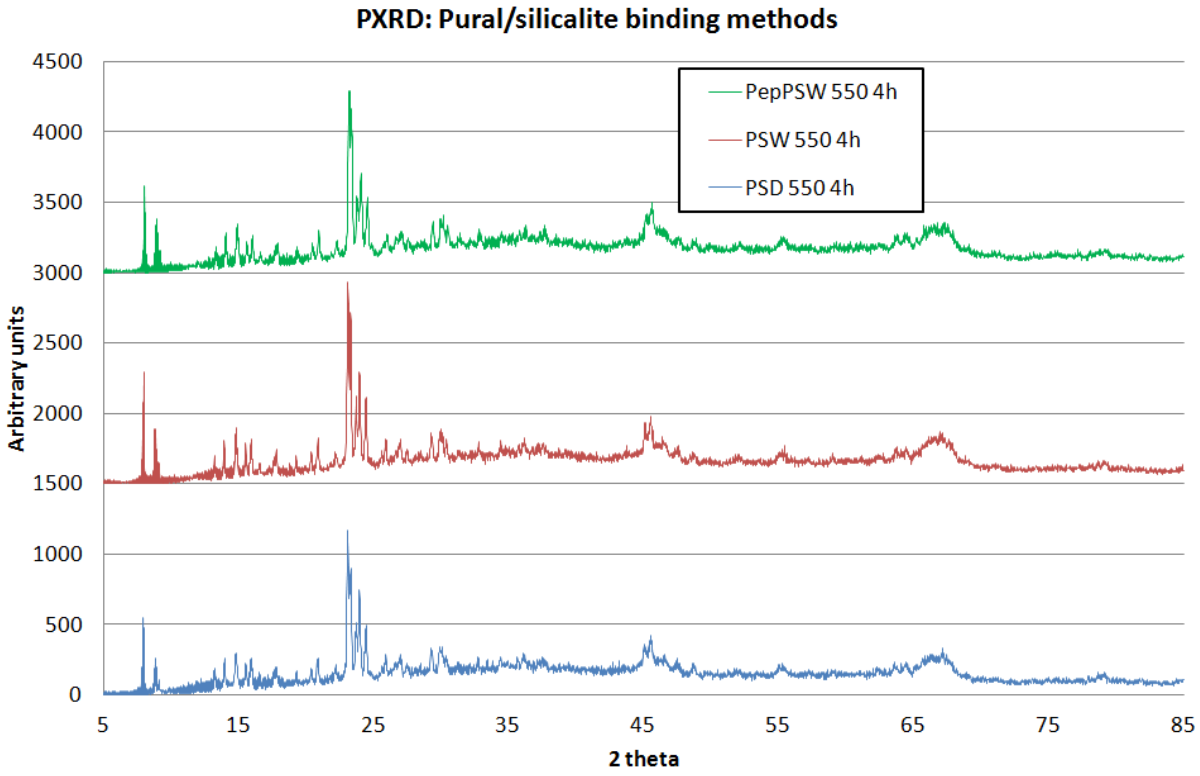

Figure 6.7: PXRD patterns of binding method studies. Measurements were obtained as described in section 2.6.6.

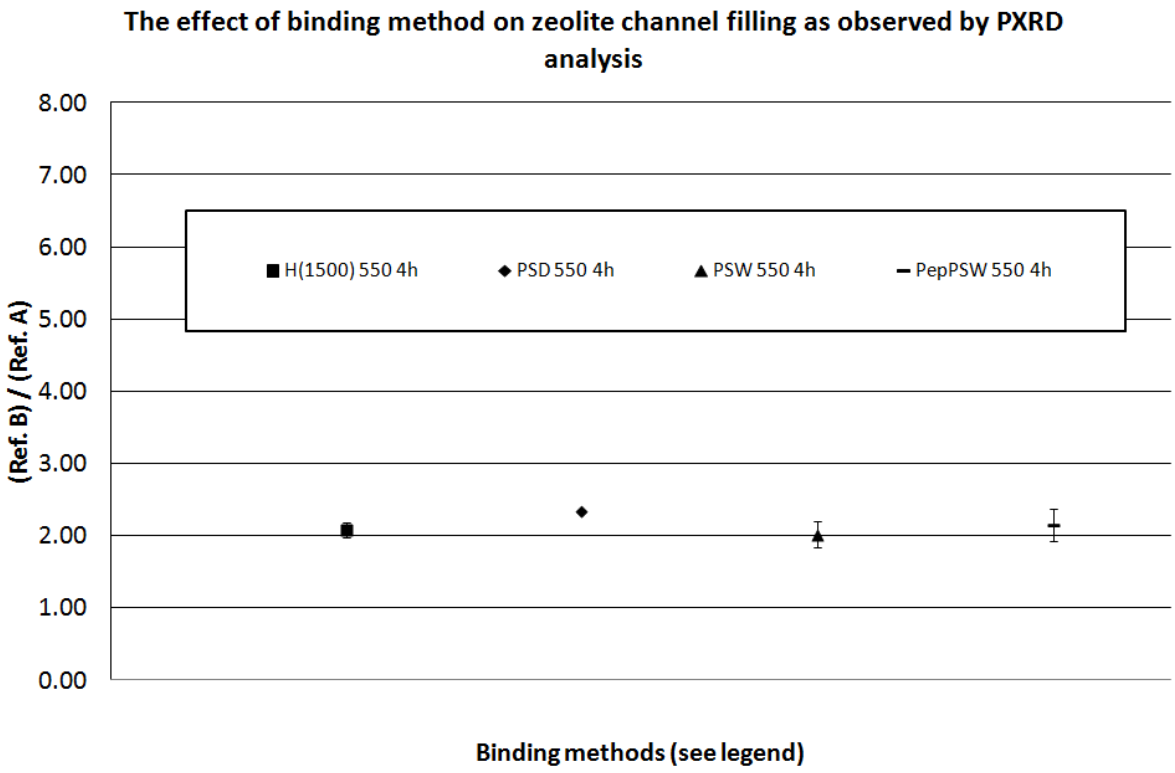

Figure 6.8: PXRD – Zeolite channel filling for binding method studies. 'Ref. A' = Σ[(101), (011), (200), (020) and (111) reflection intensities] and 'Ref. B' = Σ[(501), (051), (151), (303) and (133) reflection intensities]. Error bars correspond to ± the furthest outlier of repeat measurements.

With respect to MAS-NMR spectra (Fig. 6.9), the ^{27}Al spectra of each Pural-bound catalyst were very similar.

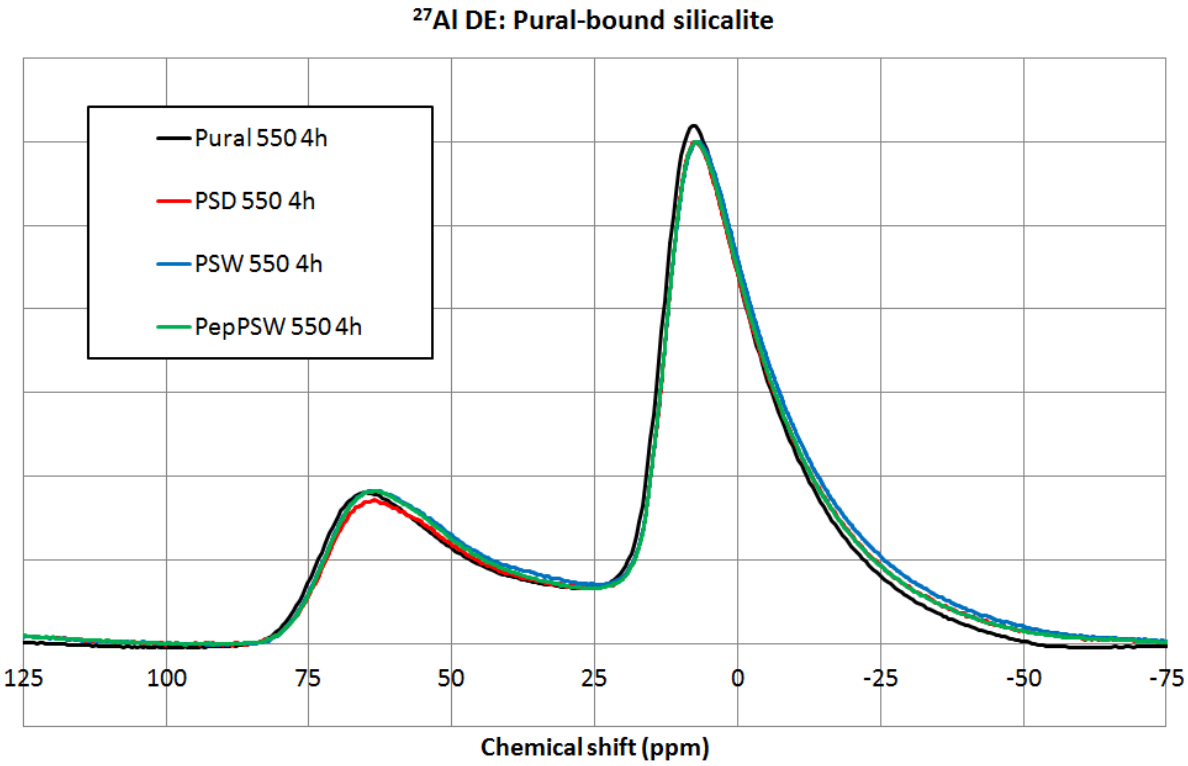

Figure 6.9: ^{27}Al MAS-NMR for binding method studies. All spectra were obtained on a Varian VNRS 400.

All Pural-bound systems may perhaps possess slightly greater tetrahedral / octahedral peak intensities than Pural 550 4 h but the breadth of signals makes quantification problematic.

Close inspection of the ^{29}Si MAS-NMR spectra in Fig. 6.10 shows an increased signal at *ca*. -107 ppm for all Pural-bound materials. This is indicative of an increase in the proportion of Si(1Al) (relative to Si(0Al)) and consistent with aluminium insertion into the zeolite framework. The signal at *ca*. -103 ppm = silanol groups and *ca*. -112 ppm = Si(0Al) environments.

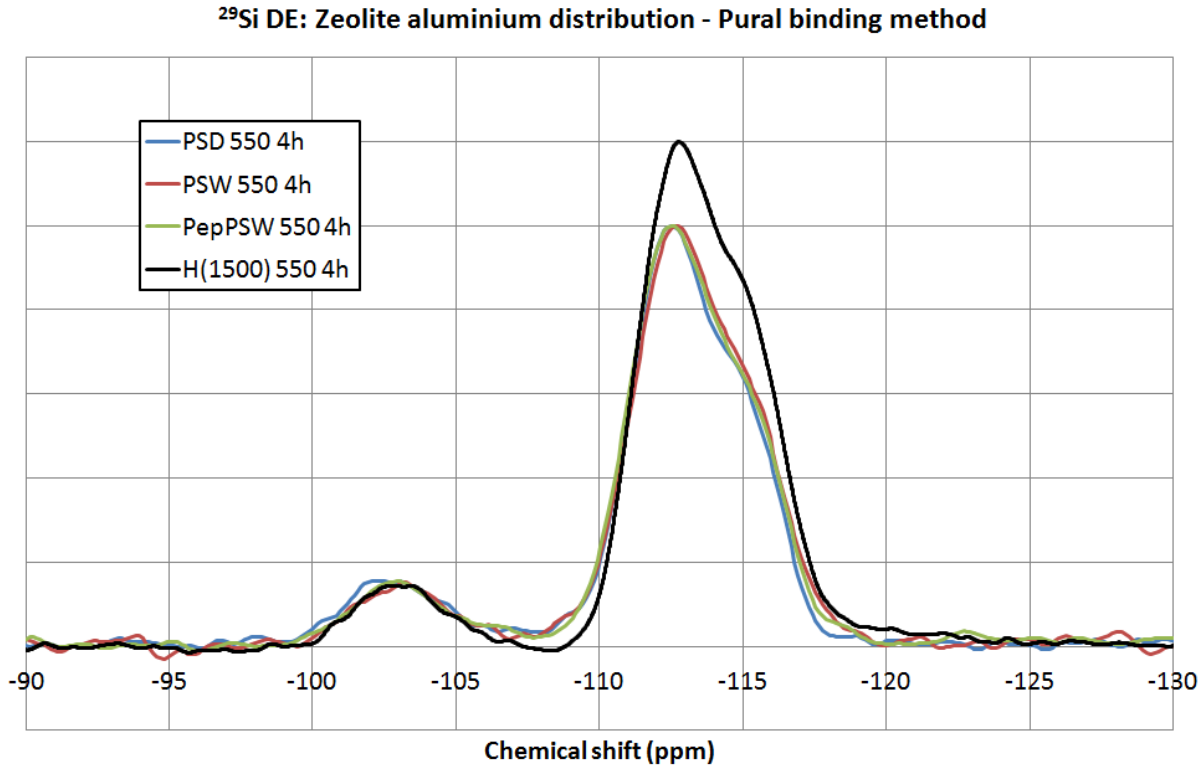

Figure 6.10: ^{29}Si MAS-NMR spectra for binding method studies. H(1500) 550 4 h ^{29}Si MAS-NMR spectra were obtained on a Varian VNMRS 400. Pural-bound ^{29}Si MAS-NMR spectra were obtained on a Varian Unity Inova 300.

6.2.3 **Textural analyses**

As previously mentioned in section 5.2.3 the binder may contribute to pore blockage.

Material	Measured BET SA (m^2/g)	t-plot µpore SA (m^2/g)	Total pore vol. (cm^3/g)	Ads. Iso. Type
H(1500) 550 4 h	326 ± 10	324 ± 10	0.19 ± 0.01	I
Pural 550 4 h	241 ± 2	N. Q.	0.39 ± 0.02	IV
Theoretical 56/44 wt. % mix	289 ± 6	181 ± 6	0.28 ± 0.01	I/IV
PSD 550 4 h	260	127	0.27	I/IV
PSW 550 4 h	276 ± 8	132 ± 5	0.32 ± 0.01	I/IV
PepPSW 550 4 h	265 ± 9	119 ± 6	0.26 ± 0.00	I/IV

Table 6.2: N_2-phyisorption results for binding method studies. Ads. Iso. = Adsorption Isotherm. Adsorption isotherms can be found in the appendix. Theoretical values are the weighted mean of H(1500) 550 4 h and Pural 550 4 h components. Errors correspond to the values obtained from the furthest outlier of repeated measurements.

The BET specific surface areas and pore volumes are generally slightly lower than expected for the bound catalysts. However, the micropore surface area was approx. 30 % lower than expected – suggesting zeolite pore channel inaccessibility to exist in these materials. A similar reduction in micropore surface area has been reported with a 30 wt. % alumina-bound ZSM-5 catalyst [1]. Furthermore, all bound materials possess similar surface areas.

BJH pore size distribution plots show mesopore sizes to be similar for PSD 550 4 h and PSW 550 4 h but noticeably smaller for PepPSW 550 4 h.

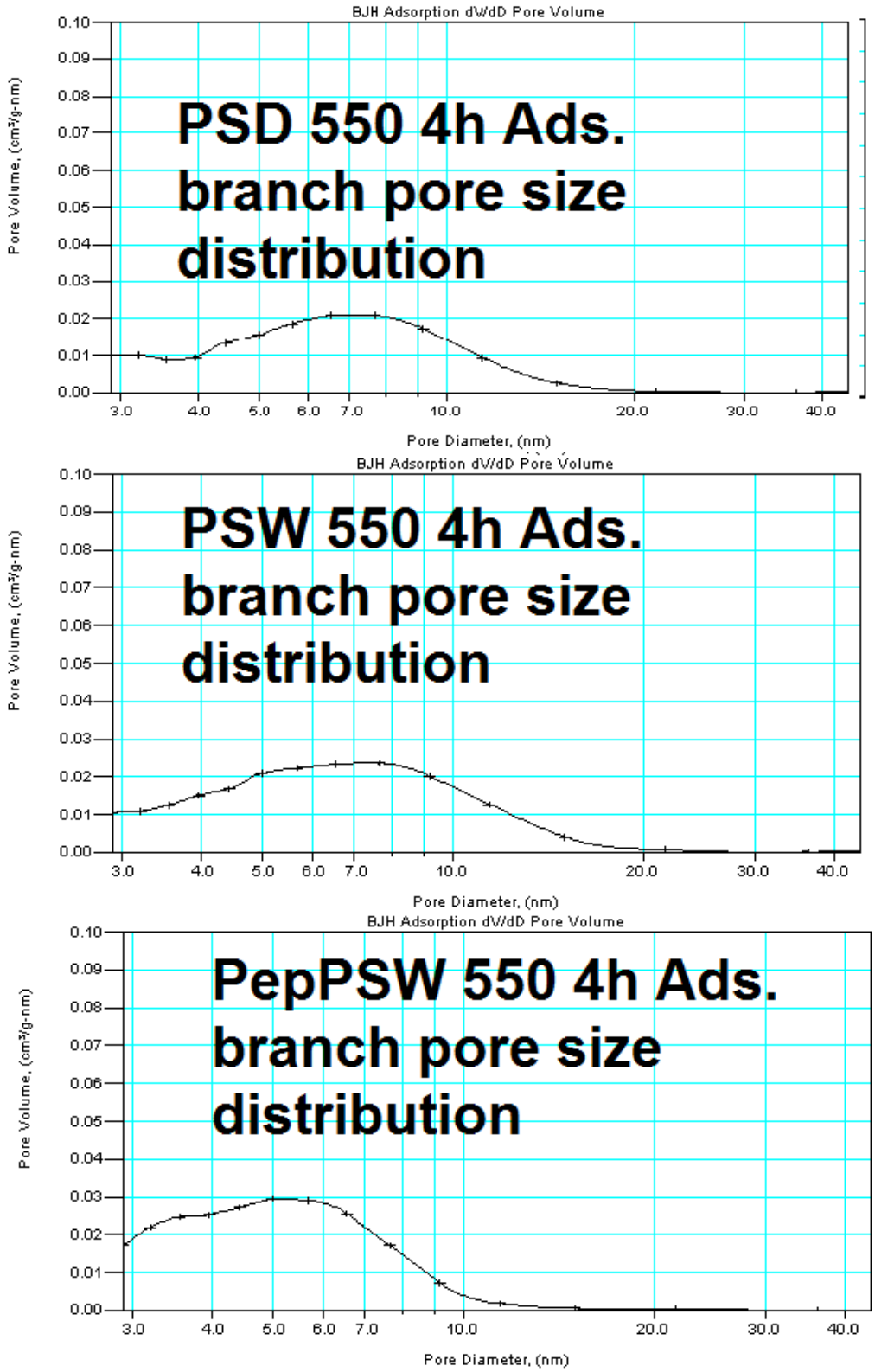

Figure 6.11: BJH pore size distributions of binding method studies. Measurements were obtained as described in section 2.6.5.

The decrease in micropore surface area and mesopore diameters of PepPSW 550 4 h suggest the peptising treatment to affect the interaction between binder and zeolite components. This may be attributed to the peptising process whereby boehmite is dispersed and the finer particles produced allow for increased interparticle surface contact. SEM-imaging was undertaken to examine this suggested increase in binder-zeolite particle interaction further.

SEM images (Fig. 6.12, Fig. 6.13 and Fig. 6.14) show the effect of binding method on the distribution of binder and zeolite particles over the external surface of catalyst bodies. A silicalite SEM image may be found in section 4.3.1.

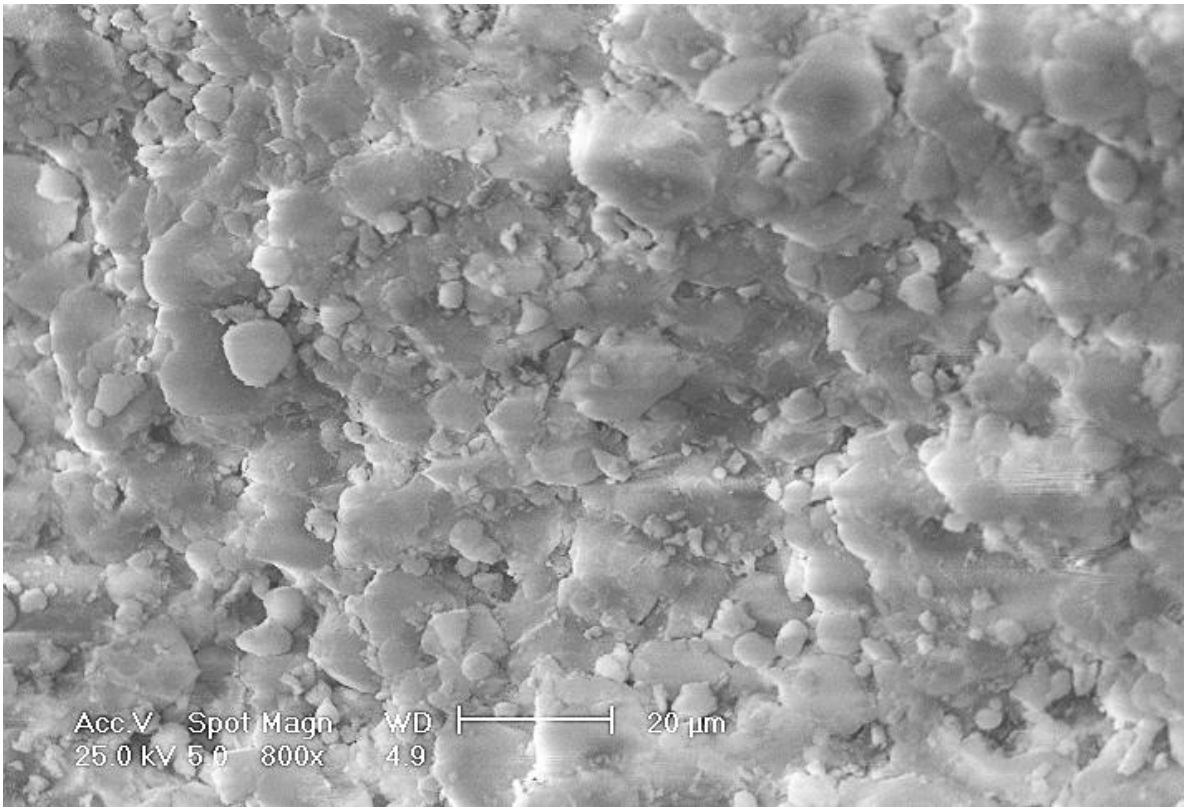

Figure 6.12: SEM image of Pural 550 4 h. Image obtained according to the method described in section 2.6.4.

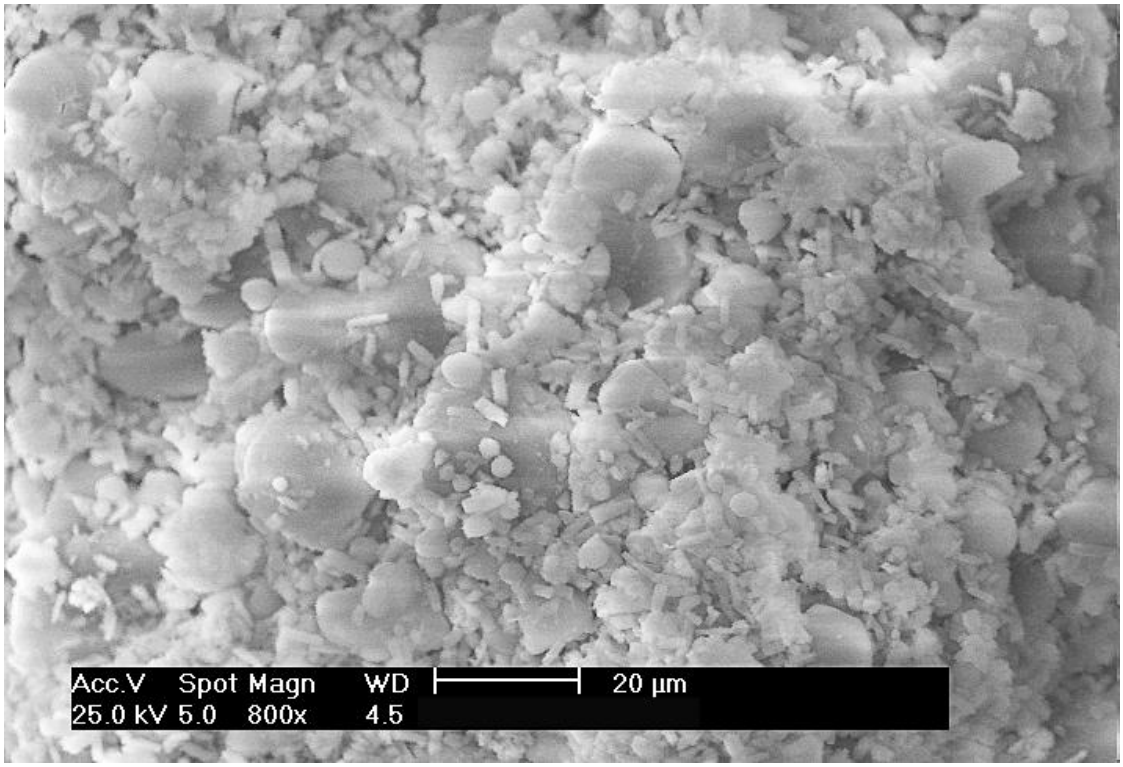

Figure 6.13: SEM image of wet-mull mixed H(1500)/Pural 550 4 h. Image obtained according to the method described in section 2.6.4.

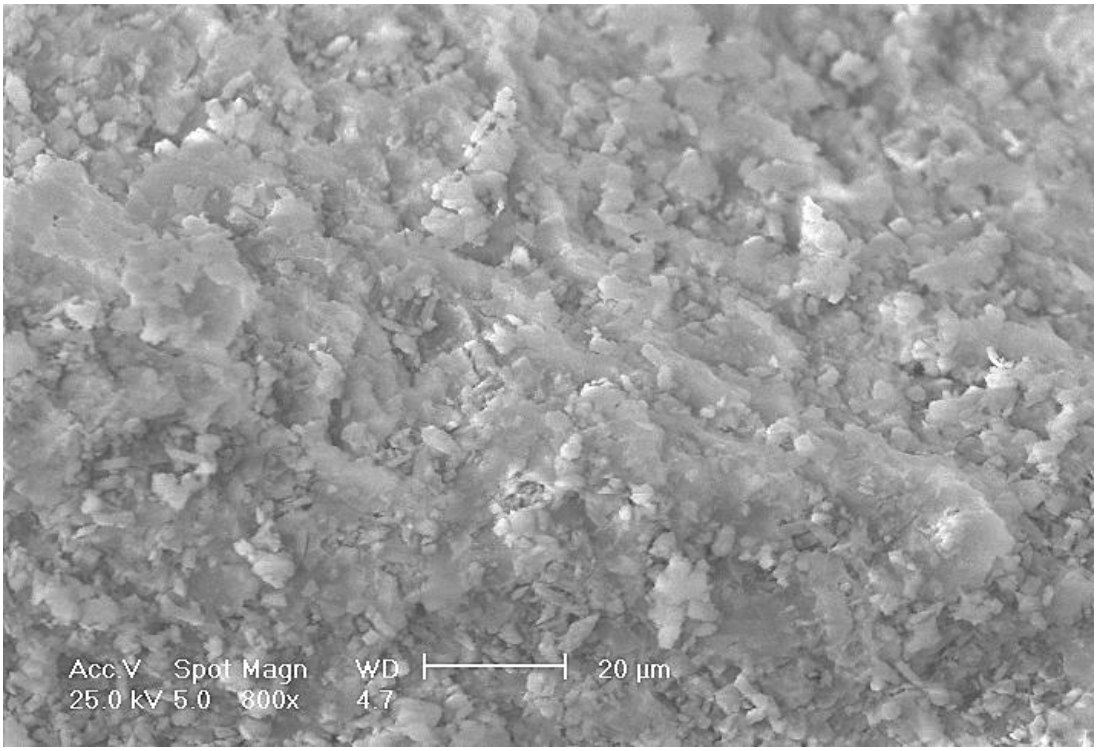

Figure 6.14: SEM image of peptised H(1500)/Pural 550 4 h composite. Image obtained according to the method described in section 2.6.4.

The external surface of Pural 550 4 h was comprised of ≤ 20 μm plate-like particles. Silicalite particles were clearly observed in Fig. 6.13 as the *ca*. 5 μm rod-like particles on the plate-like Pural particles. Dry-bound and wet-bound Pural/silicalite mixtures were indistinguishable. However, in the peptised mixture the silicalite crystals were embedded into the Pural matrix. This embedding, if it were to occur throughout the catalyst body, would be consistent with increased binder-zeolite interaction and the resulting decrease in mesopore size distribution.

6.2.4 **Catalytic testing**

The results in Fig. 6.15 showed all binding methods to result in similar methanol conversion rates between 217-256 °C. All alumina-bound materials showed similar methanol conversion rates to Pural 550 4 h.

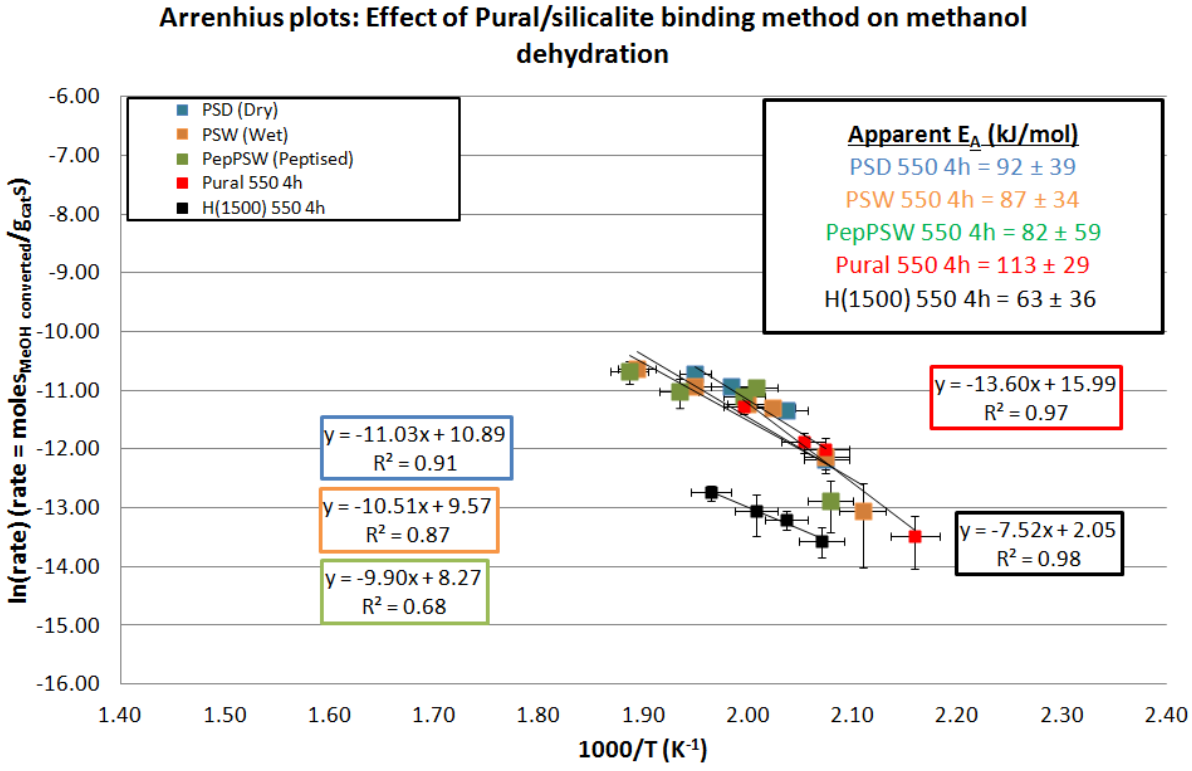

Figure 6.15: Arrenhius plots of Pural-bound H(1500) 550 4 h catalysts. Vertical error bars represent the 1st standard deviation in the values obtained for each point.

Both the apparent activation energies and the y-intercepts of alumina-bound materials were lower than those of Pural 550 4 h with both values of the Pural-bound samples in Fig. 6.15 following the order – Pural 550 4 h > PSD 550 4 h > PSW 550 4 h > PepPSW 550 4 h. With the increasing extent of binder-zeolite mixing interaction, as was indicated by SEM imaging (section 6.2.3), it may be expected that there would have been a corresponding increase in the extent of binder effects such as aluminium insertion [4] and pore blockage [2]. However, the similarities between all of the Pural-bound silicalites do not allow for definitive assessment of the effect of the different binding methods on methanol dehydration activity.

As a model study, aluminium impregnated silicalite was prepared and subjected to thermal or hydrothermal treatment. The purpose of these studies was to observe the evolution of the aluminium species in the catalyst and determine the effects of extra-framework aluminium from the effects of the binder.

6.3 Aluminium impregnation studies

6.3.1 Sample preparation

Samples were prepared as described in section 2.1.2. The aluminium impregnated silicalite contained 4.59 ± 0.07 wt. % extra-framework aluminium.

PXRD patterns in Fig. 6.16 show no additional phases following impregnation and calcination.

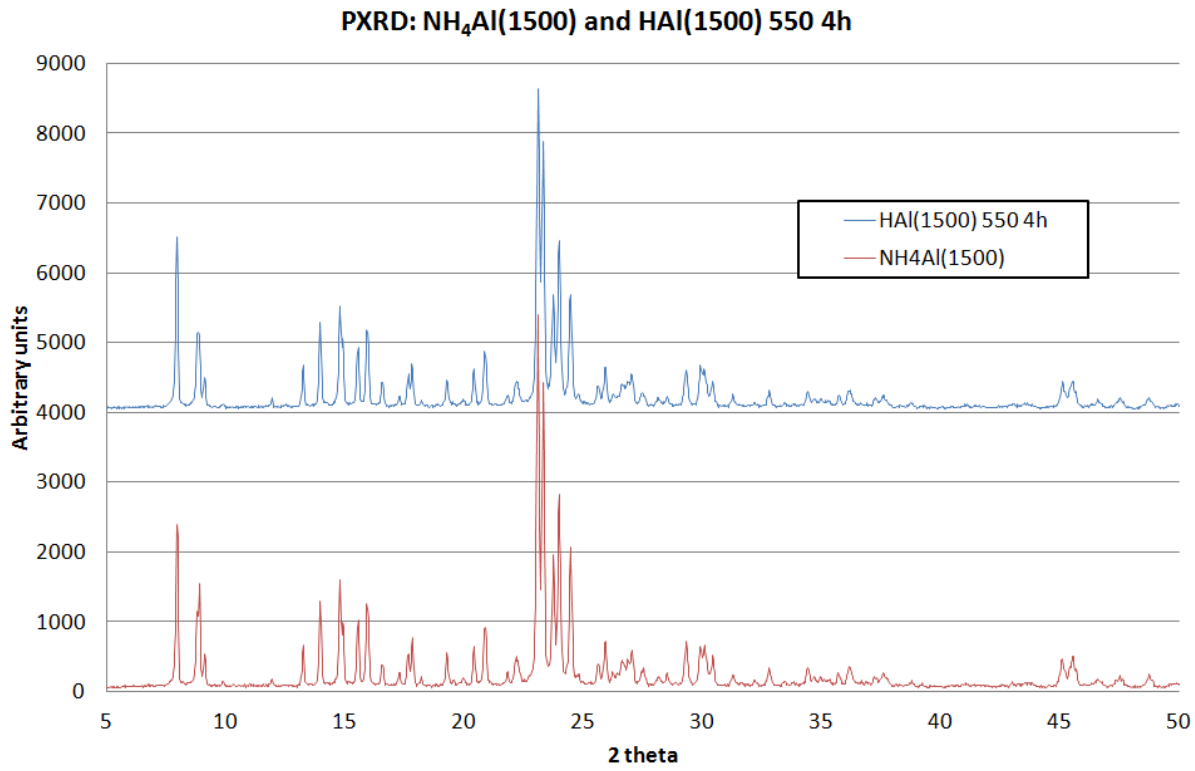

Figure 6.16: PXRD patterns of uncalcined and calcined aluminium-impregnated NH_4(1500). Measurements were obtained as described in section 2.6.6 except these patterns were obtained over 5 °- 55 ° with a step size of 0.030 °2θ and an acquisition time of 2 seconds per step.

The zeolite component was of orthorhombic symmetry and the PXRD patterns show crystallinity and pore filling to decrease following calcination.

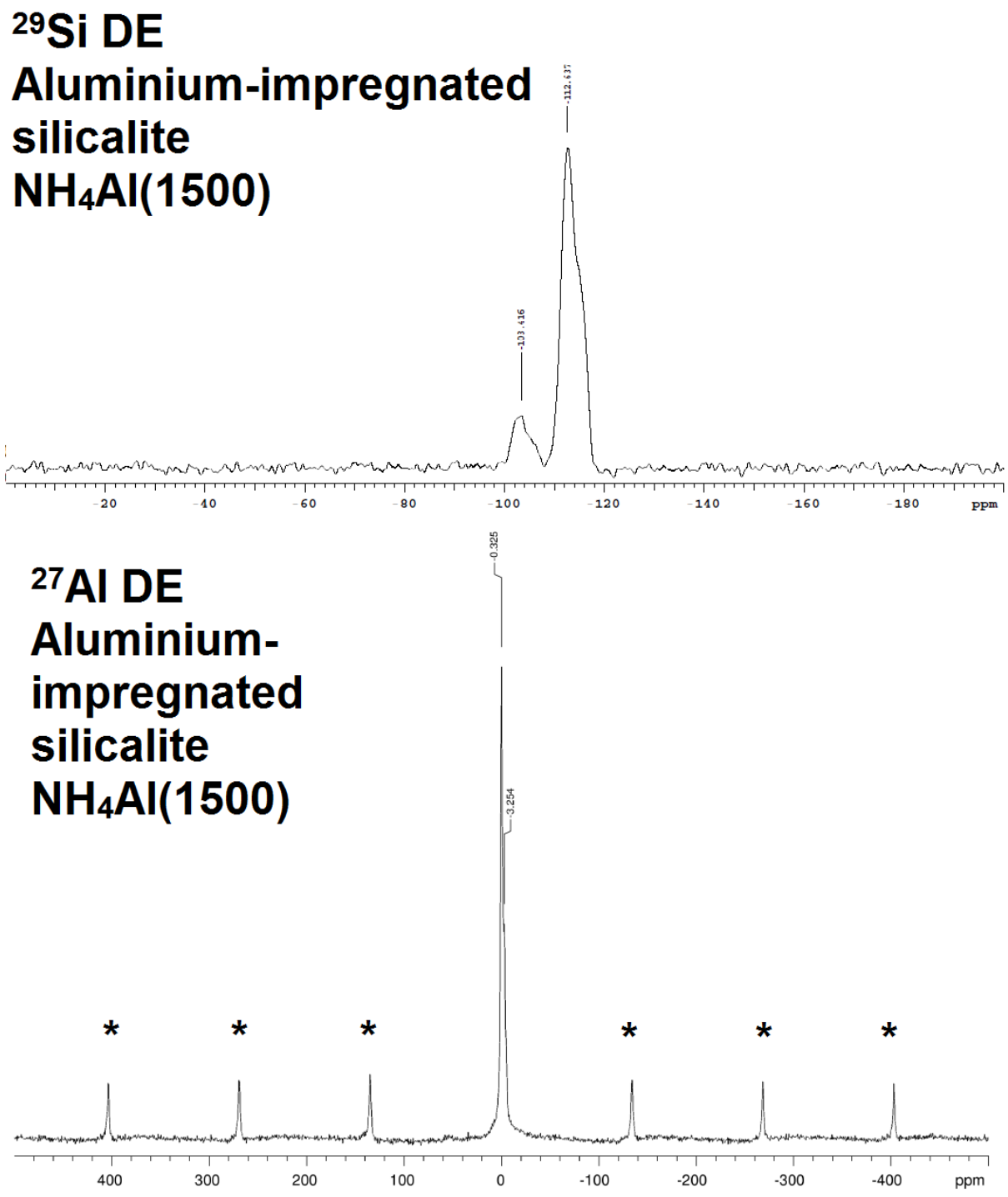

Figure 6.17: ^{29}Si MAS-NMR and ^{27}Al MAS-NMR spectra of aluminium impregnated NH_4(1500). ^{29}Si spectra were obtained on a Varian Unity Inova 300 and the ^{27}Al spectra were obtained on a Varian VNMRS 400. Asterisks (*) = Spinning side bands.

Following the impregnation process, a strong octahedral aluminium signal was detected. The octahedral coordination confirms impregnated aluminium is extra-

framework. CHN analyses of $NH_4Al(1500)$ provided values of: Carbon = Not Quantifiable, Hydrogen = 1.64 ± 0.02 wt. % and Nitrogen = 3.11 ± 0.05 wt. %. The nitrogen content of $NH_4(1500)$ was not quantifiable, therefore the nitrogen wt. % value for $NH_4Al(1500)$ was attributed to the nitrate content. Nitrate content is therefore = 13.77 ± 0.22 wt. % and attributed to the weight loss centred at *ca*. 100 °C in the TPO profile of $NH_4Al(1500)$ in Fig. 6.18. Additionally, the impregnated aluminium content was determined from the stoichiometric ratio of aluminium to nitrogen in $Al(NO_3)_3 .9H_2O$ which was (13.77 ± 0.22 wt. %) / 3 = 4.59 ± 0.07 wt. % aluminium. This is in close agreement with the 4 wt. % nominal loading value.

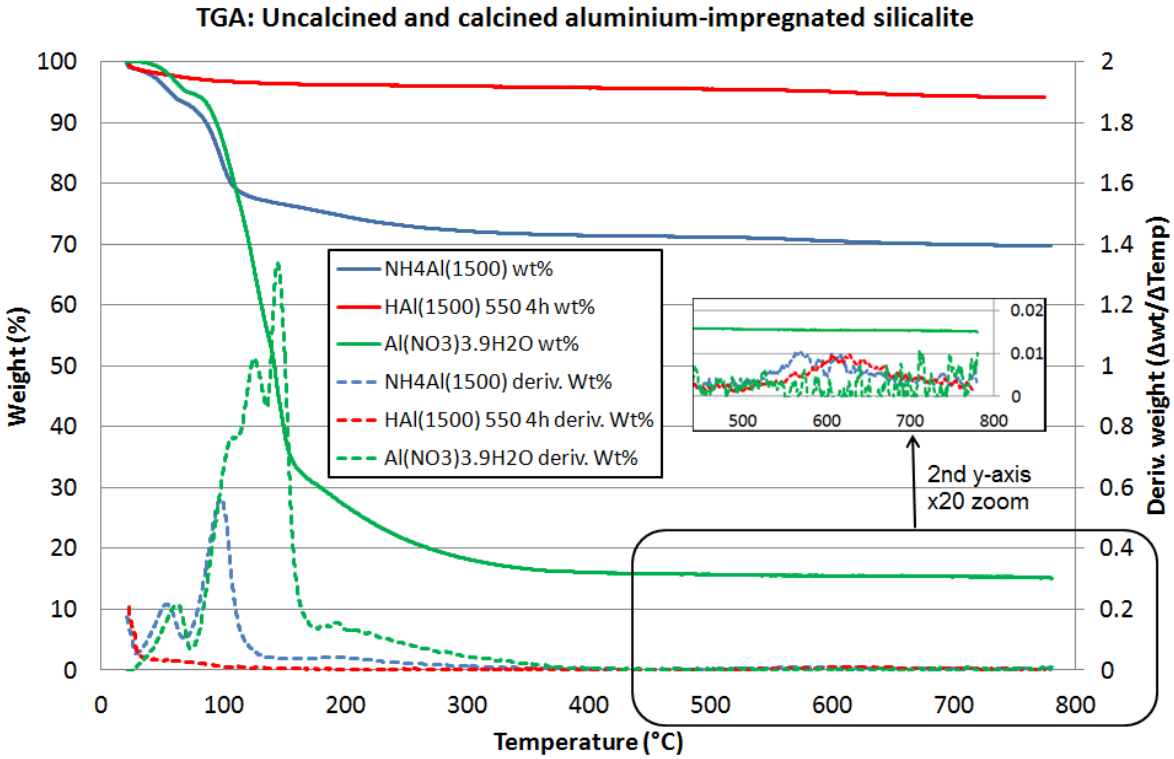

Figure 6.18: TGA measurements of aluminium impregnated ZSM-5 (1500) – nitrate decomposition. Measurements were obtained as described in section 2.6.8.

TGA analyses of $NH_4Al(1500)$ is shown in Fig. 6.18. Weight loss upto *ca.* 80 °C was attributed to initial water loss then followed by both nitrate decomposition and water loss at *ca*. 100 °C. This is consistent with aluminium nitrate nonahydrate decomposition [13]. Silanol dehydration occurred at *ca*. 625 °C. Whereas for HAl(1500) 550 4 h, water loss occurred < 100 °C, no nitrate decomposition was observed and silanol dehydration occurred at *ca*. 625 °C.

6.3.2 Thermally or hydrothermally treated catalysts

One effect of alumina binders is to synergetically increase the catalytic activity of zeolite catalysts [4]. This is believed to be the result of mobile extra-framework aluminium species, originating from the binder component being incorporated into the tetrahedral zeolite framework [1]. Increased framework aluminium content results in an increase in the number of zeolitic active sites of the catalyst.

6.3.2.1 Structural analyses

PXRD analyses of aluminium-impregnated silicalite (Fig. 6.19) showed no additional crystalline phases.

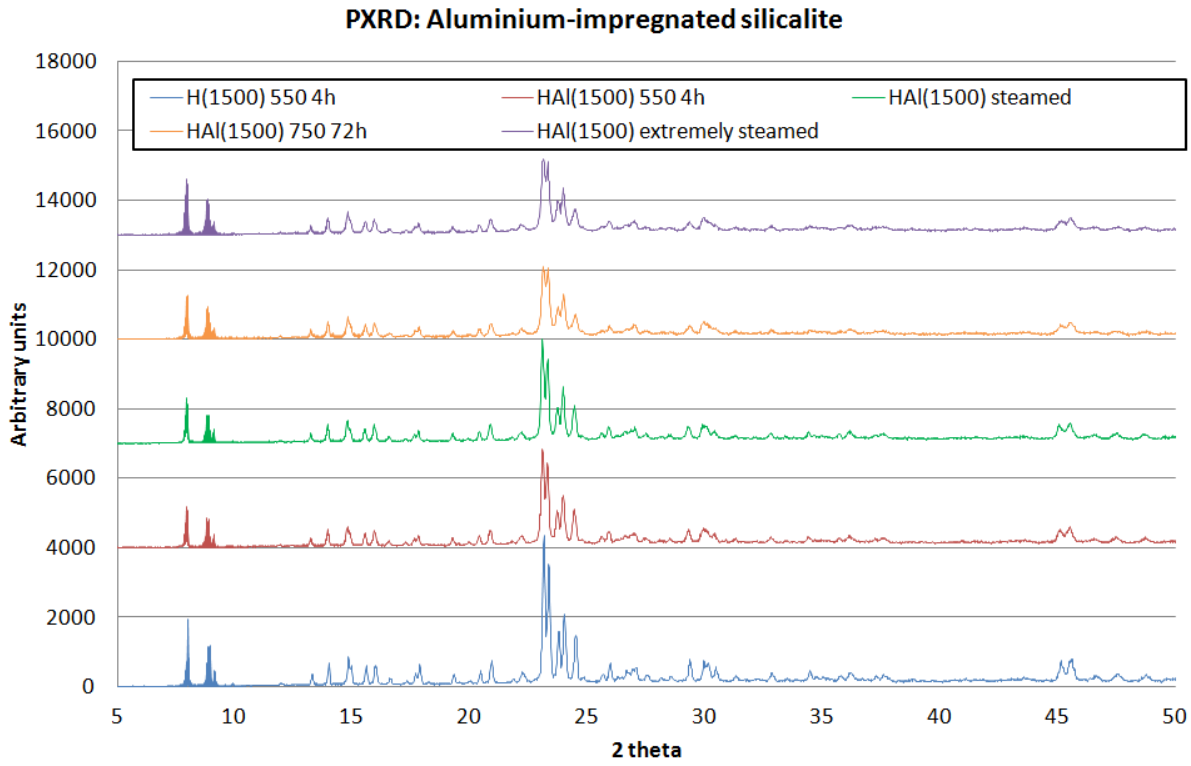

Figure 6.19: PXRD patterns of aluminium impregnated ZSM-5 (1500) materials following thermal or hydrothermal treatment. Measurements were obtained as described in section 2.6.6.

All materials retained orthorhombic symmetry. The aluminium-impregnated samples are less crystalline than the parent silicalite and crystallinity decreases further following extreme calcination, steaming and extreme steaming treatments.

Comparison of peak ratios (Fig. 6.20) suggests channels to empty with increasing treatment severity [14].

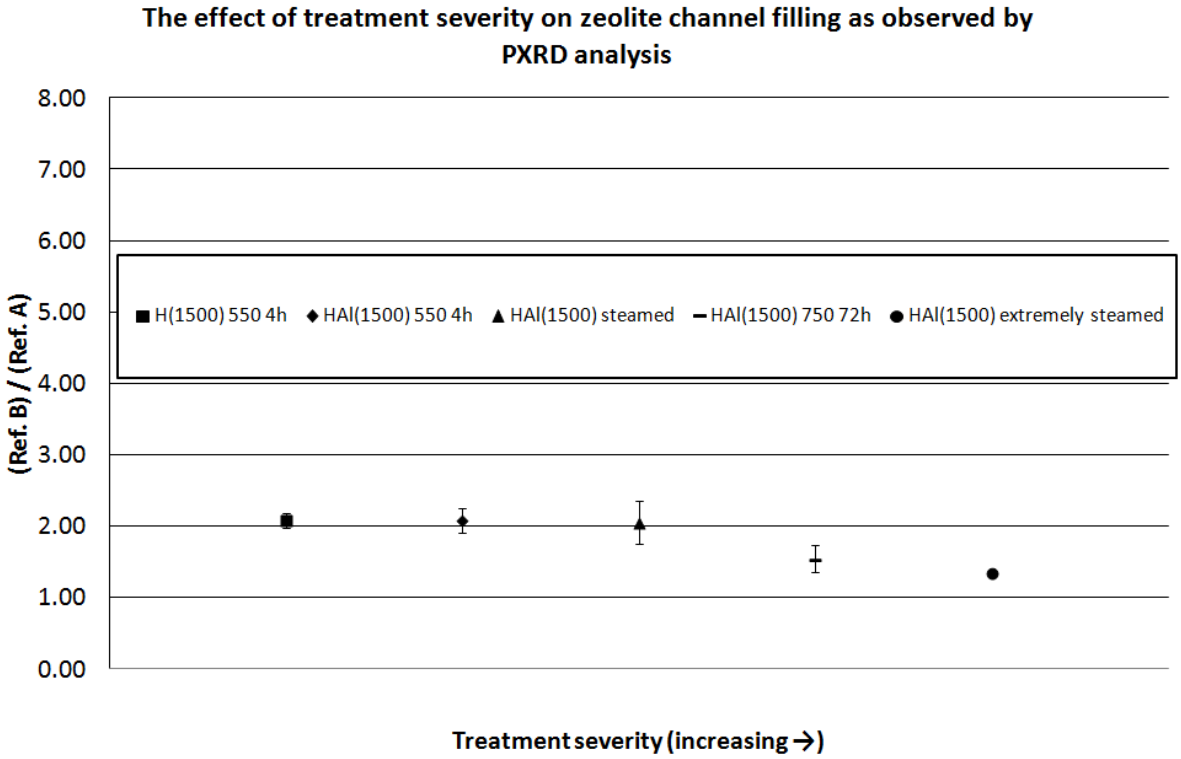

Figure 6.20: PXRD analyses of zeolite channel filling in aluminium impregnated ZSM-5 (1500) – treatment severity: 'Ref. A' = Σ[(101), (011), (200), (020) and (111) reflection intensities] and 'Ref. B' = Σ[(501), (051), (151), (303) and (133) reflection intensities]. Error bars correspond to ± the furthest outlier of repeat measurements.

The decrease in pore filling may be attributed to migration of extra-framework species to the external surface of the zeolite crystals.

All ^{29}Si MAS-NMR spectra in Figs. 6.21a-b show silicon to exist predominantly as Si(0Al). Silanol species are clearly observed in 550 4 h and steamed spectra at *ca*. -103 ppm.

Closer inspection of H(1500) 550 4 h, NH_4Al(1500), HAl(1500) 550 4 h and HAl(1500) steamed ^{29}Si MAS-NMR spectra (Fig. 6.21a) shows a slightly greater baseline at *ca*. -107 ppm. This indicates the association of aluminium with the

zeolite framework and a small degree of aluminium framework incorporation in HAl(1500) 550 4 h and HAl(1500) steamed.

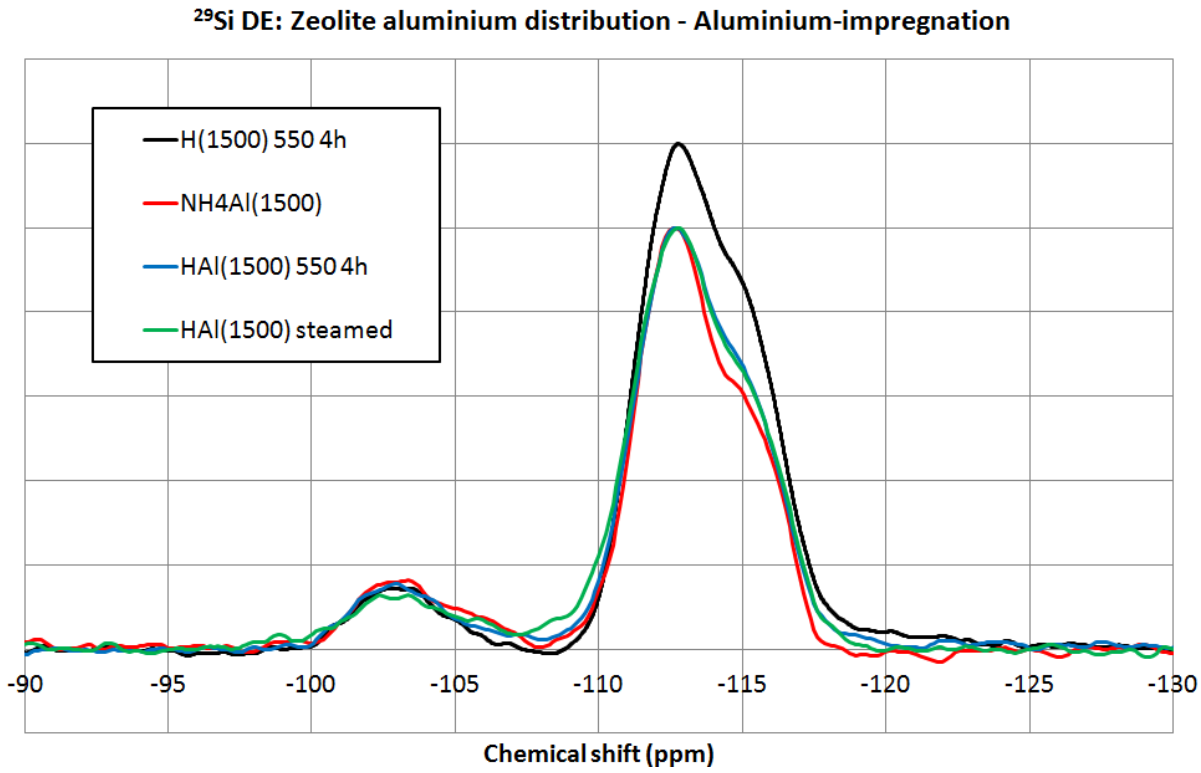

Figure 6.21a: ^{29}Si MAS-NMR spectra of aluminium impregnated ZSM-5 (1500) – calcined and steamed. H(1500) 550 4 h spectra were obtained on a Varian VNMRS 400. All aluminium impregnated ^{29}Si MAS-NMR spectra were obtained on a Varian Unity Inova 300.

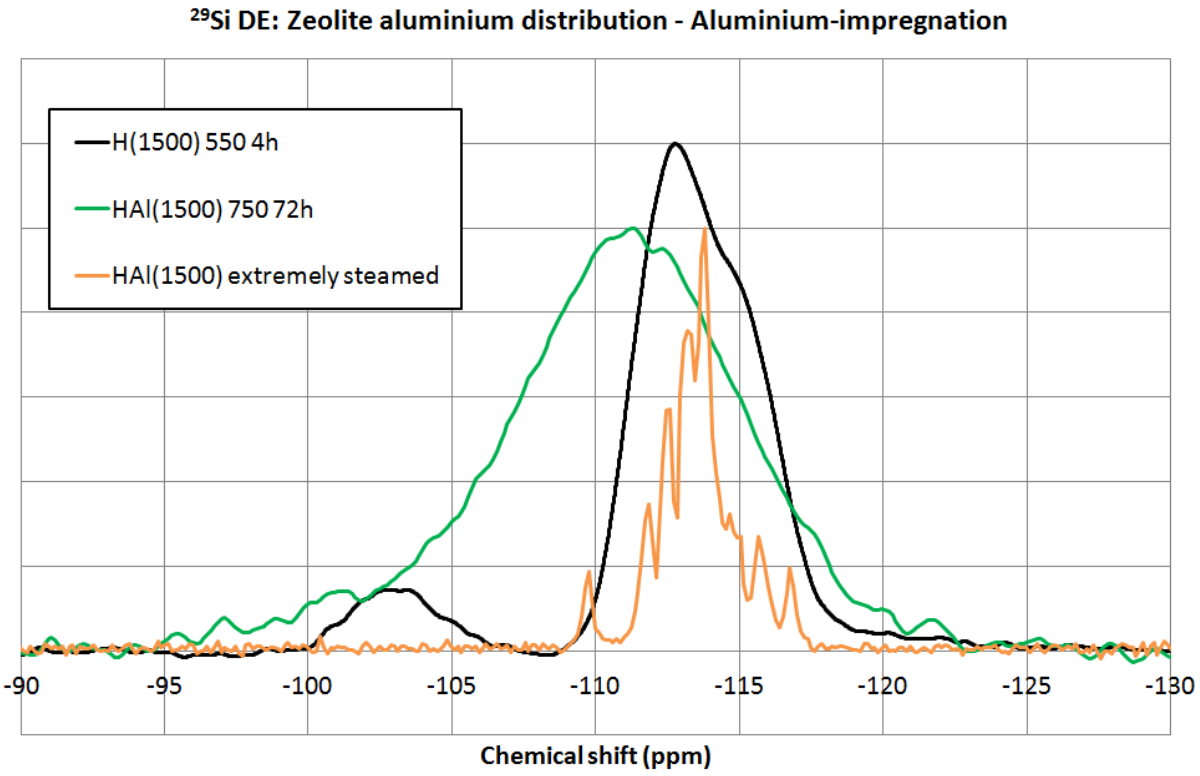

Figure 6.21b: ^{29}Si MAS-NMR spectra of aluminium impregnated ZSM-5 (1500) – extremely steamed and extremely calcined. H(1500) 550 4 h spectra were obtained on a Varian VNMRS 400. All aluminium impregnated ^{29}Si MAS-NMR spectra were obtained on a Varian Unity Inova 300.

Referring to Fig. 6.21b, the broad ^{29}Si spectra of HAl(1500) 750 72 h indicates an increase in the heterogeneity of the silicon environments. This also obscures the region associated with Si(1Al). This increase in disorder may be attributed to silanol dehydration (Fig. 6.24). HAl(1500) extremely calcined is however dehydroxylated and dealuminated. However, short range order is drastically increased in the presence of steam at 750 °C. This may be attributed to annealing of the framework, where steam further facilitates the annealing process [15]. Although the exact mechanism through which annealing occurs is still debated [16].

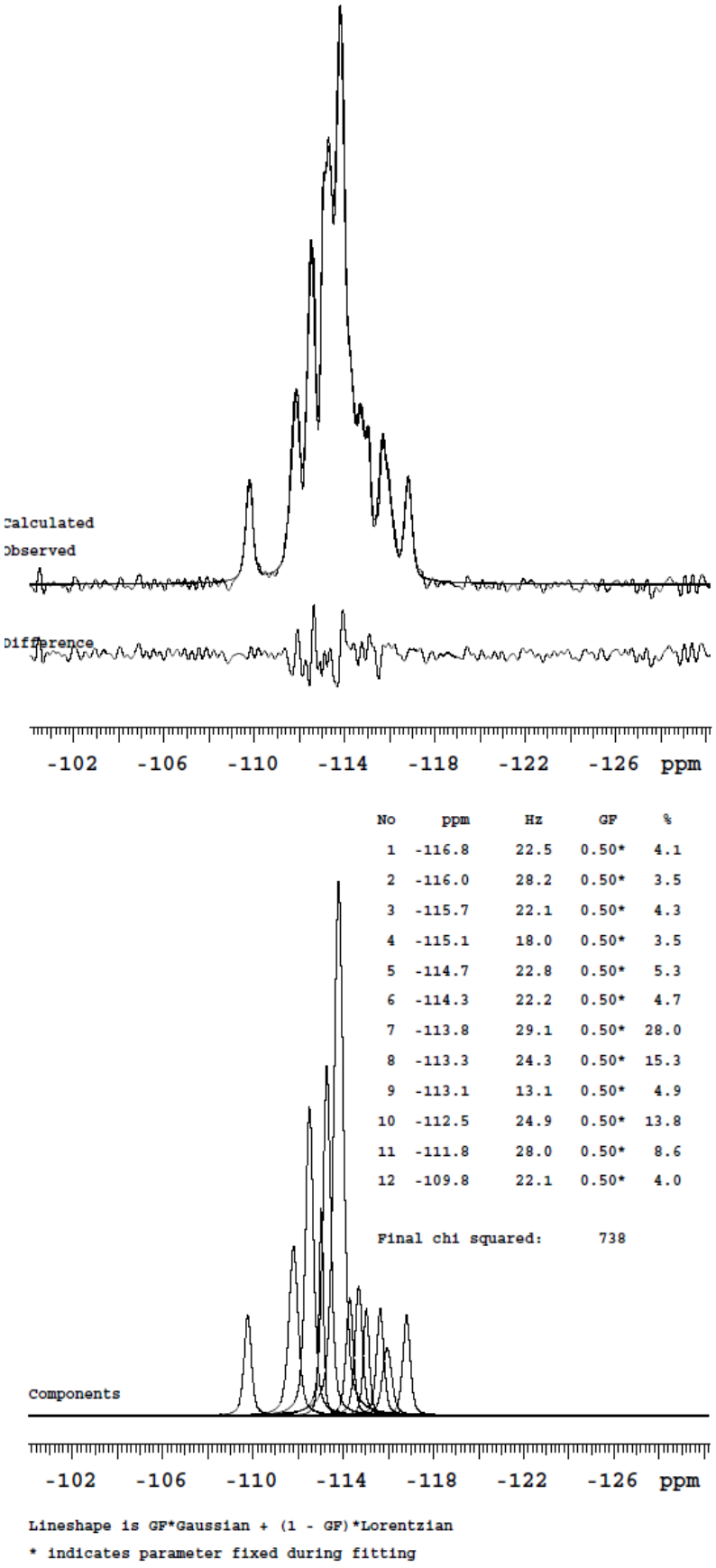

Figure 6.22: ^{29}Si MAS-NMR spectra of HAl1500) extremely steamed.

Spectra were obtained on a Varian VNMRS 400 and deconvolution was kindly performed by Dr. D. Apperley of the EPSRC Solid State NMR service at the University of Durham. The 12 peaks deconvoluted from the ^{29}Si spectra may be assigned to crystallographically inequivalent Si(0Al) sites within the orthorhombic unit cell structure [17]. However, Klinowski [18] suggests silicalite to possess 24 inequivalent tetrahedral sites (and therefore exist in monoclinic form) on the basis of peak intensity ratios. From the deconvolution, taking 4.0 % signal intensity as a base unit, the 12 peaks observed possess peak intensity ratios of 1.0 : 0.9 : 1.1 : 0.9 : 1.3 : 1.2 : 7.0 : 3.8 : 1.2 : 3.5 : 2.2 : 1.0. The total peak intensity based upon this normalisation is *ca*. 24, suggesting 24 inequivalent tetrahedral sites within the unit cell. This not in agreement with PXRD results for HAl(1500) extremely steamed, which appears orthorhombic and would be expected to only possess 12 inequivalent Si(0Al) sites.

Examination of ^{27}Al MAS-NMR spectra following each of the thermal or hydrothermal treatments shows the impregnated octahedral aluminium undergoes transformation (Fig. 6.23a-b).

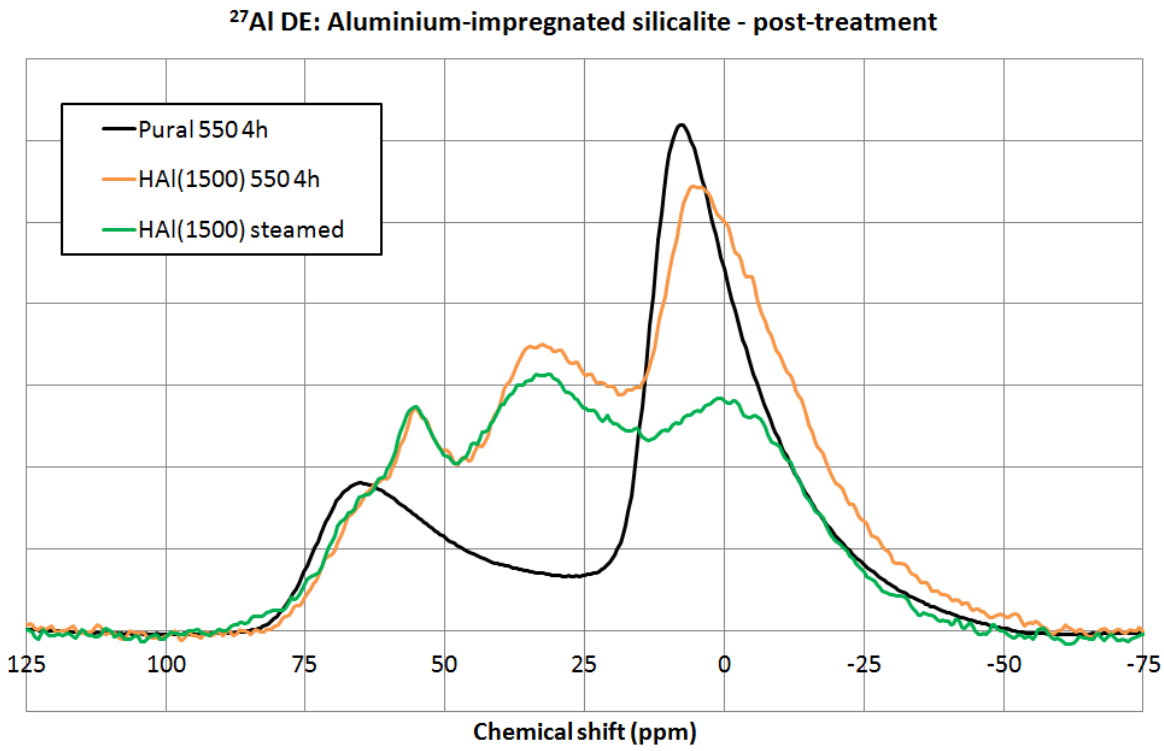

Figure 6.23a: ^{27}Al MAS-NMR spectra of aluminium impregnated ZSM-5 (1500) - 550 °C treatments. All spectra were obtained on a Varian VNMRS.

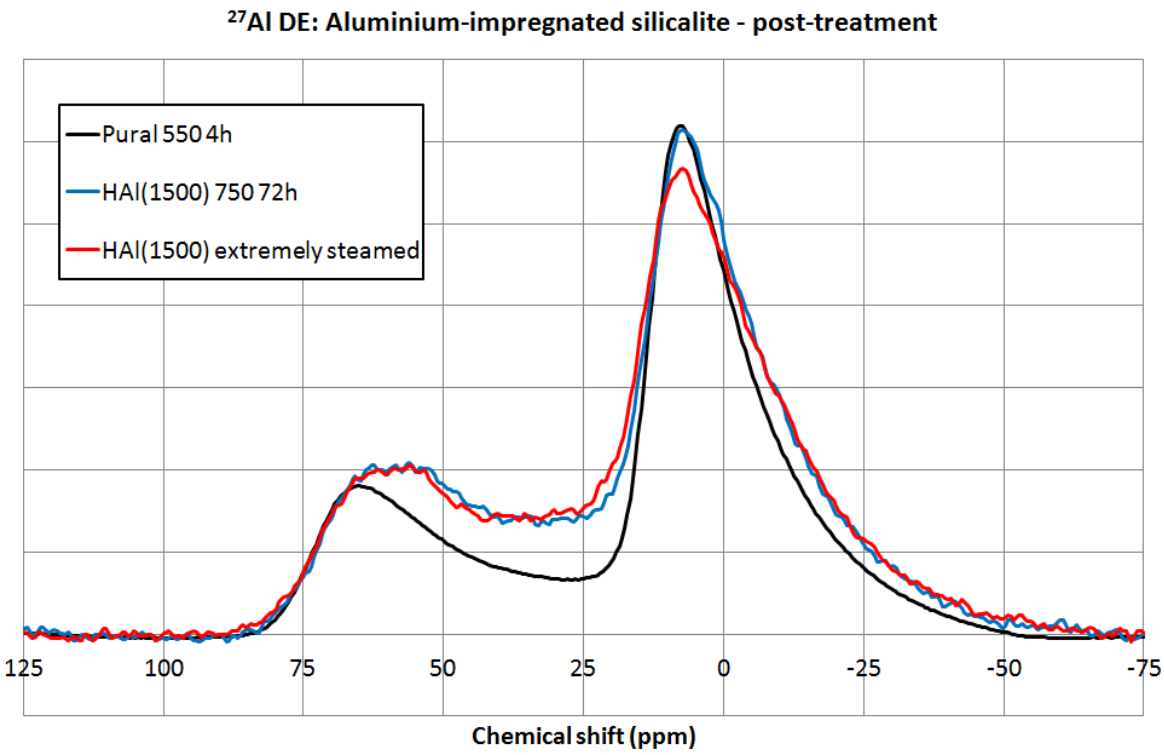

Figure 6.23b: ^{27}Al MAS-NMR spectra of aluminium impregnated ZSM-5 (1500) - 750 °C treatments. All spectra were obtained on a Varian VNMRS.

In Fig. 6.23a, it can be seen that aluminium in both HAl(1500) 550 4 h and HAl(1500) steamed was converted into a mixture of tetrahedral, 5-coordinate and octahedral species. The presence of a high proportion of 5-coordinate material makes interpretation difficult. The breadth of the octahedral signal, combined with the appearance of a tetrahedral shoulder at *ca*. 65 ppm suggested the presence of γ-Al_2O_3-like species. The sharper tetrahedral signal at *ca*. 55 ppm is attributed to framework inserted aluminium.

If it is then assumed that γ-Al_2O_3 species are produced following thermal or hydrothermal treatment then a disproportionately high amount of tetrahedral and 5-coordinate aluminium exists in both HAl(1500) 550 4 h and HAl(1500) steamed samples. This greater proportion of tetrahedral aluminium in these two materials indicates aluminium insertion into the zeolite framework.

Following extreme calcination or extreme steaming (Fig. 6.23b), the impregnated aluminium is converted to a mixture approaching *ca*. 30 % tetrahedral : 70 %

octahedral. Between these spectral results and the decrease in channel filling suggested by PXRD analyses, it is proposed that the impregnated aluminium may cluster into γ-Al_2O_3-like crystallites on the external surface of the zeolite crystals. Further structural information may be obtained from thermal analyses of the aluminium-impregnated materials. TGA analyses (Fig. 6.24) show silanol dehydration at *ca*. 640 °C in only HAl(1500) 550 4 h and HAl(1500) steamed. The conditions of preparative treatments of HAl(1500) 750 72 h and HAl(1500) extremely steamed being sufficient to dehydrate silanol groups prior to TGA analyses.

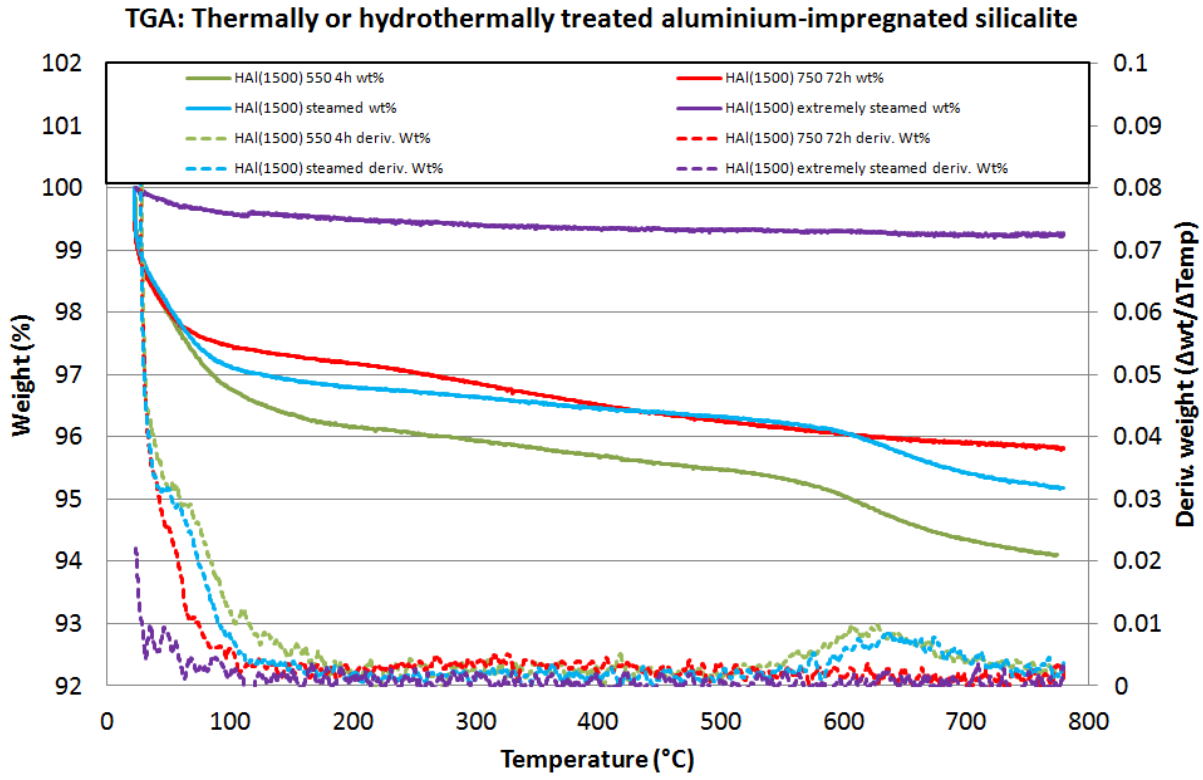

Figure 6.24: TGA measurements of thermally or hydrothermally treated aluminium impregnated ZSM-5 (1500)**.** Measurements were obtained as described in section 2.6.8. The increase in wt. % at *ca*. 120 °C for HAl(1500) extremely steamed is an artefact.

HAl(1500) 750 72 h contained more adsorbed H_2O than HAl(1500) extremely steamed. The low water adsorption content of HAl(1500) extremely steamed is attributed to the increased hydrophobicity of the dealuminated, dehydroxylated and annealed MFI framework.

6.3.2.2 **Textural analyses**

N_2-physisorption isotherms of Al-impregnated silicalite are shown below (Fig. 6.25a-b). All materials show type-I adsorption isotherm characteristics consistent with microporous materials.

The low pressure step at *ca*. 0.2 P/P_o in the N_2-adsorption isotherm of observed for HAl(1500) extremely steamed (Fig. 6.25b) was attributed to a N_2-adsorbate phase change [19]. This phase change is from a less-dense disordered phase to a more-dense ordered phase with increasing pressure. It is believed that although a monoclinic to orthorhombic phase transition in the MFI material may contribute to the increased adsorption, it would not provide the additional pore volume required for the increased N_2-adsorption at this pressure [20]. This low pressure step was also observed in ZSM-5 (280) and H(23) extremely steamed samples (see appendix). N_2-physisorption results in Table 6.3 below show all materials to retain high surface areas. Surface areas and pore volumes decrease following aluminium impregnation and increasing treatment severity with the exception of HAl(1500) extremely steamed.

Material	Measured BET SA (m^2/g)	Total pore vol. (cm^3/g)	Ads. Iso. Type
H(1500) 550 4 h	326 ± 10	0.19 ± 0.01	I
HAl(1500) 550 4 h	300 ± 12	0.17 ± 0.01	I
HAl(1500) S	295	0.17	I
HAl(1500) 750 72 h	272 ± 24	0.16 ± 0.01	I
HAl(1500) XS	353	0.21	I

Table 6.3: N_2-physisorption results for aluminium impregnated ZSM-5 (1500). Results were obtained as described in the experimental section 2.6.5. Ads. Iso. = Adsorption Isotherm. Adsorption isotherms are shown in Figs 6.25a-b. S = Steamed and XS = Extremely steamed. Errors correspond to the furthest outliers of repeat measurements.

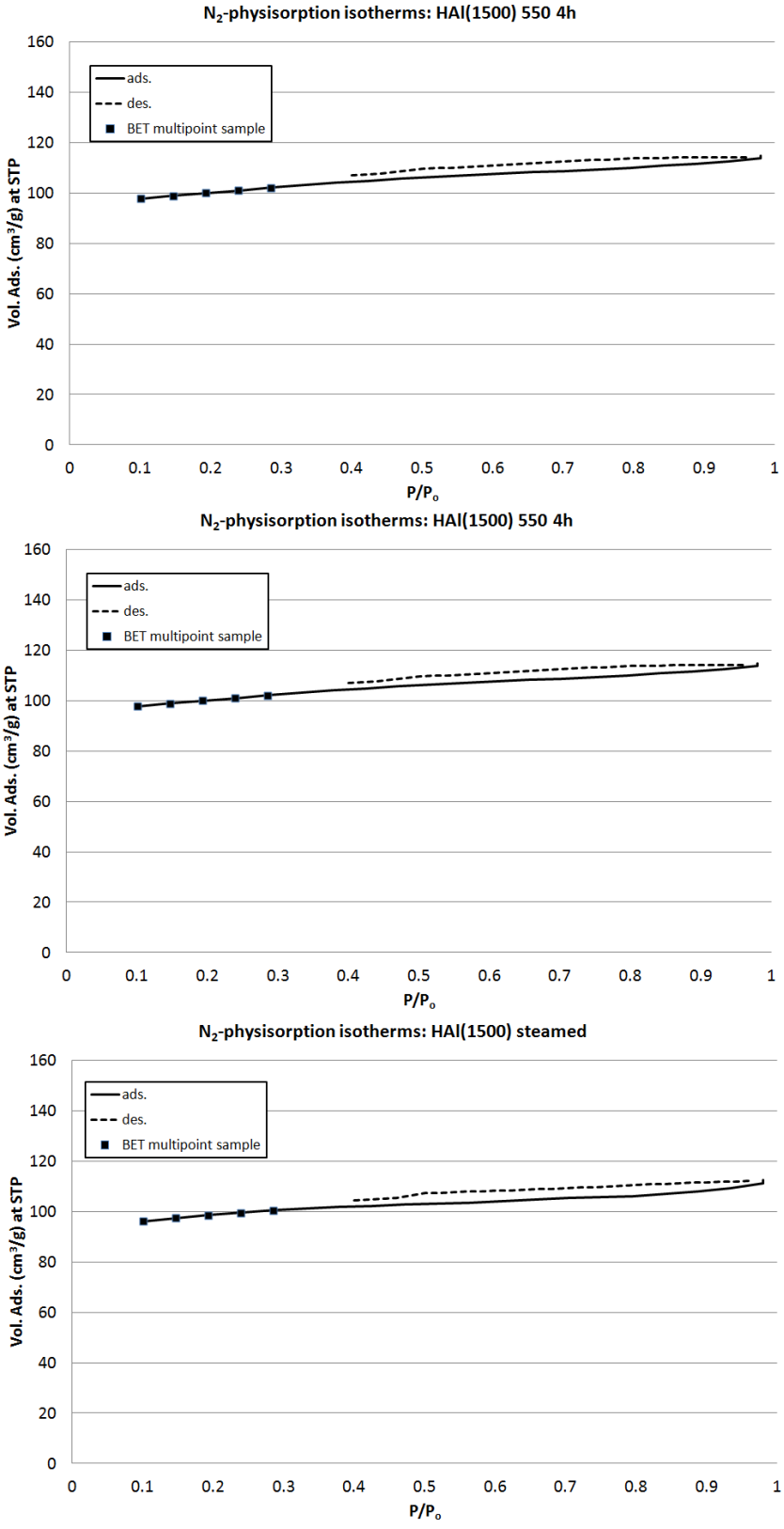

Figure 6.25a: N_2-physisorption isotherms of aluminium impregnated ZSM-5 (1500) - 550 °C treatments. All adsorption isotherms were obtained as described in section 2.6.5.

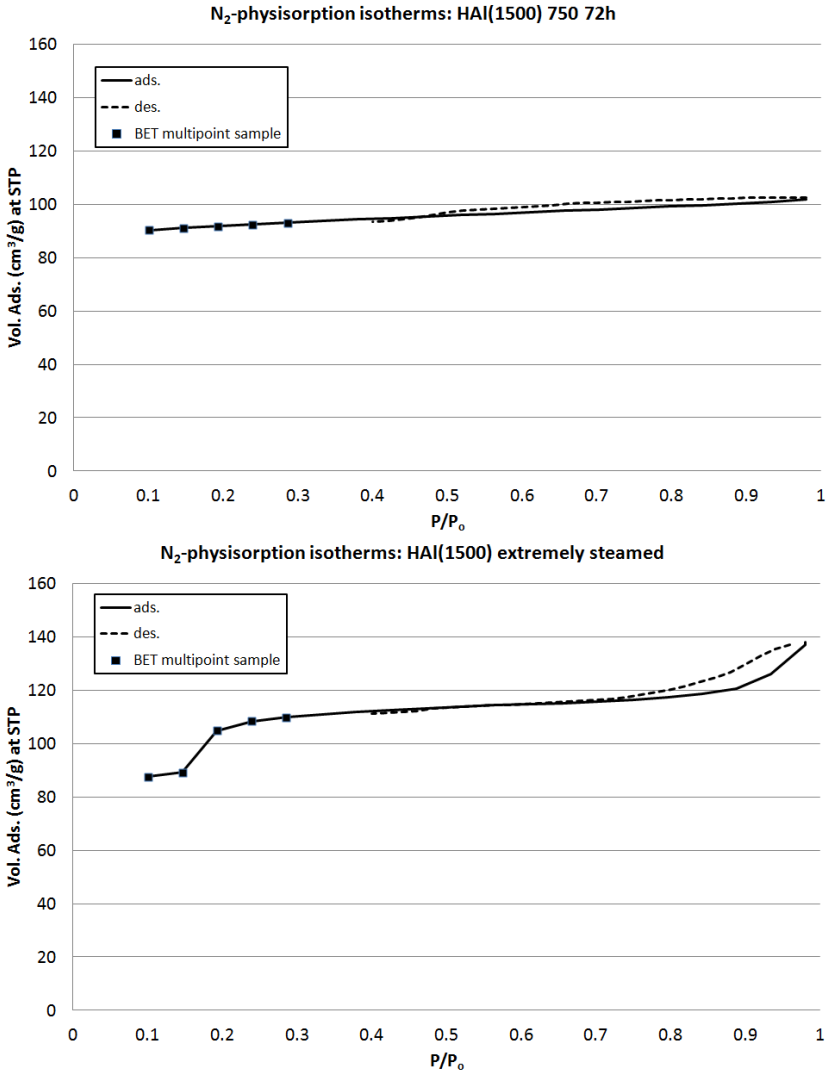

Figure 6.25b: N_2-physisorption isotherms of aluminium impregnated ZSM-5 (1500) - 750 °C treatments. All adsorption isotherms were obtained as described in section 2.6.5.

As previously mentioned, extra-framework aluminium species may contribute to channel blockage [21,22]. The observed decrease in surface areas following aluminium impregnation may be attributed to partial channel blockage though not channel filling (Fig. 6.20) analogous to 'plugging' described in section 5.2.3. Additionally, the lower N_2-physisorption results for HAl(1500) 750 72 h may be attributed to partial pore blockage by the disordered framework. The higher N_2-physisorption results of HAl(1500) extremely steamed are attributed to the increased short-range ordering of the silicalite framework, increased micropore accessibility.

6.3.2.3 **Catalytic testing**

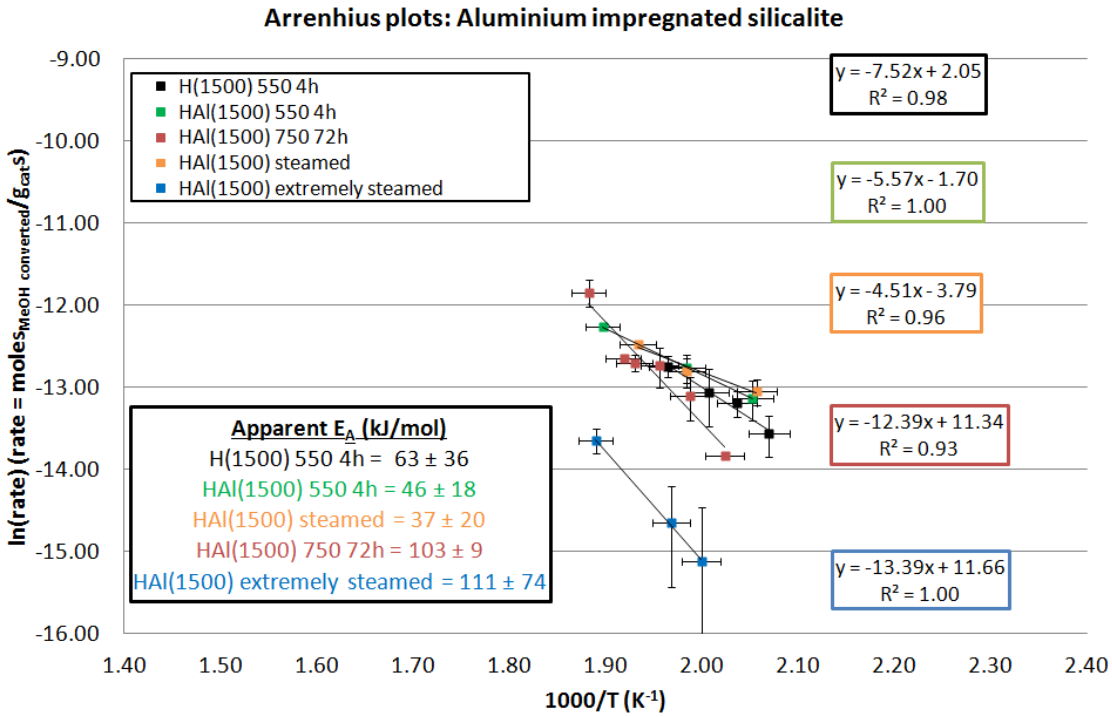

Figure 6.26: Arrenhius plots of aluminium impregnated H(1500). Vertical error bars represent the 1st standard deviation in the values obtained for each point.

Comparison of H(1500) 550 4 h, HAl(1500) 550 4 h and HAl(1500) steamed samples over a methanol dehydration reaction temperature range of 210 -258 °C in Fig. 6.26 shows very similar MeOH conversion rates. In both of these aluminium impregnated samples, both the apparent activation energy and y-intercepts have decreased but these values are still close and not outwith the error of one another. MAS-NMR (Figs. 6.21a and 6.23a) spectra support both a slight increase in Si(1Al) content and an increase in the proportion of tetrahedral to octahedral aluminium following calcination and steaming as well. It is possible that new active sites are very strong and provide the observed catalytic activity but it is more likely that a combination of new active sites and mass transfer limitations are the cause of the observed Arrenhius plots but both effects are very minor on methanol dehydration.

Comparison of H(1500) 550 4 h, HAl(1500) 750 72 h and HAl(1500) extremely steamed over 210 – 258 °C shows an increase in apparent activation energy and y-intercept. In combination with MAS-NMR spectra (Figs. 6.21b and 6.23b), the Arrenhius plots would suggest a combination of zeolite framework dealumination

and the formation of proposed γ-Al_2O_3-like clusters to be the cause of these observations.

Comparison of HAl(1500) extremely steamed to Pural 550 4 h (Fig. 6.15) shows both materials to give similar apparent activation energies and Pural 550 4 h to possess a higher y-intercept than HAl(1500) extremely steamed. If the proposed γ-Al_2O_3-like clusters were as active as Pural 550 4 h, then it may be envisaged that little/no contribution towards methanol conversion comes from the dealuminated silicalite component and a dominant contribution comes from the extra-framework aluminium of the HAl(1500) extremely steamed material. The lower y-intercept value of HAl(1500) extremely steamed would then be reflecting its lower aluminium content and number of active sites than Pural 550 4 h.

6.4 Conclusions

Pural SCF 55 (boehmite) was dehydrated to mesoporous Pural 550 4 h (γ-Al_2O_3) following calcination. Surface area and pore volume were insensitive to pre-calcination pelleting.

No significant structural differences were observed with different Pural-binding methods. ^{29}Si MAS-NMR showed approximately the same slight increase in Si(1Al) content following boehmite-binding and calcination (550 °C for 4 h) irrespective of method. Texturally, micropore surface areas were lower than that predicted by the sum of constituent parts and zeolite channel filling, according to PXRD analyses, was insensitive to binding method. Mesopore size distributions were lower for peptised Pural-bound zeolites and this was consistent with the increased interaction of binder-zeolite particle contact associated with the treatment. This was also consistent with SEM-imaging. Catalytic testing showed methanol conversion rates of the Pural-bound silicalites to be very similar to Pural 550 4 h between 217-256 °C.

Aluminium-impregnated silicalite samples showed impregnated octahedral aluminium to gradually transform, with increasing thermal or hydrothermal treatment severity, into a tetrahedral / octahedral mixture similar to that of γ-Al_2O_3.

The symmetry of all silicalite containing samples was orthorhombic from PXRD analyses. However, conflicting results exist for HAl(1500) extremely steamed which appeared orthorhombic by PXRD analysis but monoclinic by interpretation of deconvoluted ^{29}Si MAS-NMR spectra. A degree of aluminium insertion occurred in calcined and steamed samples according to ^{29}Si MAS-NMR. Arrenhius plots of the calcined and steamed aluminium impregnated silicalite samples showed no significant change in methanol dehydration behaviour from that of H(1500) 550 4 h. The Arrenhius plots of extremely calcined and extremely steamed HAl(1500) samples showed increased apparent activation energy and an increase in the number of active sites. This was consistent with both zeolite dealumination and the formation of γ-Al_2O_3-like species.

6.5 References

[1] J. S. J. Hargreaves and A. L. Munnoch, Catal. Sci. Technol., 3 (2013) 1165-1171.

[2] X. Wu, Ph.D. Thesis, Texas A. M. University (2003).

[3] M. Guinet and N. S. Gnep, Appl. Catal., 146 (1996) 33-64.

[4] D. S. Shihabi, W. E. Garwood, P. Chu, J. N. Miale, R. M. Lago, C. T-W. Chu and C. D. Chang, J. Catal., 93 (1985) 471-474.

[5] C. N. Satterfield, Heterogeneous Catalysis in Industrial Practice, 2nd Ed., (1991) ISBN: 0070548862.

[6] M. Du, Z. Qin, H. Ge, X. Li, Z. Lű and J. Wang, Fuel Process. Technol., 91 (2010) 1655-1661.

[7] A. J. D. Bates and J. Bridgwater, Chem. Eng. Sci., 55 (2000) 3003-3012.

[8] International Centre for Diffraction Data, PDF-4+: 00-021-1307.

[9] International Centre for Diffraction Data, PDF-4+: 00-029-0063.

[10] M. –H. Lee, C.-F. Cheng, V. Heine and J. Klinowski, Chem. Phys. Lett., 265, (1997) 673-676.

[11] T. C. Chou and T. G. Nieh, J. Am. Ceram. Soc., 74 (1991) 2270.

[12] B. C. Lippens, Ph.D. Thesis, Delft University (1961).

[13] B. Pacewska and M. Keshr, Thermochimica Acta, 385 (2002) 73-80.

[14] J. S. J. Hargreaves, Cryst. Rev., 11, 1 (2005) 21-34.

[15] R. M. Dessau, K. D. Schmitt, G. T. Kerr, G. L. Woolery and L. B. Alemany, J. Catal., 104 (1987) 484-489.

[16] A. A. Sokol, C. R. A. Catlow, J. M. Garces and A. Kuperman, J. Phys.: Condens. Matter 16 (2004) 2781–2794.

[17] C. A. Fyfe, G. C. Gobbi, W. J. Murphy, R. S. Ozubko and D. A. Slack, J. Am. Chem. Soc., 106 (1984) 4435-4438.

[18] J. Klinowski, Progress in NMR spectroscopy, 16 (1984) 237-309.

[19] P. L. Llewellyn, J. -P. Coulomb, Y. Grillet, J. Patarin, G. Andre and J. Rouquerol, Langmuir, 9 (1993) 1852-1856.

[20] J. C. Groen, L. A. A. Peffer and J. Perez-Ramirez, Microp. Mesop. Mater., 60 (2003) 1-17.

[21] A. Corma, M. Grande, V. Fornes, S. Cartlidge and M. P. Shatlock, Appl. Catal., 66 (1990) 45–57.

[22] A. Corma, M. Grande, V. Fornes and S. Cartlidge, Appl. Catal., 66 (1990) 247–255.

7 Summary

After establishing the reaction conditions for methanol dehydration to dimethyl ether over H^+-form zeolites, Na^+-form zeolites and γ-Al_2O_3, zeolites were compared to isostructural boron, iron and gallium silicates for methanol dehydration. The MeOH conversion rates (at fixed temperatures between 168 °C and 258 °C) were shown to decrease in the order Al > Ga > Fe >> B for materials of similar heteroatom content. After showing zeolites to provide the highest methanol conversion rates they were subsequently studied in conjunction with binders and model catalysts to determine whether any binder effects on the catalytic behaviour occurred. Colloidal silica-bound H-ZSM-5 (23) showed lowered methanol dehydration rates because of migration of sodium from the binder to the zeolite component and also due to zeolite channel filling. Sodium-exchange studies showed sodium to retard extra-framework aluminium formation and damage the zeolite framework; this effect was believed to have been more dominant than extra-framework aluminium trapping by the silica matrix. Degradation of the zeolite framework was particularly apparent under extreme steaming conditions. Porosity characteristics were also altered with the binder component providing additional mesoporosity whilst filling the zeolite channels. Following calcination of boehmite-bound zeolites, additional mesoporosity was provided by the alumina matrix. The effect of binding method on methanol dehydration in H-ZSM-5 (1500)/γ-Al_2O_3 composites was very minor but all displayed a low degree of aluminium insertion into the zeolite framework. This resulted in enhanced methanol dehydration rates. Impregnated aluminium was believed to have been inserted into the zeolite framework to a low extent following calcination and steaming but extreme calcination and extreme steaming resulted in dealumination. The extra-framework species adopted a tetrahedral/octahedral ratio similar to that of γ-Al_2O_3.

Ultimately, binders were observed to affect methanol dehydration over zeolite catalysts. In conjunction with sodium-exchange and aluminium impregnation studies the effects of sodium and extra-framework aluminium generation have been distinguished from those of the binder in general.

8 Future work

There are a number of potential avenues for future exploration in the work described within this thesis, as outlined in the following bullet points:

- Alternative metal exchange studies. In this study only the effects of sodium-exchange were examined showing largely detrimental effects on the catalyst structure and catalytic activity. However, sodium also beneficially retarded the zeolite from dealumination. Extra-framework aluminium was observed in calcined ZSM-5 (23) and dealumination can be a major mode of deactivation for zeolite catalysts which can lead to the necessary replacement of costly catalysts. As such, it would be interesting to examine the effects of low level exchange of alternative metals (such as caesium, magnesium and rare earths) for their effects on dealumination as well as their structural and catalytic properties. The aim of which being to improve catalyst resistance to dealumination whilst minimising losses in catalytic activity.

- The use of alternative probe reactions. These would allow for further research into binder effects which were not explored in this work such as coke precursor trapping. This effect may lengthen catalyst lifetimes in processes where coking occurs and deactivation occurs by coking.

- It would be interesting to undertake studies with a wider range of binder materials. Clays such as kaolinite or montmorillonite would be of interest because they are materials more likely to be used on a large scale (such as FCC) rather than more costly high purity boehmites such as Pural SCF 55. As such, the extent of each of the binder effects would likely be more comparable to those observed in an industrial process employing these binders.

9 Appendix

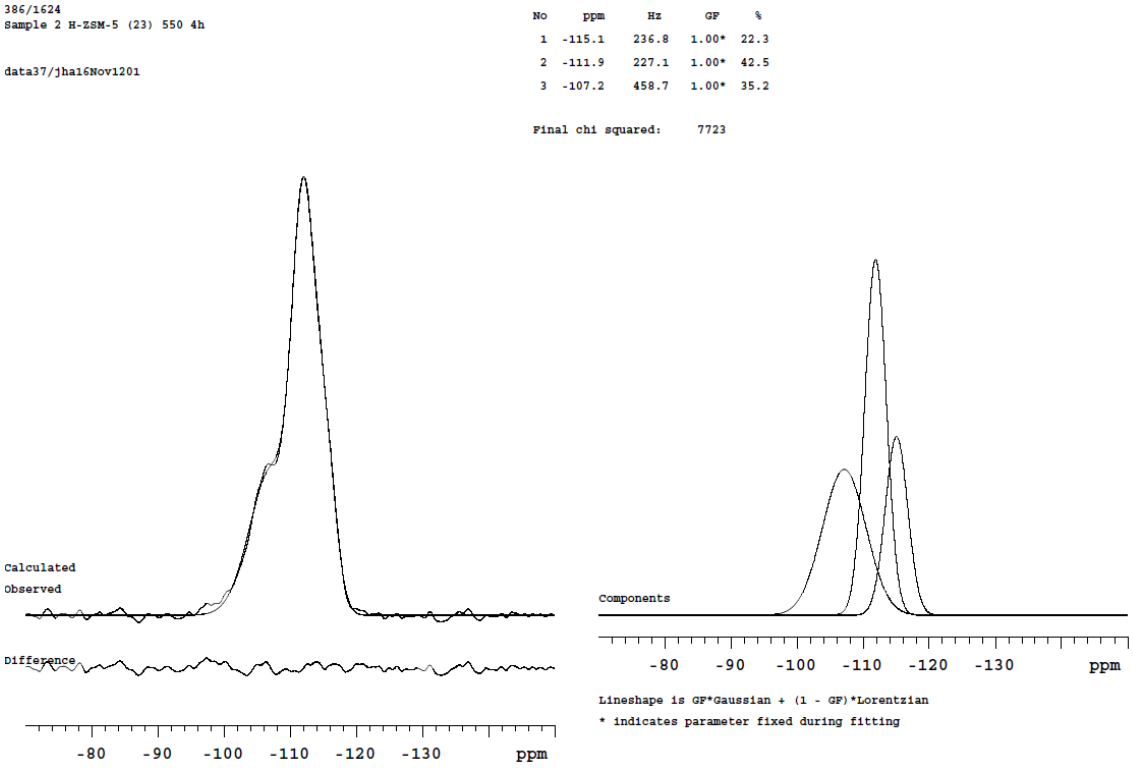

Figure 9.1: Deconvolution of ^{29}Si spectra of H(23) 550 4 h.

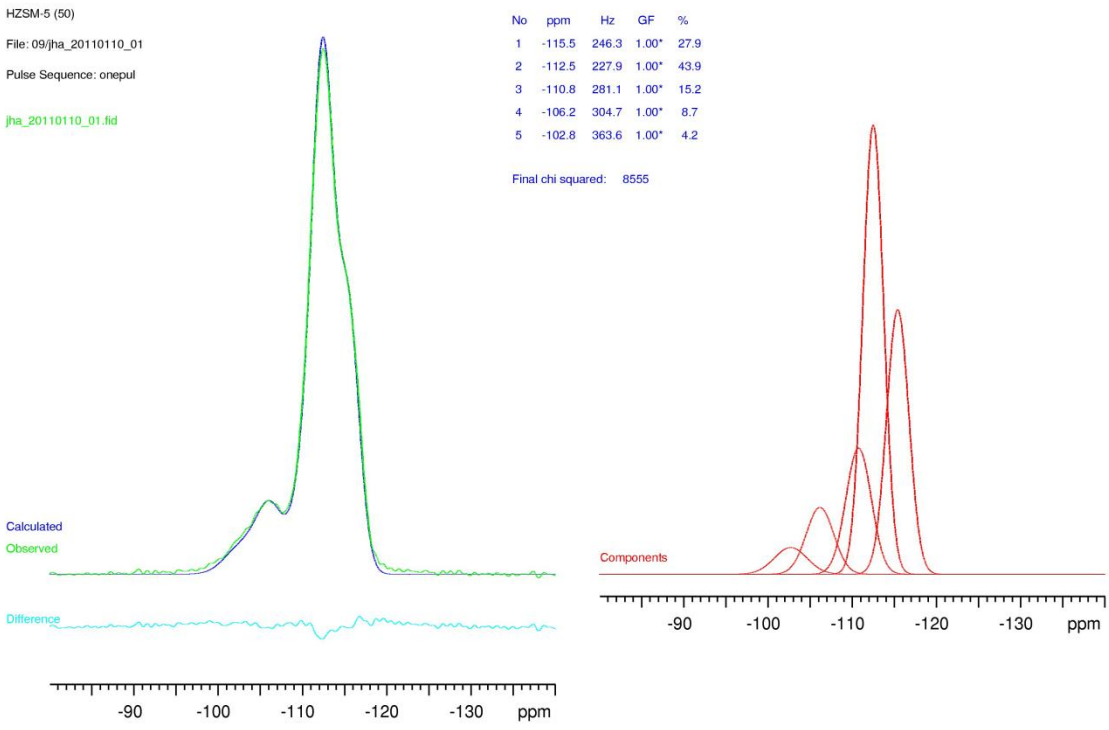

Figure 9.2: Deconvolution of ^{29}Si spectra of H(50) 550 4 h.

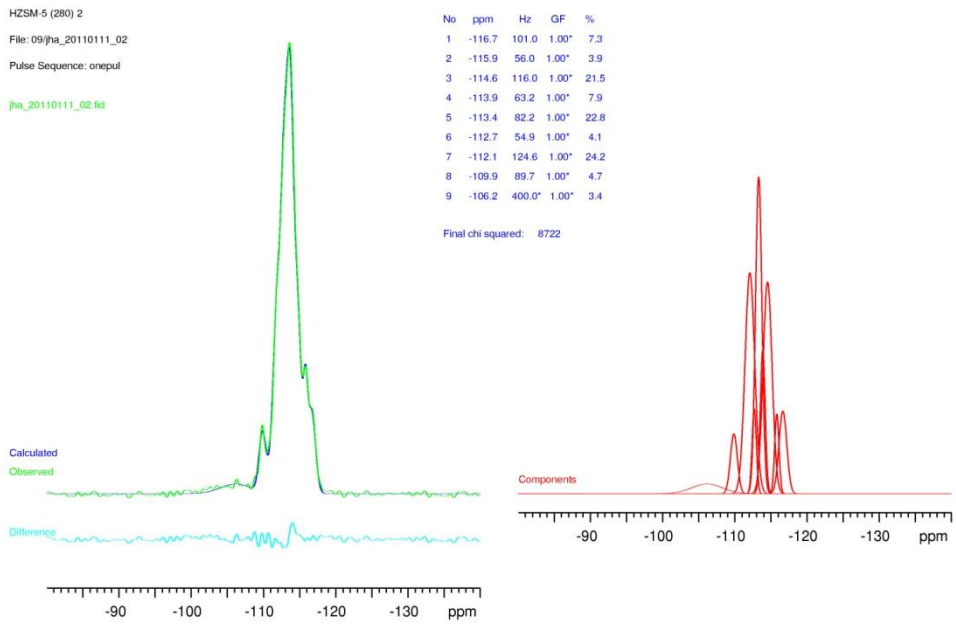

Figure 9.3: Deconvolution of ^{29}Si spectra of H(280) 550 4 h

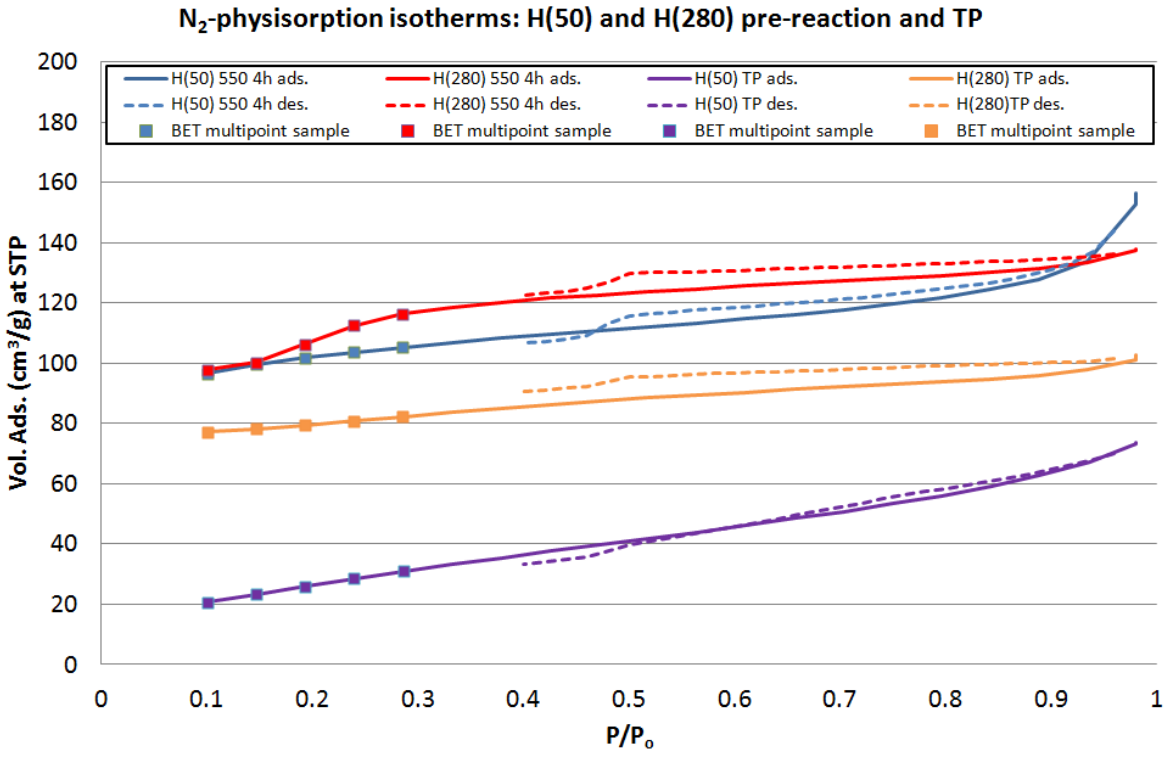

Figure 9.4: H(50) 550 4 h TP and H(280) 550 4 h TP adsorption isotherms.

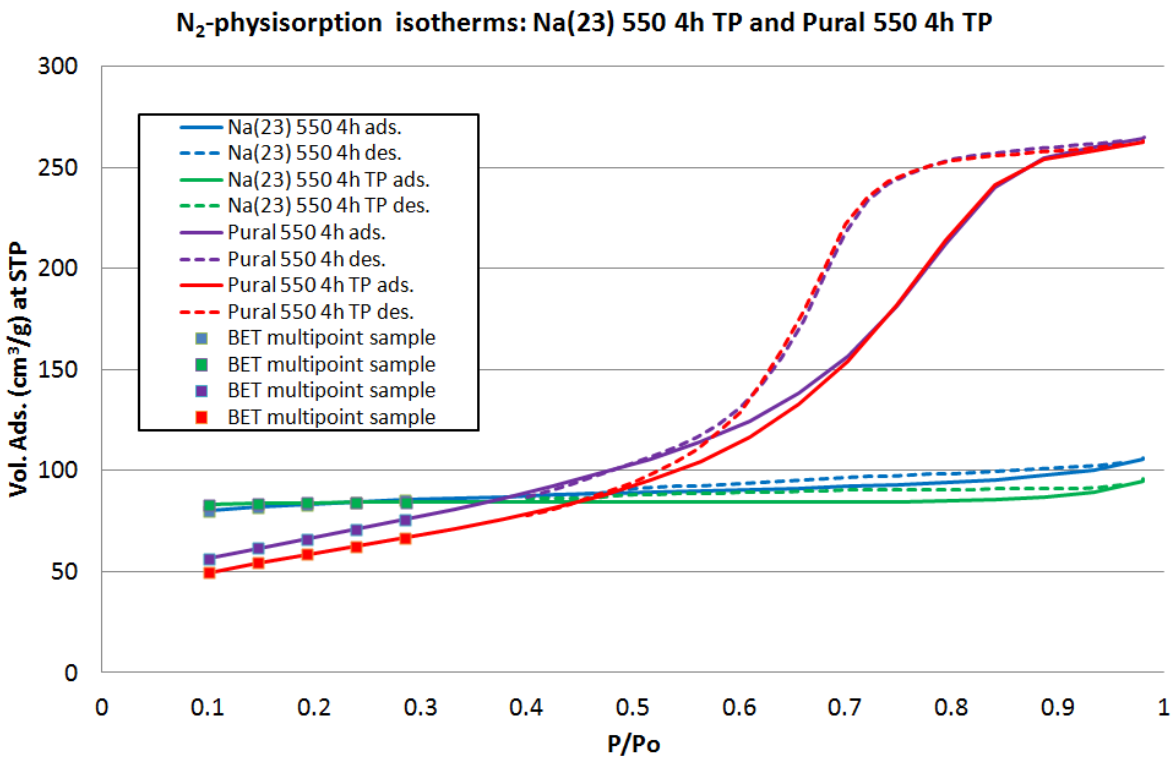

Figure 9.5: Na(23) 550 4 h TP and Pural 550 4 h TP adsorption isotherms.

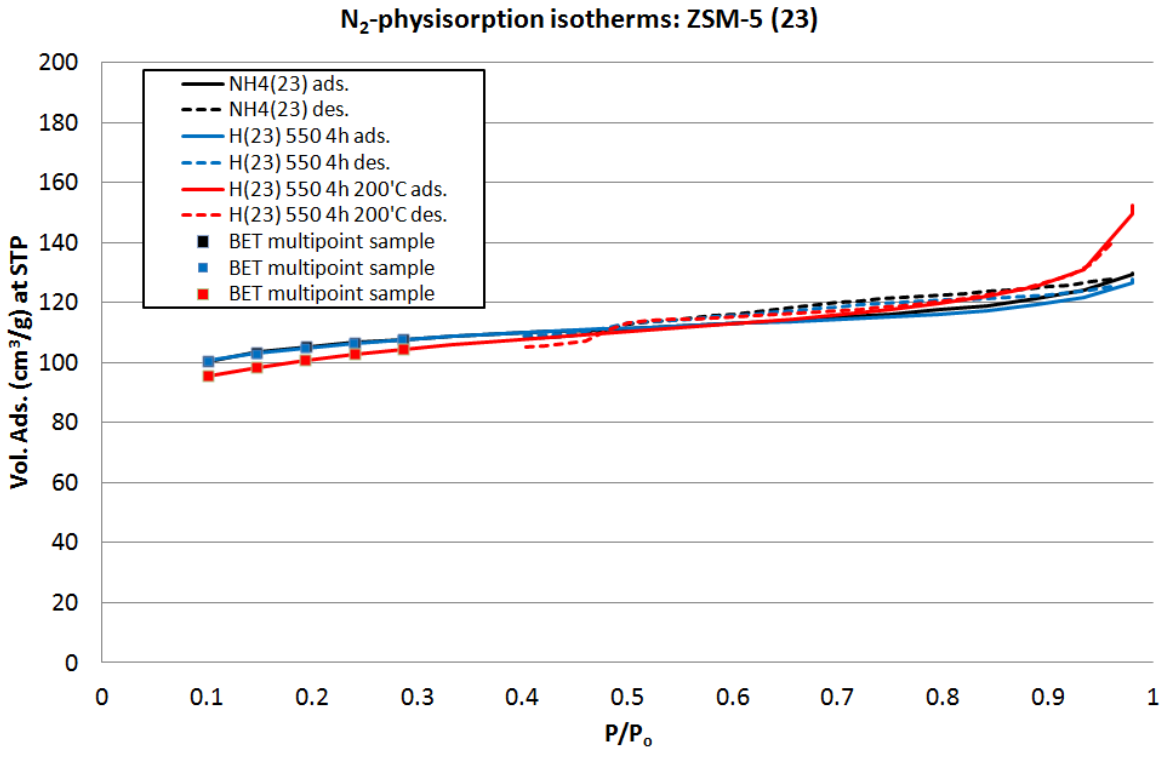

Figure 9.6: ZSM-5 (23) adsorption isotherms.

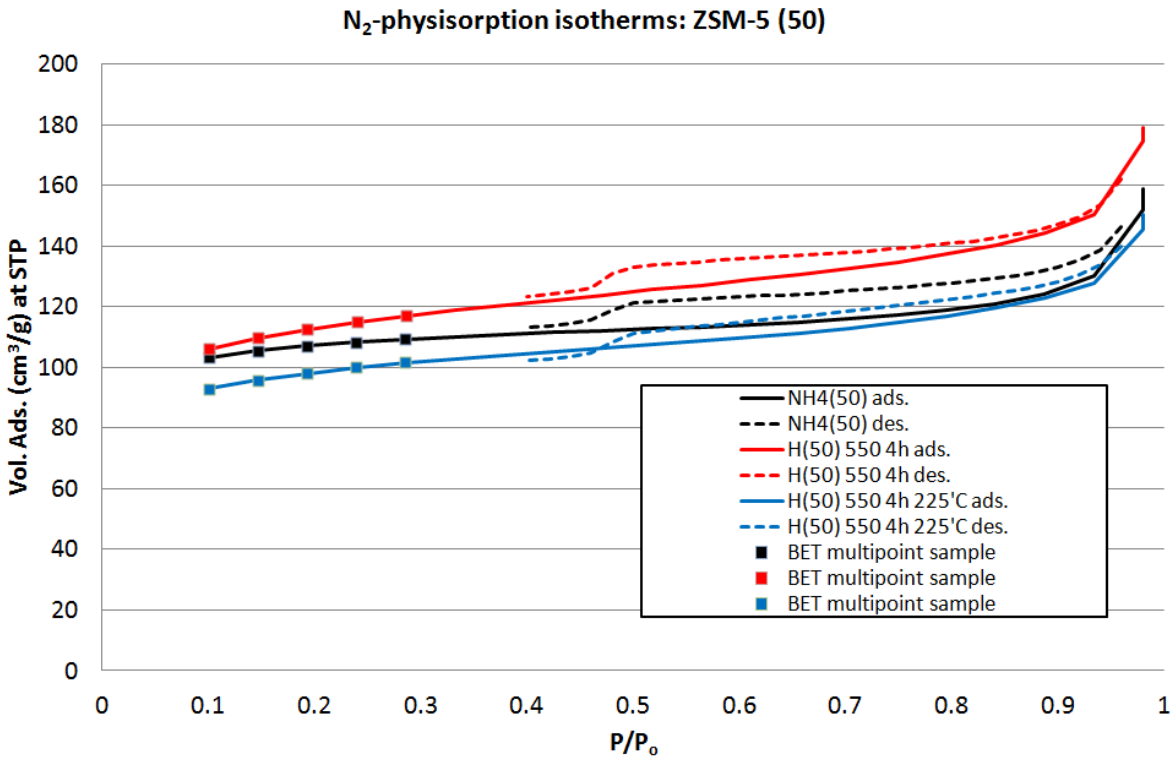

Figure 9.7: ZSM-5 (50) adsorption isotherms.

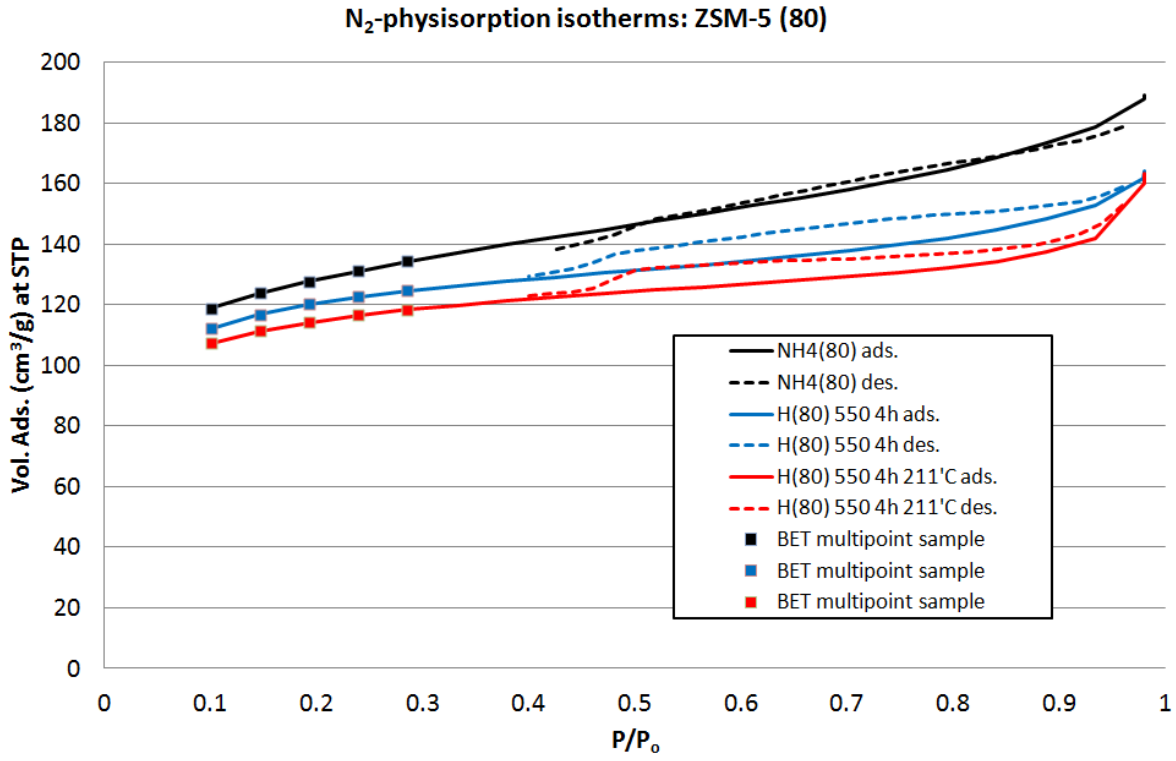

Figure 9.8: ZSM-5 (80) adsorption isotherms.

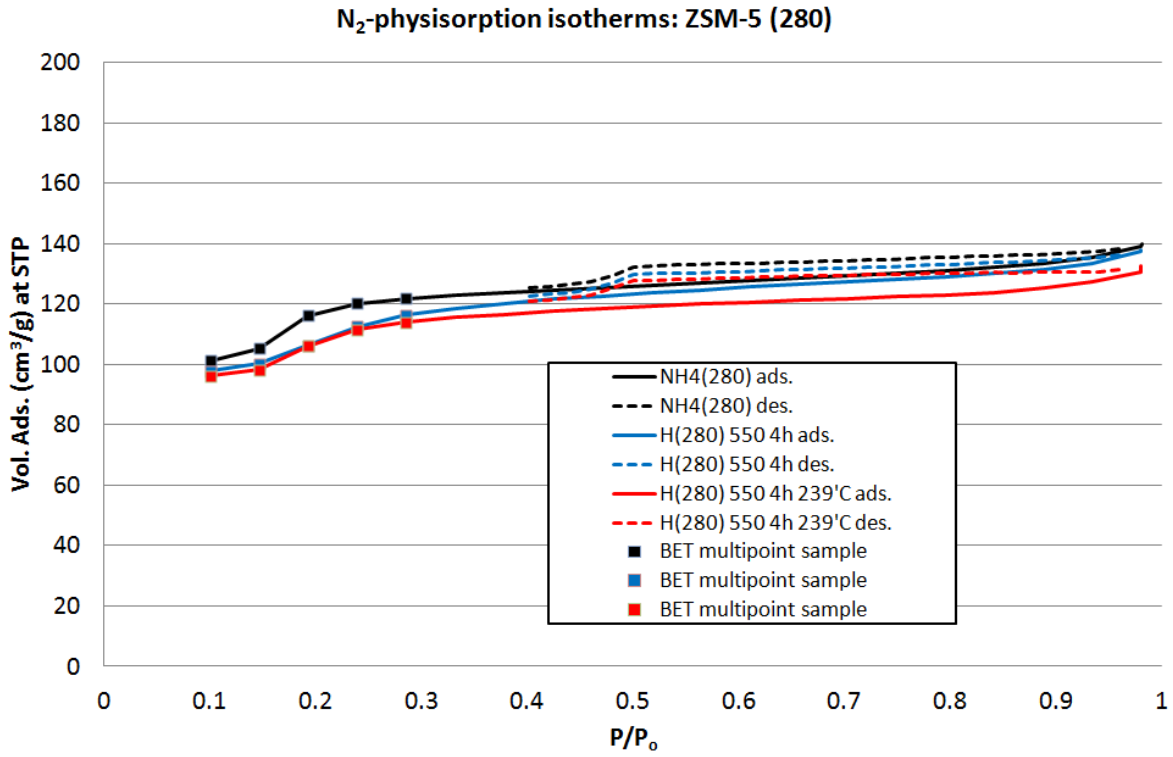

Figure 9.9: ZSM-5 (280) adsorption isotherms.

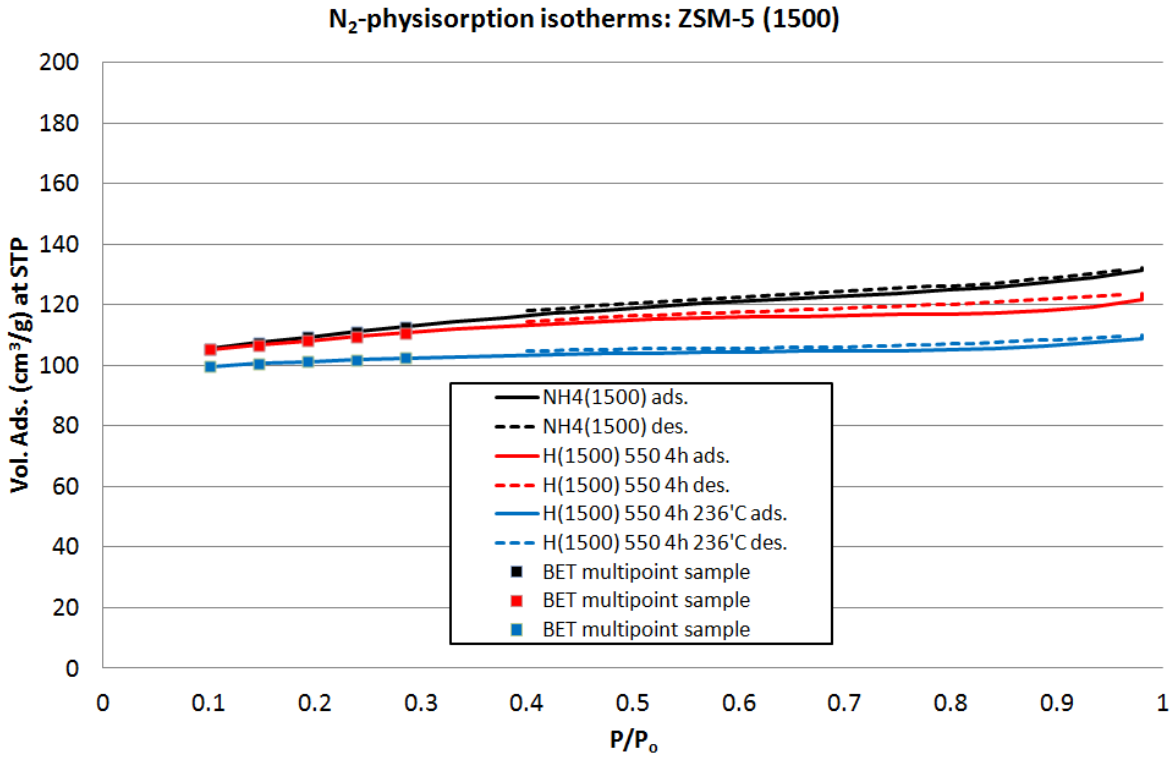

Figure 9.10: ZSM-5 (1500) adsorption isotherms.

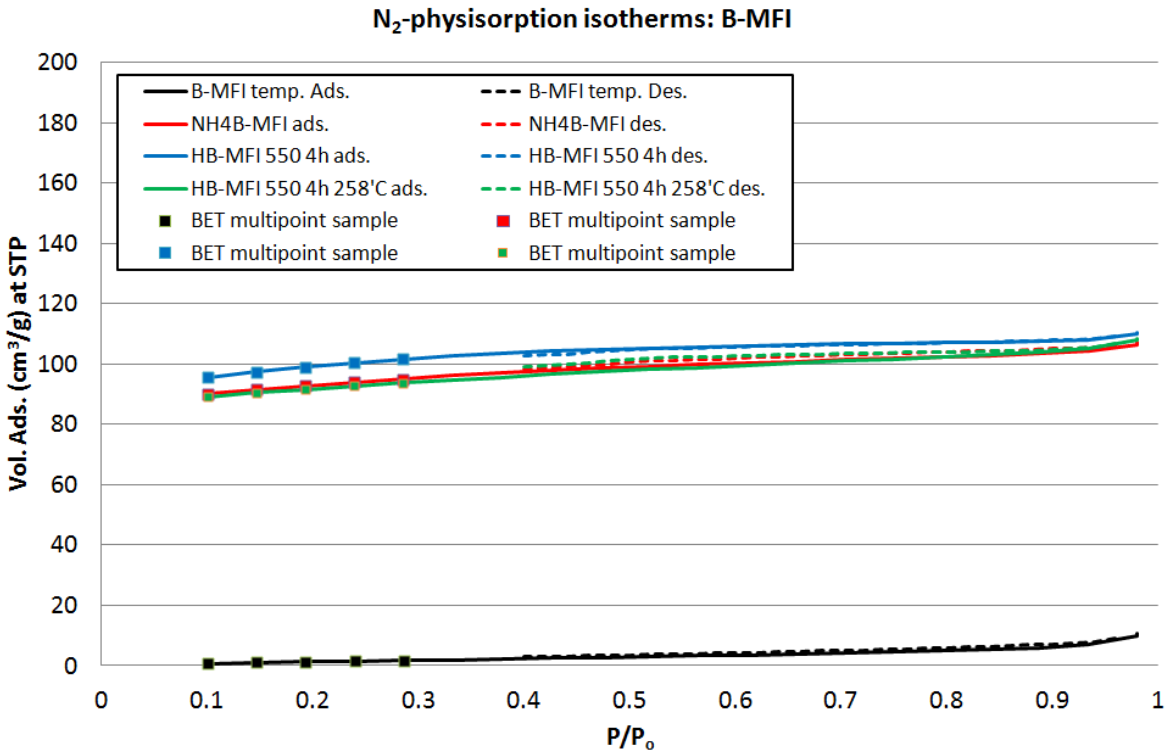

Figure 9.11: B-MFI adsorption isotherms**.**

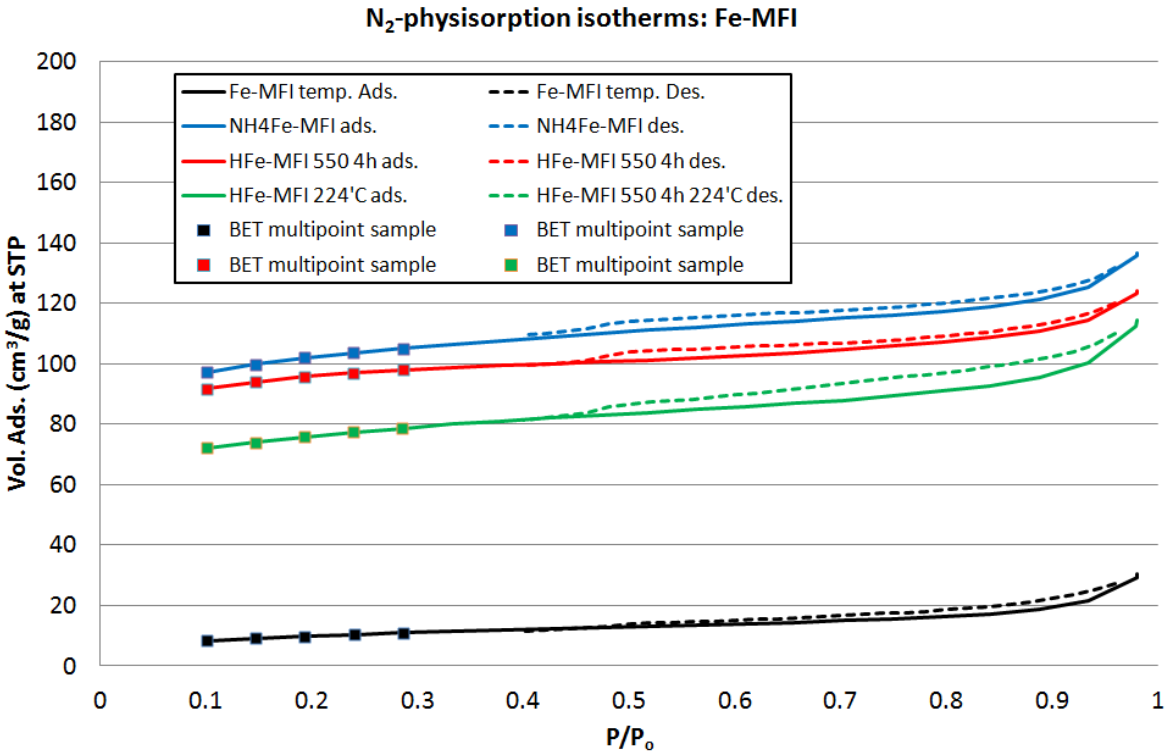

Figure 9.12: Fe-MFI adsorption isotherms

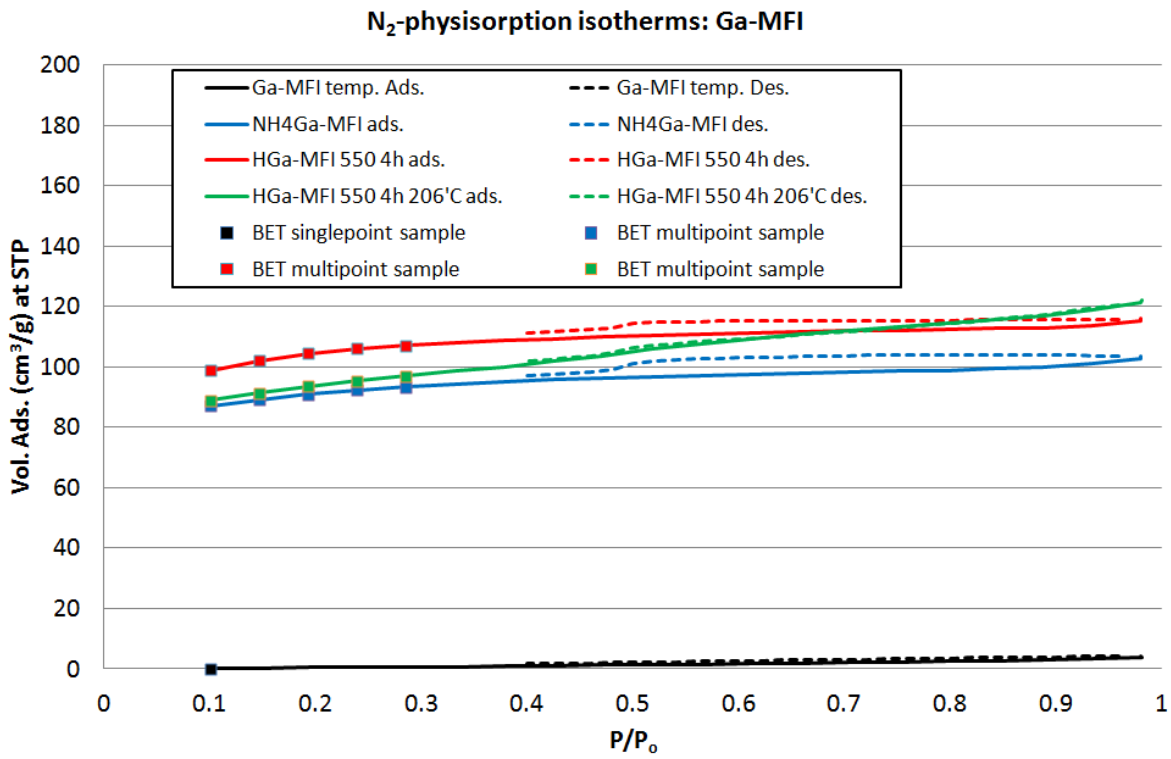

Figure 9.13: Ga-MFI adsorption isotherms

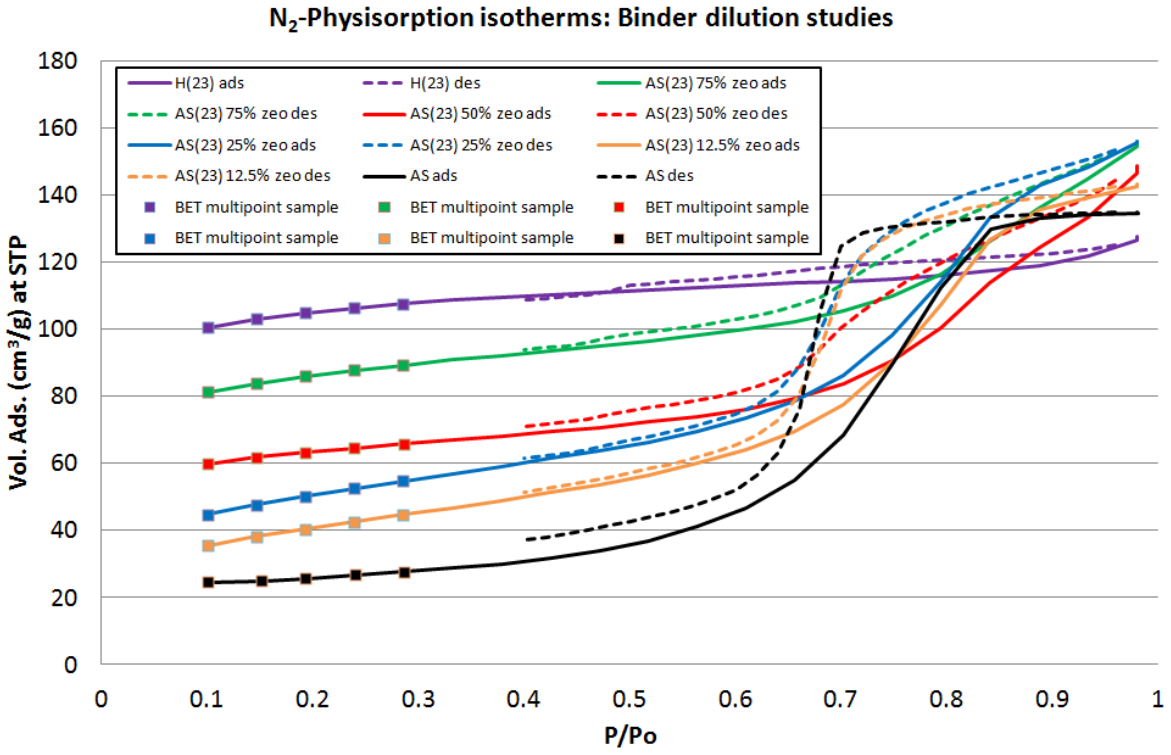

Figure 9.14: Binder dilution adsorption isotherms

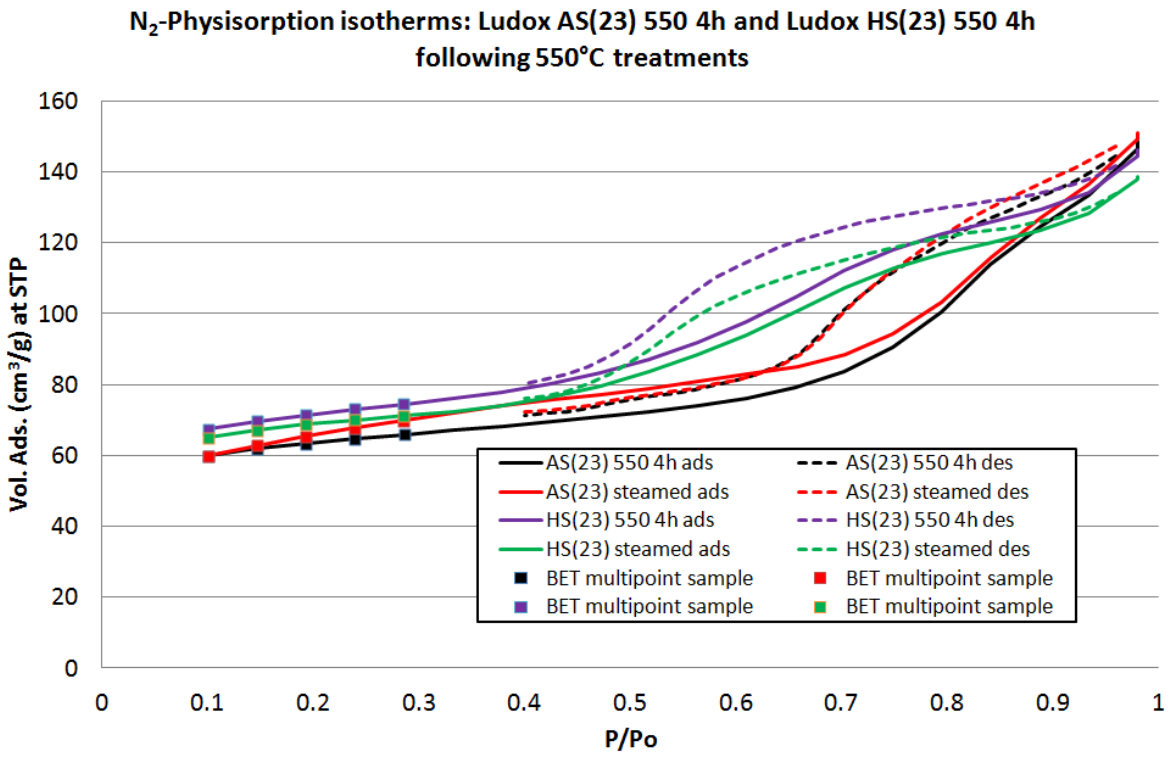

Figure 9.15: Ludox AS(23) and HS(23) 550 °C treated adsorption isotherms

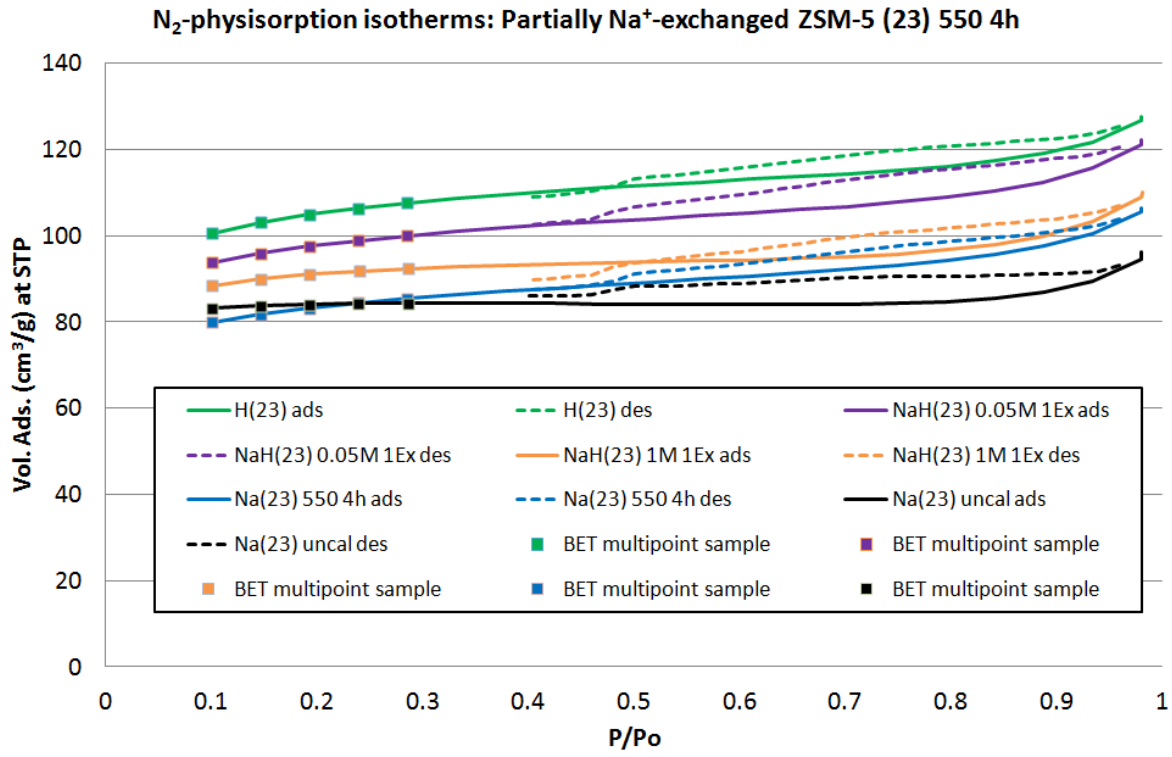

Figure 9.16: Sodium-exchanged ZSM-5(23) adsorption isotherms

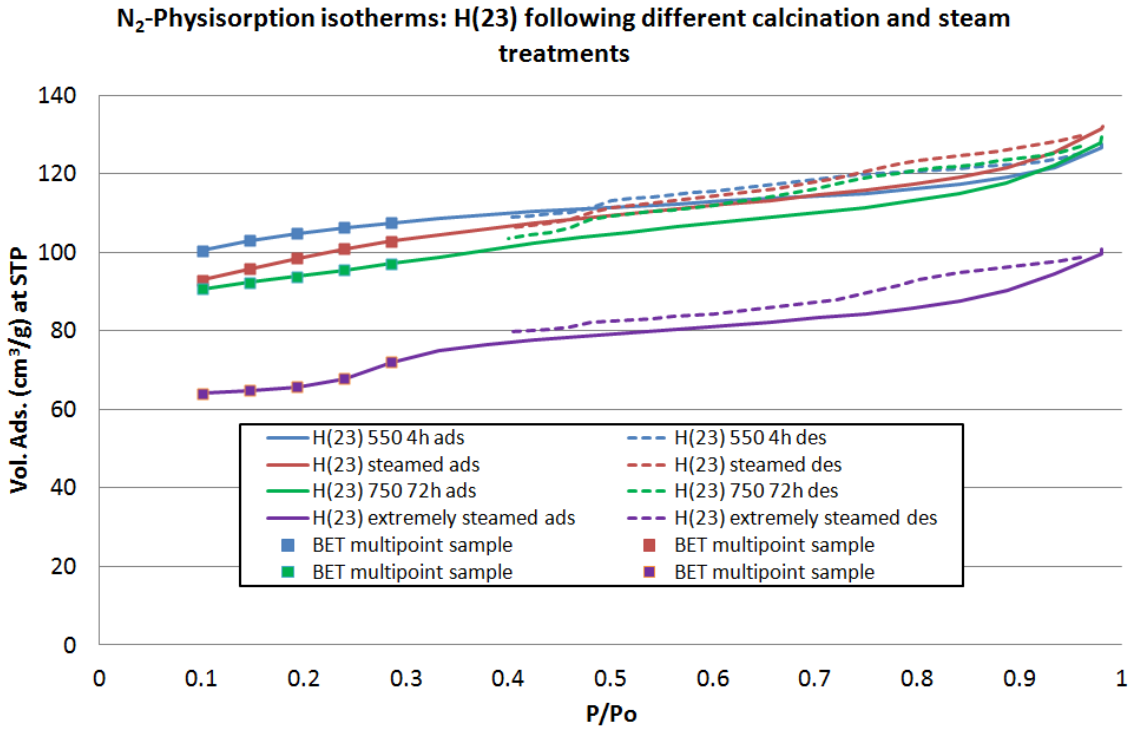

Figure 9.17: Thermally and hydrothermally treated H(23) 550 4 h adsorption isotherms.

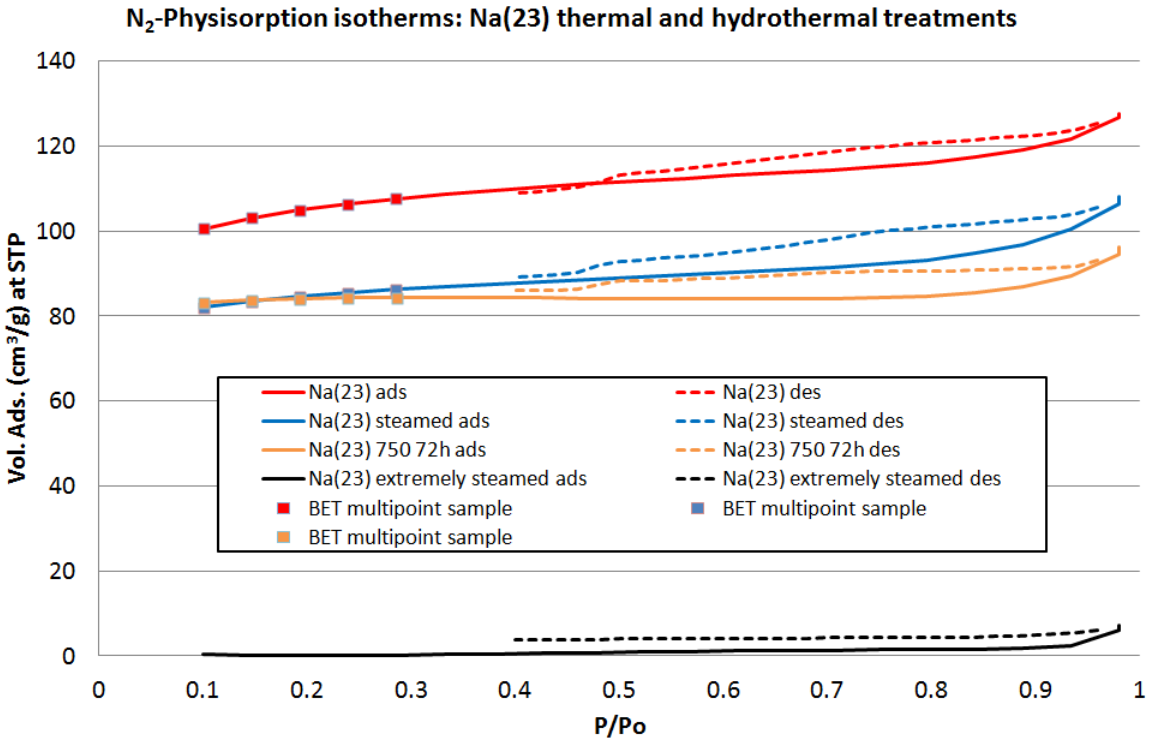

Figure 9.18: Thermally and hydrothermally treated Na(23) 550 4 h adsorption isotherms.

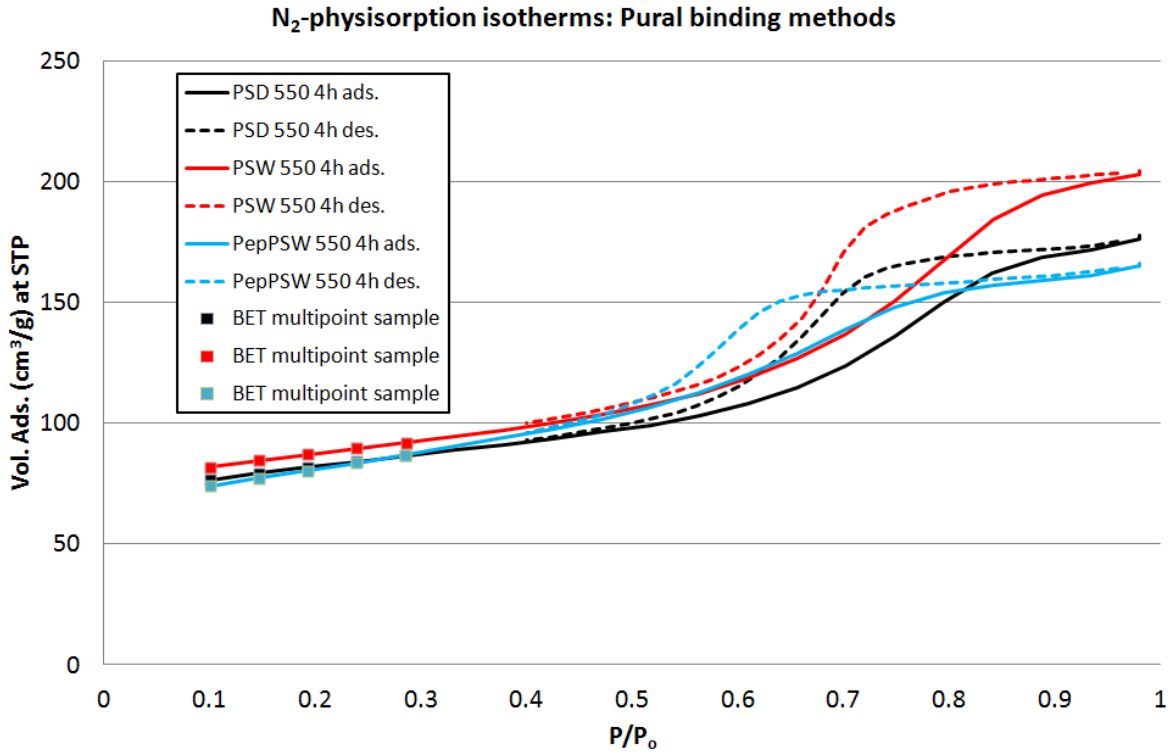

Figure 9.19: Pural binding methods adsorption isotherms